Design, Modeling and Control of Continuum Robots and Dexterous Wrists with Applications to Transurethral Bladder Cancer Resection

By

Nima Sarli

Dissertation

Submitted to the Faculty of the

Graduate School of Vanderbilt University

in partial fulfillment of the requirements

for the degree of

DOCTOR OF PHILOSOPHY

in

Mechanical Engineering

September 30, 2018

Nashville, Tennessee

Approved:

Nabil Simaan, Ph.D.

Michael Goldfarb, Ph.D.

Karl Zelik, Ph.D.

Jason Mitchell, Ph.D.

Duke S. Herrell, M.D.

To my dearest parents

Maryam Kor and Ghol-John Sarli

& to my beloved sister

Sarah.

ACKNOWLEDGMENTS

I would like to thank my advisor, Professor Nabil Simaan. It was his tremendous knowledge, valuable guidance, continuous support and unabated dedication that shaped me into what I am today in my profession and made this dissertation possible. I cannot acknowledge him enough for this.

I would like to thank my dear girlfriend, Fatemeh Hadi for her support, patience, companionship and sacrifices she made during the past five years.

I am indebted to my colleagues for their valuable suggestions, for helping make my learning an enjoyable and stimulating experience and for being great parties in five great years of my life. Long Wang, Rashid Yasin, Giuseppe Del Giudice, Andrew Orekhov, Colette Abah, Jason Pile, Haoran Yu, Rajarshi Roy and Aditya Bhowmick. Thank you!

My gratitude goes as well to the mechanical engineering department staff Myrtle Daniels, Jean Miller, Suzanne Weiss, Renee Tomlin and Paul Van Wulven. It was their help that made this journey easier.

Lastly, I wish to thank my dearest parents and sister whose continuous support and patience in these years away from them have given me the motivation to realize this achievement. To you I dedicate this thesis!

TABLE OF CONTENTS

LIST OF TABLES

LIST OF FIGURES

CHAPTER 1

INTRODUCTION

The earliest application of computer-guided robotic surgery was in the area of neurosurgery where a modified Puma 200 robot was used to perform a stereotactic brain biopsy. Neurosurgery was the first area where surgical intervention was experimented since the skull rigidity facilitates localization of anatomical landmarks. This procedure was carried out at Memorial Hospital of Los Angeles in 1985 by Kwoh *et al.* [1, 2]. Ever since, computer-aided surgery (Also loosely called robotic surgery) has continued to disrupt the surgical arena. This has impacted orthopedics [3–13], neurosurgery [14–16], cardiology [17–24] and urology (e.g. see review in [25], works on laparoscopic nephrectomy [26–35], prostatectomy [36–39] and brachytherapy [40–42]).

In particular, urology has seen a substantial impact since researchers began to use robots to overcome instrument limitations in laparoscopy to be able to carry out more complicated tasks (for example, see [43–45]). The first surgical robot approved by the Food and Drug Administration called AESOP (Computer Motion Inc., Goleta, California, USA) maneuvered endoscopes by receiving user inputs from a foot pedal/joystick [46]. The use of AESOP in laparoscopic procedures eliminated the need for human camera assistants, reduced instruments collision and provided more stable camera control [47, 48]. Later, Computer Motion developed ZEUS robot, a master-slave tele-presence system that incorporated an AESOP and three other similar robotic arms to hold and position instruments. This system was teleoperated by a surgeon sitting at a surgeon's console. In 1997, the da Vinci surgical system (Intuitive Surgical®, Inc. Sunnyvale, CA, USA) was used to perform a laparoscopic

cholecystectomy in Belgium [49]. Like ZEUS, the da Vinci is a master-slave robotic system. It consists of a surgeons console , a patient-side cart with three or four robotic arms, a visualization system and special cable-driven wrists (EndoWrist®). The da Vinci replicates the surgeons hand motions at the master hands into the corresponding scaled-down movements of instruments inside the patient and it also filters tremors. Currently, the da Vinci platform is the predominant commercial surgical robotic system with more than 3 million minimally invasive procedures performed since 2000, mostly for laparoscopic prostatectomies and hysterectomies [50–52].

Yet, this progress in robotic surgery has not crossed over to transurethral resection of bladder tumors (TURBT), a procedure where the bladder tumors are resected by a resectoscope. Instrument limitations such as reduced resection accuracy, lack of intracavitary tool-tip dexterity, sparse instrumentation repertoire and lack of *in vivo* feedback have impeded progress in TURBT improvement. The goals of this dissertation is to explore the mechanics of manual resection to shed light on its performance and then to introduce a first surgical system for TURBT. This demands an intricate mechanical design but also more importantly requires devising novel algorithms to make viable a surgical procedure in such a confined, flexible and free-form space as urinary bladder.

Among all cancers, bladder cancer is the 7^{th} most commonly diagnosed in males and the 11^{th} in females worldwide [53]. According to the American Cancer Society® report, it is the 4^{th} most common cancer among men in US [54]. Approximately 75% of all bladder cancers is categorized as non-muscle-invasive (NMIBC) that are tumors either confined to the mucosa (stage Ta, CIS) or sub-mucosa (stage T1) [55]. Although TURBT remains the gold standard for the diagnosis and treatment of NMIBC, it suffers several limitations. A major challenge is insufficient resection [56]. Surgeons often have to trade off two risks: deep resections at the cost of increased chances for bladder perforation or shallower resections at the cost of higher likelihood of leaving behind residual tumor. Apart from tool dexterity limitations, the tumor boundaries and depth of penetration is often not distinguishable.

All in all, it is not possible to perform en-bloc resection in contrast with general oncologic principles. Therefore, the tumors are removed piecewise hence increasing the likelihood of recurrence which would demand repeat procedures (restaging TUR or re-TUR). In a study by Adiyat *et al.* [57], 70% of patients had visible tumor at the time of re-TUR and 30% had tumors at the original site. Considering all these factors, bladder cancer has the highest overall treatment costs per patient among all cancers [58–60]. A more thorough investigation into challenges of TURBT and its current status is covered in chapter 2 of this dissertation.

1.1 Motivation and Knowledge Gaps

This dissertation is motivated by four key knowledge gaps that form the foundation for its contribution. These knowledge gaps include: (a) Quantification of surgical performance during manual resection of bladder cancer tumors, (b) Collaborative telemanipulation requirements for successful TURBT, (c) The challenges and the potentials of robot-assisted TURBT have not been explored yet. (d) A thorough kinematic/static analysis of an open-ended wire-driven wrist. The following is a detailed description of these items:

Baseline for manual resection: The current practice of manual transurethral resection of bladder cancer tumors lacks performance benchmarks. Several studies have postulated that surgeons tend to under-resect tumors (e.g. [57, 61]) and that this could be an important factor to repeated resection procedures. There is no published work characterizing the kinematic limitations of the current repertoire of instrumentation or presenting estimates to the expected resection accuracy in different anatomical regions of the bladder.

Assistive telemanipulation requirements for successful TURBT: When accessing deep anatomy through a narrow access route such as in TURBT, several problems arise that challenge our current knowledge of how to deploy robotic intervention successfully. These challenges stem from the fact that the robots needed for completing such surgical procedures often have a high number of degrees of freedom and they are required to coordinate

visualization and manipulation while respecting limitations of both visualization and manipulation tools. For example, the TURBT robotic system presented in this work has nine actuated joints (excluding the distal laser arm). Also, the dexterous robot (a continuum robot) and the visualization endoscope emanate from a narrow access channel thereby coupling the manipulation and the management of the endoscope motion in order to successfully manipulate the robot without occluding visualization of the surgical site. Therefore, there is a need for redundancy resolution algorithms that can address the specific needs of TURBT while allowing the user to use a typical telemanipulation interface. These algorithms must also include coordinated motion of the robot and the endoscope thereby alleviating the need for the user or an assistant to control visualization.

Deployability challenges for robot-assisted TURBT: The feasibility of robot-assisted TURBT has not been explored yet. The research community currently lacks an understanding of the challenges facing successful deployment of such robotic systems for TURBT. Such knowledge is only acquired through experimental testing of prototype systems such as the one presented in this work. Lessons learned through this experience will hopefully inform designers of future systems for TURBT.

Performance characterization of open-ended wire-driven wrists: The design of surgical systems for confined spaces often requires dexterous wrists to augment distal dexterity. Such wrists allow delicate motions in a small workspace with often more range of motion than human hands can provide. In fact, this has been one of the key advantages that robotic surgery has offered since its inception. The majority of the existing commercial surgical wrists often use a pull/release *closed-loop* wire transmission where a single motor is used to drive a closed-loop wire in both directions. In such designs, the wire loop initially requires a relatively high pretensioning to ensure it does not go slack during operation and this can generate friction and substantial stresses on the wires. In addition, wire rope extension due to fatigue and creep limits the useful life-cycle of surgical instruments with closed-loop actuation.

In an alternative wire transmission known as *open-ended* wire drive, one end of a wire is connected to the moving link while the other end is pulled by an actuator. In this paradigm, pretension of each wire is directly affected by its dedicated actuator. As the number of actuators is more than the degrees of freedom, it is possible to have a more accurate compensation of motion losses and estimation of external forces. In addition, such devices can provide robustness to wire creep thereby potentially increasing the useful lifespan of surgical tools. To design and analyze such wrists, it is important to consider the effects of wire forces on their characteristics such as payload, workspace, positioning accuracy, etc.

1.2 Scope of Work

To improve TURBT, key advances in four areas are essential: 1. Improve intra-vesicular surveillance and staging, 2. Improve resection accuracy, dexterity and instrument reach in all aspects of the bladder, 3. Provide means for delivering a future imaging modality to identify tumors *in vivo*, 4. Provide a means for monitoring resection depth and enforcing methods to minimize perforation risks.

A major core of this scientific endeavor was in developing a robotic platform for bladder surveillance and tumor resection that addresses the aforementioned required advancements. This transurethral surgical platform henceforth called **TURBot** (TURBT Robot) (see Fig. (1.1)) is deployed transurethrally in the bladder and is capable of accessing all regions, in particular the poorly accessible bladder neck and performing resections/ablations. Through the three $\varnothing 1.8mm$ working channels of TURBot's miniature multi-backbone continuum robot (MBCR), various instruments such as graspers, custom flexible cameras and other imaging probes can be deployed to facilitate resection/ablation and provide sensory feedback. This concept of an MBCR for TURBT (called Prototype 0) was first presented in [62, 63] where an early feasibility study was performed on phantom models and an explanted bovine bladder. Prototype 0 lacked several key elements needed for successful deployment of TURBT, which motivated the development of TURBot. In this regard, TUR-

Bot is a first robotic system deployed for evaluation in animal experiments. With continued development and clinical translation, this system could significantly improve the standard of care for TURBT while overcoming surgeon skill barriers and eventually reducing recurrence rates and repeat resections.

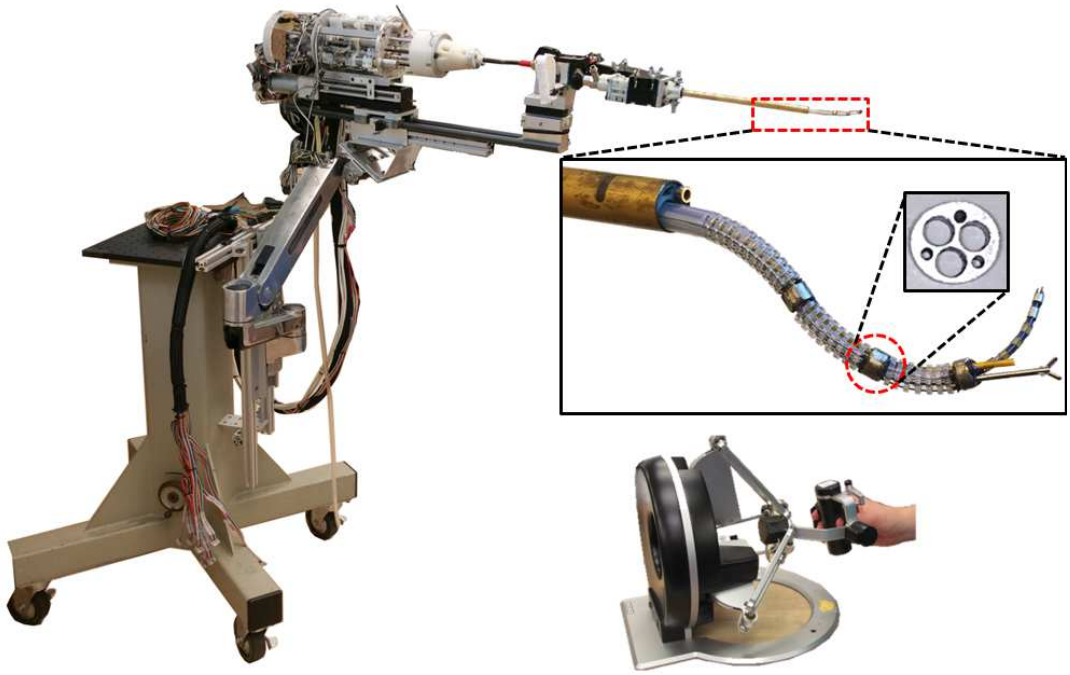

Figure 1.1: TURBot: a master-slave robotic system for surveillance and transurethral resection of urinary bladder.

Apart from development of precisely-controllable dexterous tools, in order to enhance the current status of TURBT, it is also essential to understand the kinematics of manual resection and to characterize this procedure quantitatively. This was a motivation to develop a kinematic model and to introduce performance measures based on this model. This not only identifies and allows comparison of resection quality on different bladder regions, but also establishes a baseline for manual resection that can be used for assessment of future novel tools and robots for TURBT. This topic is discussed in detail in chapter (3).

At the end of this dissertation, a new avenue is explored that regards a thorough exposition of an open-ended wire-actuated wrist for robotic minimally-invasive surgery (MIS) applications. Essentially, the wrist as illustrated in Fig. (1.2), has two parallelogram mech-

anisms incorporated with the design in [64]. The wrist has a pitch and dual yaws (grasping) motion (See Fig. (1.2)-a). The focus of the study is on the analysis of the architecture and the particular mechanical embodiment simply provides an example case study.

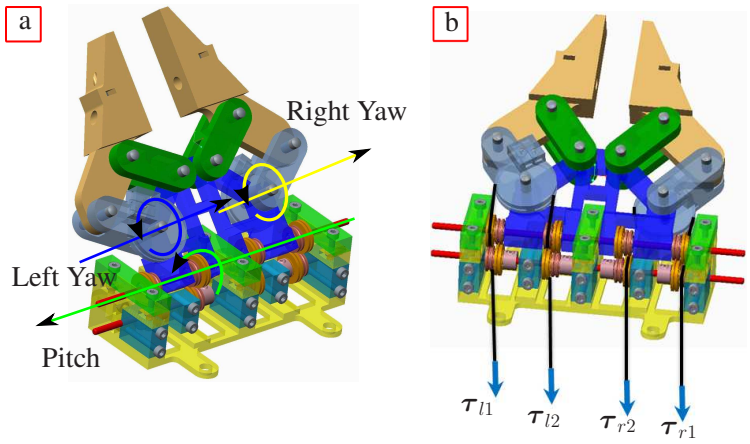

Figure 1.2: 3-DoF wire-driven wrist: (a) Degrees of freedom include pitch, left and right yaw, (b) Wire routing: Antagonistic actuation of τ_{l1},τ_{l2} and τ_{r1},τ_{r2} in pairs generates pitch motion while antagonistic actuation of τ_{l1} and τ_{l2} (τ_{r1} and τ_{r2}) yields left (right) yaw or grasping motion.

The following enumerates the contributions presented in this dissertation:

1. Kinematic modeling of resection by a standard resectoscope: The direct and inverse kinematics as well instantaneous kinematics are developed for manual resection. This models helps provides an important tool in studying resection accuracy/dexterity in different areas of bladder.

2. Characterization of resection performance of the current standard resectoscopes: Using the developed kinematic model of manual resection, several performance measures are introduced to evaluate resection dexterity/accuracy. These measures are then correlated with experimental data to determine which are more relevant in defining resection accuracy in lateral and in depth directions.

3. Constrained redundancy resolution of a multi-segment continuum robot: To control the MBCR end-effector while respecting the constrained imposed by the resectoscope sheath access channel (tubular constraint), when a portion of a segment retracts

inside the sheath, the entire segment posture should go straight to ensure TURBot safety. However, this causes loss of the robot mobility which in turn jeopardizes successful task completion. An elaborate high-level control scheme is developed in chapter (5) to address this problem. Depending on how many segments of the MBCR are constrained by the tubular constraint, the task description and the instantaneous kinematic changes. The proposed control architecture takes into account these changes and switches smoothly between different methods to efficiently utilize the TURBot available dexterity to accomplish the task while warranting tubular constraint.

4. Telemanipulation paradigms for transluminal surgical robots: The constrained redundancy resolution should be incorporated within higher-level telemanipulation framework. The user interacts with this framework by providing reference (command) motion signals by using a master haptic interface. Two telemanipulation paradigms namely *eye-in-hand* and *eye-to-hand* arise in the context of robotic MIS systems. The former is generally used when the primary visual feedback is supplied by a camera mounted on the robot end-effector. The latter is utilized when the camera is placed in a stationary location viewing the robot and the surgical site. This method was used for phantom and animal studies in chapter (6). This method is explained in more details in section (5.2.2).

5. Redundancy resolution to minimize visual occlusion: A problem that arises in transluminal robotic surgery (or in NOTES robotic surgery in general) is the visual occlusion caused by the presence of the robot and other tools in the field of view. During robotic surgery - and especially when using continuum robots for added dexterity - this problem is exacerbated because the body of the continuum robot often emanates from the access channel in close proximity to the tip of the endoscope. To minimize the encumbered occlusion, a redundancy resolution algorithm is proposed for

the control of a continuum robot that utilizes the robot redundancy to drive itself outside the field of view while completing the task with its end-effector. The proposed method is general and can be applied to any redundant robot.

6. Analysis of an open-ended wrist architecture for Robotic MIS: The focus and the contribution is on the analysis of the architecture rather than the particular mechanical embodiment. The relationship between the jaws forces and the wire loads are derived and the wrist positioning error, compliance and load bearing capability are analyzed. A basic model for actuation compensation is presented. The methods developed for these analyses are general and can be applied to any open-ended wire-driven wrist.

1.3 Outline

This dissertation is organized as follows: Chapter (2) covers a brief history of computer-aided surgery in urology and an overview of current status of TURBT. In chapter (3), a standard resectoscope performance in TURBT is analysed and evaluated by simulations as well as experimentally. In chapter (4), the design details of the TURBot system are explained. The calibration and the control algorithms of TURBot are brought in chapter (5). In chapter (6), the system is evaluated through phantom and animal studies. The minimization of visual occlusion by a redundancy resolved-rate control method is described in chapter (7). In chapter (8), modeling, analysis and evaluation of the 3-DoF wire-driven wrist is presented. This thesis is concluded in chapter (9) by presenting a summary of all chapters and proposition of potential future research directions.

CHAPTER 2

BACKGROUND

2.1 A Brief History of Computer-Aided Surgery in Urology

The first case of application of robotic principles in urology was performed in Imperial College London in 1989 where Davies *et al.* used an industrial 6-DoF PUMA robot to manipulate a resectoscope to perform transurethral resection of prostates (TURP) on a potato enclosed in a box (See Fig. (2.1)) [36, 65]. TURP is a surgical procedure to treat urinary problems due to the prostate enlargement. They performed some initial exploratory human trials in 1991 to identify challenges and required improvements [66].

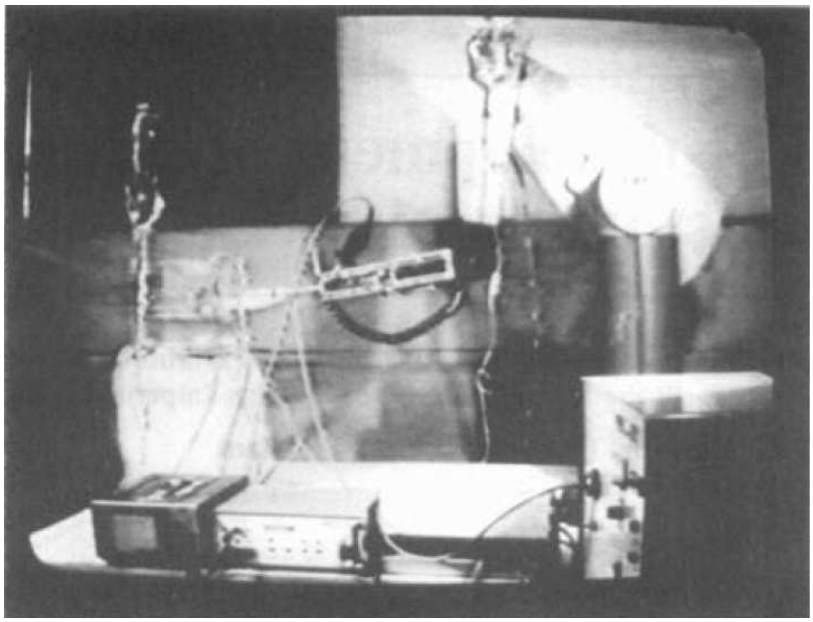

Figure 2.1: Experimental setup for a feasibility study of using robots for prostate surgery: a PUMA robot resecting a potato enclosed in a box ([36])

Their eventual prototype called PROBOT consisted of a circular safety frame to ensure

the robot did not violate its workspace and a 4-DoF mechanized conventional resectoscope shown in Fig. (2.2). This allowed rotation, tilting and insertion of an entire resectoscope along with extension/retraction of the cutting element (e.g. a loop) though the resectoscope. They tested PROBOT in 1997 on 10 patients for full (or nearly full) prostate resection [66]. In all cases, complete relief from urine outflow obstruction was reported.

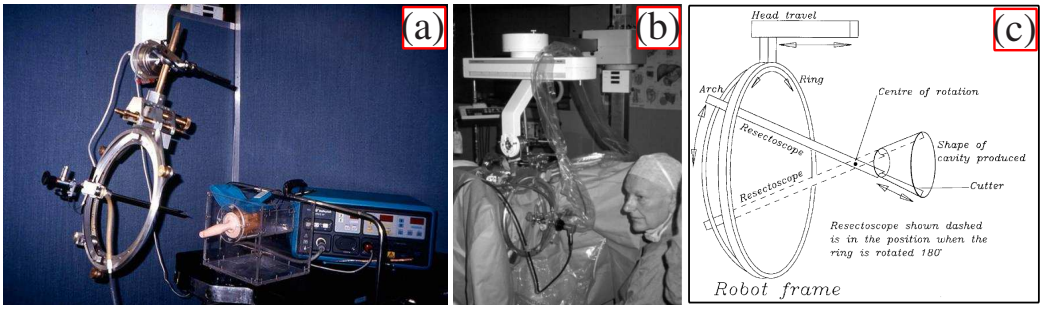

Figure 2.2: (a) PROBOT: first robot in urology used for prostate resection, (b) PROBOT in clinical trails, (c) PROBOT degrees of freedom: rotation, tilt and insertion/retraction of the resectoscope and the cutting element.(image source:www.wired.com, [67],[66])

Telerobotic was starting to flourish in 1990's when laparoscopy was experiencing major roadblocks. The instrument repertoire in manual laparoscopy was limited and hence only useful for relatively simple surgical tasks for instance tissue removal and basic tissue closure. Therefore, several researchers began to combine robotics with MIS to synergise more efficient tools and techniques to perform more complicated surgical procedures [43–45]. Among them, Taylor *et al.* at IBM Watson Research Center in Yorktown Heights, New York developed a 7-DoF Laparoscopic Assistant Robotic System (LARS) that holds and pivots the laparoscope about the point where it enters the abdominal wall [45]. The LARS mechanical structure is based on a parallel four-bar linkage and a remote-center-of-motion (RCM) to accommodate the patient's abdominal entry port.

In 1994, the Food and Drug Administration (FDA) approved the first surgical robot. AESOP (Automated Endoscopic System for Optimal Positioning) developed by Computer Motion Inc. (Goleta, California) was a robotic arm to position endoscopes that could be controlled by foot pedal/joystick and later by voice commands [46]. The use of AESOP

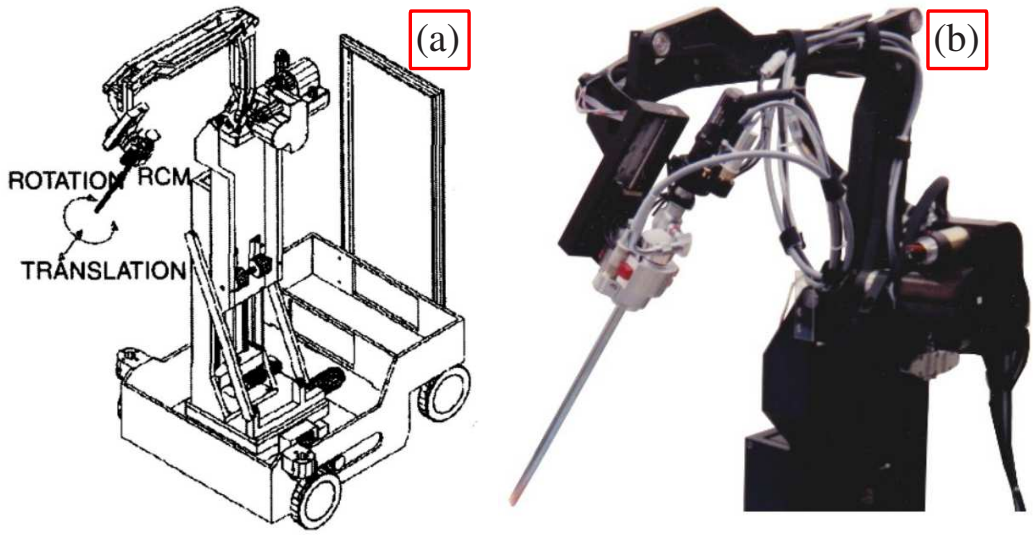

Figure 2.3: Laparoscopic Assistant Robotic System (LARS): (a) schematic diagram ([45]), (b) a picture of upper portion ([68]).

in laparoscopic procedures eliminated the need for human camera assistants, reduced instruments collision and provided more stable camera control [47, 48]. Later, Computer Motion used similar arms to hold and position instruments along with an AESOP to position the laparoscopic camera. This system called ZEUS consists of a surgeons console and three AESOP arms that attached to the patient operating table. In June 1998, Dr. Frank Diamiano performed a reanastomosis of a fallopian tube using ZEUS [69]. This system was cleared by FDA in 2001. Combined with a telecommunication system (marketed under the name SOCRATES™ Robotic Telecollaboration System), ZEUS opened the area of telesurgey and telementoring where the surgeon or trainer can be located thousands of miles away from the patient or the trainee. This culminated in Lindbergh Operation in 2001, the first transcontinental robot-assisted laparoscopic cholecystectomy (removal of gall bladder) performed by Jacques Marescaux operating in New York, USA on a patient in Strasbourg, France [70].

The past decade has seen the emergence of a few commercial systems in urology. Sensei® X by Hansen® Medical (acquired by Auris Health, Inc., Redwood City, California) and da Vinci platform (Intuitive Surgical®, Inc. Sunnyvale, CA, USA) are two of such

systems. Sensei® X robotic catheter system was developed for catheter ablation procedure. In catheter ablation, a small catheter is steered into the heart via a leg vein. Then a radio-frequency energy is delivered through the metal tip of the catheter to ablate selected parts of the heart. This robotic system consists of: (a) a surgeon console including monitors to display endoscopic, fluoroscopic, and other procedure-specific imaging and a master haptic device (2.4-a); (b) a Remote Catheter Manipulator (RCM) at the patient side to deliver the catheters (2.4-b). Although Sensei® X was developed for cardiovascular applications, Aron *et al.* passed a custom-built, passive, flexible ureteroscope through the robotically controlled catheter system to be used for performing ureterorenoscopy [71]. ureterorenoscopy is a diagnostic or therapeutic procedure where a flexible endoscope is placed transurethrally to the ureters and the kidney to inspect and biopsy kidney stones or to remove them. This system was used in flexible ureterorenoscopic examination of five female swine [72]. After some improvements over their system, the authors performed the first clinical study in robotic ureteroscopy on 18 patients who had renal calculus (kidney stones) with successful outcomes [73].

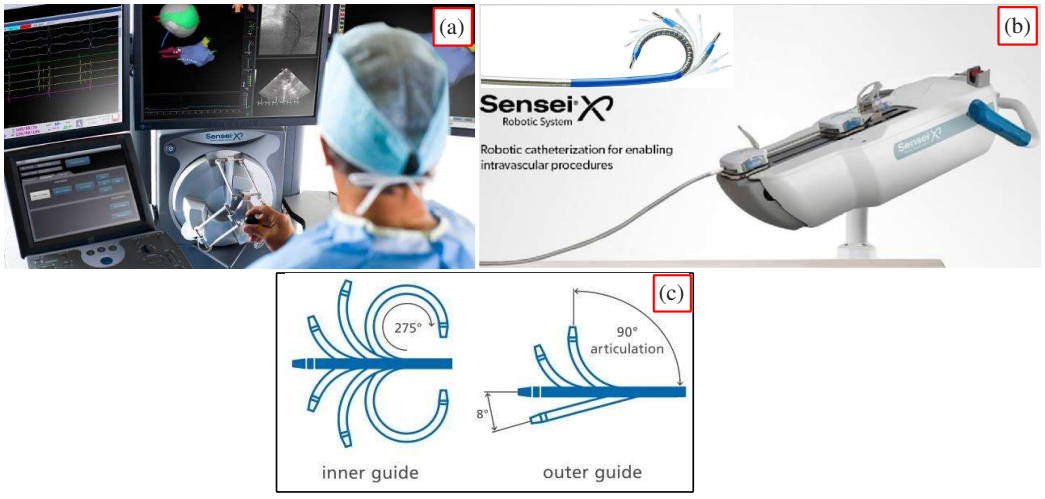

Figure 2.4: Sensei® X robotic catheter system: (a) master console, (b) Remote Catheter Manipulator. Inset is the sheath, (c) motion of inner and outer guides of *Artisan extend Control Catheter* .(image source: www.hansenmedical.com)

The da Vinci platform (Intuitive Surgical®, Inc. Sunnyvale, CA, USA. See Fig. (2.5)-a) that received CE mark and FDA approval in 1999 and in 2001 respectively is currently the mainstream surgical robot with more than 3 million minimally invasive procedures performed since 2000 . Even though it was originally designed for coronary artery surgery, its primary application is for laparoscopic prostatectomies and hysterectomies [50–52]. The da Vinci is a master-slave robotic system that consists of a surgeons console , a patient-side cart with three or four robotic arms, a visualization system and custom cable-driven wrists (EndoWrist®). The da Vinci replicates the surgeons hand motions at the master hands into the corresponding scaled-down movements of instruments inside the patient and it also filters tremors.

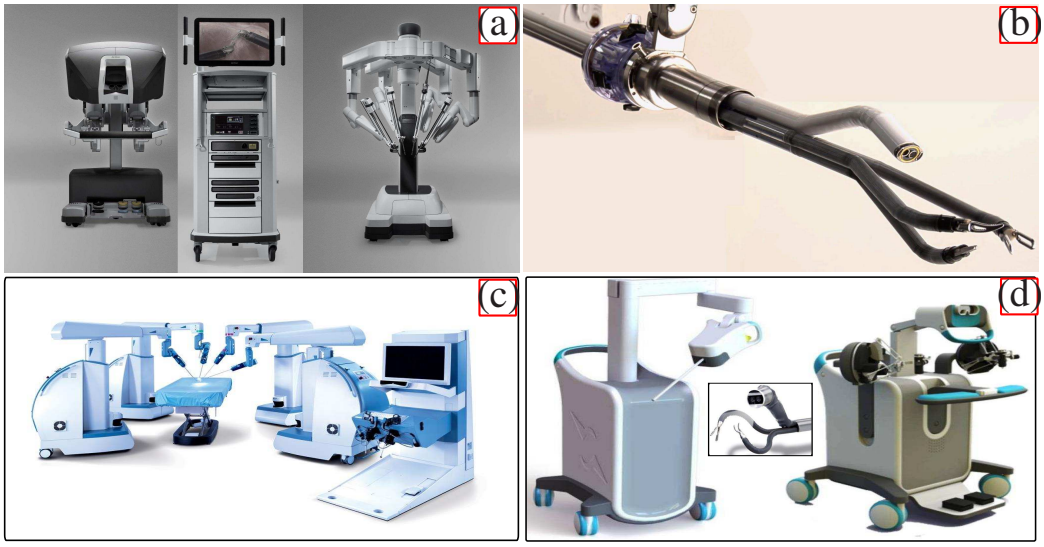

Figure 2.5: Current and upcoming surgical robots with applications in urology: (a) da Vinci® (Intuitive Surgical®, Inc. Sunnyvale, CA, USA), (b) da Vinci® Sp™(compatible with da Vinci® Xi), (c) Senhance™ (TransEnterix®, Inc., Morrisville, NC, USA), (d) SPORT™ (Titan Medical™, Inc., Toronto, Ontario, Canada). All images are extracted from the companies websites.

There are several emerging robotic systems with applications in urology. da Vinci® Sp™ (Fig. (2.5)-b) is developed for urologic single incision laparoscopic surgery (SILS, also called single port access surgery or SPAS). The multi-instrument robotic slave is compatible with the latest da Vinci® Xi robot (Fig. (2.5)-a). It delivers a stereoscopic camera

and three articulated instruments through a 25 mm cannula. These Instruments have two more degrees of freedom than the conventional da Vinci single-site instruments. This system is FDA approved however it won't be marketed until mid 2018. Senhance™ (TransEnterix®, Inc., Morrisville, NC, USA) or previously known as Telelap ALF-X (Fig. (2.5)-c) is intended for laparoscopic surgery in the abdomen and pelvis [74]. It is composed of a remote console, three robotics arms and reusable surgical instruments [75]. Haptic force feedback and eye-sensing camera control are the exclusive features of this robot. Senhance™ had clinical trials in Europe and was approved by FDA in 2017. SPORT™ (Titan Single Port Orifice Robotic Technology by Titan Medical™, Inc., Toronto, Ontario, Canada) is another promising multi-instrument master-slave system for laparoscopic surgery (Fig. (2.5)-d). This system is an adaptation of IREP robot developed earlier by Simaan *et al.* [76] at Columbia university. Based on the company's claim, it's cheaper, more versatile and more agile than the competitors. Its *camera insertion tube* packs two multi-articulated instruments and a stereoscopic camera. Perhaps, a major difference from the da Vinci® Sp™ is that the instruments are wire-driven continuum robots (as opposed to linkages). SPORT™ is currently undergoing pre-clinical evaluations and is not FDA approved. For a review of other upcoming robotic technologies in urology, the reader is referred to reference [77].

2.2 Overview of TURBT Status

Urinary bladder cancer was the 9th most common cancer in 2012 composing 3.1 % of all cancers [78]. Bladder cancer accounts for about 5% of all new cancers in the US and it is the fourth most common cancer in men, but it is less common in women [79]. According to the American Cancer Society (ACS) the expected number of newly diagnosed BC patients in 2017 in the US is estimated at 79,030 and the estimated associated BC deaths includes 16,870 patients [79]. Transurethral Resection of Bladder Tumor (TURBT) and pathological staging are standard surgical therapies for non-muscle invasive bladder cancer (NMIBC) and integral parts of the diagnostic evaluation and progression monitoring

of all bladder tumors [80–82]. Despite progress in recent decades, through use of cautery resection loops, laser ablation and endoscopes, TURBT is still associated with significant patient morbidity [83, 84]. The quality of the first Trans-Urethral Resection (TUR) procedure greatly affects patient prognosis, treatment follow-up, and treatment cost [85, 86]. Due to the high recurrence rates (partly associated with incomplete tumor resection on initial TUR [86–89]), BC has the highest per patient treatment costs out of all cancers [84,90].

Current TURBT outcomes depend highly on surgical skill with surgical outcomes varying significantly between low volume rural hospitals and high volume specialized hospitals. Also, recurrence rates following TURBT for NMIBC vary greatly between institutions from 7% to 45% [85]. Complications such as bladder wall perforations and incomplete resections have been attributed to surgical tool limitations.

Contrary to typical oncologic surgery where tumors are resected in one piece (en-block) to prevent spread of malignant cells, BC tumor resection is currently carried out piece-meal; hence possibly contributing to seeding other cancer sites [91]. Although en-block TURBT was recently demonstrated clinically [92,93] it remains difficult or impossible depending on lesion location and surgeon expertise [94]. Current devices prevent validation of a clinical standard for en-bloc resection [95] and acceptance by the Urologic community.

In addition to being a standard surgical therapy for NMIBC, TURBT is also an integral part of the diagnostic evaluation of all bladder tumors. It does, however, have its shortcomings. Initial TURBT is associated with imperfect clinical staging and incomplete tumor removal. An accurate pathological diagnosis, which is determined by depth of tumor invasion, is crucial for staging urothelial carcinomas. The stage of a patients BC plays a key role in determining the patients treatment and prognosis. The urologist is responsible for accurately sampling bladder tissue for evaluation, and should include muscularis propria (detrusor muscle) for adequate staging. The frequency with which muscularis propria was sampled by urologists in a community practice was studied by Maruniak *et al.* and they found that up to 51% of documented cases of urothelial neoplasms lacked muscularis pro-

pria from the pathologic specimen [96]. Specimens missing muscle layers cannot confirm complete tumor resection.

Although TURBT remains the gold standard for the initial diagnosis and treatment of NMIBC, the early recurrence rate at 3 months is high, up to 45% [85]. In a combined analysis of seven randomized studies, the recurrence rate following TURBT for NMIBC varied greatly between institutions from 7% to 45% [82]. This large difference was unexplained by other factors assessed, such as tumor type or treatment so the authors concluded that the quality of TURBT and surgeon skill greatly impact recurrence rate. Similar conclusion was also found in [97] with regards to use of blue light or photodynamic diagnosis (PDD) and resection of BC.

The quality of first TURBT determines the patients prognosis and corresponding treatment costs [84]. Despite recommendations for eradication of all visible tumors during initial TURBT, a large number of patients are seen with residual or overlooked tumors. A study of 150 consecutive patients with NMIBC undergoing repeat transurethral resection within 6 weeks of the initial procedure found 76% with residual tumor [86]. Herr and Donat studied 1,312 patients with NMIBC who underwent repeat transurethral resection (re-TUR) and found residual disease in 51%-78% of patients, depending on tumor stage [86]. Of patients with initial papillary non-invasive disease (pTa) at first TURBT, 15% were found to have invasive disease (pT1 or pT2) at re-TUR. Of patients with initial pT1 disease, 30% had muscle-invasive disease on re-TUR. These high rates of residual tumors suggest that initial TURBT fails to achieve radical resection [87, 98].

Divrik *et al.* have investigated the effect of re-TUR on recurrence rates in patients with T1 BC in a prospective randomized trial [99]. Recurrence was observed in 26% of patients in the re-TUR group compared to 63% of patients who did not undergo re-TUR. The overall recurrence-free survival for the re-TUR group was 74% compared to 37% in the patients who did not undergo re-TUR (log rank 0.0001). Zurkirchen *et al.* [87] performed a retrospective study to evaluate the persistence of carcinomas after a first resection. The study did

not evaluate technique or effect of tools used but rather compared experts to novices while including residents supervised by experts during resection in the expert group. They concluded that 26%-37% of carcinomas persist after a first resection suggesting non-complete resection and they recommended a second resection 4-6 weeks following the first TUR to increase the chances of obtaining complete resection. This study, and others (e.g. [89]), demonstrate a clear positive effect of re-TUR on recurrence rates. Others (e.g. [100]) also suggest the use of chemotherapy to reduce recurrence; however, chemotherapy has no discernible effect on progression and long-term survival [101] and it does not compensate for incomplete resection [99].

The technical challenges of manual TURBT procedures are associated with considerable clinical ramifications. In addition to incomplete resections in first TURBT, studies at up to 5% of all TUR procedures have noted perforations in the bladder due to full wall resection, or damage deep enough to impact the bladder exterior [82, 102]. In a multicenter prospective experimental study, high variability in the quality of resection was noted and attributed to variability in surgeon technique [58]. Ukai *et al.* [103] further suggested that lesion location influences resectability. In certain areas of the bladder, the ideal angle of approach to a tumor may be kinematically infeasible and the bladder wall cannot be appropriately reached or traced. Wilby *et al.* [104] have attributed instrumentation as a significant limitation influencing resection quality. The anatomic constraints of transurethral access make reaching the anterior regions of the bladder difficult or infeasible without external manipulation. As with visualization, for approaching anterior aspects of the bladder, suprapubic pressure is applied to bring the bladder wall into the reachable workspace of the rigid resectoscope.

En-bloc TURBT presents fertile ground for improvement. In typical oncologic surgery, suspicious tissue is resected in one coherent piece to ensure malignant cells are not spread. In stark contrast, TURBT resection occurs piece-meal as the tumor is shaved down in stages. En-bloc resection may limit the role of seeding and recurrence rate after resection

[91]. Though the technique has been shown clinically [103, 105, 106], the limited dexterity of rigid resectoscopes makes en-bloc resection difficult or impossible depending on the lesion location and the surgeons technical skill [94]. A clinical standard for en-bloc resection has been deemed infeasible with currently available devices [95]. The instrumentation limitations prohibited en-bloc TURBT in randomized trials [104] and therefore the general acceptance of en-bloc TURBT by urologists is currently unattainable.

The high recurrence rates and long survival periods make BC treatment a significant financial burden with the highest lifetime treatment costs compared to other cancers [84, 100, 107]. TURBT is currently performed manually using straight resectoscopes and laser/-cautery loops. Outcomes of TURBT are variable and highly dependent on the experience and technical ability of the urologic surgeon and the location of the tumor. Anterior tumors are especially tricky to accurately resect due to the inability of straight surgical tools to curve up from the point of entry to the bladder. Surgeons currently rely on pubic pressure and resectoscope tilt to reach the anterior aspects of the bladder. However this technique has limited success in obese patients due to a thick fat layer. Further, inadequate surveillance and tumor staging have been associated with misdiagnosed tumors and with a high recurrence rate [108]. Reliance on white light based imaging (visualization of the bladder interior using endoscopes) complicates the task of ensuring positive resection margins while use of PDD using blue light is limited by use of straight instruments resulting in diagnosis artifacts due to incidence of light at shallow angles in anterior aspects of the bladder. This makes the success of PDD highly dependent on the skill of the surgeons [95, 97].

2.3 A Brief Overview of Novel Imaging Technologies for TURBT

Traditionally, urine cytology and standard (white light) cystoscopy have been used in bladder cancer diagnosis and treatment. However, urine cytology does not have enough sensitivity for low-grade lesions and does not provide information about the stage of disease. Standard cystoscopy is invasive though minimally. Moreover it lacks specificity (rate

of true negatives) for flat malignancies [109, 110]. Recent technologies such as photodynamic diagnosis [111, 112] (PDD or blue-light cystoscopy) and Narrow-band imaging (NBI) [113] have shown to improve tumor margin detection. Some other new imaging techniques include positron emission tomography (PET), lymphotropic nano-particle enhanced magnetic resonance imaging (LNMRI), CT/MR cystography, virtual cystoscopy, MR spectroscopy and intra-operative ultrasound. Figure 2.6 shows the current status of technology development and validation for imaging modalities in bladder cancer.

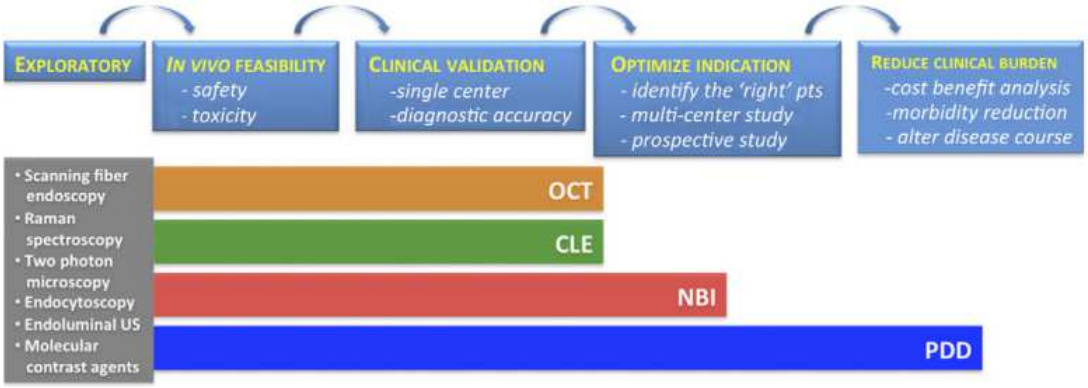

Figure 2.6: Phases of technology development and validation for imaging modalities in bladder cancer, picture from [114]. (OCT=Optical Coherence Tomography, CLE=Confocal Laser Endomicroscopy, NBI=Narrow-Band Imaging, PDD=Photodynamic Diagnosis, US=Ultrasound)

PDD and NBI offer macroscopic imaging of the tissue, i.e. they can survey a large area and provide contrast enhancement. In contrast, OCT (Optical Coherence Tomography) and CLE (Confocal Laser Endomicroscopy) provide a microscopic image of tissue microstructure. NBI was reported to have sensitivities (true positive rate) in the range of $93\% - 100\%$ and specificities of $65\% - 82\%$ [115–118]. OCT is an optical technology analogous to ultrasound, however light is utilized in lieu of sound waves. It can produce online bladder cancer staging by providing cross-sectional images below the mucosal surface. OCT was found to have sensitivities of $75\% - 100\%$ and specificities of $65\% - 90\%$ in bladder cancer detection [119–121].

Ultrasound offers several advantages over other modalities including lack of harmful

radiations, real-time imaging, low cost, facility of integration with robotic systems and small footprint. Several ultrasonic techniques have been used to assess bladder cancers, including transabdominal, transrectal and transurethral (also called endoluminal) ultrasonography [122–125]. The former two techniques can detect extra-vesical tumor involvement, but are not generally helpful in determining the degree of bladder wall invasion. The latter is more valuable in evaluating the stage of tumors confined to the bladder wall [124]. Figure 2.7 from [125] shows a high-frequency (20 MHz) endoluminal ultrasound (ELUS) image. Three layers in the bladder wall can be distinguished: the hyperechogenic mucosa/submucosa, hypoechogenic muscle, and hyperechogenic adventitia. Sakamato *et al.* performed transurethral ultrasound examination on 24 patients with 40 tumors [126]. Their results showed that it was difficult to detect bladder tumors in the bladder neck or dome and those of less than $5mm$ anywhere while those of larger than that were detected with 90% accuracy. It is worth mentioning that the majority of the studies for application of ultrasound in bladder cancer diagnosis were conducted in the 80's and 90's. Ever since, there has been a considerable improvement in the ultrasound technology. For example, contrast-enhanced ultrasound (CEUS) especially in 3D mode has been shown to be superior to 2D US in differentiating non-invasive from invasive bladder tumors [127–129].

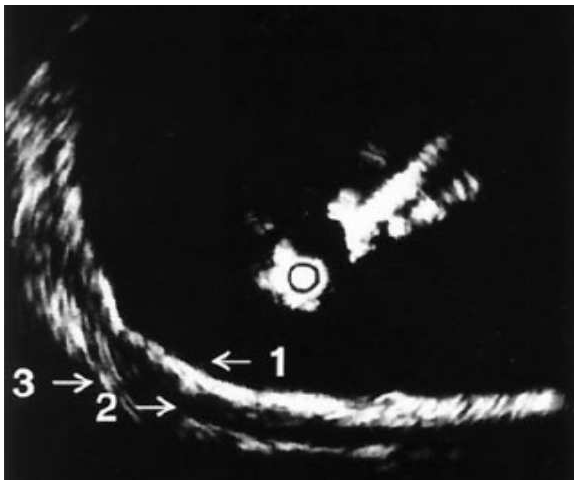

Figure 2.7: 20-MHz endoluminal transducer depicts three layers in bladder wall: hyperechogenic mucosa/submucosa (1), hypoechogenic muscle (2), and hyperechogenic adventitia (3) , picture from [125]

CHAPTER 3

INVESTIGATION OF MANUAL RESECTION TOOLS FOR TRANSURETHRAL BLADDER CANCER RESECTION

3.1 Background

Bladder cancer is the fourth most common cancer among men in the US, with an estimated 74,000 new cancer diagnoses, and 16,000 related deaths predicted for 2015 [130]. *Transurethral Resection of Bladder Tumor* (TURBT) is the standard procedure for staging and diagnosis of bladder cancers and treatment of non-muscle invasive tumors (NMIBC). It is typically performed in an outpatient setting under general anesthesia.

During TURBT, a resectoscope is inserted transurethrally to provide access for an endoscope and a cautery loop to reach the surgical site, (Fig. 3.1). A *continuous-flow* resectoscope is used to partially distend the bladder by regulating the irrigation inflow and outflow. Figure 3.2 shows standard resectoscope components. It consists of a telescope lens (30° or 70°), a sheath, a working element and a blind obturator as shown in Fig. 3.2. The inset in the top right is a close-up view of an electrocautery wire loop. During tumor resection, the cautery loop is inserted distally to the surgeon and beyond the tumor. The cautery loop is then carefully pulled proximally towards the surgeon to scoop out the tumor tissue.

Recent technological developments such as enhanced endoscope designs, new laser techniques, and imaging modules have improved safety and functionality of TURBT. For example, recent imaging modalities include photodynamic diagnosis, narrow-band imaging, optical coherence tomography and confocal laser endomicroscopy [61, 131]. Nonetheless, it is still a challenging procedure for surgeons and associated with potential patient

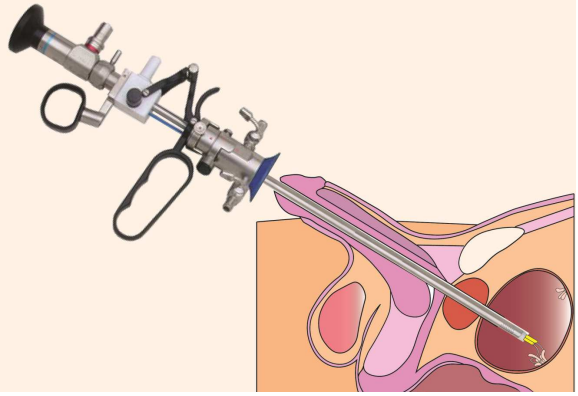

Figure 3.1: TURBT Procedure.

morbidity [60, 83]. Hindrances to improvement include tool limitations such as lack of intracavitary distal dexterity and in-vivo sensory feedback as well as sparse instrumentation repertoire. Numerous complications have been at least partly attributed to tool limitations such as bladder wall perforations[132], irrigant absorption (due to perforation)[133], bleeding [132] and damage to the ureteric orifices[134].

The quality of the first TURBT procedure greatly influences patient prognosis, treatment follow-ups and costs [57, 61]. TURBT guidelines recommend that all visible tumors be removed along with a margin of deeper *detrusor muscle* for staging [135]. Correct staging is critical as muscle invasive disease requires aggressive management with bladder removal, whereas non-invasive disease can often be managed with endoscopic resection and intravesical treatments. However, optimal performance has remained elusive. Insufficient resection (under-resection) has been reported in numerous studies in the literature although it has not been investigated closely [61]. In a study by Adiyat and colleagues [57], 70% of patients had visible tumor at the time of restaging TURBT (re-TUR). Among these, 30% were located at the original site. A host of other literature confirm inadequate resection as a challenge in TURBT resulting in understaging, inappropriate treatment regimens, earlier recurrence and likely progression of disease [56, 58, 61, 136–138]. Contributing to under-resection is the fact that surgeons have to balance two risks during tumor resection. A shallow resection is likely to leave behind residual tumor. Deep resection can lead to

perforation of the bladder, which is a severe complication also potentially spilling tumor into the abdominal cavity.

American Urological Association and European Association of Urology guidelines recommend re-TUR after initial TURBT in any cases where residual or invasive disease is suspected. Repeat TURBT aims to detect residual tumors and to correctly stage tumors by levels of invasiveness. For non-muscle invasive disease, many patients undergo multiple TURBTs because of high recurrence rates. As a consequence, bladder cancer has the highest overall treatment costs per patient among all cancers ranging from 96000 to 187000 US dollars in 2001 [58–60].

To overcome some of these challenges, multiple groups including our team have developed robotic systems for transurethral resection [62, 108, 139, 140]. We demonstrated a proof-of-concept telesurgical system [62, 141] and carried out ex-vivo experiments on bovine bladder to prove its efficacy in targeting different regions of the bladder for both surveillance and intervention [63]. This system is composed of a distal dexterous multi-backbone snake-like robot that is deployed through the urethra and can pass multiple instruments and visualization modules (flexible fiberscope) through its working channels [62, 141].

TURBT is in general considered successful if the early recurrence rate is low, the tumor is not under-resected allowing accurate staging and no complications occur [142]. These benchmarks are fairly subjective and qualitative. In our earlier study, we proposed a purely kinematic measure to assess TURBT and also to compare resection accuracy/dexterity in different regions of an assumed spherical bladder model [143]. To the authors' knowledge, this is the only available investigation in this issue despite the fact that TURBT is a commonly performed urologic surgery. In this chapter, we carry out a thorough analytical study of various kinematic measures affecting resection quality. We employ a kinematic computational framework to assess the introduced measures locally (on a bladder point) based on a non-dimensionalized distance as well as regionally (in 16 bladder regions). In order to

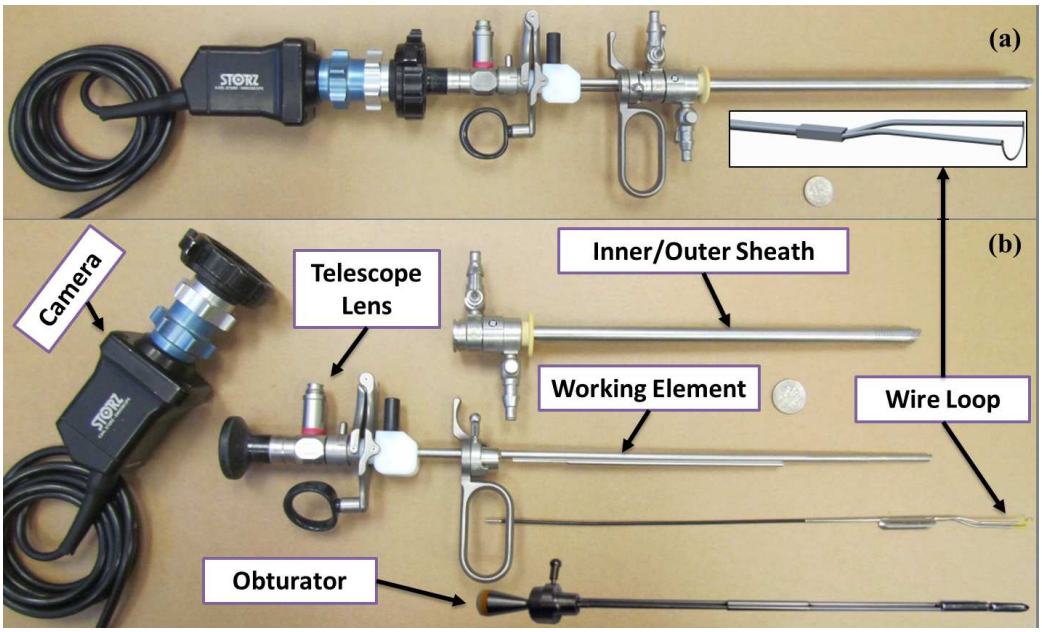

Figure 3.2: A standard 26-Fr resectoscope: (a) assembled , (b) constituent parts.

characterize the measures that are potentially more faithfully descriptive of resection accuracy, we design and perform experiments and then evaluate resection accuracy in normal (depth) and tangential directions. We show that resection accuracy cross-correlates with several kinematic measures. By utilizing the opted kinematic measures based on correlation coefficients, we draw inferences on comparing resection accuracy/dexterity in different regions of the bladder. The results of this study highlight resection dexterity amenability in different bladder regions from a kinematic point of view. More importantly, it provides quantitative measures for resection performance. These measures can be used as benchmarks for novel tools or robots for TURBT.

This chapter is structured as follows: in section 3.2.1, the kinematics of resection by a standard resectoscope is modeled as a mechanism with three revolute joints and one prismatic joint (RRRP). The direct and instantaneous kinematics are then derived. Then, a formulation of the Jacobian from hand motion to the resectoscope tip motion subspace is obtained in 3.2.2. Kinematic measures are introduced and determined analytically. An algorithm is subsequently provided to compute these measures throughout the bladder points

as well as regions. In 3.2.3, the experimental protocol to identify higher correlated kinematic measures is explained and resection variables (measures) are introduced to evaluate accuracy. Sections 3.3.1 and 3.3.2 delineate simulation and experiment results in details. The discussion of these results and their implications is addressed in 3.3.3. We finally concluded this chapter in section 3.4 by summarizing the outcomes and future directions. This study targets both clinicians and engineers. The involved clinical material does not hinder the latter to gain an understanding of the methods and the contributions. The clinical reader can safely skip the technical parts in sections 3.2.1 and 3.2.2.

3.2 Methods

3.2.1 Kinematic Modeling of Straight Resectoscope

Modeling Assumptions

The resectoscope is modeled as a four degree-of-freedom (DOF) mechanism. The DOF's include three rotations (yaw,pitch,roll) and a translational motion along the longitudinal axis of the resectoscope. These configuration variables are expressed as q_1, q_2, q_3, q_4 respectively and defined later in this section. Based on measurements from demonstrations by the collaborating surgeons, we have estimated the limits of first angle to be $|q_1| \leq 38^\circ$ for men and $|q_1| \leq 54^\circ$ for women. Similarly, the second angle is also constrained: $-60^\circ \leq q_2 \leq 50^\circ$.

The bladder is assumed as a sphere of radius $r_b = 50[mm]$ approximately corresponding with a distended bladder with a volume of $600[ml]$ [144]. In reality, a distended bladder is rather blob-like. Nonetheless, the purpose of the measures introduced in this study is to provide a comparative benchmark . Therefore, in this sense, the assumption of a spherical bladder is warranted and facilitates modeling.

In addition, we define the angle γ as shown in Fig. 3.3. This angle depicts the angular location of the point of contact between the cautery loop and the local tangent of the bladder

surface ($\mathbf{p}$). This angle is measured from the line connecting the center of the cautery loop with the mid-point of the circular cautery segment to the line passing through the center of the cautery loop and the current tissue contact point on the cautery loop (See Fig. 3.3-a).

During resection, surgeons are inclined to use the loop arc such that $|\gamma| \leq 20^{\circ}$. This assumption is used in calculation of performance measures while considering the useful resection workspace.

The loop in general has a right angle but some surgeons may prefer to change this angle to facilitate resection in some regions (e.g. the bladder dome). For simplicity, we will consider a right-angle loop throughout. In addition to these assumptions, a fulcrum point located at $\lambda = 30$ mm from the bladder neck (See Fig. 3.3-b)) is hypothesized based on the mechanics of TURBT practice.

Frame Assignments and DH Parameters

Figure 3.3 illustrates the schematics of a resectoscope. DH parameters are used to identify the kinematics of a resectoscope and six frames are assigned as shown. Figure 3.3-a also illustrates the tip of the electrocautery loop and the last two frames assigned at the center of the loop arc ($\mathbf{o}$) and the perimeter of the arc respectively ($\mathbf{p}$).

In Table 3.1, the pertaining DH parameters are represented. Based on the frame assignment shown in Fig. 3.3 , $q_1(q_2, q_3)$ is the rotation of $\mathbf{R}_1(\mathbf{R}_2, \mathbf{R}_3)$ about moving frame $\hat{\mathbf{z}}_1(\hat{\mathbf{z}}_2, \hat{\mathbf{z}}_3)$ measured from $\hat{\mathbf{x}}_0(\hat{\mathbf{x}}_1, \hat{\mathbf{x}}_2)$ and q_4 is the linear displacement of the resectoscope along the sheath axis ($\hat{\mathbf{z}}_4$) with an offset of $\eta \triangleq \lambda + r_b$ from the fulcrum. λ is the distance from the fulcrum to the bladder neck (tool entry point), r_b is the bladder radius and ν is the loop center offset with respect to the loop axis (shown in Fig. 3.3-a)

Table 3.1: DH Parameters

i	a_{i-1}	α_{i-1}	d_i	θ_i
1	0	0	0	q_1
2	0	$\pi/2$	0	$\pi/2 + q_2$
3	0	$\pi/2$	0	q_3
4	ν	0	$\eta + q_4$	0

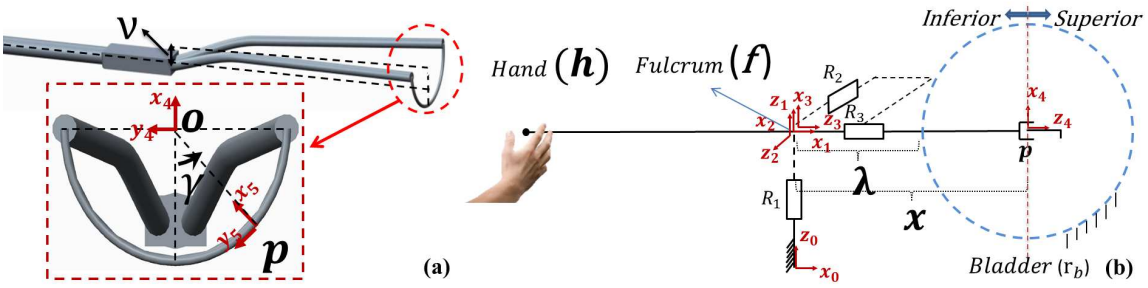

Figure 3.3: Schematics of a resectoscope: (a) electrocautery (wire/cutting) loop and the assigned frames (b) resectoscope model as an RRRP mechanism

Link Transformations

The direct kinematics of the resectoscope can be calculated by determining successive homogeneous transformations denoted by ${}^{i-1}\mathbf{T}_i$ from the base frame to the last frame:

$$ {}^{0}\mathbf{T}_5 = {}^{0}\mathbf{T}_1 \, {}^{1}\mathbf{T}_2 \, {}^{2}\mathbf{T}_3 \, {}^{3}\mathbf{T}_4 \, {}^{4}\mathbf{T}_5 \tag{3.1} $$

This leads to the following transformation:

$$ {}^{0}\mathbf{T}_4 = \begin{bmatrix} s_1 s_3 & c_3 s_1 & c_1 c_2 & (\eta + q_4) c_1 c_2 \\ -c_1 s_2 c_3 & +c_1 s_2 s_3 & & +\nu(s_1 s_3 - c_1 s_2 c_3) \\ -c_1 s_3 & s_1 s_2 s_3 & c_2 s_1 & (\eta + q_4) s_1 c_2 \\ -c_3 s_1 s_2 & -c_1 c_3 & & -\nu(c_1 s_3 + s_1 s_2 c_3) \\ c_2 c_3 & -c_2 s_3 & s_2 & (\eta + q_4) s_2 + \nu c_2 c_3 \\ 0 & 0 & 0 & 1 \end{bmatrix} \tag{3.2} $$

$$ {}^{4}\mathbf{T}_5 = \begin{bmatrix} c_\gamma & -s_\gamma & 0 & -r_L c_\gamma \\ s_\gamma & c_\gamma & 0 & r_L s_\gamma \\ 0 & 0 & 1 & 0 \\ 0 & 0 & 0 & 1 \end{bmatrix} \tag{3.3} $$

where r_L is the radius of the resection cautery loop and s_i, c_i denote $\sin(q_i)$ and $\cos(q_i)$ respectively.

Instantaneous Kinematics

Based on observations of transurethral resection procedure, the hand and the imparted loop motions that are involved are mainly translational. As such, in the following sections, transurethral resection is treated as a task of point contact with the tissue and the focus is on the ability of the surgeon to impart a linear velocity to the resection point $\mathbf{p}$. Thus, in the remainder of the analysis, only the translational components of the Jacobians from configuration space to the tool tip motion space and hand motion space are sought.

The instantaneous kinematics Jacobians for the center of the loop are given by:

$$\mathbf{J}_{o,v} = \begin{bmatrix} \nu(c_2 s_3 + c_3 s_1 s_2) & -\nu c_1 c_2 c_3 & \nu(c_1 s_2 s_3 + s_1 c_3) & c_1 c_2 \\ -l_c c_2 s_1 & -l_c c_1 s_2 & & \\ \nu(s_1 s_3 - c_1 s_2 c_3) & -\nu s_1 c_2 c_3 & \nu(s_1 s_2 s_3 - c_1 c_3) & s_1 c_2 \\ +l_c c_1 c_2 & -l_c s_1 s_2 & & \\ 0 & -\nu s_2 c_3 + l_c c_2 & -\nu c_2 s_3 & s_2 \end{bmatrix} \tag{3.4}$$

$$\mathbf{J}_{o,\omega} = \begin{bmatrix} 0 & s_1 & c_1 c_2 & 0 \\ 0 & -c_1 & s_1 c_2 & 0 \\ 1 & 0 & s_2 & 0 \end{bmatrix} \tag{3.5}$$

where $\mathbf{J}_{o,v}$ is the translational Jacobian, $\mathbf{J}_{o,\omega}$ is the rotational Jacobian. Therefore, the total Jacobian

$$\mathbf{J}_o = \begin{bmatrix} \mathbf{J}_{o,v} \\ \mathbf{J}_{o,\omega} \end{bmatrix} \tag{3.6}$$

For the point $\mathbf{p}$ on the loop arc perimeter.

$$\mathbf{v}_p = \mathbf{v}_o + \boldsymbol{\omega}_{loop} \times \boldsymbol{\rho}_{op} \tag{3.7}$$

where $\boldsymbol{\omega}_{loop}$ is the angular velocity of the loop, $\boldsymbol{\rho}_{op} = -r_L \hat{\mathbf{x}}_5$ is the vector from $\mathbf{o}$ to $\mathbf{p}$. $\hat{\mathbf{x}}_5$ is the unit direction vector of the x-axis of frame $\{5\}$ described in frame $\{0\}$. On the other

hand:

$$\mathbf{v}_o = \mathbf{J}_{o,v}\dot{\mathbf{q}} \tag{3.8}$$

$$\boldsymbol{\omega}_{loop} = \mathbf{J}_{o,\omega}\dot{\mathbf{q}} \tag{3.9}$$

$\dot{\mathbf{q}} \in \mathbb{R}^{4\times 1}$. Therefore

$$\mathbf{v}_p = \mathbf{J}_{p,v}\dot{\mathbf{q}} \tag{3.10}$$

where $\mathbf{J}_{p,v} \in \mathbb{R}^{3\times 4}$ is the linear velocity Jacobian of the point $\mathbf{p}$ that can be reformulated as

$$\mathbf{J}_{p,v} = \mathbf{S}_{p,o}\mathbf{J}_o \tag{3.11}$$

where

$$\mathbf{S}_{p,o} = \begin{bmatrix} \mathbf{I}_3 & -(\boldsymbol{\rho}_{op})^\wedge \end{bmatrix}_{3\times 6} \tag{3.12}$$

is the linear velocity transformation from $\{4\}$ to $\{5\}$. $(.)^\wedge$ is the cross-product matrix and $\mathbf{I}_3 \in \mathbb{R}^{3\times 3}$ is an identity matrix. By the same token, the linear velocity Jacobian of the point $\mathbf{h}$ can be determined. Thus,

$$\mathbf{v}_h = \mathbf{J}_{h,v}\dot{\mathbf{q}} \tag{3.13}$$

where $\mathbf{J}_{h,v} \in \mathbb{R}^{3\times 4}$ is the linear velocity Jacobian of the point $\mathbf{h}$:

$$\mathbf{J}_{h,v} = \mathbf{S}_{h,o}\mathbf{J}_o \tag{3.14}$$

and

$$\mathbf{S}_{h,o} = \begin{bmatrix} \mathbf{I}_3 & -(\boldsymbol{\rho}_{oh})^\wedge \end{bmatrix}_{3\times 6} \tag{3.15}$$

where $\boldsymbol{\rho}_{oh} = -l\hat{\mathbf{z}}_4$ and l is the resectoscope length is designated at the distance between point $\mathbf{h}$ and point $\mathbf{o}$.

3.2.2 Resection Performance Analysis

In order to quantify manipulation capability of a resectoscope and to compare resection quality in different bladder regions, performance measures should be introduced and computed. An ideal measure (or measures) captures all the factors affecting resection outcome. It is our hypothesis that the major contributing factors are resection dexterity and visual perception. The subject of this study is on the former and fortunately the existing Jacobian-based measures in robotics and mechanisms literature are well-suited for this intent. Herein, we define the subspaces $S_i = \{v_i \subset \mathbb{R}^n | \ \|v_i\| = 1\}$ and $S_o = \{v_o \subset \mathbb{R}^m | \mathcal{J} v_i = v_o\}$ as *unit-norm input space* and *output space* respectively. Let us iterate the most prominent of such measures in conjunction with these two subspaces. The most common measure is *Manipulability* criterion [145, 146]. It is a measure of the volume of the hyperellipsoid $\mathbf{v}_o$ in *output space*. Kinematic Conditioning Index (*KCI*) [147] is another measure that indicates motion isotropy in *output space*. Both of these measures are directly associated with the singular values of the Jacobian matrix $\mathcal{J}$. Indeed, manipulability is the product of the singular values. *KCI* is the ratio of the minimum to the maximum singular value and is always between 0 and 1 with larger values showing more isotropy in the *output space*. Though less common, the minimal singular value is another Jacobian-based measure [148]. It represents the minimal scaling from *unit-norm input space* to *output space*.

Our hypothesis is that resection limitations are partly due to dexterity deficiencies of a rigid tool and dexterity is reflected in such measures. Therefore, by exploring these *kinematic performance measures*, we can identify dexterity limitations and its correlation with resection accuracy. However, the former cannot be directly employed in association with $\mathbf{J}_{h,v}$ or $\mathbf{J}_{p,v}$. This is due to the fact that we have no interest in configuration space to task space ($\dot{\mathbf{q}} \rightarrow \mathbf{v}_p$) or configuration space to hand motion space ($\dot{\mathbf{q}} \rightarrow \mathbf{v}_h$), rather what is of interest is relating instantaneous linear motions in hand motion space (analogous to *unit-norm input space*) to the linear motions in the task space(analogous to *output space*)($\mathbf{v}_h \rightarrow$

$\mathbf{v}_p$). In this regard, the velocity transformation from the former to the latter should be determined. Based on Eqs. 3.13 3.10,

$$\mathbf{v}_p = \mathbf{J}_{p,v}\mathbf{J}^{\dagger}_{\mathbf{h},\mathbf{v}}\mathbf{v}_h \tag{3.16}$$

where $\mathbf{J}^{\dagger}_{\mathbf{h},\mathbf{v}}$ is Moore-Penrose pseudo-inverse of $\mathbf{J}_{h,v}$ and equals [149]:

$$\mathbf{J}^{\dagger}_{\mathbf{h},\mathbf{v}} = \mathbf{J}^{\mathbf{T}}_{\mathbf{h},\mathbf{v}}(\mathbf{J}_{\mathbf{h},\mathbf{v}}\mathbf{J}^{\mathbf{T}}_{\mathbf{h},\mathbf{v}})^{-1} \tag{3.17}$$

For brevity, let us define

$$\mathbf{J} \triangleq \mathbf{J}_{p,v}\mathbf{J}^{\dagger}_{\mathbf{h},\mathbf{v}} \tag{3.18}$$

Having determined $\mathbf{J}$, multiple kinematic measures are assessed in *tangential* and *normal* directions. Which of such measures are more relevant are established by properly designed experiments explained in section 3.2.3. In the following subsections, the kinematic measures are derived analytically and discussed. Also an algorithm is proposed that is used to compute these measures.

Kinematic Dexterity Measures

In tangential dexterity/accuracy evaluation, we are interested in hand motions causing task-space motions tangential to the bladder surface. Therefore a transformation is sought that maps a particular subspace of hand motions -the one causing tangential motions in task space, to the subspace of task-space tangential motions. In normal dexterity evaluation, a hand-space-to-task-space mapping is sought that causes task space motions normal to the sphere. In this case, hand and task subspaces of interest are both lines. To determine the normal task space motion mapping, the normal vector to the sphere surface should be calculated at each point. Using spherical coordinates (ρ, θ, ϕ) on frame $\{b\}$ to locate each

sphere point, the normal vector is

$$\hat{e}_\rho = [cos(\theta)sin(\phi), sin(\theta)sin(\phi), cos(\phi)]^T \tag{3.19}$$

as shown in Fig. 3.4. Frame $\{b\}$ is a translation of $\{0\}$ to the sphere center. The projection matrix that maps $\mathbf{v}_p$ on the normal direction is

$$\mathbf{P}_n = \hat{e}_\rho \hat{e}_\rho^T \tag{3.20}$$

where $\mathbf{P}_n \in \mathbb{R}^{3\times3}$. Substituting for $\hat{e}_\rho$ from Eq. (3.19) in Eq. (3.20)

$$\mathbf{P}_n(\theta,\phi) = \begin{bmatrix} c_\theta^2 s_\phi^2 & s_\theta c_\theta s_\phi^2 & c_\theta s_\phi c_\phi \\ s_\theta c_\theta s_\phi^2 & s_\theta^2 s_\phi^2 & s_\theta s_\phi c_\phi \\ c_\theta s_\phi c_\phi & s_\theta s_\phi c_\phi & c_\phi^2 \end{bmatrix} \tag{3.21}$$

Therefore, pre-multiplying both sides of (3.16) by $\mathbf{P}_n$

$$\mathbf{v}_{p,n} = \mathbf{J}_n \mathbf{v}_h \tag{3.22}$$

where $\mathbf{v}_{p,n} = \mathbf{P}_n\mathbf{v}_p$, $\mathbf{J}_n = \mathbf{P}_n\mathbf{J}$. Note that $rank(\mathbf{J}_n) = 1$. The normal singular value is defined herein as

$$\sigma_n \triangleq \sigma(\mathbf{J}_n) \tag{3.23}$$

For tangential direction, pre-multiplying both sides of (3.16) by $\mathbf{P}_t$ would yield

$$\mathbf{v}_{p,t} = \mathbf{J}_t \mathbf{v}_h \tag{3.24}$$

where $\mathbf{v}_{p,t} = \mathbf{P}_t\mathbf{v}_p$, $\mathbf{J}_t = \mathbf{P}_t\mathbf{J}$ and $\mathbf{P}_t$ is the complementary projector to $\mathbf{P}_n$ and thus

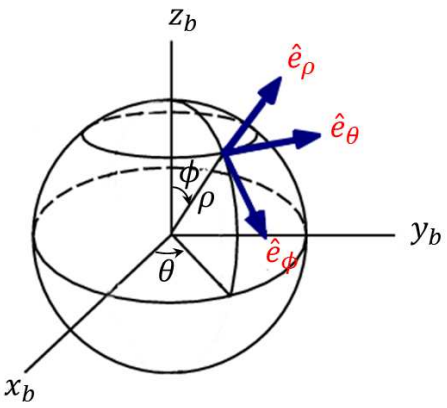

Figure 3.4: Spherical coordinates on bladder spherical model

$\mathbf{P}_t = \mathbf{I} - \mathbf{P}_n$ [150]. Determining $\mathbf{J}_t$, the following tangential measures are defined:

$$\sigma_{min,t} \triangleq \sigma_{min}(\mathbf{J}_t), \boldsymbol{KCI}_t \triangleq \frac{\sigma_{min,t}}{\sigma_{max,t}}, \mu_t \triangleq \sigma_{min,t}\,\sigma_{max,t} \tag{3.25}$$

where $\sigma_{max,t} \triangleq \sigma_{max}(\mathbf{J}_t)$

Such measures are pointwise in that the evaluation is performed on one single point in task space (though for a range of practical points on the cautery loop). To determine performance in an area, these measures would be integrated on that area and divided by the area to yield an average value. Accordingly,

$$\bar{\sigma}_{min,t} = \frac{\int_A \sigma_{min,t} ds}{\int_A ds}, \overline{KCI}_t = \frac{\int_A KCI_t ds}{\int_A ds}, \bar{\mu}_t = \frac{\int_A \mu_t ds}{\int_A ds} \tag{3.26}$$

where A represents the area of interest.

Algorithm for Kinematic Dexterity Measures Evaluation

Algorithm 1 presents the calculation of the kinematic measures in the bladder spherical model. This procedure starts with finding $q_i^{\{j\}}$, the j$^{\text{th}}$inverse kinematic solution (See Appendix A). Unit tangential/normal velocity is assumed at the resection point $\mathbf{p}$. The instantaneous kinematic equation (3.16) is then used to obtain $\mathbf{v}_h$. After this step, the Euclidean norm of $\mathbf{v}_h$ is calculated and the original $\mathbf{v}_p$ is scaled by the reciprocal of the norm.

These scaled vectors would form the manipulability ellipse on the given plane. The ratio of the minimum to the maximum norms would yield the local KCI_t and their product yields local μ_t. To determine σ_n, the unit velocity in the direction normal to the sphere surface is calculated in world coordinate frame $\{0\}$ for each point. Then hand velocity is computed from equation (3.16). The inverse of the Euclidean norm of this velocity is computed and denoted by σ_n. Finally, the average of the measure under consideration among all resection points on the loop ($-20 \leq \gamma \leq 20$) and inverse kinematic solutions ($q_i^{\{j\}}$) is determined as the kinematic measure at point $\mathbf{p}$.

This algorithm determines pointwise measures. To quantify performance within the bladder half-octant, eq. (3.26) is applied. The discretization of these equations over an area results in an average over discrete points in that area. Thus, to compare these measures in different regions of a bladder, the sphere model is divided into 16 equal zones, each $45°$ apart in both azimuth and altitude as demonstrated in Fig. 3.5. These zones are numbered 1-16 for identification and called half-octants (H/O) throughout the rest of this chapter. In this figure, the bladder dome is situated at the superior area and the anterior/posterior area is to the positive/negative $\hat{\mathbf{z}}_b$ direction.

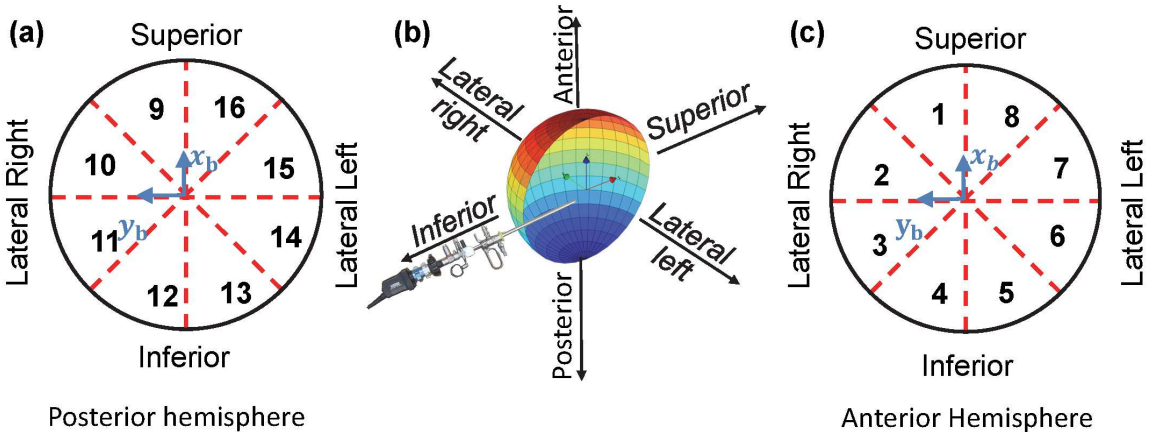

Figure 3.5: Bladder half-octants: (a) posterior hemisphere, (b) anatomical directions (c) anterior hemisphere

Next, all measures are computed at uniformly distributed points at all 16 half-octants. Subsequently, the average values are determined and reported per half-octant using Algo-

rithm 1. These values are shown in Table 3.3.

Algorithm 1 Computation of Kinematic Measures

Input: Given point **p** on sphere
  for $-20^\circ \leq \gamma \leq 20^\circ$ **do**
    for $q_i^{\{j\}}$ inverse kinematic solution **do**
      Specify $[\mathbf{V}_{p,t}]_{3\times n} = [\mathbf{v}_{p,t}^{(1)}\mathbf{v}_{p,t}^{(2)}...\mathbf{v}_{p,t}^{(n)}]$ where $\mathbf{v}_{p,t}^{(i)} = [\cos(\alpha_i), \sin(\alpha_i), 0]^T$ and $0 \leq \alpha_i \leq 2\pi$
      Specify $\mathbf{v}_{p,n} = [1, 0, 0]^T$
      Calculate $[\tilde{\mathbf{V}}_{p,t}]_{3\times n} = [\tilde{\mathbf{v}}_{p,t}^{(1)}\tilde{\mathbf{v}}_{p,t}^{(2)}...\tilde{\mathbf{v}}_{p,t}^{(n)}]$ located on the desired plane and $\tilde{\mathbf{v}}_{p,n}$, unit velocity at point **p** normal to the sphere surface where $\tilde{\mathbf{v}}_{p,t}^{(i)} = {}_4^0R\mathbf{v}_{p,t}^{(i)}$, $\tilde{\mathbf{v}}_{p,n} = {}_4^0R\mathbf{v}_{p,n}$ and ${}_4^0R$ is the rotation transformation from $\{0\}$ to $\{4\}$
      Calculate $\mathbf{V}_{h,t} = \mathbf{J}_{h,v}\mathbf{J}_{p,v}^{\dagger}\tilde{\mathbf{V}}_{p,t}$, $\mathbf{v}_{h,n} = \mathbf{J}_{h,v}\mathbf{J}_{p,v}^{\dagger}\tilde{\mathbf{v}}_{p,n}$ where $[\mathbf{V}_{h,t}]_{3\times n} = [\mathbf{v}_{h,t}^{(1)}\mathbf{v}_{h,t}^{(2)}...\mathbf{v}_{h,t}^{(n)}]$
      Calculate $m^{(i)} \approx \|\mathbf{v}_h^{(i)}\|_2$
      Determine $\sigma_{min,t} = \frac{1}{\max(m^{(i)})}, \sigma_{max,t} = \frac{1}{\min(m^{(i)})}$
      Determine $KCI_t = \frac{\sigma_{min,t}}{\sigma_{max,t}}, \mu_t = \sigma_{min,t}\,\sigma_{max,t}$
      Determine $\sigma_n = \frac{1}{\|\mathbf{v}_{h,n}\|_2}$
    end for
  end for
  Compute average $\sigma_{min,t}, KCI_t, \mu_t, \sigma_n$
Output: average $\sigma_{min,t}, KCI_t, \mu_t, \sigma_n$

3.2.3 Experimental Investigation

There are multiple reasons that motivate an experimental investigation into manual resection by the current standard resectoscopes used in TURBT. First, it is desired to explore correlations between the proposed kinematic measures and resection quality to find which kinematic measures correlate with resection performance. Second, we wish to verify chronic under-resection in TURBT as it has not been well studied though the incidence is well documented (e.g. [61],[57]). In addition, a comparison of real resection accuracy in different bladder areas gives insight into comparative resectability of different bladder regions. In addition, we attempt to provide a standard experimental protocol that can be used by designers to compare the efficacy of any new device (robots for transurethral resection e.g.[62, 141, 151]) against a standard resectoscope or any other tool. Hence, An experimental protocol for TURBT in multiple points of a hypothetical sphere in space was designed

and implemented. The following subsections present the experimental protocol.

Experimental Procedure

TURBT phantoms were created using a standard $\varnothing 60[mm] \times 15[mm]$ petri dish filled with a mixture of $23[gr/L]$ agar (Sigma-Aldrich #A7002-250G) and $110[gr/L]$ milk in distilled water. Milk was used to eliminate any potential visual cue of the sample depth by providing opacity. Then, a disk of $13.65[mm]$ in diameter and $6[mm]$ in height was placed in the center of the agar mixture on top of its surface. The disk was subsequently removed after the mixture was cured to leave a cavity for the mock-up lesion. The lesion was made out of the same agar mixed with red glitter which was poured into the cavity and allowed to cure at room temperature. The final product was a matte agar gel with a colored lesion in the center top as shown in Fig.3.6-a.

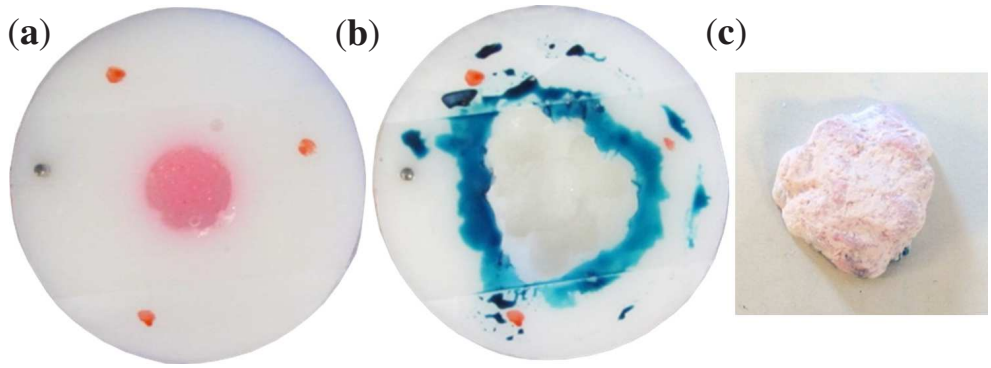

Figure 3.6: Sample (a) before resection, (b) after resection, (c) resected volume

Considering the geometric symmetry of the bladder sphere relative to the tool kinematics, it can be inferred that all kinematic measures are solely functions of the distance from the bladder neck. A non-dimensionalized distance $\overline{x} = \frac{x-\lambda}{r_b}$ is adopted here where x is the x-component of $\mathbf{p}$ in frame $\{0\}$ (See Fig. 3.3). Several points on a hypothetical sphere at various distances are selected including $\overline{x} = 0.4, 0.6, 0.8, 1.0, 1.3, 1.7, 2.0$. It was not possible to perform resection on regions with $\overline{x} < 0.4$ due to experimental set-up space constraints. To place the petri dishes at these locations, a *PUMA 560*® robot was used. Automatic C-code generation was done by MATLAB Real-Time Simulink® and real-time

implementation was carried out by MATLAB xPC Target™. A suitable location in the workspace of the robot was identified as the bladder center based on typical patient bladder location with respect to the surgeon in an operating room. The desired locations represented as end-effector poses (end-effector center position and orientation) were obtained in world coordinate frame through successive rotation matrices. The corresponding robot joint variables were computed by applying the inverse kinematics solution of the PUMA 560 according to [152]. Then the robot was commanded to servo to the desired pose by means of a gravity-compensated PD (proportional-derivative) control in joint space.

Fig. 3.7 represents the experimental setup. It was designed to mimic the clinical TURBT procedure as closely as feasible. Therefore, the overall layout of the setup and the associated geometric dimensions were selected with the clinical settings in mind. As such, the constraint point for the resectoscope was assumed $30[mm]$ off from the bladder neck ($\lambda = 30$). A flexible ring on an adaptor was mounted on a tripod with adjustable height and tilting head. The ring provided a soft pivot point for the resectoscope similar to the real anatomy. A cardboard panel was mounted on the adaptor and a drape was laid over the robot end-effector during resections to prevent any visual cue of the sample depth. Therefore, the surgeon could only observe the surface of the phantoms by a standard endoscopic lens which displayed the resection site on a standard endoscopy monitor display.

Three surgeons were asked to resect the entire lesion along with $3mm$ margin in all directions (tangential and normal) using a 26Fr Storz resectoscope. In other words, the surgeons were required to remove a cylinder of slightly larger dimensions than the red lesion. This was to help simulate the clinical circumstances where the tumor boundaries were not generally visible and the surgeons were recommended to remove tumors with marginal tissue in order to help tumor staging. The order of presentation of samples was randomized to avoid biasing the results by multiple successive trials. The surgeons were not provided with any information as to the quality of their resections to eliminate learning

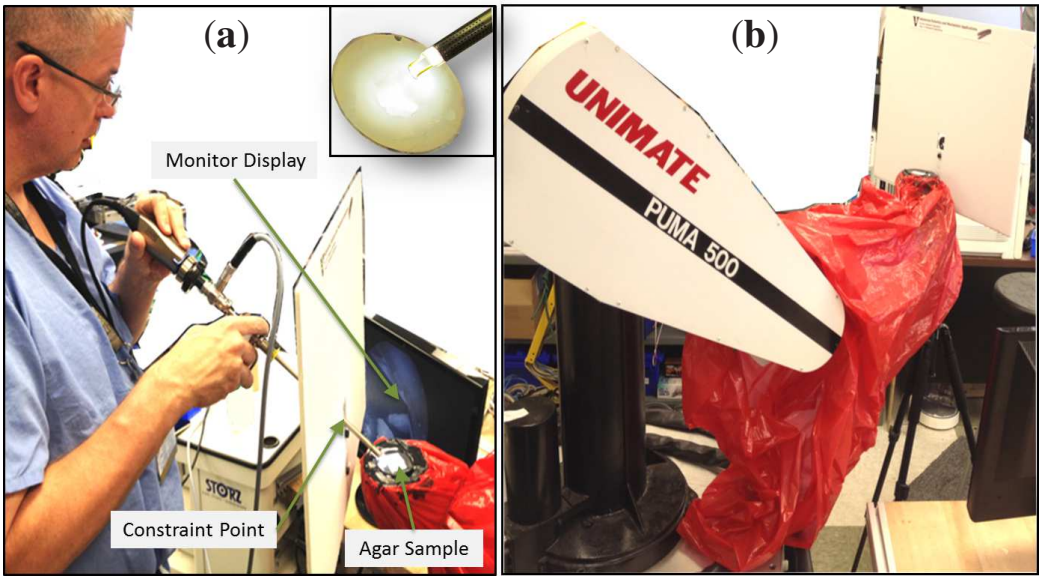

Figure 3.7: Experimental setup (a) surgeon resecting an agar sample, inset is a close-up view of resection site, (b) robot used to position agar samples

and thus potentially biasing the results.

After completion of resections(Fig. 3.6-b), the cavity was first filled and allowed to cure. The cured cast was then removed from the surrounding agar . There was no diffusion of the two agar into one another as observed by the different colors of the original agar (pale white due to use of milk when preparing the agar) and the later translucent agar. Powder talc was then applied to the surface of the removed agar with a brush (Fig. 3.6-c) and then it was scanned using a 3D laser scanner (*FaroArm Fusion*). Talc helps block the body reflection of the translucent agar that can cause undulated inaccurate surface scans. The repeatability of the scanning device is a maximum $0.104[mm]$.

Geomagic® was used for the 3D render and record of the scan. Geomagic can display the point cloud scanned by *FaroArm* and can also produce surfaces and volumes. In turn, the scanned points can be exported to various standard CAD formats.

Resection Accuracy Measures

Table 3.2 enumerates and defines the resection measures that are henceforth used to

investigate the accuracy of each resection trial. In this table, p, q denote the number of

Table 3.2: Resection Measures

Symbol	Definition	Formulation
M_t	**Tangential Mean**: average of the radial distances over all resection points of the resected volume	$(1/p)\sum_{i=1}^{p} r_i$
E_t	**Tangential Error**: average radial errors over all resection points of the resected volume, $r_{ref} = 9.82[mm]$	$r_{ref} - M_t$
M_n	**Normal Mean**: average of resection points depths	$(1/q)\sum_{i=1}^{q} z_i$
E_n	**Normal Error**: average of resection points depth errors, $z_{ref} = 9[mm]$	$z_{ref} - M_n$

points selected for tangential and normal mean computations, respectively. z_{ref} and r_{ref} is the resection desired depth and radius based on the lesion depth and radius along with $3mm$ margin.

Resection Measures Computation

The scan data was exported as *stl* files to be processed by a code written in MATLAB® that computed the resection measures in Table 3.2.

The method used to calculate resection measures is as follows. First, The bottom boundary of the removed agar (sample top surface boundary) was sought at a height level of $0.1-0.2[mm]$ max from the bottom. This is necessary since the bottom edge of the sample is not distinguishable as the sharp edges do not reflect the laser beam back at the same direction and are therefore 'lost' in the scan. The selected bottom surface was then meshed by a rectangular grid. The mesh resolution size was chosen such that it produced approximately 2000 grid cells. For resection normal measures, the average depth of the points inside each grid cell was determined and used as a representative of the respective cell i. These values were stored and used to compute the normal resection measures. For tangential measures, after selection of the bottom surface, the model was sectioned to twenty horizontal slices. Each slice was divided into 10-degree sectors. Next, the average of the points were calculated per sector. These average points were stored and used to determine the tangential resection measures.

Table 3.3: Mean translational KCI, manipulability, min. singular value and normal singular value in bladder half-octants

H/O num.	$\mathbf{KCI_t}/\boldsymbol{\mu_t}$	$\boldsymbol{\sigma_{min,t}}/\boldsymbol{\sigma_n}$	**H/O num.**	$\mathbf{KCI_t}/\boldsymbol{\mu_t}$	$\boldsymbol{\sigma_{min,t}}/\boldsymbol{\sigma_n}$
1	0.83/0.11	0.30/0.54	9	0.83/0.11	0.30/0.54
2	0.68/0.10	0.26/0.35	10	0.68/0.10	0.26/0.35
3	0.41/0.10	0.20/0.22	11	0.41/0.10	0.20/0.22
4	0.38/0.08	0.14/0.17	12	0.38/0.08	0.14/0.17
5	0.38/0.08	0.14/0.17	13	0.38/0.08	0.14/0.17
6	0.41/0.10	0.20/0.22	14	0.41/0.10	0.20/0.22
7	0.68/0.10	0.26/0.35	15	0.68/0.10	0.26/0.35
8	0.83/0.11	0.30/0.54	16	0.83/0.11	0.30/0.54

3.3 Results

3.3.1 Simulation Results

Algorithm 1 was implemented by a code in MATLAB®. The simulation parameters were selected similar to a real cautery loop deployed in a straight resectoscope as follows: $l = 500$[mm], $\nu = 3.75$[mm] , $r_L = 5.2$[mm]. Other simulation parameters were presented in section 3.2.1.

Fig. 3.8-b presents the tangential manipulability ellipses on the right lateral bladder hemisphere. These ellipses were calculated based on Algorithm 1. It is noted that the surgeon inserts the resectoscope through the bladder neck (base inferior) toward the positive $\hat{\mathbf{x}}_b$ direction. Fig. 3.8-a and 3.8-c are the side-view projections of the left and right quadrants of the same hemisphere. Note the higher eccentricity of ellipses in the inferior right quadrant (Fig. 3.8-a) in comparison to superior right quadrant (Fig. 3.8-c). Higher eccentricity corresponds to reduced isotropy of kinematic dexterity and diminished KCI_t.

The average kinematic measures in each H/O are reported in Table 3.3. This table helps compare the dexterity of manual resection in various regions.

Fig. 3.9 presents plots of the four introduced kinematic measures with respect to the non-dimensionalized distance $\overline{x}$. Note that the tool workspace is also drawn using assumptions in section 3.2.1, however it is not presented here for brevity. It is verified that the

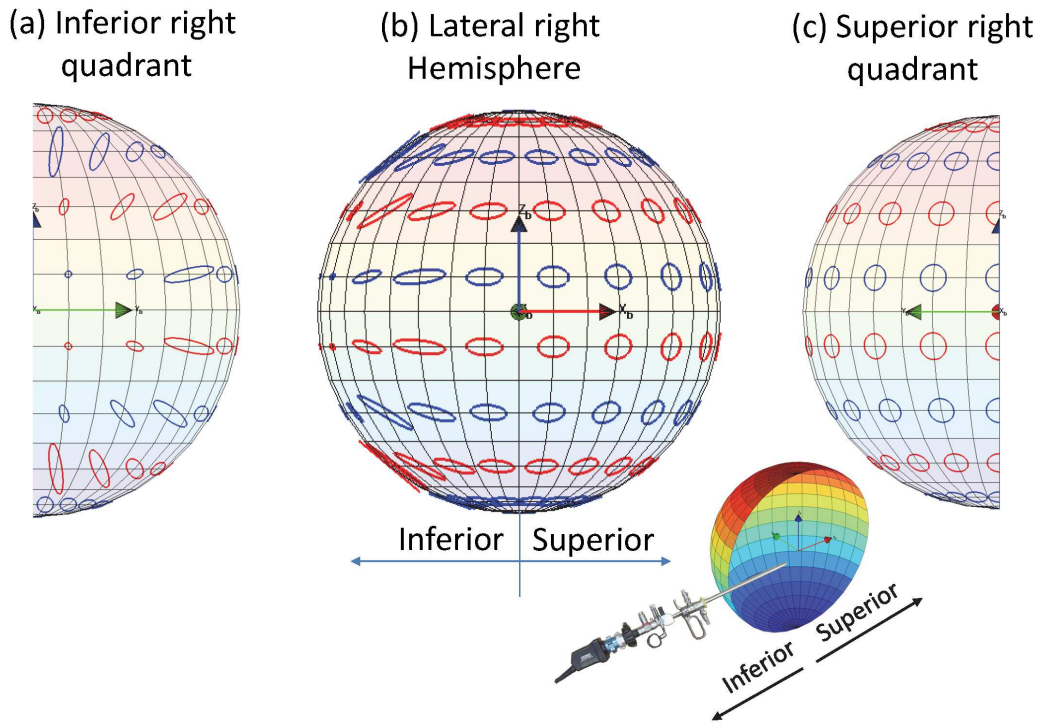

Figure 3.8: Projections of the tangential manipulability ellipses on the right lateral bladder hemisphere. Bottom right inset provides anatomical context

assumed distended bladder model always lies within the tool workspace. Hence, configuration limits do not affect simulation results.

The last simulation includes a contour plot of KCI_t in superior and anterior hemispheres of the bladder. These two plots are brought next. Spherical coordinates are used here to better locate each point on the bladder. θ and ϕ are the angles with respect to $\hat{\mathbf{x}}_b$ and $\hat{\mathbf{z}}_b$ directions respectively.

3.3.2 Experimental Results

Figure 3.11-a shows box plots of normal and tangential mean versus non-dimensionalized distance in 40 resection trials by the surgeons. The red line, the $+$ symbol and the small circle represent the median, the mean and outlier data. The red and the blue dashed line marks the desired resection depth and radius respectively ($z_{ref} = 9[mm], r_{ref} = 9.82[mm]$). Fig. 3.11-b shows the errors in the same trials.

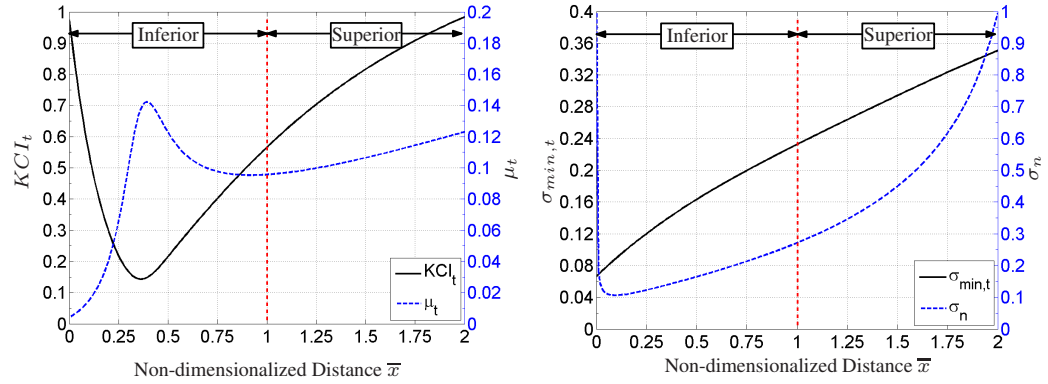

(a) (b)

Figure 3.9: Plots of (a) KCI_t(black) and μ_t(blue), (b) $\sigma_{min,t}$(black) and σ_n(blue) vs non-dimensionalized distance $\overline{x}$

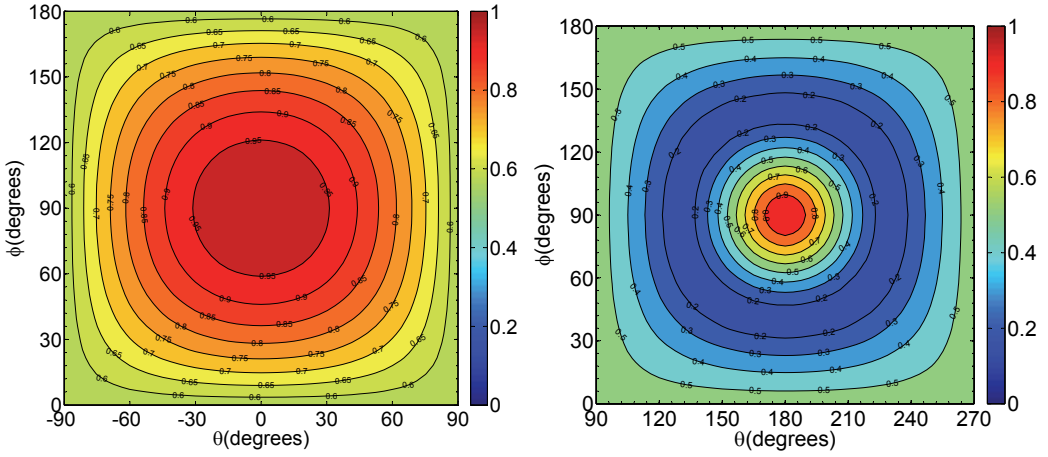

(a) (b)

Figure 3.10: Contour plots of KCI: (a) superior hemisphere, (b) inferior hemisphere

Table 3.4 shows correlation coefficients and %95 confidence intervals for resection measures against tangential and normal measures in the experimental trials. The confidence intervals brought in parentheses are obtained by 5000 bias-corrected and accelerated (BCa) bootstrap sample sets [153]. Stronger results are boldfaced.

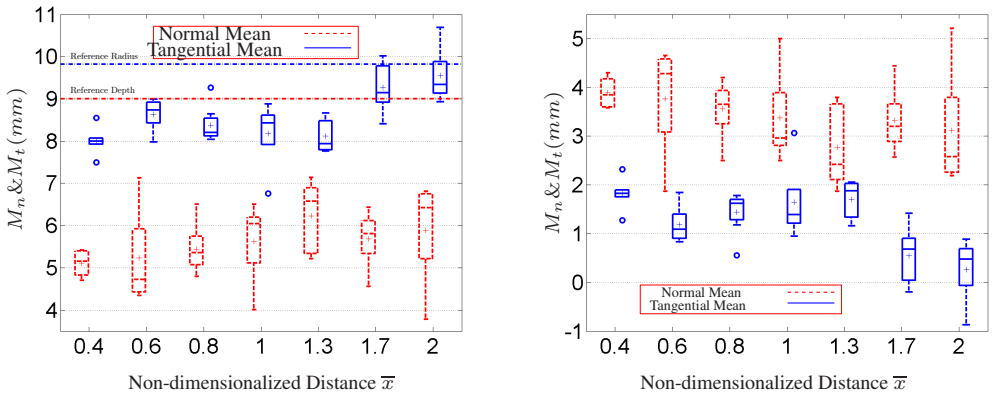

(a) (b)

Figure 3.11: Plots of (a) M_n(normal mean) and M_t(tangential mean), (b) E_n(normal error) and E_t(tangential error) vs non-dimensionalized distance $\overline{x}$

Table 3.4: Correlation coefficients and %95 confidence intervals for resection measures against kinematic measures

	$\boldsymbol{\sigma_{min,t}}$	$\mathbf{KCI_t}$	$\boldsymbol{\mu_t}$	$\boldsymbol{\sigma_n}$
$\mathbf{E_t}$	**-0.56(-0.72,-0.31)**	**-0.52(-0.69,-0.25)**	-0.09(-0.41,0.22)	**-0.64(-0.79,-0.44)**
$\mathbf{E_n}$	-0.32(-0.59,0.09)	-0.34(-0.60,0.05)	-0.17(-0.08,0.40)	-0.23(-0.52,0.26)

3.3.3 Discussions

Examining the box plots in Figs. 3.11 confirms that the surgeons almost always under-resect in both tangential and normal directions. More specifically, normal and tangential error medians for the selected distances are $\{3.85,4.28,3.65,2.96,2.42,3.20,2.58\}$ and $\{1.82,1.09,1.62,1.39,1.88,0.68,0.48\}$ respectively. This agrees with the chronic under-resection as hypothesized in previous literature (e.g. [61],[57]).

In regards to tangential accuracy, the results in Table 3.4 suggest that it has a relatively strong correlation with σ_n ((-0.79,-0.44)) and $\sigma_{min,t}$ ((-0.72,-0.31)) and medium correlation with KCI_t ((-0.69,-0.25). Hence, all these measure could be suited kinematic measures. The correlation between tangential error and normal singular value may seem counter-intuitive. However, it is important to note that tangential error computation is performed throughout the depth. From a different perspective, all singular values of manipulability

ellipsoid i.e. $\sigma_{min,t}, \sigma_{max,t}, \sigma_n$ may be candidates for manipulability - tangential or overall and therefore affect resection accuracy - in normal or tangential directions. Amongst these, σ_n has the largest variation with respect to distance in simulations (0-1, See Fig. 3.9-b). This can explain why it may represent higher correlation against resection accuracy measures.

The correlation coefficient between normal error and kinematic measures are also reported in Table 3.4 although the confidence intervals indicate medium, little or no linear correlation. This is justified by insufficient depth perception. In other words, the surgeon cannot determine properly how deep he/she is resecting. This alludes to the importance of visualization enhancement in TURBT. On the other hand, Table 3.4 shows there is a weak correlation between tangential manipulability and resection accuracy. This implies tangential manipulability cannot capture resection accuracy and therefore is not a proper measure. In fact, simulation results in Fig. 3.9-a shows that tangential manipulability varies between $0 - 0.14$ and for the most part of the distance span ($0.3 \leq \overline{x} \leq 2$), it's $0.08 - 0.14$. This small variation is responsible for low correlations. This can also be verified by inspecting H/O values in Table 3.3 where the four H/O's 1-4 (also 8-5,9-12,16-13) have only slightly different tangential manipulability values of $0.11, 0.10, 0.10, 0.08$.

Based on Table 3.3, the mean KCI_t in H/O's 1-4 is $0.83, 0.68, 0.41$ and 0.38 respectively. This is in a decreasing order from the bladder dome to the bladder neck with a highest to lowest ratio of about two. The same values hold for half-octants 8-5,9-12,16-13. The values for this series of H/O's are equal due to the sphere symmetry. Overall, it is inferred that average KCI_t over the lateral walls almost doubles as H/O's go further away from the bladder neck (tool entry point) and closer to the bladder dome zone. The normal and minimum tangential singular values exhibit a decreasing trend as well ($0.54 - 0.17$ and $0.30 - 0.14$ respectively). Indeed, σ_n and $\sigma_{min,t}$ are approximately 335% and 214% higher in the dome zone than in the neck zone. Though the rate of change is lower for $\sigma_{min,t}$. It is noteworthy that tumors are generally said to be difficult to resect at bladder dome, anterior

and neck. Nevertheless, this is not necessarily attributed to kinematic limitations. In fact these areas may be too far to reach when the bladder is distended (anterior/dome) or out of the field of view (anterior/dome/neck) [61]. Hence, improved visualization technologies or depth perception enhancement should be beneficial in these zones.

A close examination of Fig. 3.9-a suggest that KCI_t decreases at a steep slope until it reaches a minimum of 0.16 at $\overline{x} = 0.36$. Moving further away, it increases at a lesser slope until it matches unit KCI_t at bladder dome ($\overline{x} = 2$). This trend is also identifiable by analyzing the eccentricity of the ellipses plotted in Fig. 3.8. In detail, let us take a series of ellipses in red. From left where $\overline{x} = 0$, the ellipse is a small circle implying unit KCI_t with fairly small singular values. Toward positive $\hat{\mathbf{x}}_b$, the eccentricity begins to increase corresponding to lower KCI_t until a specific point ($\overline{x} = 0.36$). After that, the ellipses gradually become more isotropic until $\overline{x} = 2$ where full isotropy is achieved.

The minimum/maximum/average KCI_t is $0.56/1/0.80$ at the Superior and $0.16/1\ /0.37$ at the inferior hemisphere. Therefore, the superior hemisphere has higher kinematic feasibility for resection (almost 218% higher KCI_t on average). This can be also concluded by comparing eccentricity of the ellipses in Fig. 3.8-a and Fig. 3.8-c. The average KCI_t over the entire bladder is 0.59.

Normal singular value falls sharply from 1.00 to 0.11 at $\overline{x} = 0.09$, but increases steadily until it reaches unity at $\overline{x} = 2$. The reason for the sharp fall is the location of the fulcrum point $\boldsymbol{f}$ to the left of the bladder neck and the obtuse angle between the resectoscope axis and the bladder surface normal directions at areas close the bladder neck. On the other hand, $\sigma_{min,t}$ represents a steady increase from 0.07 to 0.35 versus the non-dimensionalized distance $\overline{x}$.

3.4 Conclusion

TURBT is a minimally-invasive surgical procedure used to diagnose bladder cancer and treat non-muscle invasive bladder cancer where a surgeon removes visible tumor with

an electrosurgical loop that cuts the tumor out. This study mainly addresses the kinematic measures in this procedure. After modeling the kinematics, several Jacobian-based measures are proposed including tangential kinematic conditioning index, tangential manipulability, tangential minimum singular value and normal singular value. Experimental trials simulating clinical TURBT is performed by three surgeons and the resection accuracy in tangential and normal (depth) directions are measured. It is verified that the surgeons generally under-resect. On further investigation, it is shown that tangential accuracy correlates relatively strongly with normal singular value and moderately with tangential kinematic conditioning index and tangential minimum singular value. A weak linear correlation with tangential manipulability is substantiated hence disqualifying it as a measure. On the other hand, normal resection accuracy is demonstrated to be weakly correlated with any of the kinematic measures suggesting that other factors may influence this variable. It it our judgment that visualization enhancement should considerably improve depth resection outcomes.

The certified measures are utilized to compare kinematic accuracy/dexterity locally in all bladder points based on the distance from the bladder neck and regionally in 16 bladder zones.

This study has few limitations. The cylindrical lesion assumption with $3[mm]$ margins for resection procedure is a simplification of clinical TURBT procedure. In reality, bladder tumors can have many different appearances. Often times, they appear as tissue lumps that protrude from bladder wall. However, the adopted model in this study is the most viable model that could be actualized in a repeatable way. Also, this model does not alter the kinematics of resection procedure. In addition, the resection study was limited in scope and size by focusing on a small number of experienced urologists. This limitation stems from a realization that the number of resections and effort involved in analyzing each resection sample limit the ability to expand this study to span a large number of study subjects. We therefore focused on only experienced surgeons in order to eliminate potential confounding

factors. Nevertheless, we believe this study reports a first attempt at correlating theoretical measures for resection dexterity with experimental data. As such, it contributes a first effort that we hope will seed and power future studies in this area.

CHAPTER 4

TURBOT: A TELEROBOTIC PLATFORM FOR TRANSURETHRAL BLADDER CANCER RESECTION AND SURVEILLANCE

The chapter presents the design and evaluation of a telerobotic transurethral robotic system for TURBT application. The clinical motivation was elaborately explained in section 2.2 and in chapter 1. In this chapter, the prior related work is surveyed. The system components are then delineated. In chapter 5, the control and the telemanipulation algorithms are described. In chapter 6, experimental evaluation of the system on phantoms and swine studies are explained.

4.1 Related Work

Towards improvement of the resectoscope, Pantuck *et al.* [154] described an iteration to the cautery element of a resectoscope such that the standard linear hand grip imparts side-to-side lateral rotation of the electrocautery loop. They evaluated the device in a multicenter clinical trial for safety and efficacy without complications. Nagele *et al.* [155] and Fritsche *et al.* [156] report water-jet-induced enucleation of bladder tumors proving feasibility of en-bloc resection of tumor sizes up to 7.5 cm. This technology that uses a probe called HybridKnife® allows the tumor to be elevated from the bladder wall by injecting a saline-based fluid at 25-30 atm submucosally that also acts as a cushion to decrease perforation incidents. The tumor is then dissected by the probe. Apart from such few advances toward improving instrumentation for TUR procedures, the fundamental method has not changed significantly since the early 1930's. Progress in the instrumentation including

improved visualization, increased manipulation precision and intra-vesicular dexterity will yield significant improvements in TUR techniques and patient outcomes.

Computer controlled technology enabled substantial progress in urology through improvements to positioning accuracy, repeatability and dexterity of surgical instrumentation. The earliest application of robotics in urology involved retrofitting a resectoscope with motorized joints and applying it endoluminally for TURP procedure (e.g. see PROBOT in Fig. (2.2)) [36, 66]. Babbar and Hemal [25] review the state of the art in percutaneous urologic surgical procedures, noting that robot assistance has gained wide acceptance in prostatectomy, cystectomy and nephrectomy. Research platforms for image guided brachytherapy have also shown initial success. Goldenberg *et al.* [157], Tokuda *et al.* [158] and Mozer *et al.* [159] present and review various robotic systems for guidance of needle placement with parallel real-time fluoroscopy, magnetic resonance imaging or computed tomography imaging.

Several transurethral robotic system have been developed as shown in Fig. (4.1), however the vast majority of them target treatment of Benign Prostatic Hyperplasia (BPH) either through TURP or HoLEP (Holmium Laser Enucleation of the Prostate) procedure (Another new technology is robotic waterjet-assisted enucleation [160]). Davies and Harris developed PROBOT, a 4-DoF robot that actuates a standard resectoscope (Fig. (2.2) and Fig. (4.1)-a) for TURP [36, 66]. Sanchez de Badajoz *et al.* developed a master-slave system for TURP (Fig. (4.1)-b) [161, 162]. The master is a motorized standard resectoscope to maintain the familiar TURP technique for the surgeon. The slave is a 4-DoF robot that replicates the master motions. Hashimoto *et al.* [163] presented a *tubular organ resection manipulator* for TURP (Fig. (4.1)-c). This 4-DoF robot displaces the prostate to the side by a bending arm at the tip to prevent damage to the urethra and then resects by a cutter. Chopra *et al.* used an MR-imaging controlled transurethral ultrasound applicator for prostate cancer treatment (Fig. (4.1)-d) [164]. The applicator can rotate and insert/retract the ultrasound transducer. Holmium Laser Enucleation of the Prostate (HoLEP) is a

modern alternative to TURP that has been shown to have better outcomes [165]. In this procedure, Holmium laser is applied in contact with the tissue for resection. Since HoLEP is difficult to perform, several researchers developed transurethral robotic systems to streamline the procedure. Ho *et al.* developed the 4-DoF CALRP laser manipulator and tested it in cadaveric experiments (Fig. (4.1)-e) [166]. Russo *et al.* report a catheter-like flexible wire-driven robot that houses a laser fiber and can be passed through a working channel of a resectoscope (Fig. (4.1)-f) [167]. This robot called ASTRO can detect contact forces through FBG sensors routed through its structure. Hendrick *et al.* report a system composed of a statically balanced endoscope and two concentric-tube 3-DoF flexible robots for HoLEP (Fig. (4.1)-g) [168].

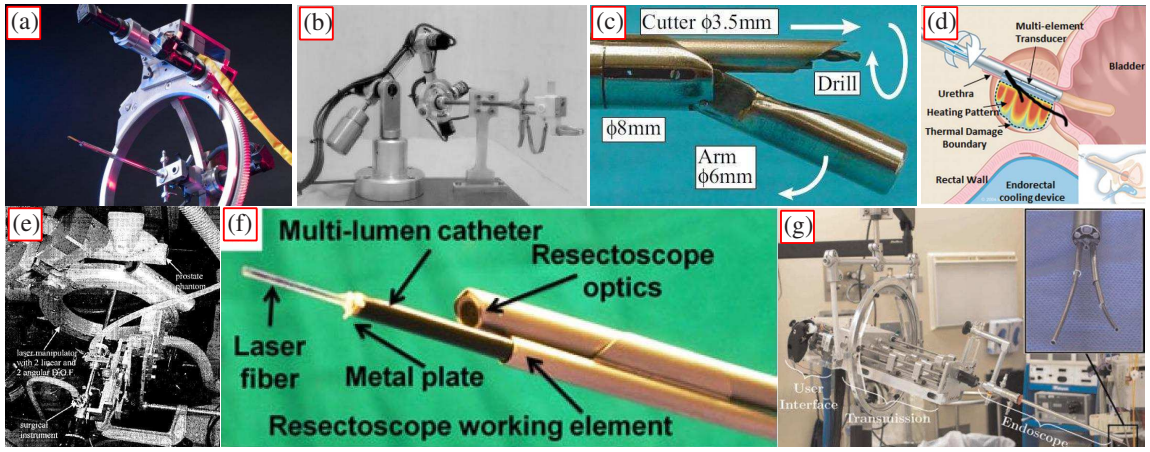

Figure 4.1: Transurethral robots for prostate surgery: (a) PROBOT, a 4-DoF motorized resectoscope for TURP (Image source: http://www.imperial.ac.uk) [36, 65, 66], (b) Master arm of telerobotic system for TURP [162]: 4-DoF motorized working element of a resectoscope, (c) 4-DoF tubular organ resection manipulator for TURP [140], (d) 2-DoF Magnetic Resonance imaging - controlled transurethral ultrasound applicator for thermal treatment of prostate cancer [164], (e) 4-DoF CALRP laser manipulator for TURP [166], (f) ASTRO: a 2-DoF multi-lumen catheter-like robot with integrated FBG sensor for contact force sensing toward HoLEP application [167], (g) A bi-manual 2×3-DoF concentric-tube based robot integrated in an offset endoscope for HoLEP [168].

In the upper urinary tracts surgical domain , Aron and Desai proposed adaptation of Sensei® X robotic catheter system (See Fig. (2.4)) for direct visualization and treatment of kidney stones and tested on an eighteen patient clinical feasibility trial [71–73].

In regards to transurethral robots developed for urinary bladder, a 1.5 mm laser scanning fiber endoscope (SFE) was developed by Seibel *et al.* that can provide full RGB color and high-resolution imaging with 70-degree filed-of-view (Fig. (4.2)-a) [169]. By incorporating the developed custom SFE in a robotic steering mechanism actuated by shape memory alloys (SMA) (Fig. (4.2)-b), cystoscopic examinations were performed automatically thus ensuring a thorough inspection of the entire bladder surface [108]. Soper *et al.* used this mechanism to scan the bladder surface automatically while obtaining images [170]. The purpose of their device is to use robotics to fully automate bladder surveillance to relieve this duty off of a surgeon and perhaps relegate it to a physician assistant (PA). Using this apparatus, they scanned a spherical bladder phantom automatically by stitching video images and generating surface mosaics [170, 171]. Xianming Ye *et al.* developed a wire-actuated hinged multi-segment mechanism to manipulate a similar ⌀ 1.2 mm SFE for autonomous bladder scanning [172]. This multi-segment mechanism allowed the tip to be normal to the bladder wall and to remain at a certain distance away from it to capture better images. Image stitching was again used to generate 3D panoramas. This system was tested on a human bladder phantom and it was shown that 60% of the inner walls could be scanned.

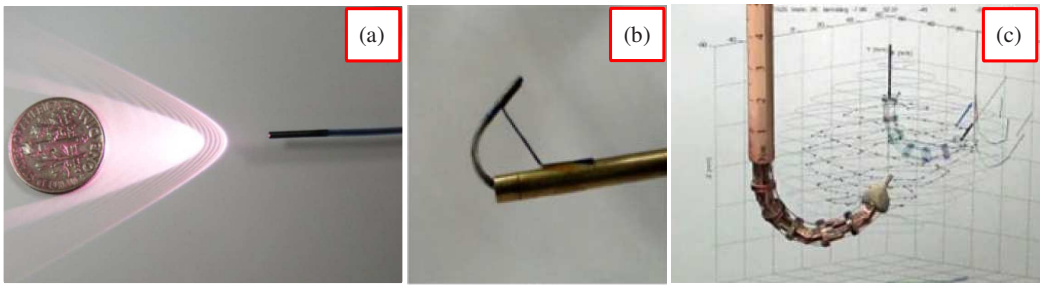

Figure 4.2: (a) Scanning fiber endoscope (SFE) probe developed by Seibel *et al.* [169]. Rigid distal tip is ⌀ 1.5 mm and 9 mm long, (b) Shape-memory-alloy-based steering mechanism to manipulate the SFE probe [108], (c) A different wire-actuated multi-segment steering mechanism that manipulates a ⌀ 1.5 mm SFE probe [172].

Goldman, Bajo and Simaan developed an early-stage proof-of-concept robot for TURBT shown in Fig. (4.3)[62]. This robot fits though a standard resectoscope with an inner bore larger than 5 mm. The robot has seven actuators and a two-segment snake-like device that allows each segment to bend in two Degrees of Freedom (DoF). The snake robot has three working channels that allow the deployment of a standard biopsy tool, a custom fabricated fiberscope with 10000 fibers and integrated light source and a third working channel that was used for delivering an ablation laser fiber. The device is axially actuated along the resectoscope axis. This robot was integrated in a telemanipulation system. It was demonstrated that the telemanipulation tracking accuracy outside the bladder was $0.48mm$ (root mean square error). The viability of biopsy and laser ablation inside an explanted bovine bladder was also demonstrated [62, 63].

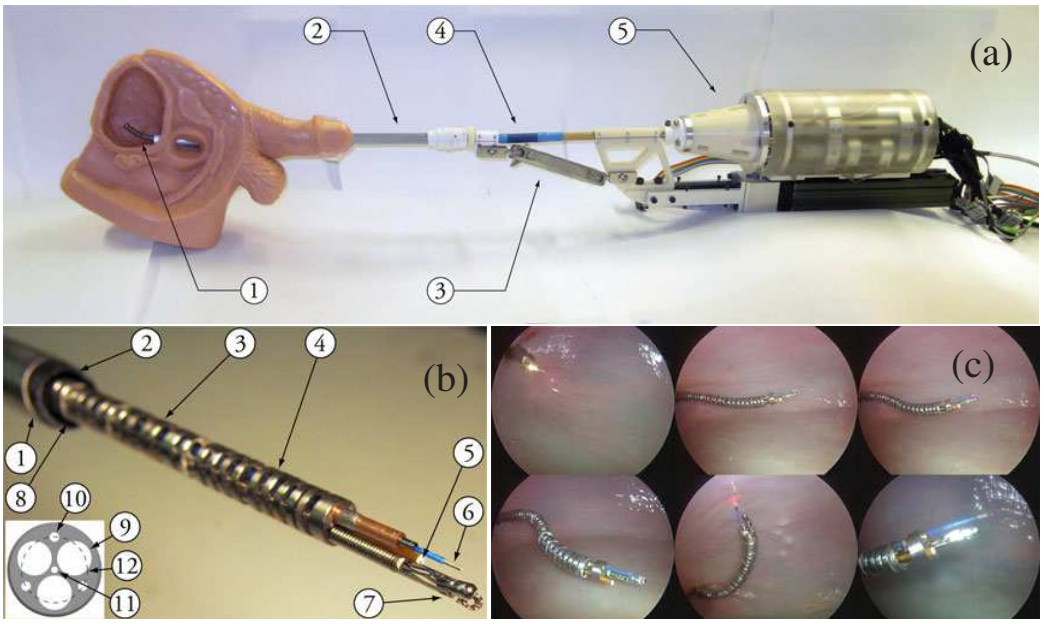

Figure 4.3: (a) Surgical slave of earlier bladder robot deployed into a mockup bladder, (b) Tooling includes fiberscope with light, biopsy cup, ablation laser fiber, (c) The robot operating inside an explanted bovine bladder

More recently, Coemert *et al.* [173] presented a bi-manual instrument with manual actuation for TURBT application as shown in Fig. (4.4)-a. They conducted preliminary studies demonstrating pick and place and gross targeting tasks. Large instrument diameter

(12.7mm), manual transmission and performance limitations are the primary shortcomings of their prototype. Xu *et al.* [174] reported a preliminary design concept of a dual-arm robotic system for transurethral procedures pending full assembly, integration and testing (See Fig. (4.4)-b).

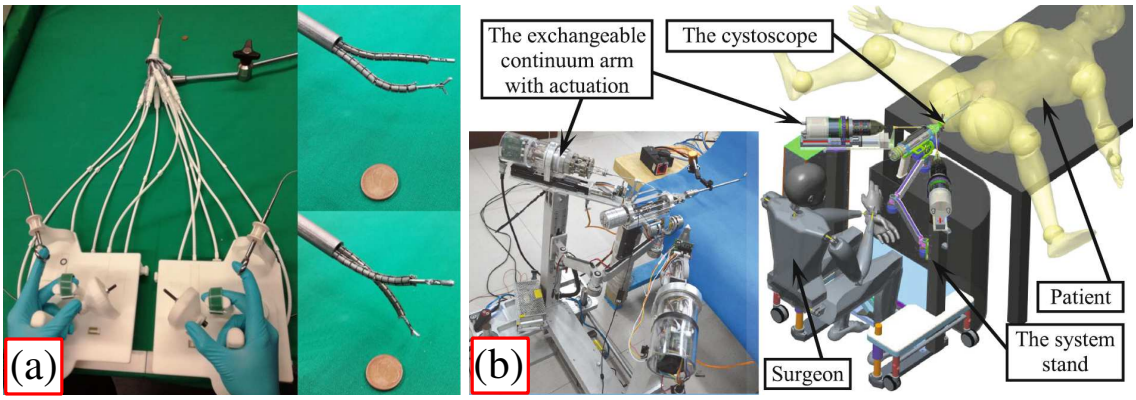

Figure 4.4: (a) dual-arm manual manipulator for TURBT (each arm is 3-DoF, note this is a manually-controlled mechanism) [173] (b) preliminary construction of a dual-arm surgical system for transurethral procedures [174].

4.2 Technical Gaps

In order to enhance TURBT procedure, several technical challenges should be addressed as follows.

1. Anatomy shape and access constraints: Compared to all other natural orifice surgery procedures, transurethral access limits the motion of the tools to only insertion and limited tilting about a vaguely defined fulcrum point near the bladder neck. More importantly, TURBT is unique in that it requires tools that can bend within the confined space of bladder while offering the ability to manipulate when bending completely backwards when inspecting or resecting near bladder neck (called *retroflexion*). Perhaps, the only other natural orifice procedure demanding comparably elaborate motion articulation is transanal procedures. Nevertheless, the tools can wiggle within the confines of an expanding access channel in a transanal scenario.

Despite high articulation requirements of TURBT, a resectoscope offers at most four degrees of freedom with limited dexterity as the rotational mobility (except for roll motion) requires pivoting action about an imaginary point close to the bladder neck. Novel surgical tools (such as a novel working element reported in [154]) do not address this issue. The transurethral robots designed for TURP or HoLEP (See Fig. (4.1)) do not possess enough degrees of freedom and were not designed for TURBT. The da Vinci surgical system® is inordinately bulky for the desired workspace and generally limited to use of 4-DoF dexterous wrists with limited workspace thus it cannot be used for TURBT either. Therefore, there is a need for tools that offer more intra-vesical dexterity with extreme flexing capabilities.

2. Anatomy/lesion indefiniteness: Apart from shape and access constraints, the thickness of the bladder wall is unknown. One study reports it is on average $3.3 \pm 1.1mm$ and $3 \pm 1mm$ for normal adult men and women respectively [175]. However, the thickness can vary $1 - 5mm$ depending on the filling stage and $0.5 - 10mm$ for different populations [176]. In addition, the tumor margin is often not distinguishable and its depth penetration is unknown. Though, it should be mentioned that recent imaging modalities such as photodynamic diagnosis [111, 112] (PDD or blue-light cystoscopy) and Narrow-band imaging (NBI) [113] as opposed to conventional white-light cystoscopy have improved tumor margin detection.

3. Visualization limitations: Lack of depth perception limits the surgeon's ability in spatial navigation and manipulation of the tool. It gets particularly more confounding in retroflexed postures to resect areas close to the bladder neck.

Goldman's system reported in [62] was the only robot designed for TURBT procedure. But it lacked several features that are necessary for a preclinically/clinically deployable system:

1. The dexterity is not sufficient. Providing higher dexterity with at least 7 DoF of

movement within the bladder is a necessity.

2. The imaging capabilities are not sufficient as it only uses a 10k-resolution fiberscope deployed in a working channel. Providing more imaging modules and better imaging quality should be considered.

3. The ablation/resection instrument should be controlled independently from the main MBCR. This provides more dexterity and helps triangulation.

4. A suitable collaborative telemanipulation paradigm is required to allow telemanipulation in the image frame. This is especially more important to enable retroflexed resections.

Addressing these limitations guided the development of TURBot. The eventual goal of this system is to offer surgeons for the first time a system that can ensure full surveillance coverage, provide accurate dissection and enable en-block resection.

4.3 Design Goals and Specifications

The key design goal for TURBot is to allow dexterous resection/ablation in all regions of the bladder in a pre-clinical setting. The goal for testing in a pre-clinical setting (e.g. animal experiments) requires that the system design allows easy sterilizability and clinical deployment. To achieve this goal, we identified several design attributes and specifications that guided our design and subsequent evaluation.

(a) Remotized actuation: A remote actuation unit helps separate the electromechanical and electronics components and circuitry while reducing the weight of the MBCR.

(b) Modularity and Assembly/Disassembly facility: The slave robot is a composition of several subassemblies such as robot-integrable resectoscope, actuation unit and MBCR that can be assembled/disassembled with minimal effort. In addition, these indepen-

dent units should be modular to facilitate assembly/disassembly and potential modification of constituent parts.

(c) Seperability: the resectoscope and the actuation unit need to be easily mounted/dismounted in order to facilitate deployment.

(d) Deployability: The robot should be deployed into the urethra with minimal weight to be manipulated by the surgeon while offering endoscopic view to allow the surgeon to safely navigate the resectoscope tip into the bladder space.

(e) Safe constrained access telemanipulation: The surgeon should be able to operate the system from any perspective (either using a fixed endoscope or using a view from a tip camera). Also the surgeon should be able to operate the robot even when it folds back on itself to reach regions close to the bladder neck. In addition, the robot should be able to seamlessly handle access constraints (e.g. operating the MBCR when it is partially within a constrained resectoscope access channel).

Though there is no pre-determined resection accuracy specification in the literature we chose $0.1mm$ as a design goal since it significantly exceeds manual resection as evaluated in chapter 3. Therefore, we specified a desired tool tip motion resolution of $0.1mm$. This specification was used to guide the design and choice of components for the actuation. In addition, we wanted each segment of the MBCR to be able to move $\pm 90^{\circ}$ in 1 second for motion responsiveness requirement set by our clinician team members. Additional details of how these specifications guided the design of the actuation unit for this system are provided in section 4.4.2.

4.4 Robotic System Components

To address the design attributes outlined above, TURBot was designed as shown in Fig. (4.5). This system includes a modular robotic arm with several quick disconnect interfaces. The actuation unit ⑦ easily separates from the supporting arm ② and from the MBCR stem ⑤. The resectoscope ⑥ also easily separates from the supporting arm ② and

the MBCR stem ⑤ and also allows fast deployment and removal of a straight endoscope. These quick disconnect interfaces use shear pins as previously reported and tested in [177].

The above-mentioned quick-disconnect points allow the surgeon to deploy the resectoscope into the bladder without maneuvering the entire surgical slave. The supporting arm ② was designed to be a statically balanced arm to allow easy adjustment of the robot once deployed into the bladder. The seperability of the actuation unit supports ease of service, interchangeability of MBCR stems and an interface for sterile draping all the non chemically cleaned or sterile electromechanical components. According to this design, the MBCR stem, resectoscope and endoscope should be pre-sterilized.

The key components of the TURBot system shown in Fig. (4.5)-a are: a surgical slave unit (① in Fig. 4.5-a or Fig. 4.5-b, a statically balanced arm (Ergotron® LX HD LCD Arm, items ②) mounted on a mobile base (item ③) and a 7-DoF haptic master device (Force Dimension Omega.7, item ④). The surgical slave unit is composed of a 6-DoF three-segment multi-backbone continuum robot (MBCR) with three working channels (item ⑤), a custom-designed *robot-compatible resectoscope* (item ⑥) that guides the MBCR and a $\varnothing 3mm$ endoscope into the surgical site and a 10-DoF actuation unit (item ⑦). The resectoscope and the actuation unit are mounted on a locking linear guide (igus® Drylin).

The three $\varnothing 1.8mm$ working channels of the three-segment MBCR ($\varnothing 5mm$, segments lengths: $18, 20, 15mm$) are used for deploying a $\varnothing 1.65mm$ DLA, a $\varnothing 1.6mm$ custom fiberscope (10K pixels) and a $\varnothing 1.0mm$ grasper. The DLA is essentially a 2-DoF single-segment MBCR that controls the motions of a Holmium laser fiber (Boston Scientific Flexiva™ TracTip 200). Each 2-DoF segment of the MBCR is actuated by three active joints that control the linear motions of the superelastic NiTi backbones by pushing/pulling to cause bending in a desired direction (pitch and yaw motion). The consecutive segments backbones are deployed concentrically to minimize actuation coupling between segments. End disks, made out of Aluminum, terminate each segment of the MBCR and are affixed to the backbones ends. The body of the MBCR was made from a custom PTFE extrusion.

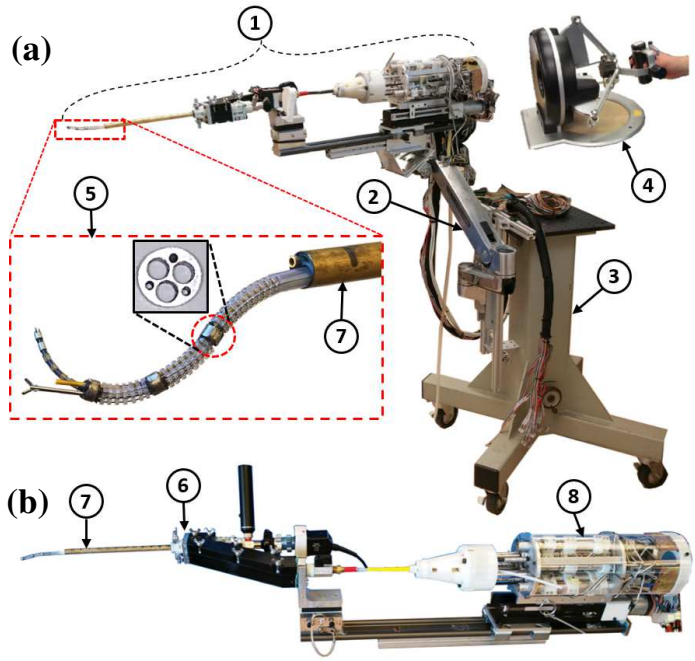

Figure 4.5: (a) TURBot system: surgical slave ①, statically-balanced arm ②, mobile base ③, master haptic interface ④. (b) surgical slave of TURBot: three-segment MBCR ⑤, robot-compatible resectoscope ⑥, resectoscope sheath ⑦, actuation unit ⑧.

The primary goal of the surgical slave shown in Fig. (4.5)-b is to deliver the dexterous multi-backbone continuum robot (MBCR) and provide visualization into the surgical site in a convenient way. It is composed of a dexterous 3-segment MBCR, a custom-designed *robot-integrable resectoscope* that guides the MBCR and the visualization module into the surgical site and also has inlet/outlet irrigation ports and the 10-DoF actuation unit. Nine DoFs are dedicated to actuating the MBCR and a linear stage with $120mm$ stroke (Heydon Kerk Motion Solutions) actuated by a $40W$ brushed DC motor (Hansen Corporation) provides a for-and-aft motion for the MBCR.

In section (4.4.1) and (4.4.1), the main constituent parts of the surgical slave i.e. robot-integrable resectoscope and actuation unit are explained in detail.

4.4.1 Robot-Integrable Resectoscope

In this section, the mechanical design of a custom resectoscope prototype that was fabricated in-house is presented. This resectoscope has a stem at its distal section that provides working channels for the MBCR, visualization module and irrigation. The MBCR and an endoscope can be inserted through two working channels. The resectoscope can be readily integrated into a the robotic system by sliding it onto a guide rail.

Figure (4.6) illustrates a prototype of the robot-integrable resectoscope. It is approximately 18.2 inches long, 5.1 inches wide and weighs about 980 grams (without visualization equipment). The design includes a stem (1) that mainly constitutes a custom central stem housed and sealed within an external sheath (see Fig. (4.7)), a sealed adaptor (2) which enables insertion of a visualization module and the MBCR, a 26Fr endoscope (MEDIT Inc.) along with its portable light source for visualization (3), a CCD camera (KARL STORZ) (4) that couples with the endoscope through a C-clamp connection for displaying endoscopic view on a monitor, a fully-rotatable endoscope guidance unit (5) to allow quick attachment and 360-degree rotation of the endoscope, an array of valves (6) for enabling controlled irrigation and selective sealing of the visualization and the robot access ports, a quick-release L-shaped bracket (7) for attaching and fixing the resectoscope assembly to a rail or a linear bearing and a camera fixture (8) that is connected to the quick-release bracket and helps carry the weight of the camera and the endoscope. The camera is gripped by twisting a knob that in turn rotates a twin lead screw. The entire camera fixture is made by additive manufacturing (3D-printed).

Figure (4.7)-a shows the stem that serves as a replacement for a traditional resectoscope access channel for manual tools. This stem is designed to provide the necessary clinical functions including delivery of inlet/outlet irrigation, light/imaging and a working channel for the MBCR delivery as shown in the Fig. (4.7)-b. It is composed of the central stem (1), external sheath (2), stem adaptor (3) and standard inlet/outlet luer-lock valves (4). The central stem went through several design revisions to address economical manufacturability

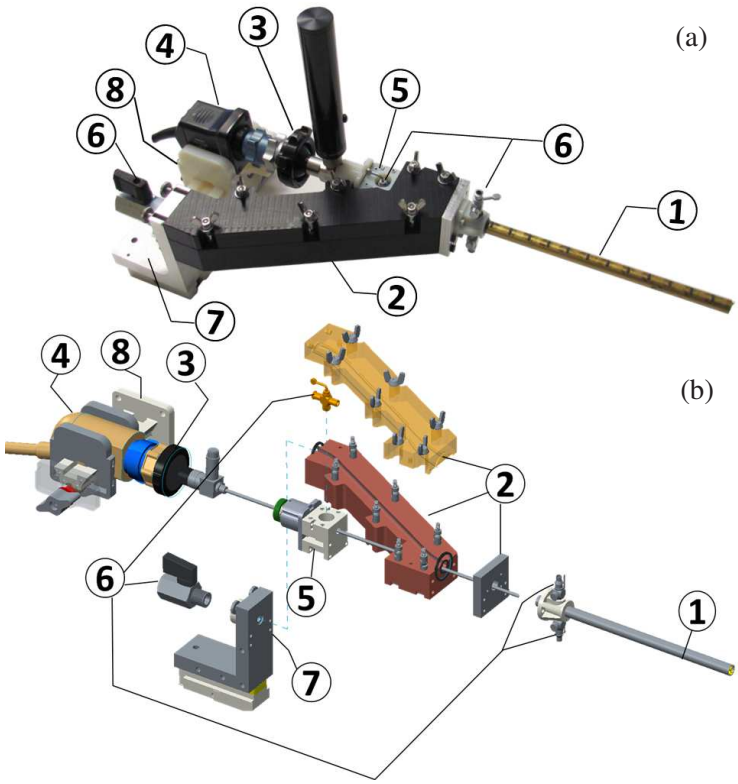

Figure 4.6: Exploded CAD view of (a) Robot-integrable resectoscope, (b) Assembled prototype. Number designation:(1) stem including a custom central stem housed and sealed within an external sheath, (2) sealed adaptor which enables insertion of a visualization module and MBCR, (3) 26Fr endoscope and portable light source, (4) CCD camera, (5) fully-rotatable endoscope guidance unit, (6) an array of valves (6) for enabling controlled irrigation and selective sealing of the visualization and the robot access ports, (7) quick-release L-shaped bracket, (8) a camera fixture.

and sufficient irrigation flow rate. Calculations were done to determine proper irrigation channel shape and size based on fluid head loss in the channel and a minimum required flow rate of 0.6 Liter/min. The visualization and the MBCR working channels are $\varnothing 3$ mm and $\varnothing 5.1$ mm respectively. The external sheath is 197 mm in length and is a standard brass alloy 260 tube having internal and external diameters of 0.351 and $3/8$ inches respectively. A 3D-printed stem adaptor attaches the stem to an aluminum block. This block is aligned with and attached to the resectoscope adaptor distal end by dowel pins and screws.

The resectoscope sealed adaptor is central to the resectoscope design. Its purpose is to ensure convenient access into the working channels of the resectoscope. These access

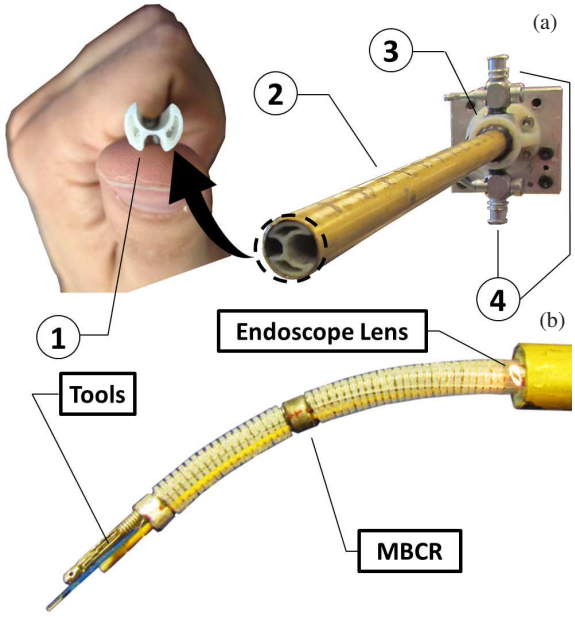

Figure 4.7: (a) Robot-integrable resectoscope stem, (b) a 5mm MBCR with tools and a 3mm endoscope lens deployed in the stem. Number designation: (1) central stem, (2) external sheath, (3) stem adaptor, (4) standard inlet/outlet luer-lock valves.

entries include robot entry at proximal end through a valve (bottom far right in Fig. (4.6)-b) and the visualization entry through the stopcock valve in the endoscope guidance unit. The sealed adaptor is comprised of two joining halves fabricated out of Delrin Acetal resin by a CNC milling machine. Front and back aluminum attachments match and connect the adaptor with the stem and the endoscope guidance unit respectively. A unique feature of the adaptor is that it can be rapidly opened hence facilitating access to the deployed instruments. This is a safety measure facilitating rapid robot extraction in case of system failure. In order to fulfill this requirement, several hinged stand-offs and wing-nut duos are used to joint bottom and top adaptor halves. In addition, all the screws connecting other parts to the adaptor are placed only in the bottom half. Calculations were performed in regards to the location of screws to prevent thread tooth stripping of plastic inserts used to secure the screws in the adaptor. The design of the adaptor guarantees complete sealing by O-rings and an O-ring chord placed at carefully selected locations.

The resectoscope can be mounted/dismounted quickly on/from a linear guide rail through

a 3D-printed attachment at the bottom of the quick-release bracket at the proximal end. A $1/32$ inch-thick slick strip with low coefficient of friction and high abrasion-resistance (ultra-high molecular weight polystyrene adhesive tape) is attached to the bottom to facilitate sliding action.

4.4.2 Actuation Unit

The secondary backbones of each of the three MBCR segments pass through the corresponding secondary backbones of its preceding segment. Three sets of three concentric NiTi backbones need to be actuated to control all nine backbones. The redundant actuation due to the use of three secondary backbones to actuate each two-DoF segment enhances payload distribution and miniaturization [178]. It also adds a safety feature to the system in case any of the backbones fails. The concentric placement of secondary backbones decouples the kinematics of segments; however it renders the design of the actuation unit challenging as it demands the actuation of three concentric backbones. The conceptual attribute requirements guiding the design architecture of the actuation unit are portability, compactness, sterilizability and Modularity. The detailed design and component selection for each joint was driven by the task specification requirements as described in section 4.4.2.1.

4.4.2.1 Derivation of Joint-Level Design Requirements

A target motion accuracy of $0.1mm$ was chosen. There is no known quantification of resection accuracy in the literature. Thus, a conservative value of $0.1mm$ was chosen since it is significantly better than the expected tip precision when manually manipulating a resectoscope having a length of in excess of $250mm$. In addition, motion responsiveness is needed to provide the surgeon the ability to move the snake robot with the necessary bending rate. Based on consultation with clinical collaborators, a bending rate of $\pm 90^{\circ}$ within 1 seconds was determined as the desired maximal bending rate for each segment. In regards to force applications, a desired value of 1 N at the tip of the robot was defined

even though the forces are minimal during normal cautery and laser resection. Given these required specifications, it is desired to determine the joint-level accuracy requirement. The remainder of this section explains this process and the results.

The kinematics of MBCR was addressed previously by [179–181]. The configuration of each segment of MBCR is represented by $\boldsymbol{\psi}_i = [\theta_{iL}, \delta_i]^T$, where $i = 1, 2, 3$ is the segment number, θ_{iL} is the bending angle and δ_i is the bending plane angle as shown in Fig. (5.1). The kinematic relation between configuration space and joint space is

$$\begin{aligned} q_{1j} &= rcos(\delta_{1j})(\theta_{1L} - \theta_0), \\ q_{2j} &= rcos(\delta_{2j})(\theta_{2L} - \theta_0), \\ q_{3j} - q_{2j} &= rcos(\delta_{3j})(\theta_{3L} - \theta_0), \end{aligned} \tag{4.1}$$

where $j = 1, 2, 3$ is the secondary backbone number, q_{ij} is the j joint variable of the segment i ($\boldsymbol{q}_i = [q_{i1}, q_{i2}, q_{i3}]^T$) and $r = 1.725mm$ is the radius of the pitch circle determining the positions of the secondary backbones in the snake disks (see Fig. (5.1)).

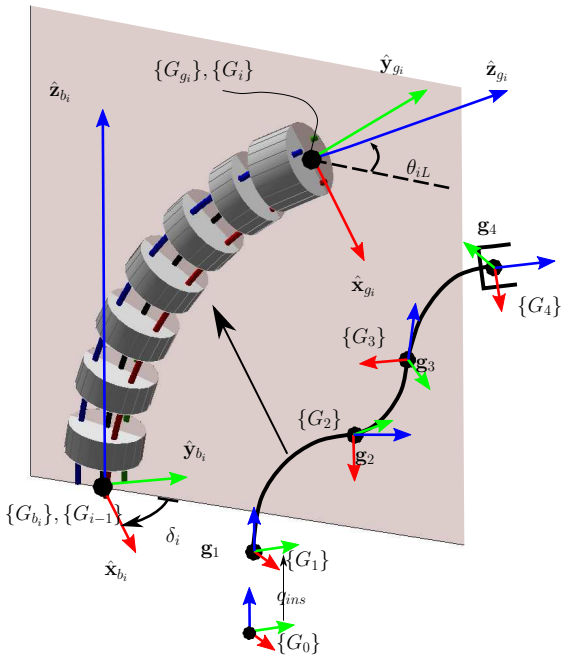

Figure 4.8: schematics of a three-segment Multibackbone continuum robot with nomenclature

To meet the motion responsiveness design requirement, i.e. bending rate of $\pm 90^{\circ}$ within 1 second, each segment actuators are required to provide maximal speeds of $4.7mm/sec$, $4.7mm/sec$ and $9.4mm/sec$ respectively. These values are obtained by substitution in Eq. (4.1).

In order to satisfy the prescribed motion accuracy of $0.1mm$, the instantaneous Jacobian relating the configuration space and the joint space should be determined. Three vector spaces are involved in this process, namely task space, configuration space and joint space. These spaces are related by the Jacobians $\mathbf{J}_{x_c\psi}$ and $\mathbf{J}_{q\psi}$ such that

$$\mathbf{J}_{x_c\psi}\Delta\psi = \Delta\mathbf{x_c}, \qquad \mathbf{J}_{q\psi}\Delta\boldsymbol{\psi} = \Delta\mathbf{q} \tag{4.2}$$

where $\mathbf{q} \in \mathbb{R}^{9\times 1} = [\boldsymbol{q}_1, \boldsymbol{q}_2, \boldsymbol{q}_3]^T, \boldsymbol{\psi} \in \mathbb{R}^{6\times 1} = [\boldsymbol{\psi}_1, \boldsymbol{\psi}_2, \boldsymbol{\psi}_3]^T, \mathbf{x}_c \in \mathbb{R}^{3\times 1}$ are joint-space, configuration-space and Cartesian-space vectors respectively. Derivation of the Jacobians is not mentioned here for brevity and the reader is referred to [182, 183] for a thorough discussion. Note that the formulations did not involve the base translation of the robot.
From equation (4.2) we obtain:

$$\Delta\boldsymbol{\psi} = \mathbf{J}^{\dagger}_{q\psi}\Delta\mathbf{q} \tag{4.3}$$

where $\mathbf{J}^{\dagger}_{q\psi}$ is Moore-Penrose pseudo-inverse of $\mathbf{J}_{q\psi}$ as determined by the following equation [149, 150]:

$$\mathbf{J}^{\dagger}_{q\psi} = (\mathbf{J}^{t}_{q\psi}\mathbf{J}_{q\psi} + \epsilon\mathbf{I}_6)^{-1}\mathbf{J}^{t}_{q\psi} \tag{4.4}$$

ϵ term is added to regularize singular configurations and $\mathbf{I}_6 \in \mathbb{R}^{6\times 6}$ is the identity matrix. Substitution of equation (4.3) in (4.2) yields:

$$\mathbf{J}_{x_cq}\Delta\mathbf{q} = \Delta\mathbf{x}_c \tag{4.5}$$

where $\mathbf{J}_{x_cq} \triangleq \mathbf{J}_{x_c\psi}\mathbf{J}^{\dagger}_{q\psi} \in \mathbb{R}^{3\times 9}$.

Equation (4.5) can be used to determine the maximal tolerable joint space error vector

to guarantee a task-space motion error having norm of of less than 0.1 mm in a specified configuration ψ. Fig. 4.9 shows the contour plots of the reciprocal of the individual joint motion accuracy to impart a 0.1 mm motion in three world coordinate unit directions $\mathbf{e}_i, \mathbf{e}_j, \mathbf{e}_k$. The values of the reciprocals are represented for $\theta_{3L} = 0°, 45°, 90°$. The horizontal and vertical axes are θ_{1L} and θ_{2L} respectively. Note that δ_i's do not affect the joint motion norm significantly, therefore they are assumed as zero. The minimum joint motion is 0.0037,0.0014 and 0.0015 mm for $\Delta\mathbf{x}_c = 0.1\mathbf{e}_i$, $\Delta\mathbf{x}_c = 0.1\mathbf{e}_j$ and $\Delta\mathbf{x}_c = 0.1\mathbf{e}_k$ respectively.

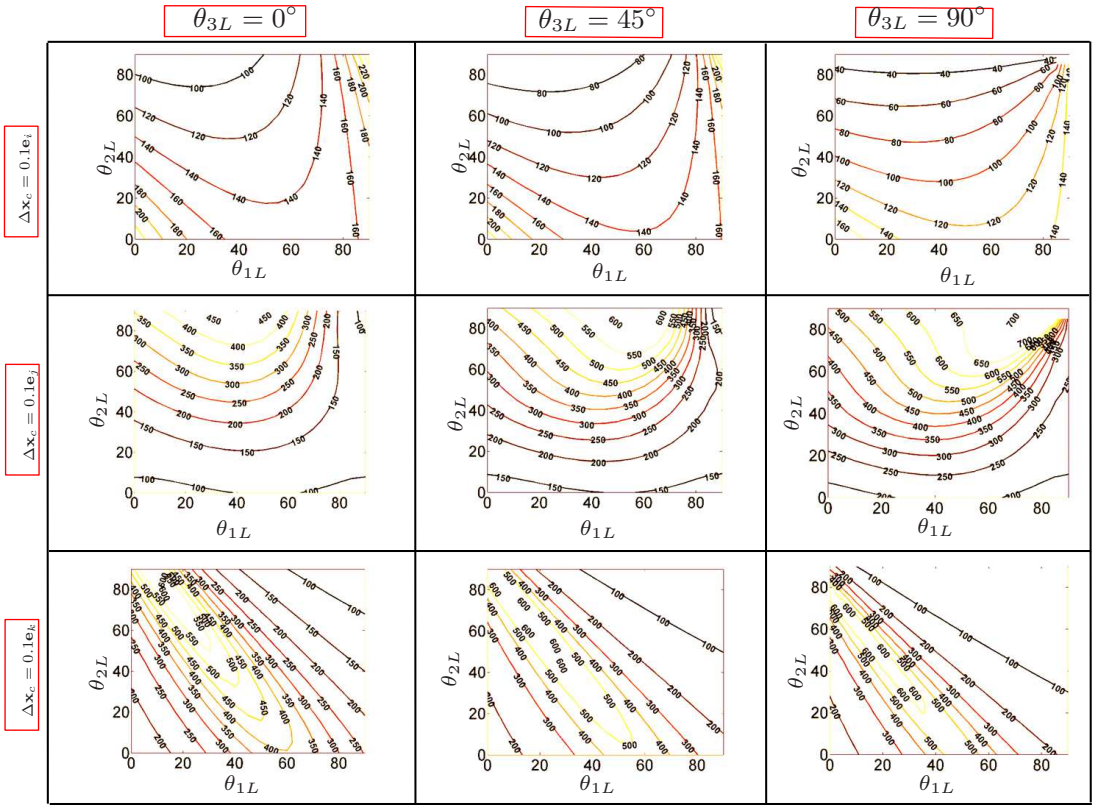

Figure 4.9: Contour plots of $\frac{1}{\|\Delta q_i\|}$ versus θ_{1L}(horizontal axis) and θ_{2L} (vertical axis) for $\delta_1 = \delta_2 = \delta_3 = 0$, $\theta_{3L} = 0°, 45°, 90°$, $\Delta\mathbf{x}_c = 0.1\mathbf{e}_i, 0.1\mathbf{e}_j, 0.1\mathbf{e}_k$

In order to determine the minimum required joint motion for all possible $\Delta\mathbf{x}_c$ directions, we consider equation (4.5) again. Using singular value decomposition and matrix

algebraic manipulations, it can be proved that

$$\|\Delta \mathbf{q}\| \geq \frac{\|\Delta \mathbf{x}_c\|}{\overline{\sigma}(\mathbf{J}_{x_c q})} \tag{4.6}$$

where $\|.\|$ and $\overline{\sigma}(.)$ represent Euclidean norm and maximum singular value respectively. Therefore,

$$\|\Delta \mathbf{q}\|_{min} = \frac{\|\Delta \mathbf{x}\|}{\max\limits_{\mathbb{Q}} \overline{\sigma}(\mathbf{J}_{x_c q})} \tag{4.7}$$

where $\mathbb{Q}$ denotes the the entire robot configuration space.

Equation (4.7) determines the required joint-level motion accuracy to meet a demanded positional accuracy. The robot configuration space was discretized and the maximum singular value was computed numerically at each configuration. The maximum value among the maximum singular values was determined. Using a $0.1mm$ task-space accuracy and $\epsilon = 10^{-7}$, the required joint-level motion accuracy was calculated as $0.0013mm$.

The first three columns of Table 4.1 summarize the simulation results using the task specifications of motion responsiveness. The last column summarizes the simulation results for actuator torques using the interaction force task specification while considering particulars of the actuation unit architecture. At the outset, static simulations using the statics model in [178] were used to determine the required actuator forces for a three segment continuum robot, but with additional consideration for flexural rigidity of deployable tools such as a fiberscope and a flexible gripper. The simulations resulted in joint force requirements that ranged from 30 N to 55 N when considering all segments. Taking into account the design architecture of the actuation unit where the actuator of the first segment carries the actuators of the other segments, we have conservatively set the required joint force of the first segment actuator to 150 N.

Table 4.1: Required joint-level specifications and the corresponding requisite gearmotor torques

Segment #	Joint stroke required	Min. joint -level position resolution	Max joint speed	Max joint force
1	4.7 mm	0.0013 mm	4.7 mm/s	150 N
2	4.7 mm	0.0013 mm	4.7 mm/s	30 N
3	9.4 mm	0.0013 mm	9.4 mm/s	30 N

4.4.2.2 Actuation Unit Architecture

The 9-DoF actuation unit is illustrated in detail in Fig. (4.10). Referring to Fig. 4.10-(a), the actuation unit (1) connects to the MBCR backbones using a *detachable actuation interface* (2). The backbones are routed from the detachable actuation interface to the MBCR through an *actuation cone* (3). The detachable actuation interface provides the conceptual attribute of separability of actuation and supports sterilizability since all the actuation unit components can be contained in a sterile drape while keeping the MBCR, cone and actuation interface as a contained assembly to undergo sterilization.

To enhance modularity and compactness, the core of the actuation unit was designed based on three identical *backbone actuation modules* (100), (200), (300). Each sub-assembly has three *cylinders* (101), (102), (103) designated for actuating the first, second and third segments of the MBCR. The three sub-assemblies are secured in place between the *front plate* (4) and *rear plate* (6). The structural stiffness of the actuation unit is provided by three structural elements, two *Aluminum beams* (9) on the sides and the *attachment base plate* (5) on the bottom. When these three components are connected to the front and the rear plate, they form the chassis of the actuation unit. Additionally, the attachment base plate connects the slave robot to the insertion stage mounted on an adjustable passive arm shown in Fig. (4.5). Figure 4.10-(d) shows the potentiometers (8) (Panasonic EWA-P10C15A14). These potentiometers provide absolute position feedback to allow homing the backbones at TURBot start-up. The incremental magnetic encoders are used for high real-time position

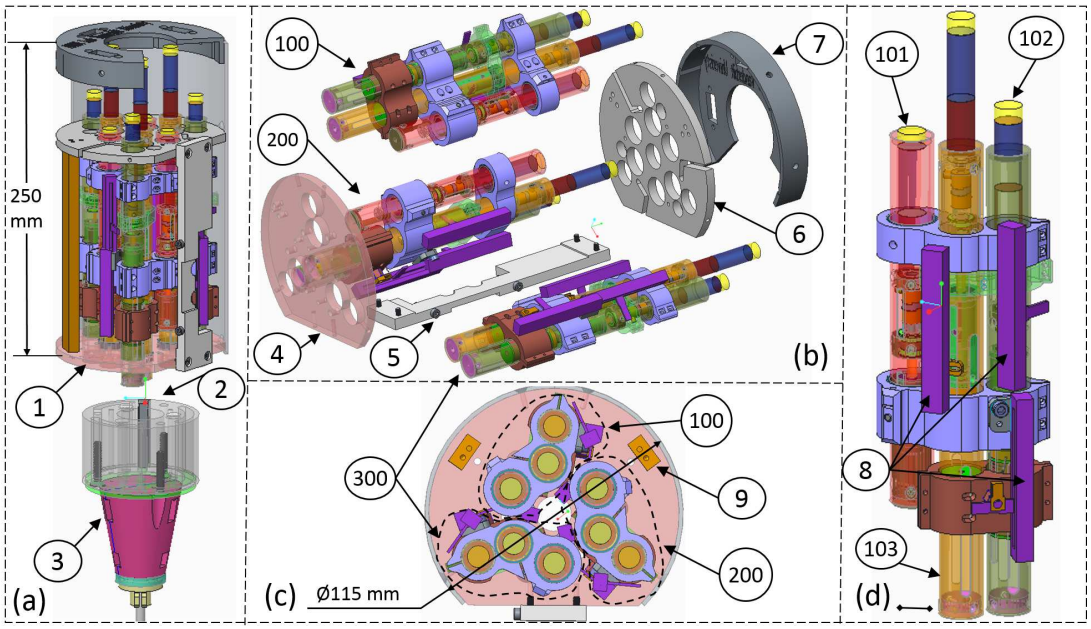

Figure 4.10: Actuation Unit Exploded view: (a) Assembly showing the actuation unit ①, the detachable actuation interface ②, and the actuation cone ③; (b) Exploded view showing the three backbone actuation modules (100)(200)(300), (c) bottom view showing axial symmetry, (d) backbone actuation module assembly

control feedback during robot operation .The choice of motors, gearheads and lead-screws and their selection justification are brought in Appendix B. For more details on the actuation unit, the detachable actuation interface and cone, the reader is referred to [177]

4.5 Conclusion

In this chapter, prior art was reviewed in regards to tools and systems that aimed for increasing the performance of bladder surveillance and transurethral resection. Then, a new telerobotic surgical platform called TURBot was presented for bladder cancer surveillance and resection. The design of TURBot was explained in details. Then, two of its primary constituents; namely the robotic slave and the robot-integrable resectoscope were delineated in details. TURBot is the only system that offers precision and intra-vesicular dexterity while providing a platform for deploying new imaging techniques and supporting traditional wire loop cautery and/or laser tumor resection/ablation instruments.

CHAPTER 5

MODELING AND CONTROL ALGORITHMS OF TURBOT

The previous chapter presented the design of TURBot; a telerobotic transurethral robotic system for TURBT application. the focus of this chapter is on the modeling, calibration and control algorithms for the teleoperated motion control of TURBot.

5.1 Kinematics of Multi-Segment MBCR

A summary of the kinematics of the TURBot's multi-segment MBCR is presented here. For detailed derivations, the reader is referred to earlier work in [182, 184, 185]. Fig. 5.1 shows a schematic of a three-segment MBCR. The configuration of the i^{th} segment ($i = 1, 2, 3$) is represented by $\boldsymbol{\psi}_i = [\theta_{iL}, \delta_i]^{\mathrm{T}}$ where θ_{iL} is the bending angle of the segment and δ_i is the angle of the plane of bending. The configuration of a multi-segment MBCR is represented by $\tilde{\boldsymbol{\psi}} = [\boldsymbol{\psi}_1^{\mathrm{T}}, \boldsymbol{\psi}_2^{\mathrm{T}}, \boldsymbol{\psi}_3^{\mathrm{T}}, q_{ins}]^{\mathrm{T}} \in \mathbb{R}^{7\times 1}$ where q_{ins} is the motion of the three-segment MBCR base disk relative to the resectoscope sheath.

We will henceforth use ${}^m\mathbf{x}$ to designate vector $\mathbf{x}$ expressed in frame $\{M\}$ and ${}^m\mathbf{R}_n$ to denote the rotation matrix relating frame $\{N\}$ to frame $\{M\}$. Also, we will use $\mathbf{x}$ to denote the position of the origin of frame $\{X\}$. For brevity, the gripper frames $\{G_i\}$ will simply be denoted by $\{i\}$. Also, we assume that the frame of the base disk of the i^{th} segment aligns with the gripper of the preceding segment (segment $i-1$). Finally, we use $\{G_0\}$ to denote a frame attached to the distal end of the resectoscope sheath and $\{W\}$ to denote the world frame.

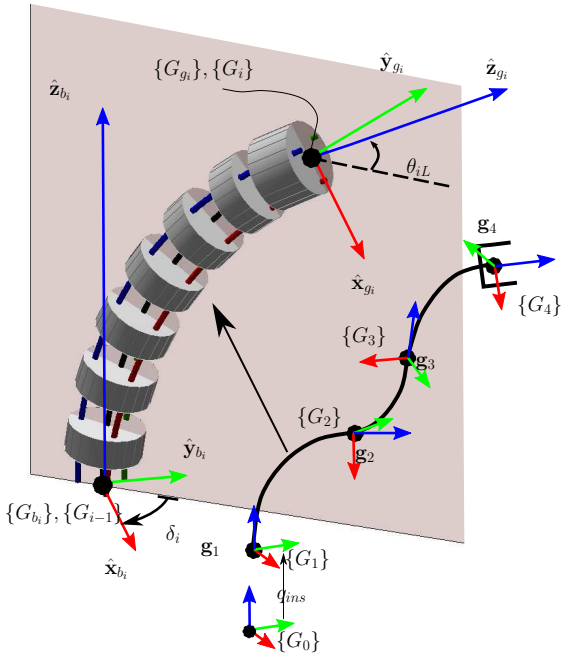

Figure 5.1: schematics of a three-segment Multibackbone continuum robot with nomenclature

The pose of a single-segment MBCR end disk was derived in [184]. Referring to Fig. 5.1, it was shown that ${}^{i-1}\mathbf{g}_{i/b_i}$ (the position of the end disk $\mathbf{g}_i$ of the i^{th} segment with respect to its base and expressed in the frame of the end disk of the preceding segment) is given by:

$$ {}^{i-1}\mathbf{g}_{i/b_i} = \frac{l_i}{\theta_{iL} - \pi/2} \begin{bmatrix} c_{\delta_i}(s_{\theta_{iL}} - 1) \\ -s_{\delta_i}(s_{\theta_{iL}} - 1) \\ -c_{\theta_{iL}} \end{bmatrix} \tag{5.1} $$

where $s_x \triangleq \sin(x)$, $c_x \triangleq \cos(x)$ and l_i is the length of the i^{th} segment. The orientation of the i^{th} gripper frame relative to the preceding segment gripper frame is given by:

$$ {}^{i-1}\mathbf{R}_i = e^{\mathbf{e}_3{}^\wedge(-\delta_i)}\, e^{\mathbf{e}_2{}^\wedge(\pi/2-\theta_{iL})}\, e^{\mathbf{e}_3{}^\wedge\delta_i} \tag{5.2} $$

where $\mathbf{e}_k, k = 1,2,3$ denote the standard basis vectors for $\mathbb{R}^3$, and $\mathbf{x}^\wedge$ denotes the cross-product matrix of vector $\mathbf{x}$.

For a multi-segment MBCR as in Fig. 5.1, the rotation matrix from the base of the i^{th} segment to the world frame $\{W\}$ can be obtained readily by a moving frame rotation sequence:

$$ {}^{w}\mathbf{R}_i = {}^{w}\mathbf{R}_0 \prod_{j=1}^{i} {}^{j-1}\mathbf{R}_j, \qquad i = 1, 2, 3 \tag{5.3} $$

where ${}^{0}\mathbf{R}_1 = \mathbf{I}_3$ (identity matrix).

The position of $\mathbf{g}_i$ is given by a vector sum of ${}^{i-1}\mathbf{g}_i$, which were expressed in (Eq (5.1)):

$$ {}^{w}\mathbf{g}_i = \sum_{j=1}^{i} {}^{w}\mathbf{R}_{j-1} {}^{j-1}\mathbf{g}_{j/b_j}, \quad i = 1, 2, 3 \tag{5.4} $$

The kinematics of the MBCR can be determined following on assumptions of negligible weight, small external wrenches, equidistant backbones and constant-curvature bending:

$$ \mathbf{J}_{x\tilde{\psi}} \dot{\tilde{\boldsymbol{\psi}}} = \boldsymbol{\xi} \tag{5.5} $$

where $\boldsymbol{\xi} = [\mathbf{v}^{\mathrm{T}}, \boldsymbol{\omega}^{\mathrm{T}}]^{\mathrm{T}}$ is the end-effector twist (linear and angular velocity of end-effector). The instantaneous kinematics Jacobian $\mathbf{J}_{x\tilde{\psi}} \in \mathbb{R}^{6\times 7}$ can be expressed as a function of the instantaneous Jacobians of the three segments

$$ \mathbf{J}_{x\tilde{\psi}} = [\mathbf{S}_1\mathbf{J}_{x\psi_1}, \mathbf{S}_2\mathbf{J}_{x\psi_2}, \mathbf{S}_3\mathbf{J}_{x\psi_3}, \$_{ins}] \tag{5.6} $$

where $\$_{ins} = [0, 0, 1, 0, 0, 0]^{\mathrm{T}}$ and $\mathbf{J}_{x\psi_i}$ is the i^{th} segment configuration-to-task space Jaco-

bian [184, 186].

$$\mathbf{J}_{x\psi_i} = \begin{bmatrix} l_i c_{\delta_i}\chi_1 & -l_i s_{\delta_i}\chi_3 \\ -l_i s_{\delta_i}\chi_1 & -l_j c_{\delta_i}\chi_3 \\ l_i\chi_2 & 0 \\ -s_{\delta_i} & c_{\delta_i} c_{\theta_{iL}} \\ -c_{\delta_i} & -s_{\delta_i} c_{\theta_{iL}} \\ 0 & -1 + s_{\theta_{iL}} \end{bmatrix} \tag{5.7}$$

$$\chi_1 \triangleq \frac{(\theta_{iL} - \pi/2)c_{\theta_{iL}} - s_{\theta_{iL}} + 1}{(\theta_{iL} - \pi/2)^2},$$

$$\chi_2 \triangleq \frac{(\theta_{iL} - \pi/2)s_{\theta_{iL}} + c_{\theta_{iL}}}{(\theta_{iL} - \pi/2)^2},$$

$$\chi_3 \triangleq \frac{s_{\theta_{iL}} - 1}{(\theta_{iL} - \pi/2)}$$

In addition, $\mathbf{S}_i$ is a twist transformation matrix (adjoint transformation) given by

$$\mathbf{S}_i = \begin{bmatrix} {}^w\mathbf{R}_{i-1} & ({}^w\mathbf{g}_i - {}^w\mathbf{g}_3)^\wedge \\ \mathbf{0}_3 & {}^w\mathbf{R}_{i-1} \end{bmatrix}, \quad i = 1, 2, 3 \tag{5.8}$$

The joint value of the j^{th} backbone of the i^{th} segment is:

$$q_{ij} = r_b c_{\delta_{ij}}(\theta_{iL} - \pi/2), \quad i = 1, 2, 3 \tag{5.9}$$

where r_b is the pitch circle radius locating the secondary backbones around the central backbone and $\delta_{ij} = \delta_i + (j-1)(2\pi/3)$. Eq. (5.9) can be modified to account for backlash, motion and force transmission losses in the elastic backbones and coupling among segments [187].

Fig. 5.2 shows a schematic diagram of TURBot control architecture. The user interacts with the system by using a 7-DoF haptic interface. This provides reference trajectories to the high-level control algorithms of TURBot through a UDP communication at 125 Hz. These algorithms are encapsulated as *Telemanipulation Tracking* and *Redundancy Resolution* blocks in Fig. 5.2. The Telemanipulation Tracking block receives the haptic device pose $({}^{m_b}\mathbf{m}_g, {}^{m_b}\mathbf{R}_{m_g})$ from the master and the camera orientation $({}^{g_0}\mathbf{R}_c)$ from an optical tracker and outputs the desired twist of MBCR end-effector $(\boldsymbol{\xi}_{des})$. This desired twist is designed to guarantee the MBCR end-effector tracks the desired position and orientation. The Redundancy Resolution block accounts for the tubular access constraints of the MBCR segments by requiring each segment partially included within the resectoscope sheath to straighten - as demonstrated in Fig. 5.7. This prevents a potential damage to TURBot MBCR and the internal sheath of the resectoscope.

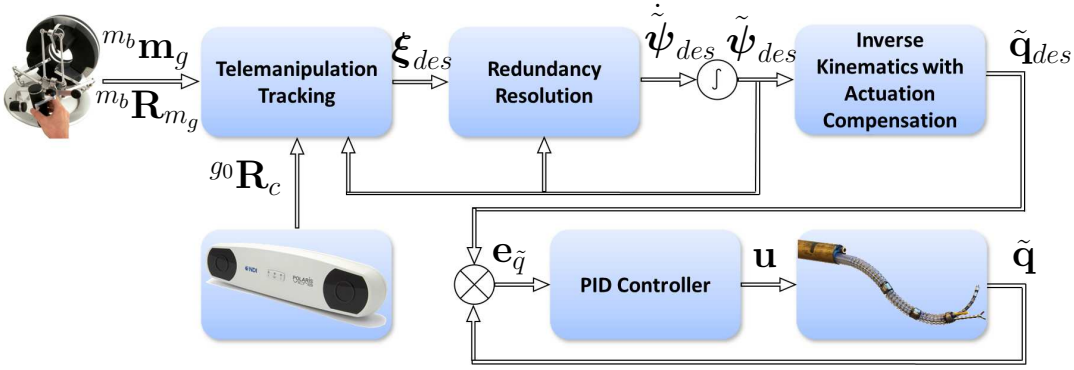

Figure 5.2: Schematic illustration of TURBot system.

The output of the Redundancy Resolution block is configuration speeds $(\dot{\tilde{\boldsymbol{\psi}}}_{des})$. A numerical integration scheme (Euler forward difference) gives the desired configuration of TURBot $(\tilde{\boldsymbol{\psi}}_{des})$. The inverse kinematic of the MBCR (Eq (4.1) with an actuation compensation model to account for backlash, friction and backbones elastic deformations yields the command joint-level variables that are fed into a PID controller on each joint at each iteration to close the joint-level error.

The control code was developed under MATLAB® R2010a/Simulink® 7.5. xPC Target operating system (MathWorks®) running at 1 KHz was used for real-time implementation. The haptic interface and the optical tracker communicated with the target machine hosting xPC Target at 125 Hz.

5.2.1 Actuation Compensation of MBCR

The kinematic equation of the MBCR described by Eq. (4.1) is not accurate because it does not take into account several factors as follows:

- The axial deflection of the backbones due to the actuation forces.
- The frictional forces acting on the long actuation lines especially in the cone (see Fig. (4.10)) and in the custom-integrable resectoscope.
- The spacer tube on MBCR constraining the backbones bending.
- The backlash in the actuation unit

Several modeling and control methods have been proposed to compensate for such uncertainties and/or unmodelled effects. Xu and Simaan used recursive least-square estimation using joint position and configuration variables measurement to estimate backlash and compensation gains of elastic rod model [188]. Simaan *et al.* proposed an actuation compensation method that extended the model in [188] by the characterization of motion transmission losses and coupling using Fourier series approximation and applying the statics model of the MBCR [182]. Bajo *et al.* proposed using both joint and configuration control feedback to enhance motion control accuracy of MBCRs [189].

Due to a limited joint stroke in the actuation unit and a fairly large backlash in the second stage of the actuation unit, a different method of actuation compensation was adopted.

Accordingly, the kinematic model in Eq. (4.1) is adapted as follows:

$$\begin{aligned}
\tilde{q}_{1j} &= \kappa_1 \cos\delta_{1j}(\theta_{1L} - \frac{\pi}{2}) + \lambda_1 sgn(\dot{q_{1j}}), \\
\tilde{q}_{2j} &= \kappa_2 \cos\delta_{2j}(\theta_{2L} - \frac{\pi}{2}) + \lambda_2 sgn(\dot{q_{2j}}), \\
\tilde{q}_{3j} &= \tilde{q}_{2j} + \kappa_3 \cos\delta_{3j}(\theta_{3L} - \frac{\pi}{2}) + \lambda_3 sgn(\dot{q_{3j}})
\end{aligned} \tag{5.10}$$

where $\tilde{q}_{ij}, i, j = 1, 2, 3$ is the compensated joint displacement, λ_i is the backlash compensation term that is measured in the actuator space (joint space). κ_i is a compensation gain. By observation, this gain was found to vary as a function of the MBCR configuration. Therefore, it is necessary to calibrate it to achieve a more accurate motion control.

5.2.1.1 Calibrating Compensation Gains

To find κ_i in Eq. (5.10), we rely on the measurement of the bending angles $\tilde{\theta}_{jL}^{measure}$ using magnetic trackers versus the command banding angle $\tilde{\theta}_{jL}^{cmd}$. Figure (5.3) shows the attached magnetic sensors for the measurement of the bending angle of the second segment and computation of κ_2. An iterative procedure outlined in Algorithm (2) converges to the calibrated compensation gain for a given segment and configuration. The obtained

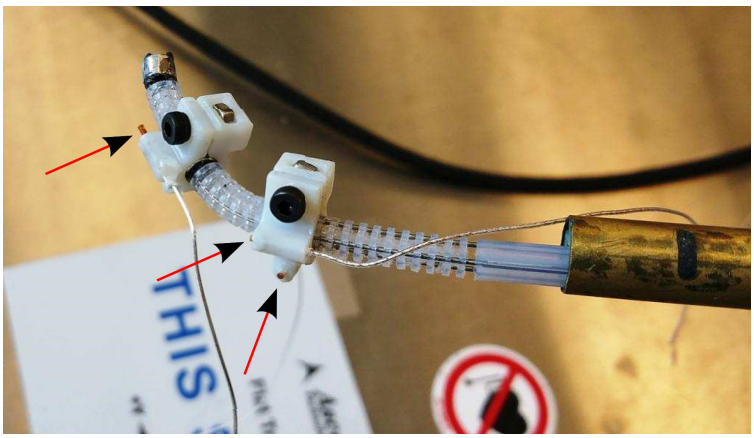

Figure 5.3: Measurement of a segment's configuration to find calibration coefficient. Arrows point to 6-DoF magnetic trackers

values of κ_i from Algorithm (2) are valid for a segment and a specific configuration. This

Algorithm 2 Calibration of compensation gains of MBCR inverse kinematic model Eq. (5.10)

Input: $\kappa_j^{(0)}$ ▷ Initial guess for compensation gain κ_j
Output: κ_j ▷ Calibrated compensation gain of segment j at a given configuration
1: $n = 0$ ▷ Initialization
2: **do**
3: $\quad n \leftarrow n + 1$
4: $\quad \kappa_j^{(n)} \leftarrow \kappa_j^{(n-1)} \frac{\tilde{\theta}_{jL}^{cmd}}{\tilde{\theta}_{jL}^{measure}}$
5: **while** $|\kappa_j^{(n)} - \kappa_j^{(n-1)}| \leq \epsilon$
6: $\kappa_j = \kappa_j^{(n)}$

algorithm was repeated for discrete points in the configuration space of each segment. The actuation compensation based on Eq. (5.10) uses these values for those select points. For the rest of the points in the configuration space of the robot, a cubic spline fit was utilized to interpolate smoothly between the values of κ_i.

5.2.1.2 Calibration Results

To determine the robot configuration set-point tracking error before calibration, each segment was commanded in increments of 5 degrees in θ_{jL} and the bending angle was measured. Figure (5.4) represents the plot of measured versus command bending angles for each segment of TURBT robot. The red line indicates the ideal case where the true and the command bending angles match. The absolute bending angle average error for segments 1,2,3 is 24.65,16.81 and 17.22 degrees respectively.

Figure (5.5) shows the plots of bending angle errors for each segment of TURBT robot after implementation of the proposed actuation compensation. The average of absolute errors in bending angle are reduced to 4.23, 4.12 and 5.26 degrees for each segment (for the workspace of $\pi/6 \leq \theta_{jL} \leq \pi/2$, $-\pi \leq \delta_j \leq \pi$).

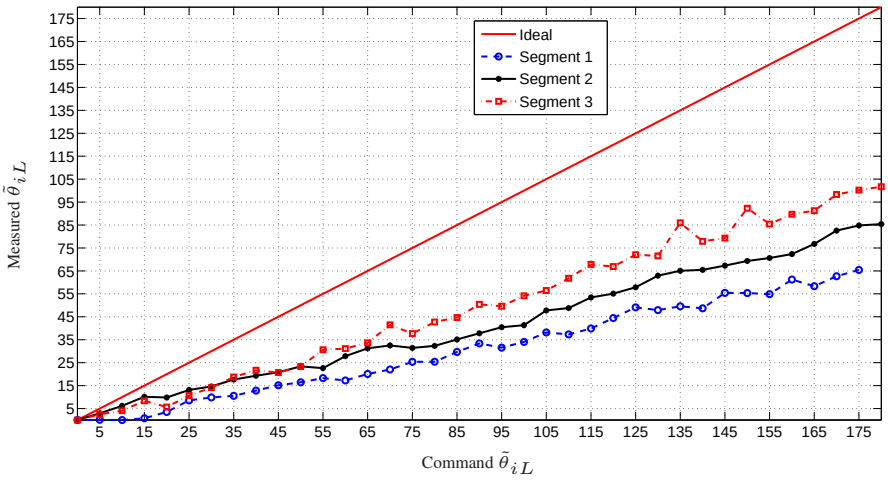

Figure 5.4: Measured versus command bending angles for each segment of TURBT robot ($\delta_1 = -30$,$\delta_2 = 0$,$\delta_3 = -30$)

5.2.2 TURBot Telemanipulation Tracking

In this section, we focus on Telemanipulation Tracking block in Fig. (5.2). For an intuitive human-machine interaction, the surgeon's wrist motions should be interpreted through a proper framework that translates them to reference motion commands of the slave robot. In the TURBot system, the surgeon's only visual feedback is delivered by an external camera. Therefore, a reasonable frame of reference for interacting with the robot is the image frame. This method, called *eye-to-hand telemanipulation* herein, was adopted for telemanipulation of TURBot. In the following section, the desired position and orientation of TURBot end effector are formulated in a resolved rate control framework. Logics for reinitializing initial master pose and computation of end effector twist are explained in section (5.2.3). Note that the world frame coincides with $\{G_0\}$. Also, when vectors are described in $\{W\}$, the frame notation is dropped for brevity.

Fig. 5.6 shows a schematic representation of eye-to-hand telemanipulation of TURBot. Naturally, the user expects that the master gripper motion specified in the master's base frame$\{M_b\}$ corresponds to the robot end effector motion in the camera frame $\{C\}$. Therefore the physical transformation between the frames of the master and the robot base is

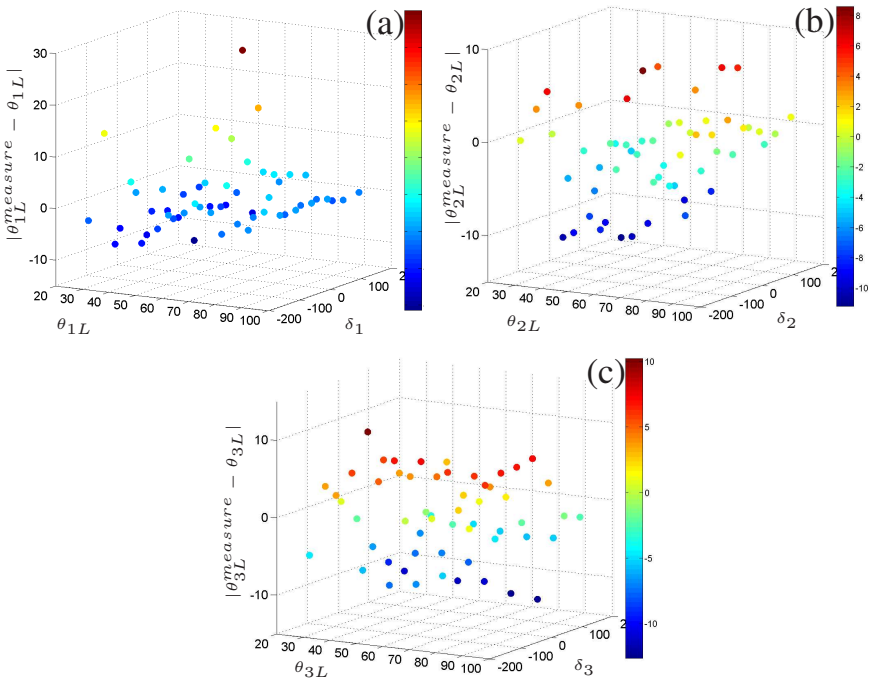

Figure 5.5: Bending errors throughout the configuration space of MBCR segment after compensation of actuation, (a) Segment 1, (b) Segment 2, (c) Segment 3

irrelevant. This alignment is illustrated in Fig. 5.6 as the plane $\hat{\mathbf{y}}_{m_b} - \hat{\mathbf{z}}_{m_b}$ is aligned with the plane $\hat{\mathbf{x}}_c - \hat{\mathbf{y}}_c$ of the camera frame such that $\hat{\mathbf{z}}_c$ and $\hat{\mathbf{x}}_{m_b}$ positive directions line up.

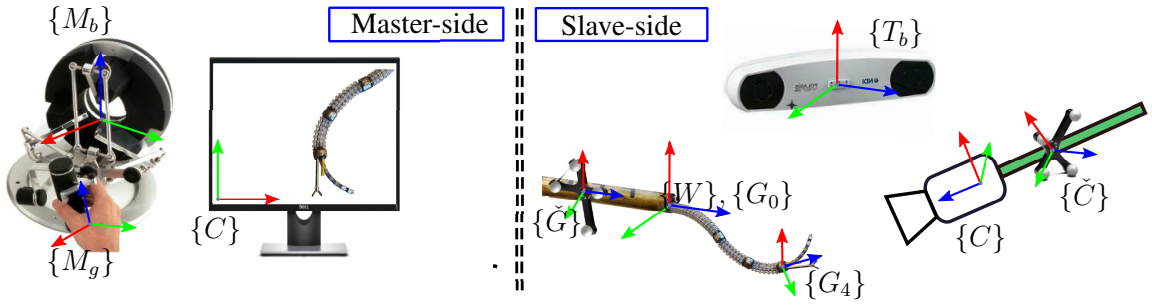

Figure 5.6: Eye-to-hand telemanipulation of TURBot

An underlying assumption is that the rotation ${}^{g_0}\mathbf{R}_c$ is known. This rotation is determined from online tracking of the camera relative to $\{G_0\}$. To achieve this, two optical markers with frames $\{\check{C}\}$ and $\{\check{G}\}$ are affixed to the camera and the resectoscope, respec-

tively. Therefore, ${}^{g_0}\mathbf{R}_c$ is given by:

$$ {}^{g_0}\mathbf{R}_c = {}^{g_0}\mathbf{R}_{\check{g}}\, {}^{t_b}\mathbf{R}_{\check{g}}^{\mathrm{T}}\, {}^{t_b}\mathbf{R}_{\check{c}}\, {}^{\check{c}}\mathbf{R}_c \tag{5.11} $$

where ${}^{t_b}\mathbf{R}_{\check{c}}$ and ${}^{t_b}\mathbf{R}_{\check{g}}$ denote the orientations of the camera marker frame and resectoscope marker frame relative to the optical tracker base $\{T_b\}$, respectively. ${}^{\check{c}}\mathbf{R}_c$ is a constant rotation from the camera (that is assumed to be aligned with the image frame) to the camera marker frame. ${}^{g_0}\mathbf{R}_{\check{g}}$ is a constant rotation from the resectoscope marker frame to $\{G_0\}$.

Motion is initiated by closing the normally open master's gripper. At that instant, the master's initial position and orientation relative to its base ($\mathbf{p}_{m\star} \triangleq {}^{m_b}\mathbf{m}_g^\star$, $\mathbf{R}_m^\star \triangleq {}^{m_b}\mathbf{R}_{m_g}^\star$) and the slave's initial position and orientation ($\mathbf{p}_{s\star} \triangleq {}^{g_0}\mathbf{g}_4^\star$, $\mathbf{R}_s^\star \triangleq {}^{g_0}\mathbf{R}_{g_4}^\star$) are stored. Then, the relative translation of the master's gripper in $\{C\}$ is determined as:

$$ {}^{c}\Delta\mathbf{p}_m = {}^{c}\mathbf{R}_{m_b}\, ({}^{m_b}\mathbf{p}_m - \mathbf{p}_{m\star}) \tag{5.12} $$

where ${}^{c}\mathbf{R}_{m_b}$ is the rotation of the master base relative to the camera frame:

$$ {}^{c}\mathbf{R}_{m_b} = \begin{bmatrix} 0 & 1 & 0 \\ 0 & 0 & 1 \\ 1 & 0 & 0 \end{bmatrix} \tag{5.13} $$

Using a translation scaling α, the desired slave position is:

$$ \mathbf{p}_{s,des} = \mathbf{p}_{s\star} + \alpha\, {}^{g_0}\mathbf{R}_c\, {}^{c}\Delta\mathbf{p}_m \tag{5.14} $$

The rotation motion reference for the slave is similarly transformed from $\{M_b\}$ to $\{G_0\}$. The master's gripper orientation relative to $\mathbf{R}_m^\star$ is denoted as $\overline{\Delta\mathbf{R}}_m$ such that ${}^{m_b}\mathbf{R}_{m_g} = \overline{\Delta\mathbf{R}}_m\, \mathbf{R}_m^\star$. Therefore:

$$ \overline{\Delta\mathbf{R}}_m = {}^{m_b}\mathbf{R}_{m_g}\, \mathbf{R}_m^{\star\,\mathrm{T}} \tag{5.15} $$

The relative rotation $\overline{\Delta\mathbf{R}}_m$ is described in $\{M_b\}$. It can be described in $\{G_0\}$ using similarity mapping:

$$\overline{\Delta\mathbf{R}}_{s,des} = {}^{g_0}\mathbf{R}_{m_b}\,\overline{\Delta\mathbf{R}}_m\,{}^{g_0}\mathbf{R}_{m_b}^{\mathrm{T}} \tag{5.16}$$

where

$${}^{g_0}\mathbf{R}_{m_b} = {}^{g_0}\mathbf{R}_c\,{}^{c}\mathbf{R}_{m_b} \tag{5.17}$$

Finally, the desired robot gripper rotation is

$$\mathbf{R}_{s,des} = \overline{\Delta\mathbf{R}}_{s,des}\,\mathbf{R}_s^{\star} \tag{5.18}$$

This rotation can be converted into an axis-angle representation and these two parameters can be used for a standard resolved rates algorithm. Algorithm (3) summarizes the steps in computation of desired pose in eye-in-hand telemanipulation.

Algorithm 3 Computation of robot desired pose: Eye-to-hand telemanipulation

Input: $\mathbf{p}_{m\star}, \mathbf{R}_m^{\star}$ ▷ Initial master gripper pose
Input: $\mathbf{p}_{s\star}, \mathbf{R}_s^{\star}$ ▷ Initial slave gripper pose
Input: ${}^{m_b}\mathbf{p}_m, \mathbf{R}_m$ ▷ Current master gripper pose
Input: ${}^{t_b}\mathbf{R}_{\check{g}}$ ▷ Current resectoscope marker frame in tracker base
Input: ${}^{t_b}\mathbf{R}_{\check{c}}$ ▷ Current camera marker frame in tracker base
Input: ${}^{g_0}\mathbf{R}_{\check{g}}$ ▷ Current resectoscope marker to slave base frame rotation
Input: ${}^{\check{c}}\mathbf{R}_c$ ▷ Camera to camera marker frame rotation
Input: α ▷ Position scale
Output: $\mathbf{p}_{s,des}, \mathbf{R}_{s,des}$ ▷ Slave desired pose

1: ${}^{g_0}\mathbf{R}_c = {}^{g_0}\mathbf{R}_{\check{g}}\,{}^{t_b}\mathbf{R}_{\check{g}}^{\mathrm{T}}\,{}^{t_b}\mathbf{R}_{\check{c}}\,{}^{\check{c}}\mathbf{R}_c$ ▷ Rotation from camera to world (slave base frame
Desired Position
2: ${}^{c}\Delta\mathbf{p}_m = {}^{c}\mathbf{R}_{m_b}\,({}^{m_b}\mathbf{p}_m - \mathbf{p}_{m\star})$ ▷ Master gripper position change in camera frame
3: ${}^{g_0}\Delta\mathbf{p}_m = {}^{g_0}\mathbf{R}_c\,{}^{c}\Delta\mathbf{p}_m$ ▷ Master gripper position change in world frame
4: $\mathbf{p}_{s,des} = \mathbf{p}_{s\star} + \alpha\,{}^{g_0}\Delta\mathbf{p}_m$ ▷ Slave reference desired position
Desired Rotation
5: $\overline{\Delta\mathbf{R}}_m = {}^{m_b}\mathbf{R}_{m_g}\,{\mathbf{R}_m^{\star}}^{\mathrm{T}}$ ▷ Master gripper rotation change in master base frame
6: $\overline{\Delta\mathbf{R}}_{s,des} = {}^{g_0}\mathbf{R}_{m_b}\,\overline{\Delta\mathbf{R}}_m\,{}^{g_0}\mathbf{R}_{m_b}^{\mathrm{T}}$ ▷ Slave desired rotation change in world frame
7: $\mathbf{R}_{s,des} = \overline{\Delta\mathbf{R}}_{s,des}\,\mathbf{R}_s^{\star}$ ▷ Slave desired rotation

5.2.3 Kinematic Control of TURBot

The desired slave pose $(\mathbf{p}_{s,des}, \mathbf{R}_{s,des})$ is next used in a resolved rates algorithm for solving the instantaneous inverse kinematics of the slave robot. Using the notation $\mathbf{p}_s \triangleq {}^{g_0}\mathbf{g}_4$ for the current end effector pose, the desired instantaneous twist of the slave robot is designed to close the position and orientation error:

$$\boldsymbol{\xi} \triangleq [v\hat{\mathbf{r}}^{\mathrm{T}}, \omega\hat{\boldsymbol{\theta}}^{\mathrm{T}}]^{\mathrm{T}} \tag{5.19}$$

where $\hat{\mathbf{r}} = \frac{\mathbf{p}_{s,des}-\mathbf{p}_s}{\|\mathbf{p}_{s,des}-\mathbf{p}_s\|}$ designates the unit vector closing the position error and $\hat{\boldsymbol{\theta}} = \frac{\hat{\mathbf{z}}_{g_4}\times\hat{\mathbf{z}}_{g_4,des}}{\|\hat{\mathbf{z}}_{g_4}\times\hat{\mathbf{z}}_{g_4,des}\|}$ is a rotation axis orthogonal to both $\hat{\mathbf{z}}_{g_4}$ and $\hat{\mathbf{z}}_{g_4,des}$ (these two vectors are the third columns of ${}^{g_0}\mathbf{R}_{g_4}$ and $\mathbf{R}_{s,des}$). Defining the position and orientation error as:

$$\delta_p \triangleq \|\mathbf{p}_{s,des} - \mathbf{p}_s\|, \quad \delta_o \triangleq \cos^{-1}(\hat{\mathbf{z}}_{g_4}^{\mathrm{T}}\hat{\mathbf{z}}_{g_4,des}) \tag{5.20}$$

We prescribe the scalar linear and angular speeds v and ω as:

$$v = \begin{cases} v_{max} \text{ , if } \|\mathbf{p}_{s,des} - \mathbf{p}_s\| > \lambda_p\epsilon_p \\ \frac{(v_{max}-v_{min})(\delta_p-\epsilon_p)}{\epsilon_p(\lambda_p-1)} + v_{min} \text{ , if } \epsilon_p < \delta_p \leq \lambda_p\epsilon_p \\ 0 \text{ , if } \delta_p \leq \epsilon_p \end{cases} \tag{5.21}$$

$$\omega = \begin{cases} \omega_{max} \text{ , if } \delta_o > \lambda_o\epsilon_o \\ \frac{(\omega_{max}-\omega_{min})(\delta_o-\epsilon_o)}{\epsilon_o(\lambda_o-1)} + \omega_{min} \text{ , if } \epsilon_o < \delta_o \leq \lambda_o\epsilon_o \\ 0 \text{ , if } \delta_o \leq \epsilon_o \end{cases} \tag{5.22}$$

where ϵ_p and ϵ_o are the convergence radii for the position and orientation errors and v_{max}, v_{min} and ω_{max}, ω_{min} are the maximal and minimal allowable speeds[1], $\lambda_p > 1$ and $\lambda_o > 1$

[1]The minimal speeds should be prescribed to ensure convergence for a chosen fixed control cycle time dt (e.g. $kv_{min}dt < \epsilon_p, k > 1$).

define the maximal position/orientation errors for which the maximal speeds will be applied to close the telemanipulation tracking error.

Since the end-effector of TURBot lacks a revolute joint (e.g. a distal roll wrist), it cannot provide roll about the end-effector longitudinal axis ($\hat{\mathbf{z}}_{g_4}$ in Fig. 7.1) when any of its segments are retracted into the resectoscope sheath. Even when all segments are unconstrained, the kinematic dexterity for distal roll motion is poor (therefore, in other designs we used a dedicated roll wrist or transmission of roll along the backbone [190]). Therefore, as a first step in kinematic control of TURBot, the commanded end-effector twist will be prescribed in end-effector frame with a reduced dimension excluding any twist specification about $\hat{\mathbf{z}}_{g_4}$. This task reduction is acceptable because the tasks of laser ablation and cautery resection is insensitive to roll about $\hat{\mathbf{z}}_{g_4}$.

To achieve the task reduction, we transform the twist $\boldsymbol{\xi}$ to end effector frame and eliminate the 6^{th} element associated with roll about $\hat{\mathbf{z}}_{g_4}$ to obtain the reduced-dimension twist $\bar{\boldsymbol{\xi}}$:

$$\overline{\boldsymbol{\xi}}_{ee} = [\mathbf{I}_5, \mathbf{0}_{5\times 1}] \begin{bmatrix} {}^{g_0}\mathbf{R}_{g_4}^T & \mathbf{0}_3 \\ \mathbf{0}_3 & {}^{g_0}\mathbf{R}_{g_4}^T \end{bmatrix} \boldsymbol{\xi} \tag{5.23}$$

where $\mathbf{I}_5$ designates the identity matrix in $\mathbb{R}^{5\times 5}$. A corresponding reduced-dimension geometric Jacobian $\bar{\mathbf{J}}_{ee}$ is defined in end effector frame:

$$\overline{\mathbf{J}}_{ee} = [\mathbf{I}_5, \mathbf{0}_{5\times 1}] \begin{bmatrix} {}^{g_0}\mathbf{R}_{g_4}^T & \mathbf{0}_3 \\ \mathbf{0}_3 & {}^{g_0}\mathbf{R}_{g_4}^T \end{bmatrix} \mathbf{J}_{x\tilde{\psi}} \tag{5.24}$$

Such that:

$$\overline{\mathbf{J}}_{ee}\dot{\tilde{\boldsymbol{\psi}}} = \overline{\boldsymbol{\xi}}_{ee} \tag{5.25}$$

When the MBCR is unconstrained by the resectoscope sheath, equation (5.25) is solved for configuration speeds $\dot{\tilde{\boldsymbol{\psi}}}$ using an appropriate redundancy resolution as described below. Finally, the desired configuration is obtained by integration of $\dot{\tilde{\boldsymbol{\psi}}}$ and converted to a cor-

responding joint values vector $\mathbf{q}$ using the segment-level MBCR inverse kinematics (5.9), which is passed on as a reference value for a joint-level PID position controller. The next section provides details of the redundancy resolution.

5.2.3.1 Constrained Redundancy Resolution

When the MBCR is fully outside the resectoscope sheath, it can utilize all its 7 DoFs to perform resection (Fig. 5.7-(a)). However, when a segment is constrained inside the resectoscope sheath, the MBCR loses two DoFs per a constrained segment. Bajo *et al.* used a task priority redundancy resolution [191] combined with a *configuration space virtual fixture* for a two-segment MBCR with translation [192]. The role of the virtual fixture was to command the proximal segment to a safe banding angle (close to straight orientation) when it began to retract into the sheath. While this guarantees the MBCR safety, it does not use the remaining mobility to fulfill the task efficiently. The reason is the tubular constraint is enforced at the expense of filtering the configuration commands. In this section, we present a different resolution of redundancy that provides a more systematic and judicious use of the MBCR DoFs accounting for the constraint status.

Depending on the number of constrained MBCR segments, the instantaneous kinematics changes. Accordingly, the task description should be updated to ensure efficient utilization of MBCR mobility. In the following, each case of constraint status shown in Fig. 5.7 is treated individually.

Case (I): No segment is constrained.: All 7 DoFs of TURBot are used to accomplish the 5-DoF task. The redundant DoFs are used for configuration limit avoidance. A weighted redundancy resolution is used following [193]:

$$\dot{\boldsymbol{\psi}}_{des} = \overline{\mathbf{J}}_{ee}^{+}\overline{\boldsymbol{\xi}}_{ee} \tag{5.26}$$

where $\overline{\mathbf{J}}_{ee} = [\overline{\mathbf{J}}_{ee}^{(1)}, \overline{\mathbf{J}}_{ee}^{(2)}, \overline{\mathbf{J}}_{ee}^{(3)}, \mathbf{J}_4] \in \mathbb{R}^{5\times 7}$, $\overline{\mathbf{J}}_{ee}^{(i)}, i = 1, 2, 3$ is obtained from (5.24) by

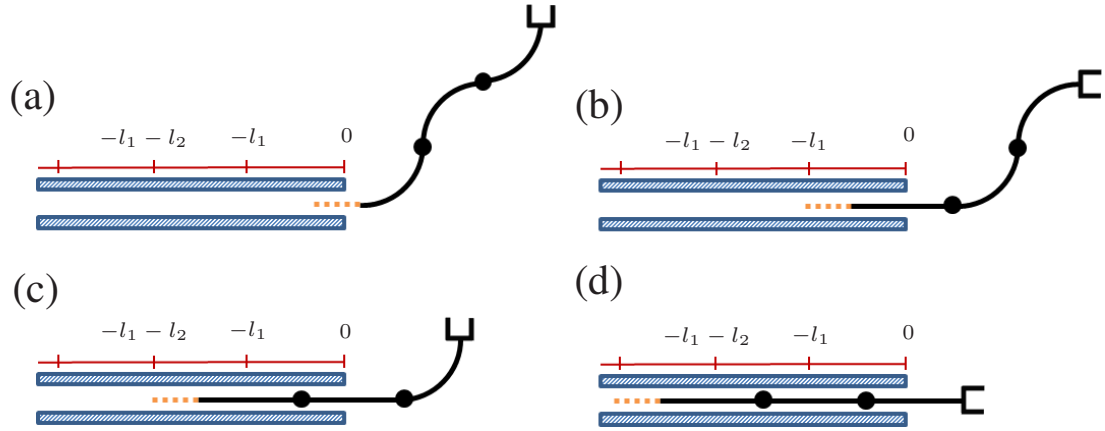

Figure 5.7: Tubular constraint imposed by the internal sheath of resectoscope. Red grated line shows q_{ins}. (a) Case (I) - no segment is constrained ($q_{ins} \geq 0$). (b) Case (II) - proximal segment is constrained ($-l_1 \leq q_{ins} < 0$). (c) Case (III) - proximal and middle segments are constrained ($-l_1 - l_2 \leq q_{ins} < -l_1$). (d) Case (IV) - all segments are constrained ($q_{ins} < -l_1 - l_2$).

replacing $\mathbf{J}_{x\tilde{\psi}}$ with $\mathbf{J}_{x\psi}$ of the i^{th} segment, $\mathbf{J}_4$ is the description of $\hat{\mathbf{z}}_{g_0}$ in frame $\{G_4\}$ appended with zeros in its last 2 elements, and $(.)^+$ is the regularized weighted Moore-Penrose pseudo-inverse [150]:

$$\overline{\mathbf{J}}_{ee}^{+} = \mathbf{W}_1^{-1}\overline{\mathbf{J}}_{ee}^{T}(\overline{\mathbf{J}}_{ee}\mathbf{W}_1^{-1}\overline{\mathbf{J}}_{ee}^{T} + \epsilon\mathbf{I}_5)^{-1} \tag{5.27}$$

$\mathbf{W}_1 \in \mathbb{R}^{7\times7}$ is a positive-definite weight matrix that is defined to help keep $\tilde{\boldsymbol{\psi}}$ away from its limits [193] and ϵ is a kinematic regularization factor.

Case (II): Proximal segment is constrained: In this case, the proximal segment bending angle (θ_{1L}) converges exponentially to a safe bending angle ($\theta_{1L,s} = \pi/2$) while δ_1 remains constant. Having lost two DoFs, the remaining five DoFs are utilized to accomplish the 5-DoF task. Therefore,

$$\begin{aligned} \dot{\theta}_{1L,des} &= k_d(\theta_{1L,s} - \theta_{1L,des}), \quad \dot{\delta}_{1,des} = 0, \quad k_d > 0 \\ \dot{\tilde{\boldsymbol{\psi}}}_{23,des} &= \overline{\mathbf{J}}_{ee,234}^{+}(\dot{\bar{\boldsymbol{\xi}}}_{ee} - \overline{\mathbf{J}}_{ee}^{(1)}\dot{\boldsymbol{\psi}}_{1,des}) \end{aligned} \tag{5.28}$$

where $\tilde{\boldsymbol{\psi}}_{23} = [\boldsymbol{\psi}_2^T, \boldsymbol{\psi}_3^T, q_{ins}]^T \in \mathbb{R}^{5\times1}$, and $\overline{\mathbf{J}}_{ee,234} = [\overline{\mathbf{J}}_{ee}^{(2)}\overline{\mathbf{J}}_{ee}^{(3)}, \mathbf{J}_4] \in \mathbb{R}^{5\times5}$.

Case (III): Proximal and middle segments are constrained: The bending angles of both the proximal and the middle segments converge exponentially to their safe values ($\pi/2$) while δ_1, δ_2 remain constant. The robot has three DoFs left and it is no longer possible to achieve the 5-DoF tracking task. Therefore the 5-DoF task is demoted to a 3-DoF position tracking task. Thus,

$$\begin{aligned} \dot{\theta}_{iL,des} &= k_d(\theta_{iL,s} - \theta_{iL,des}), \dot{\delta}_{i,des} = 0, i \in \{1,2\} \\ \dot{\tilde{\boldsymbol{\psi}}}_{3,des} &= \overline{\mathbf{J}}_{ee,34}^{tran\,+}(\mathbf{v}_{ee} - \overline{\mathbf{J}}_{ee,12}^{tran}\dot{\boldsymbol{\psi}}_{12,des}) \end{aligned} \tag{5.29}$$

where $\mathbf{v}_{ee} = [\mathbf{I}_3, \mathbf{0}_{3\times2}]\overline{\boldsymbol{\xi}}_{ee}$ is the end-effector linear velocity described in $\{G_4\}$, $\boldsymbol{\psi}_{12} = [\boldsymbol{\psi}_1^T, \boldsymbol{\psi}_2^T]^T \in \mathbb{R}^{4\times1}$, $\tilde{\boldsymbol{\psi}}_3 = [\boldsymbol{\psi}_3^T, q_{ins}]^T \in \mathbb{R}^{3\times1}$, $\overline{\mathbf{J}}_{ee,12}^{tran} = [\overline{\mathbf{J}}_{ee}^{(1)^{tran}}, \overline{\mathbf{J}}_{ee}^{(2)^{tran}}] \in \mathbb{R}^{3\times4}$ and $\overline{\mathbf{J}}_{ee,34}^{tran} = [\overline{\mathbf{J}}_{ee}^{(3)^{tran}}, \mathbf{J}_4^{tran}] \in \mathbb{R}^{3\times3}$. The superscript '*tran*' denotes the translational component of Jacobian.

Case (IV): All segments are constrained: The task is demoted to the velocity component along the resectoscope sheath i.e. the z-component of linear velocity $v_z = \$_{ins}^{\mathrm{T}}\boldsymbol{\xi}$. Hence,

$$\begin{aligned} \dot{\theta}_{iL,des} &= k_d(\theta_{iL,s} - \theta_{iL,des}), \dot{\delta}_{i,des} = 0, i \in \{1 \ldots 3\} \\ \dot{q}_{ins,des} &= v_z \end{aligned} \tag{5.30}$$

5.2.3.2 Re-initialization of Initial Pose

When the user first engages telemanipulation by closing the gripper of the master interface the *initial pose* of the slave and master $(\mathbf{p}_{s\star}, \mathbf{R}_s^\star)$ and $(\mathbf{p}_{m\star}, \mathbf{R}_m^\star)$ are updated, respectively. Due to motion scaling, the user may reach the workspace boundary of the master, which would require him/her to disengage the master in order to reposition its gripper within its workspace and then to subsequently re-engage telemanipulation of the slave. The initial poses of the master and slave are updated every time the gripper of the master is used to re-engage telemanipulation. However, when the slave robot encounters resec-

toscope sheath constraints, its desired twist $\boldsymbol{\xi}_{s,des}$ is cast into the form corresponding with the constraint cases defined in the preceding section. Under some circumstances, the master/slave initial pose have to be updated to prevent discontinuity in $\boldsymbol{\xi}_{s,des}$. The particular circumstances where it's necessary to re-initialize the master/slave pose is as follows:

- Switching from Case (IV) to Case (III): The desired twist prior to switching is a linear velocity along the resectoscope sheath. Upon switching, the desired twist is promoted to a linear velocity vector in the direction of position error. This sudden change is avoided by resetting the slave robot initial pose to the pose at the onset of telemanipulation re-engagement.

- Switching from Case (III) to Case (II): The promotion from a 3-DoF twist to a 5-DoF twist can lead to similar unwanted MBCR motion. In this case, re-initialization of initial orientations solves this issue.

Algorithm (4) summarizes the ad-hoc re-initializations for the above cases.

5.3 Conclusion

This chapter covered kinematic modeling, actuation compensation and calibration of TURBot system. The compensation of actuation includes backlash compensation and calibrated gains in the joint-to-configuration direct kinematic model of the MBCR. These gains were determined experimentally for discrete points in the workspace and they were interpolated with cubic splines for all other points. The backlash stems from the application of flexible material in the motion transmission chain. The compensation of this backlash involves the measurement of this flexibility and adding to or subtracting from the command joint displacements at the instances of motion direction change.

Next, an eye-to-hand telemanipulation paradigm was discussed that provides a user that only has a 2D visual feedback of the workspace an intuitive telemanipulation framework.

Algorithm 4 Resetting Initial Master/slave Poses

Input: l_1, l_2, l_3 ▷ MBCR segment lengths
Input: $q_{ins}(k)$ ▷ Current MBCR insertion
Input: $q_{ins}(k-n)$ ▷ MBCR insertion at n^{th} previous iteration
Input: ${}^{m_b}\mathbf{m}_g, {}^{m_b}\mathbf{R}_{m_g}, {}^{g_0}\mathbf{g}_4, {}^{g_0}\mathbf{R}_{g_4}$ ▷ Current master/slave gripper poses
Input: $\mathbf{p}_m^{en}, \mathbf{R}_m^{en}, \mathbf{p}_s^{en}, \mathbf{R}_s^{en}$ ▷ Engage master/slave gripper poses
Output: $\mathbf{p}_{m\star}, \mathbf{R}_m^{\star}, \mathbf{p}_{s\star}, \mathbf{R}_s^{\star}$ ▷ Initial master/slave gripper poses

if $(-l_1 \leq q_{ins}(k) < 0)$ & $(-l_1 - l_2 \leq q_{ins}(k-n) < -l_1)$ **then**
  $\mathbf{p}_{m\star} \leftarrow \mathbf{p}_m^{en}$ ▷ Hold master engage position
  $\mathbf{R}_m^{\star} \leftarrow {}^{m_b}\mathbf{R}_{m_g}$ ▷ Reset master initial rotation to current rotation
  $\mathbf{p}_{s\star} \leftarrow \mathbf{p}_s^{en}$ ▷ Hold slave engage position
  $\mathbf{R}_s^{\star} \leftarrow {}^{g_0}\mathbf{R}_{g_4}$ ▷ Reset slave initial rotation to current rotation
else if $(-l_1 - l_2 \leq q_{ins} < -l_1)$ & $(-l_1 - l_2 - l_3 \leq q_{ins}(k-n) < -l_1 - l_2)$ **then**
  $\mathbf{p}_{m\star} \leftarrow {}^{m_b}\mathbf{m}_g$ ▷ Reset master initial position to current position
  $\mathbf{R}_m^{\star} \leftarrow \mathbf{R}_m^{en}$ ▷ Hold master engage rotation
  $\mathbf{p}_{s\star} \leftarrow {}^{g_0}\mathbf{g}_4$ ▷ Reset slave initial position to current position
  $\mathbf{R}_s^{\star} \leftarrow \mathbf{R}_s^{en}$ ▷ Hold slave engage rotation
else
  $\mathbf{p}_{m\star} \leftarrow \mathbf{p}_m^{en}$ ▷ Hold master engage position
  $\mathbf{R}_m^{\star} \leftarrow \mathbf{R}_m^{en}$ ▷ Hold master engage rotation
  $\mathbf{p}_{s\star} \leftarrow \mathbf{p}_s^{en}$ ▷ Hold slave engage position
  $\mathbf{R}_s^{\star} \leftarrow \mathbf{R}_s^{en}$ ▷ Hold slave engage rotation
end if

This image-based telemanipulation framework only requires an extrinsic camera and robot pose information and does not need camera intrinsic parameters calibration.

Finally, a hierarchical resolved-rate algorithm was described for telemanipulation that takes into account the tubular constraint on the MBCR enforced by the resectoscope sheath. The algorithm utilizes the insertion state to evaluate which segments are constrained and assigns the task to the available free segments. This involves demoting a 5-DoF task of position-pitch-yaw tracking to a 3-DoF position tracking when there is only one free segments and promoting it back when at least two segments are free. It also ensures smooth switching between these different scenarios by re-initialization of command velocities and an appropriate modeling of instantaneous kinematic during switching instances.

CHAPTER 6

EVALUATION OF TURBOT

The clinical motivation for TURBot was explained in section 2.2 and in chapter 1. The main components and the design of TURBot were presented in chapter 4. In chapter 5, the modeling and the pertaining control algorithms were explained in details. TURBot functionality was validated through extensive simulations and experimental procedures. In this chapter, the experimental evaluation of TURBot on a bladder phantom is presented in section 6.1. The goal of this study is to assess the performance of TURBot as well as a statistical comparison of robotic versus manual transurethral resection of bladder. Then, in-vivo test results where the system was tested in swines is explained in section 6.2. A final conclusion closes this chapter by summarizing the outcomes of the studies.

6.1 User Study

A 3D-printed phantom model of a human bladder was used to assess the performance of TURBot. More importantly, manual and robotic resection was compared to address the important question of whether robotic resection can provide better outcomes. Towards this goal, a female bladder model was fabricated by additive manufacturing with two holes to place mock-up tumors made of agar.

In manual TURBT, the surgeon pivots the resectoscope about an imaginary fulcrum point near the bladder neck and moves it by using four motions i.e. three rotations (roll, pitch, yaw) and an insertion. A robotic suite for TURBT should ideally replicate these macro motions as well as providing finer motions at the tip for a more dexterous motion

than manual TURBT (as the MBCR does in our system). The current prototype of TURBot is mounted on statically-balanced passive arm that does not actively control the angles of approach of the resectoscope sheath with respect to the bladder entrance. To compensate for this lack of degrees of freedom and to facilitate our investigation, another robot (a PUMA560) was used to orient the angles of the TURBot resectoscope sheath with respect to the bladder body. The PUMA560 robot was commanded via a joystick interface and it was programmed to satisfy a remote-center-motion (RCM) movement around a fulcrum point representing the bladder entrance point.

Manual resections by a standard 26 Fr resectoscope (STORZ) were conducted at the same tumor locations and then a statistical analysis was conducted to verify a difference between the robotically and the manually resected sample groups. The next subsections present the experiments and their outcomes in details.

6.1.1 Experimental Setup

The experimental setup for robotic resection is shown in Fig. 6.1. It consists of the TURBot system ①, PUMA560 robot ②, a human bladder phantom ③ , mock-up tumor ④, master device (Omega.7® ⑤ (Force Dimension)), a 3-DoF joystick ⑥ for RCM control of PUMA560, an optical tracker ⑦ (NDI Polaris Vicra), endoscope and camera with an attached marker ⑧, electrosurgical generator ⑨ used for tumor resection and a monitor screen ⑩ to display camera feed.

The female patient bladder phantom shown in Fig. 6.1 has an approximate volume of 336 mL and was obtained under an IRB approved protocol to gather computed tomography 3D scans of patient bladders. DICOM images of the bladder were imported in *3DSlicer* to create a 3D model in stl format. This model was then imported in *Autodesk Meshmixer* and post-processed in several steps to add the required holes and the screw fixtures. The model was split in half to expose the interior for video recording during experiments and for easier placement of tumors dishes. The final model was fabricated by an FDM 3D-printer. Prior

to printing, the model was modified to provide a $\varnothing 15$ mm urethral opening or entrance hole. Two cylindrical holes of $\approx \varnothing 32$ mm were created for placing mock-up tumor dishes that were secured in place by screws. One was located close to the left lateral wall of the bladder (denoted by LW) and represented an easy to reach pose with a rigid resectoscope. The other was situated at the bladder neck toward the left side (denoted by N). The latter was impossible to reach by a rigid resectoscope without resorting to compression of the bladder through pubic pressure (which was not feasible in a rigid phantom).

During preliminary setup for robotic resections, the PUMA560 end effector was first brought to a proper pose such that the bladder phantom was oriented in an anatomically appropriate manner similar to a patient's pose during clinical TURBT. Then, the TURBot slave was deployed through the urethral opening in the phantom (see insets in Fig. 6.1). Since the objective is to evaluate the dexterity of TURBot's MBCR arm, we did not use the PUMA560 robot for simultaneous adjustment of approach into the bladder. Therefore, the tests presented below, represent a more stringent case than would be available if in the future the statically balanced arm of TURBot were to be replaced by an active arm.

The setup for manual resections involved a subset of the components in robotic resection. A standard resectoscope (STORZ) with a 26-Fr electrocautery loop was used. To ensure similar circumstances to the robotic resections by TURBot, the resectoscope endoscope was not utilized during resections.

6.1.2 Mock-up Lesions

To create a mock-up lesion, a $\varnothing 11.2mm$ disk was placed in the center of a $\varnothing 31.75mm$ round dish and filled with a mixture of $17.5\, gr/L$ agar (Sigma-Aldrich #A7002-250G) and $50\, gr/L$ milk in distilled water. The disk was subsequently removed after the mixture was cured to leave a cavity for the mock-up lesion. The lesion was made of the same agar mixed with colored glitter which was poured into the cavity and allowed to cure at room temperature. The final product was a matte agar gel with a cylindrical colored lesion

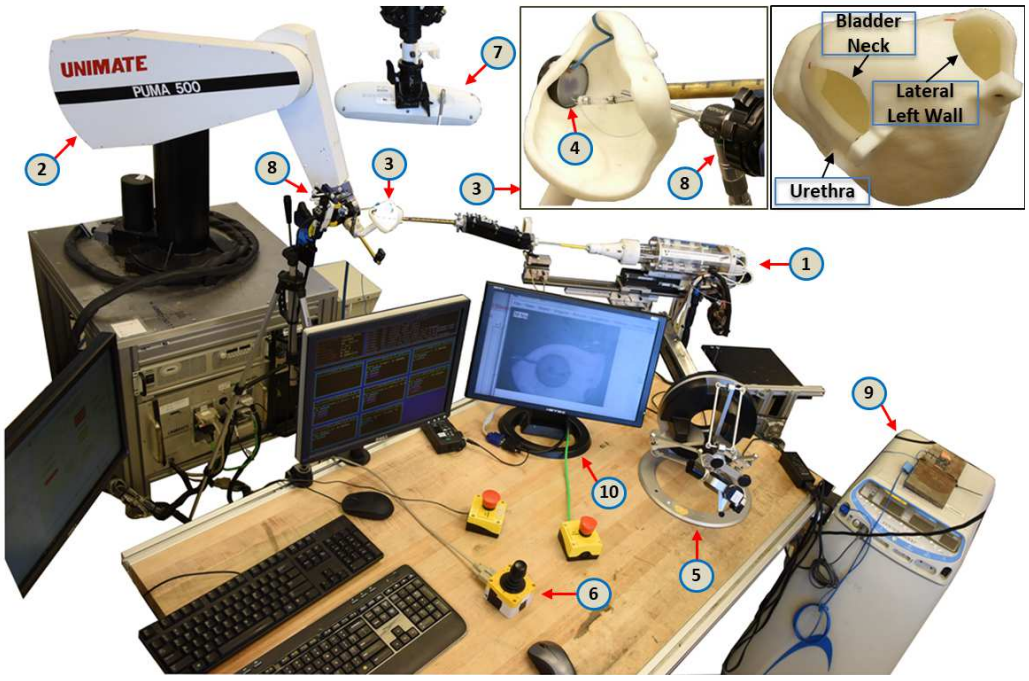

Figure 6.1: Experimental setup to perform robotic TURBT on a bladder phantom. Inset shows MBCR deployed in the phantom. ① TURBot slave, ② PUMA560 robot, ③ bladder phantom, ④ mock-up tumor, ⑤ Omega.7 haptic device, ⑥ 3-DoF joystick, ⑦ Optical tracker, ⑧ Endoscope and camera with an attached marker, ⑨ Electrosurgical generator, ⑩ Monitor screen. Corner inset shows the 3D-printed female bladder phantom ($\approx$ 336 mL).

($\varnothing 11.2mm$) in the center as shown in Fig. 6.2-a. Four pins were placed in the agar as landmarks to register pre-resection and post-resection images.

6.1.3 RCM Control of PUMA560

The RCM teleoperation of the phantom mounted on PUMA560 end effector restores the ability to orient the robot-compatible resectoscope relative to the phantom. In order to achieve this, it is assumed that the user is controlling the orientation of the resectoscope through the joystick. Thus, the imparted angular velocity of the resectoscope is determined. To incur the same motion by moving the bladder phantom instead, while the resectoscope remains stationary, the angular velocity of the bladder phantom imparted by the PUMA560

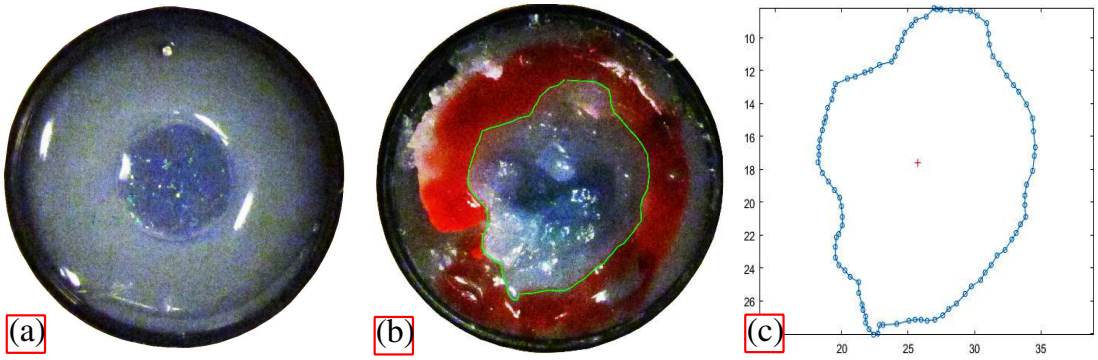

Figure 6.2: Sample agar tumor dish: (a) a pre-resection sample; tumor size is controlled during fabrication ($\varnothing 11.2mm$), (b) sample was put at the bladder neck (N) and resected; boundaries of resected region were marked to facilitate segmentation, (c) segmented region and center of tumor after registration of pre-resection image to post-resection image.

end-effector should be equal in magnitude and negative in direction. Hence

$$ {}^{p_b}\boldsymbol{\omega}_{p_g} = -{}^{p_b}\mathbf{R}_f \, {}^{f}\boldsymbol{\omega}_{rscp}, \quad {}^{p_b}\mathbf{v}_{p_g} = {}^{p_b}\boldsymbol{\omega}_{p_g} \times {}^{p_b}\mathbf{r}_{fp_g} \tag{6.1} $$

where ${}^{p_b}\mathbf{v}_{p_g}$,${}^{p_b}\boldsymbol{\omega}_{p_g}$ is the desired linear and angular velocity of the end effector frame $\{P_g\}$ described in PUMA560 base $\{P_b\}$ as shown in Fig. 6.3(a), ${}^{p_b}\mathbf{R}_f$ is the rotation from a fulcrum point frame $\{F\}$ to $\{P_b\}$ and ${}^{p_b}\mathbf{r}_{fp_g}$ is the vector joining the origins of $\{F\}$ and $\{P_g\}$. ${}^{f}\boldsymbol{\omega}_{rscp}$ is the desired angular velocity of the resectoscope described in $\{F\}$ which was determined based on the following mapping shown in Fig. 6.3(b) between the joystick and the resectoscope orientation angles: Joystick left/right, up/down and twist motion was mapped to the resectoscope azimuth (θ), inclination (ϕ) and roll (γ) angles respectively. Hence, resectoscope angular velocity is:

$$ {}^{f}\boldsymbol{\omega}_{rscp} = \dot{\phi} \, {}^{f}\hat{\mathbf{e}}_\theta + \dot{\theta} \, {}^{f}\hat{\mathbf{e}}_k + \dot{\gamma} \, {}^{f}\hat{\mathbf{e}}_\rho \tag{6.2} $$

where $\dot{\phi}$, $\dot{\theta}$ and $\dot{\gamma}$ represents the rate of change of inclination, azimuth and roll angle respectively. Referring to Fig. 6.3(b), $\hat{\mathbf{e}}_\rho$ and $\hat{\mathbf{e}}_k$ are the unit vectors along the resectoscope sheath and along the $\hat{\mathbf{z}}_f$ direction respectively. $\hat{\mathbf{e}}_\theta$ is the unit vector normal to the projection

of the sheath on the $\hat{\mathbf{x}}_f - \hat{\mathbf{y}}_f$ plane. These unit vectors expressed in the frame $\{F\}$ are:

$$
\begin{aligned}
{}^f\hat{\mathbf{e}}_\theta &= [-\sin(\theta), \cos(\theta), 0]^{\mathrm{T}}, \\
{}^f\hat{\mathbf{e}}_\rho &= [\cos(\theta)\sin(\phi), \sin(\theta)\sin(\phi), \cos(\phi)]^{\mathrm{T}} \\
{}^f\hat{\mathbf{e}}_k &= [0, 0, 1]^{\mathrm{T}}
\end{aligned}
\tag{6.3}
$$

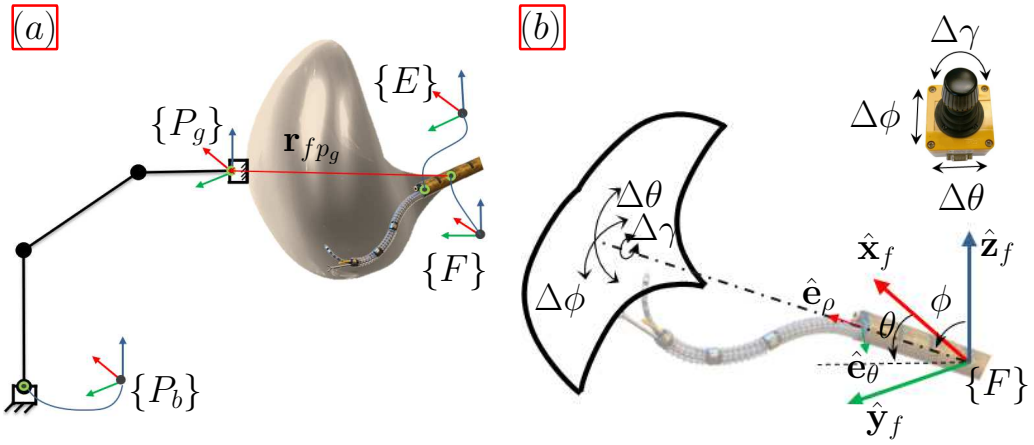

Figure 6.3: teleoperated remote-center-of-motion control of bladder phantom about fulcrum point $\mathbf{f}$: (a) $\{E\}$ is at the tip of resectoscope, $\{P_g\}$ is PUMA560 end-effector frame, $\{P_b\}$ is PUMA560 base frame. Relative scales are distorted for clarity. (b) Joystick-to-resectoscope mappings. θ, ϕ and γ are azimuth, inclination and roll angles of the resectoscope respectively.

In Eq. (6.1), ${}^{p_b}\mathbf{R}_f$ was provided by an optical tracker. To determine ${}^{p_b}\mathbf{r}_{fp_g}$, an optical marker denoted as $\{P_m\}$ was attached to the PUMA560 end-effector and the fulcrum was then digitized. ${}^{p_b}\mathbf{r}_{fp_g}$ was then computed as:

$$
{}^{p_b}\mathbf{r}_{fp_g} = -{}^{p_b}\mathbf{R}_{p_g}\,{}^{p_g}\mathbf{T}_{p_m}\mathbf{r}_{p_m f} \tag{6.4}
$$

where $\mathbf{r}_{p_m f}$ is the measurement readout of the optical tracker, ${}^{p_g}\mathbf{T}_{p_m}$ is a known constant homogeneous transformation from PUMA560 marker frame to its gripper frame and ${}^{p_b}\mathbf{R}_{p_g}$ is the rotation from PUMA560 base to its gripper frame obtained from the direct kinematic formulation.

Equation (6.1) constitutes the command twist of PUMA560 end-effector. Given the command twist, the instantaneous kinematics of PUMA560 was applied to calculate the desired joint rates as follows [194]. The instantaneous kinematics of PUMA560 is:

$$\mathbf{J}_{xq}\dot{\mathbf{q}} = \dot{\mathbf{x}}_g \tag{6.5}$$

where $\dot{\mathbf{x}}_g \in \mathbb{R}^{6\times 1} = [\mathbf{v}_g^{\mathrm{T}}, \boldsymbol{\omega}_g^{\mathrm{T}}]^{\mathrm{T}}$. Application of inverse of Jacobian gives the joint rates:

$$\dot{\mathbf{q}} = \mathbf{J}_{xq}^{+}\dot{\mathbf{x}}_g \tag{6.6}$$

To calculate the inverse of Jacobian, an inverse of singularity-value decomposition (SVD) is used:

$$\mathbf{J}_{xq}^{+} = \mathbf{V}\boldsymbol{\Sigma}^{-1}\mathbf{U}^{\mathrm{T}} \tag{6.7}$$

where $\mathbf{J}_{xq} = \mathbf{U}\boldsymbol{\Sigma}\mathbf{V}^{\mathrm{T}}$ is the SVD of $\mathbf{J}_{xq}$. A simple singularity filtering approach is applied to determine $\boldsymbol{\Sigma}^{-1}$ to handle singularities as follows:

$$\boldsymbol{\Sigma}^{-1} = \begin{cases} \frac{1}{\sigma_i}, & \text{if } \sigma_i > \epsilon \\ 0, & \text{otherwise.} \end{cases} \tag{6.8}$$

where parameter ϵ was selected as 0.03. An Euler integration was applied on Eq (6.7)to determine the motors command motions.

6.1.4 Experimental procedure

After an initial training, three users were asked to resect lesions while avoiding to stride outside the lesions margins. The resection performance was gauged based on the tangential accuracy and duration of resections. 66 and 30 robotic resections were conducted at the bladder left lateral wall (LW) and neck (N) locations respectively. 66 manual resections

were performed by the same users at the lateral wall. Repetition of the experiments using standard manual tools verified that one cannot carry out resection at the bladder neck without resorting to aggressive deformation of the bladder. Therefore, no manual resection was conducted at the neck.

6.1.5 Accuracy Calculation

A pre-resection and post-resection image was taken from each sample (see Fig. 6.2-(a,b)). Then, the two images were registered by MATLAB to find the center of the lesion in the post-resection image. Three of the pin centers in the agar model were used as registration landmarks and the fourth one was used to determine registration accuracy. Then, the resected area was segmented manually in MATLAB. Fig. 6.2(c) shows the segmented boundary of a resected samples at the bladder neck. The registered lesion center is displayed by a red $'+'$. The resection accuracy for each sample was determined by the duration and the *tangential root-mean-square (RMS) error* of a resected sample defined as follows:

$$e_{t,rms} = \left(\frac{1}{p} \sum_{i=1}^{p} (r_{ref} - r_i)^2 \right)^{\frac{1}{2}} \tag{6.9}$$

where r_i is the radial distance between the registered lesion center and the point $i = 1..p$ on the segmented region boundary. $r_{ref} = 5.6mm$ is the desired radius of resection.

6.1.6 Results

Fig. 6.4 shows box plots of resection RMS error and duration in each experimental group: manual at lateral wall (LW), robotic at lateral wall, robotic at neck (N). The median and the mean are represented by a notch and a round dot respectively. The bounds of the box represent upper and lower quartiles of the data and the tails represent maximum and minimum values of the data.

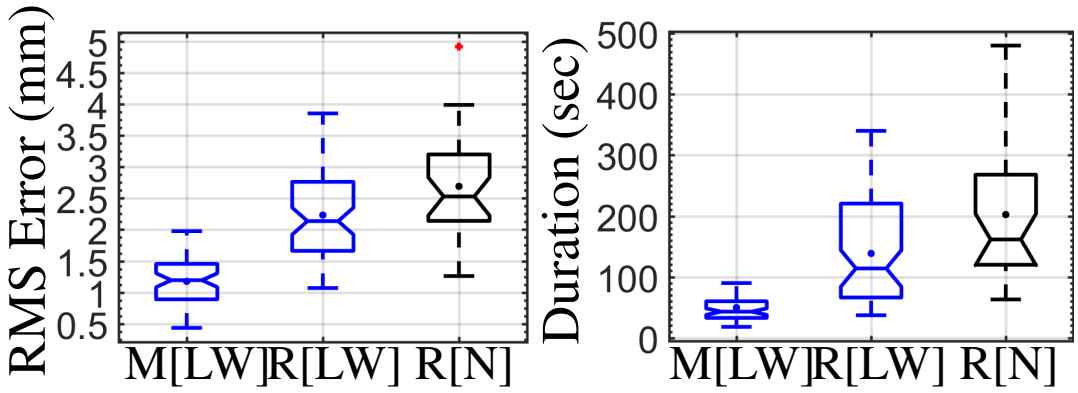

Figure 6.4: Resection tangential RMS error and duration in three resection groups. mean value is displayed by •. (M=Manual, R=Robotic, LW=Lateral Wall, N=Neck)

Table 6.1 lists the means values of the two accuracy measures and their standard deviations for the same groups. A paired t-test was used to compare resection groups performances. The resection accuracy at LW was $1.18 \pm 0.38mm$ and $2.23 \pm 0.68mm$ for the manual and the robotic group respectively. The resection duration at the same location was $50 \pm 21sec$ (manual) vs 139 ± 83 (robotic). Therefore, the robotic resection performance was worse than manual with $1.05mm$ larger RMS error (p-value < 0.001, 95% confidence interval of $[0.86, 1.25]$) and $89sec$ higher durations (p-value < 0.001, 95% confidence interval of $[68, 110]$). Robotic resection at N was conducted with an average accuracy of $2.69 \pm 0.80mm$ and an average duration of $202 \pm 112sec$. In comparison, TURBot performance was worse in the N than the LW region: $0.46mm$ larger RMS error (p-value 0.005, 95% confidence interval of $[0.14, 0.78]$) and $63sec$ longer durations (p-value 0.003, 95% confidence interval of $[23, 105]$). Note the registration error to find the lesion center was determined as $0.12 \pm 0.09mm$.

Table 6.1: Resection tangential accuracy and duration

Method [Location]	**RMS Error (mm)**	**Duration (sec)**
Robotic [Lateral Wall]	2.23 ± 0.68	139 ± 83
Manual [Lateral Wall]	1.18 ± 0.38	50 ± 21
Robotic [Neck]	2.69 ± 0.80	202 ± 112
Manual [Neck]	Not Possible	Not Possible

6.1.7 Discussion

There are several reasons for the comparatively lower performance of the robotic resections. A backlash compensation mechanism closed a portion of the backlash in the actuation unit due to the flexibility of the 3D-printed transmission bridge connector in the actuation unit. However, this caused some degree of jerky motion that affected the robot motion control. At the LW region, small banding angles (high θ_{iL}) were often required to resect lesions. The calibration for small bending angles of MBCR was less accurate since unmodelled friction and dead zone phenomena are more prevailing in this regime. We believe, this played a significant role in performance degradation. At the N region, the actuation unit joint stroke limits played a more important role in impacting the performance. TURBot was often working with two maximally bent segments in retroflexed postures. This left little room for the redundancy resolution algorithm to accomplish the resection task. In practice, the MBCR could comfortably move only in certain directions and had less success in complying to motion commands in other directions.

Another reason for the lower accuracy and longer task duration using the robot was the learning curve associated with using TURBot. Although the users were given a preliminary training to operate the system, it was still fairly taxing in comparison with the standard resectoscope. Telemanipulating a 6-DoF robot is inherently more challenging than the direct handling and operation of a 4-DoF rigid tool. This requires more training to surmount the learning curve.

Other sources affecting the performance of robotic resections were lack of loop roll control as well as visual blockage caused by the MBCR body and/or the loop. While TURBot lacks the ability to control the end-effector roll, the manual resectoscope loop could be easily rotated by twisting the entire resectoscope. This helped achieve better performance in covering the lesion margins with the resectoscope. Regarding the latter, there were some end-point angles of the robot where it was difficult to see the electrocautery loop and/or the lesion. The manual tool operation did not suffer from this issue since the

loop could be pushed out further to mitigate blockage. This is addressed in chapter 7 by employing the MBCR redundancy to drive its body outside the field of view while fulfilling the primary tracking task. Future improvement includes independent roll of the resection loop using a flexible shaft through one of the working channels of the MBCR.

The experiments also highlighted the importance of depth perception. It was difficult for the users to distinguish the loop-environment contact status. In particular, this was more confounding when the tumor surface plane was not normal to the camera axis. A potential solution is a stereo-vision module with a mechanism for actively controlling the camera posture. In addition, telemanipulation motion scaling and speed could be better tuned to adapt to user preferences. Addressing these issues will be the subject of future improvements.

6.2 Animal Study

The goals of the porcine *in vivo* study were: (1) to evaluate the TURBot in accessing all regions of the bladder, (2) to evaluate robot-assisted resection/ablation of simulated bladder lesions and, (3) to explore feasibility of robot-assisted en-bloc resection. The results of three pilot in-vivo porcine studies using TURBot system are presented here and potential improvements are proposed based on experimental observations. In the following sections, the animal preparation procedure, TURBot setup, the outcomes and the challenges encountered during the animal studies are explained. we also propose solutions and remedies to overcome these challenges in section (6.2.5).

6.2.1 Animal Preparation

After fasting for 12 hours, a female swine was placed under general anesthesia. It was then transferred to the bed and situated in a supine position with her lower body tilting slightly up as shown in Fig. (6.5)-a. we chose the live swine model, as opposed to a human cadaver because it better reflects the perfusion and elasticity of intraoperative tissues, which

may affect success of the ablation technique. In addition, it allows for a more realistic testing platform with respect to evaluating OR setup and challenges in live surgery settings for future clinical applications.

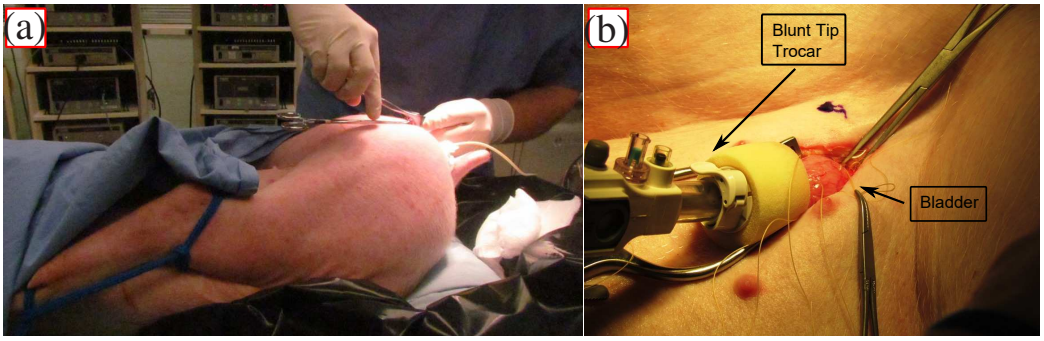

Figure 6.5: (a) Female swine posture for TURBot deployment. A surgeon is dilating the urethra for TURBot sheath insertion prior to TURBot placement, (b) Blunt tip trocar placed in the bladder anterior-inferior region

A blunt tip trocar (balloon port) was placed through the anterior (near neck) of the bladder (See Fig. (6.5)-b). A 26-Fr endoscope with a mounted camera was inserted through this port to visualize the resection/ablation process. This was followed by the dilation of the urethra to facilitate the placement of TURBot.

Next, the simulated bladder lesions for resection were created. HistoGel specimen processing gel (Ref HG-4000-012 Thermo Scientific), an aqueous gel composition, was liquefied in a $60\,^{\circ}\mathrm{C}$ water bath and then mixed with blue dye (toluidine or Methylene blue). 1-2 ml of the blue HistoGel was then injected into the bladder submucosa in multiple locations to simulate tumors. The injections were performed under direct vision from the laparoscope with 18-gauge needles generally inserted through the abdominal and outer bladder walls, thereby reducing the likelihood of puncturing the inner surface of the bladder where the liquefied gel could leak into the bladder. Lesions created on the posterior wall of the bladder necessarily had to be done by inserting the needle all the way through the anterior wall and then into the submucosa of the posterior wall. The room temperature saline irrigation in the bladder quickly cooled the HistoGel, thus solidifying it into a lesion. The lesion creation process had been previously tested and verified in bench top studies.

Figure (6.6) shows a simulated lesion with an approximate size of 8.5 mm.

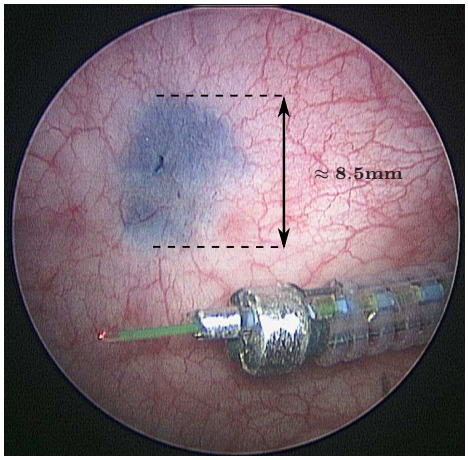

Figure 6.6: Mock-up lesion created by HistoGel.

6.2.2 TURBot Set-up & Deployment

Figure (6.7) shows the overall layout of the operating room during the robotic ablation/resection procedure. TURBot is telemanipulated by a 7-DoF haptic device (Force Dimension Omega.7 haptic device). A foot pedal is used to allow the surgeon to switch control of the master device between the 7-DoF MBCR and the 2-DoF DLA. Visualization of the robot and the workspace was provided to the surgeon using a transvesical endoscope (item (5)) and an endoscope monitor. An optical tracker (NDI Polaris Vicra, item (4)) was used to track markers attached to the robot and the transvesical camera to allow the surgeon to telemanipulate the MBCR in the endoscopic camera frame. This feature was crucial for retroflexed configurations of the MBCR.

Permission was obtained from Vanderbilt University Institutional Animal Care and Use Committee (IACUC) for a series of non-survival pilot studies. After fasting for 12 hours, the female swine (80-100 lb.) was placed under general anesthesia. It was then situated in a supine position with its hips abducted and pelvis lifted slightly to mimic a standard lithotomy position. A 10mm blunt tip trocar balloon port (Medtronic, Minneapolis, MN, USA) was placed through the anterior bladder wall, similar to a suprapubic tube. A 10mm

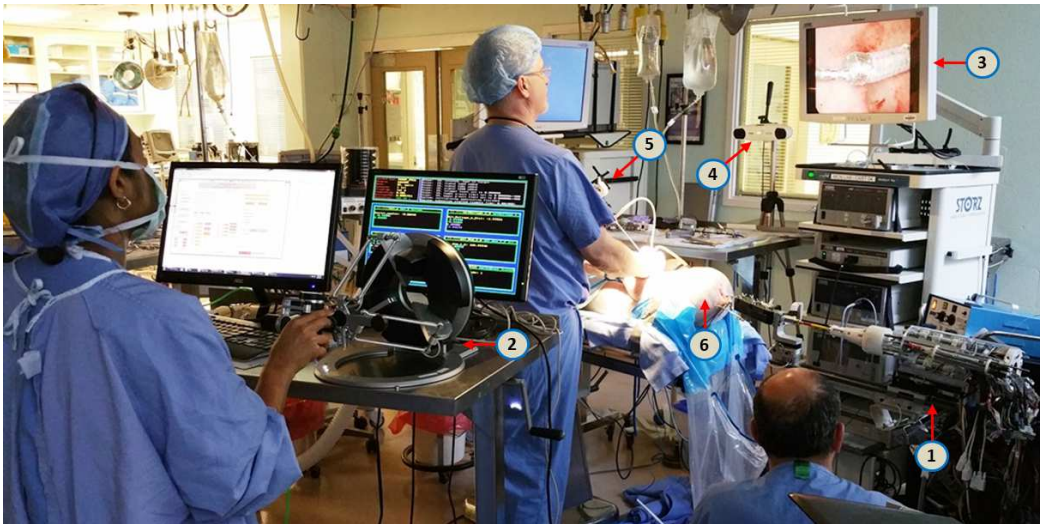

Figure 6.7: TURBot system: (1) TURBot, (2) Omega.7 master haptic interface, (3) Surgeon monitor, (4) Optical tracker base, (5) Optical marker on transvesical endoscope camera, (6) Swine

laparoscope with a mounted camera was inserted through this port to visualize the resection/ablation process. Under endoscope guidance, a guide-wire was inserted through the urethra and advanced into the bladder. Amplatz renal dilators were advanced sequentially over the guidewire to dilate the urethra and facilitate insertion of the robot resectoscope sheath. Once the sheath was in place, the guide-wire was removed. Figure (6.8) illustrates the robotic system in the deployment process.

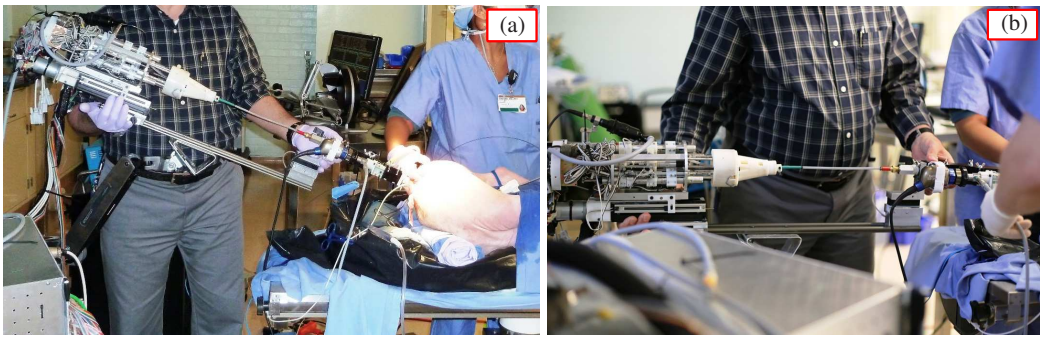

Figure 6.8: TURBot: (a) during deployment, (b) after deployment

6.2.3 Outcomes & Challenges

In terms of deployment, TURBot could be deployed without any prohibitive issues. However, there is room for streamlining the process that is mentioned in section (6.2.5). Initially, the bladder workspace coverage was tested by accessing various locations in the bladder. Then, robot-assisted resections of multiple lesions at different locations (except for the neck) were performed. En-bloc resection was attempted as the last task.

Figure (6.9) shows the MBCR successfully reaching various regions of the bladder. The bladder dome was accessible by using the insertion stage. The bladder neck could be reached with all three segments inserted into the bladder while relying on retroflexion (e.g. Fig. (6.9)-c) or with partial insertion of the MBCR segments (e.g. Fig. (6.9),e-f). The control algorithm was designed to take into account when MBCR segments were constrained inside the resectoscope sheath. It was found that the full extension of the MBCR past the distal tip of the resectoscope sheath is preferable since it better preserves distal dexterity. The snapshots in Fig. (6.10) show the MBCR reaching the bladder neck using this method.

Figure (6.11) illustrates a successful attempt to ablate an approximately 10.5 mm simulated tumor at the left lateral wall (1 Joule at 10 Hz). This was performed by only the MBCR (the DLA was not utilized). This task took approximately 4 minutes and 12 seconds. The change in tumor size that can be seen between images is due to motion of the transvesical camera.

The snapshots in Fig. (6.12) illustrate an en-bloc resection attempt. First, a 1mm grasper was extended manually to grasp the mucosal tissue (Fig. (6.12)-a,b). Then, the DLA was telemanipulated independently to traverse around the grasped tissue while firing the laser simultaneously (Fig. (6.12),c-h).

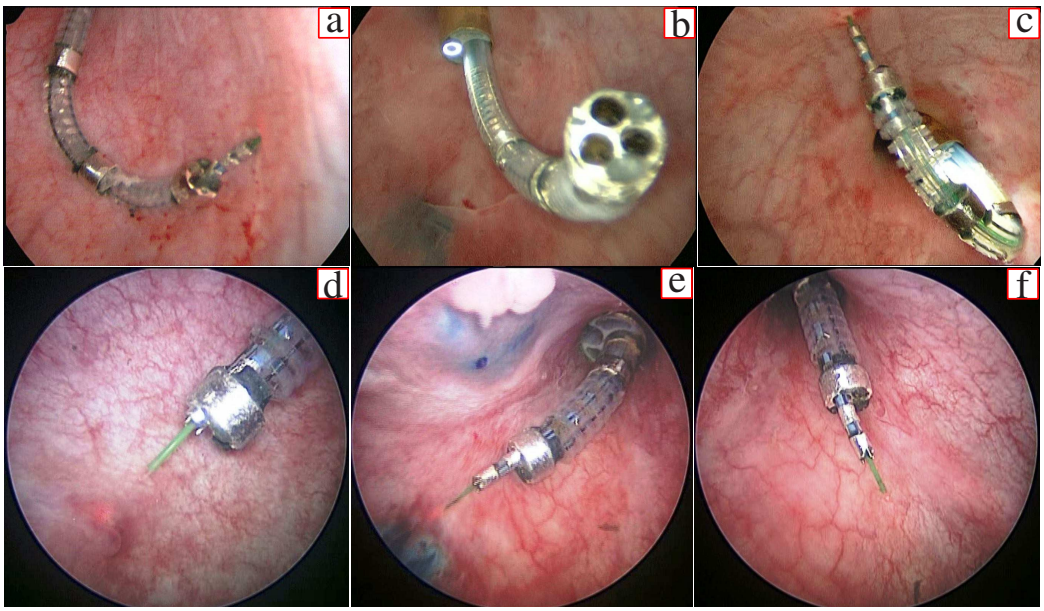

Figure 6.9: TURBot multi-backbone continuum robot reaching bladder: (a) right posterior, (b) anterior dome, (c) anterior neck, (d) left posterior, (e) left lateral (using only distal segment), (f) posterior neck (using only distal segment)

6.2.4 Discussion

TURBot could successfully reach all aspects of the bladder. In particular, either by retroflexing the MBCR or by retracting the proximal and middle segment inside the resectoscope sheath, the bladder neck could be accessed. This not only obviated the need for suprapubic compression or adjustment of bladder distension but the former approach (retroflexion) allowed finer manipulation (especially by using the DLA) than could be potentially offered by a standard rigid resectoscope. Resection at several bladder sites (excluding the neck) was conducted successfully with sub-millimetric accuracy (The accuracy was determined based on follow-up phantom studies). Compared to the observed time for manual resections in the OR, the resection time using TURBot was higher. However, this was primarily due to limited training of the surgeon on the TURBot and the small size of the laser fiber compared to that of the electrocautery loop. Furthermore, the robot speed was maintained lower than necessary as a safety precaution due to the materials incorporated into the robot construction and to enable the accomplishment of the goals of the *in*

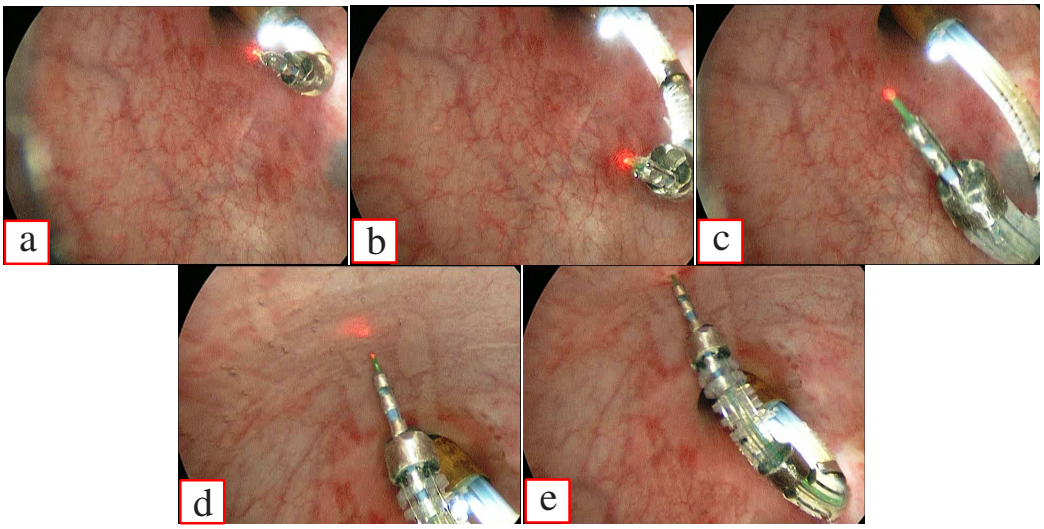

Figure 6.10: Reaching the bladder neck by simultaneously extending and retroflexing the multi-backbone continuum robot. This leaves all segments unconstrained hence more available dexterity.

vivo studies with the available resources.

Although the overall experience with TURBot was positive and instructive, several challenges were encountered during the studies that merit attention. First, the porcine bladder size was small in comparison with the human bladder. Since the MBCR segments lengths were originally designed for potential deployment in human bladder, this rendered robot manipulation and visualization challenging. In addition, the resectoscope-based en-

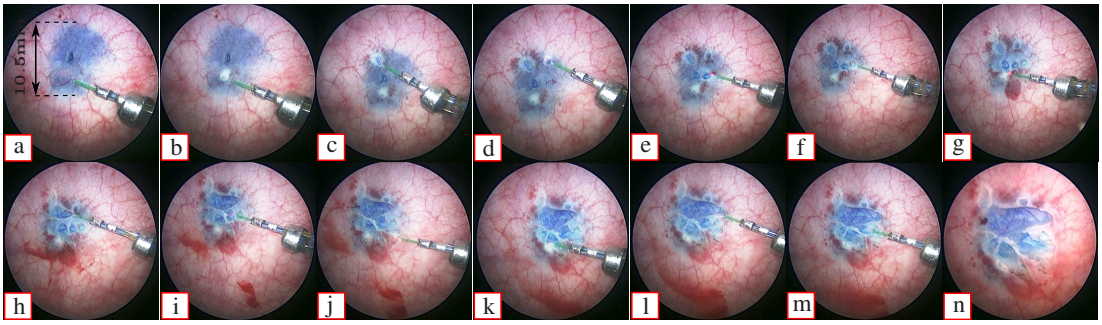

Figure 6.11: Ablating a mock-up tumor of approximately 10.5 mm size on the left lateral wall by 7-degree-of-freedom multi-backbone continuum robot (Distal Laser Arm is not utilized). Note the change of tumor size between snapshots is due to the camera displacement. Figure (n) shows post-ablation lesion.

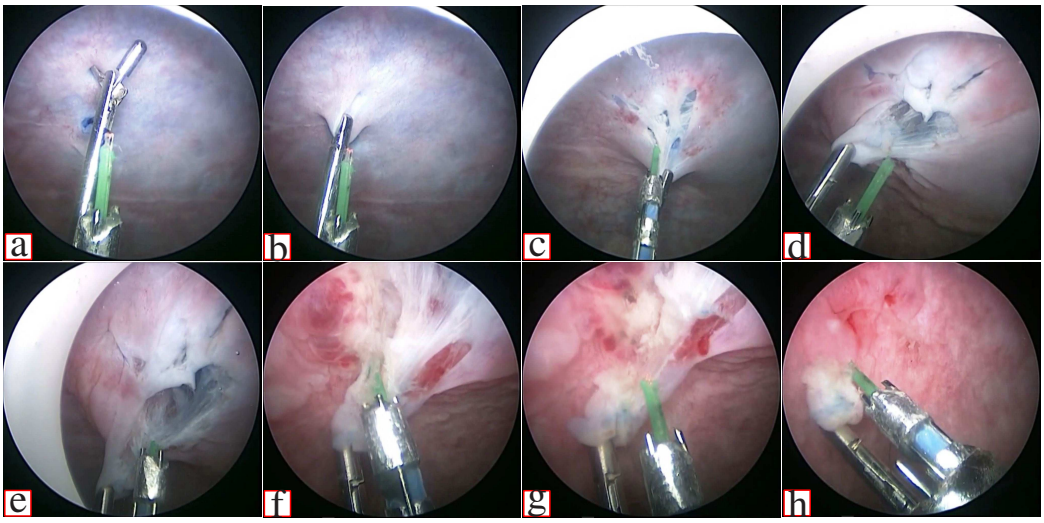

Figure 6.12: En-bloc resection attempt: (a) reaching to grasp the mucosa tissue, (b) grasping, (c)-(h) Distal Laser Arm independent control to fire on and around the grasped tissue.

doscope employed in this prototype could not provide sufficient field of view and the robot body often caused visual occlusion. As a result, the surgeon had to rely primarily on the transvesical anterior trocar-based endoscope for visualization. The balloon port in turn occupied a substantial portion of the small bladder at times disrupting access and manipulation as well as posing visual occlusion in some areas. In light of these observations, the MBCR segments lengths were shortened to alleviate such challenges. However, there was substantial size variability across various porcine bladders.

Yet another challenge was that the swine bladder had a semi-conical shape with a fairly acute angle at the bladder neck (Fig. (6.13)-c). This means that the retroflexing postures could not be utilized to target the neck zone because of the tight space. Instead, the surgeon pulled back the proximal and the middle segments in the sheath in order to use the distal segment (Fig. (6.13)-d).

One major challenge encountered during the ablation procedure was the lack of depth perception in the video feed. Therefore, it was difficult to maneuver the laser tip in the plane of the tumor and sometimes it would perforate the tumor or move just over the surface. Once the laser perforated the surface of the tumor, the MBCR tip was dragged inside the

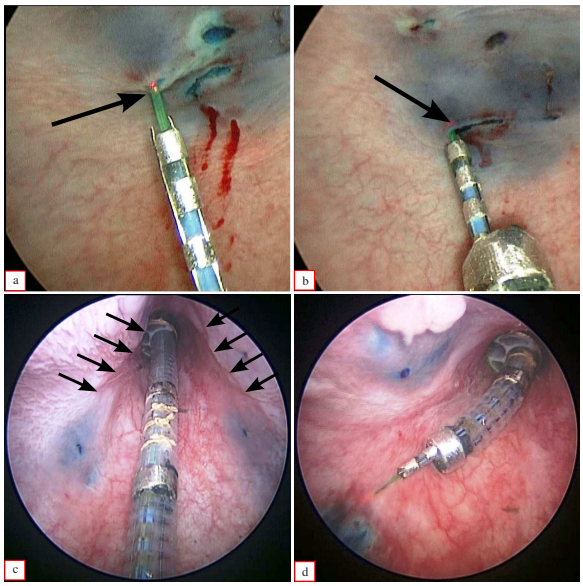

Figure 6.13: Main challenges: (a) laser fiber tip sticking to the tissue, (b) laser fiber penetrating in the mucosa and getting caught in due to sticking and tissue deformation, (c) a swine bladder with a semi-conical neck. Arrows show the neck contour, (d) reaching a lesion with distal segment.

tissue until the laser was pulled off rendering the motion control challenging as shown in Fig. (6.13)-b. A similar effect was caused by the fiber tip occasionally sticking to the mucosal layer surface as seen in Fig. (6.13)-a.

En-bloc resection was challenging since the DLA had only 2 DoFs and the grasper did not have independent articulation. Future system designs will require independent control of the grasper and a collision avoidance algorithm to alleviate the burden of the dual-arm control of the DLA and the grasper.

Another issue was the switching of the high-level control algorithm for telemanipulation between different modes during operation. Switching between modes moved the laser fiber tip to a different part of the workspace thus hindering the surgeon performance. Note that as soon as a portion of a segment was detected to be within the resectoscope sheath, the robot control algorithm straightened the segment fully to warrant the safety of the MBCR. As a result, the robot operated in multiple discrete modes where each one provided a disparate number of DoFs (1,3,5,7). It is a characteristic of the current MBCR design that

a segment may bend only in its full length (and not from the end of the constraint point on to the segment end). This issue was not encountered when the MBCR was used for macro-positioning and the DLA was used for the fine-maneuvering of the laser fiber.

6.2.5 Future Work & Recommendations

A key improvement over the current system is to use stereo vision and an actively controlled camera. Several other surgical robotic systems currently utilize stereo vision (though not in bladder surgery) such as da Vinci® Sp™ surgical system for single port surgery that has an articulated 2-DoF camera that is deployed through a $25mm$ cannula along with three other articulated instruments [195]. Bajo and Simaan evaluated *Insertable Robotic Effectors Platform* (IREP) for single port access surgery (SPAS) [196]. This system has a 3-DoF (pan-tilt-insertion) stereo camera that is deployed through a $15mm$ cannula. Nevertheless, designing a similar stereo-vision module that can be deployed through the $3mm$ camera channel in the robot-integrable resectoscope of TURBot may pose challenges.

A less challenging alternative to improve visual coverage (and not depth perception) is to use an angled endoscope (e.g. $30°$) or a variable angled lens (such as STORZ Endo-CAMeleon® that has variable direction of view from $15°$ to $90°$) whose rotation and insertion can be actively controlled by the surgeon. This could eliminate the need for the balloon port. An exploration of this concept is presented in chapter 7 with the aim of minimizing visual occlusion caused by the MBCR being close to the endoscope.

Even though the TURBot slave was mounted on a statically balanced arm (see Fig.1-a), it was still inconvenient to tilt it accurately to change the angle of resectoscope sheath with respect to the urethra. Motorizing this arm would facilitate steering the TURBot. To streamline en-bloc resection/ablation and to provide sufficient maneuverability to circumscribe the targeted tissue, a DLA with more degrees of freedom is recommended. Furthermore, motorizing the DLA insertion could be also helpful. A robotic grasper instrument would provide even more dexterity to the surgeon further facilitating en-bloc resection.

6.3 Conclusion

In this chapter, a comparison of robot-assisted and manual TURBT performance on a bladder phantom through an experimental user study and *in vivo* validation in swine was conducted. TURBot performance compared to humans was limited primarily due to hardware issues such as flexibility of the 3D-printed components in the actuation transmission. Future iterations would replace these components with stronger materials. Future improvement in visualization would be necessary to overcome visual field occlusion by the robot. A more accurate calibration for actuation compensation such as in [187] can also improve accuracy. Assistive features such as vision-based virtual fixtures to control resection depth will be incorporated to guide safer robot-tissue interactions.

The *in vivo* experiments demonstrated successful deployment of the TURBot, ability to retroflex within the bladder confines and reach all regions of the bladder, and ability to perform en-bloc resection using a combination of laser ablation and a grasper. The animal studies provided insights towards enabling robotic assistance for TURBT for clinical application. Lessons learned through this experience will inform designers of future systems for robot-assisted TURBT.

Despite its current limitations, TURBot is the first pre-clinically *in vivo* tested system offering intra-vesicular dexterity while supporting traditional wire loop cautery and/or laser tumor resection/ablation instruments as well as providing a platform for deploying new imaging modalities. With continued development and clinical translation, this system could significantly enhance the standard of care for TURBT.

CHAPTER 7

MINIMAL VISUAL OCCLUSION REDUNDANCY RESOLUTION OF CONTINUUM ROBOTS IN CONFINED SPACES

7.1 Introduction

The advent of less invasive robotic systems for MIS in deep surgical fields presents new challenges for robot designers and users. For example, robotic systems for operating in deep and narrow spaces (e.g. trans-oral minimally invasive surgery of the upper airways, transurethral endoscopic, transnasal-endoscopic, middle-ear endoscopic and trans-anal endocopic surgeries) present difficulties in visualization as well as in dexterous manipulation. Such difficulties stem from the fact that, in such systems, often the endoscope axis and the axis of the surgical access channel lie almost parallel to each other and with a small offset. As a result, the visual field of an endoscope can be easily occluded when the tools move in front of it. During manual MIS, surgeons can use angled lens endoscopes and can rotate the lens to shift the field of view (FOV) to follow the tool tip. During robotic surgery - and especially when using continuum robots for added dexterity - this problem is exacerbated because the body of the continuum robot often emanates from the access channel in close proximity to the tip of the endoscope. This creates severe problems of visual occlusion when the continuum robot is controlled using native resolved rates control.

This work is motivated by recent experiences we had when deploying our trans-urethral resection of bladder tumors (TURBT) system. Early ex-vivo concepts of this system were reported in [62, 63]. Our recent TURBT system including a custom surgical access channel (called a resectoscope), a *multi-backbone continuum robot* (MBCR), and a holmium laser

for resection was first presented in [197]). This system addresses the clinical needs for preliminary testing in pig experiments. However, initial evaluation has revealed the difficulties of visualization as demonstrated in Fig. 7.1-(a,b). In addition to the limited depth perception when using endoscopic surgery (e.g. as reported in [198]), other critical difficulties hindering successful use of this system in an animal trial were visual occlusion of the robot tip by its own body and the narrow visualization workspace as observed from an endoscope.

To solve these problems, we have drawn inspiration from manual endoscopic surgery where surgeons rely on the rotation of an angled lens endoscope to help maintain visualization of the end effector. Though we could have considered the use of a steerable endoscope to help solve the visual occlusion problem, we have elected to treat the case of a straight endoscope because 1) it is more restrictive, 2) the cost of a straight Hopkins rod endoscope is a fraction of the cost of a steerable endoscope, 3) sterilizable steerable endoscopes with diameters fitting our 3 mm endoscopic access channel have very narrow FOV and relatively short focal range.

To address this need, this chapter investigates the use of redundancy resolution to minimize visual occlusion while assuming that an angled-lens endoscope can be actively rotated to shift the direction of the FOV. We also assume that a computer algorithm for visually rotating re-centering of the camera view can be implemented in future applications of our method so that the user does not get disoriented when tele-manipulating such robots.

Works relevant to this research are in the area of obstacle avoidance for continuum robots and control of camera position for surgical applications in order to maintain the end effector in the FOV. Li and Xiao proposed a method for sampling the configuration space of continuum robots to produce motion plans allowing these robots to operate within constrained environments [199]. Reiter and Allen [200] who presented automatic tracking of the arms of the IREP single port access system. This work however did not consider the problem of how to control the continuum arms of the robot to minimize visual occlusion.

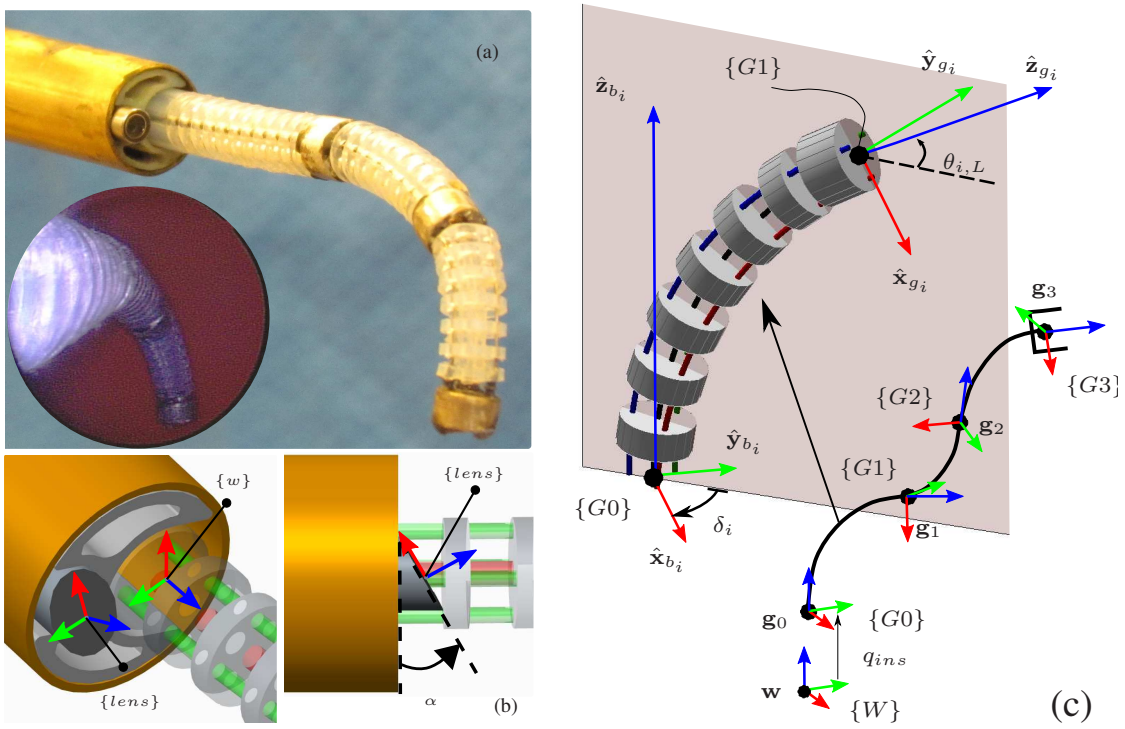

Figure 7.1: (a) TURBT robot distal section, inset shows camera view, (b) External sheath tip, (c) Multibackbone continuum robot schematic

Baumann *et al.* [201] applied a modified probabilistic roadmap method (PRM) to penalize the motions of an articulated serial robot that block the line of sight of an eye-in-hand camera while reaching the visual target [202, 203]. Leonard *et al.* used PRM and a dynamic collision checking algorithm to plan occlusion-free motions for industrial robots. They modeled the FOV of an eye-to-hand (stationary) camera as a quadtree of frustums and applied adaptive dynamic collision checking algorithms to avoid colliding pre-selected pixels in the view frustum of the camera [204]. In the area of visual servoing, preservation of visibility is of significant importance as the loss of visual information jeopardizes the stability and/or performance of feedback control. Visual target loss occurs due to the robot self-occlusion or the target departure from FOV. Therefore, designing algorithms and controllers that guarantee visible robot configurations has been a critical problem that was addressed in multiple studies [205–209]. Most - if not all - such work in the visual servoing field rely on the image space information for their algorithms. More importantly, none

of the prior literature utilizes the kinematic redundancy of the robot to address occlusion minimization.

The main contribution of this study is in utilizing the robot kinematic redundancy to minimize the FOV occlusion. To achieve this, a modified artificial potential field approach in path planning is applied to drive the robot body outside the FOV while achieving the main tracking task. The proposed algorithm can be directly applied to any redundant robot performing a task under the surveillance of a camera. Moreover, it does not require the camera intrinsic parameters calibration since it does not use image space information.

The chapter is structured as follows: In section 7.2, the problem definition is presented. In section 7.3, the solution approach is delineated in details. This includes descriptions of the potential function derivation, a suitable force field definition, the redundancy resolution framework and a visual occlusion index. Simulation results and discussions are brought in section 7.4. Finally the chapter is concluded with a summary in section 7.5.

7.2 Problem Statement and Assumptions

Based on Fig. (7.1)-b, the world coordinate frame $\{w\}$ is at the center of MBCR working channel with the z-axis along the axis of the resectoscope sheath (yellow tube). The lens coordinate frame $\{lens\}$ is attached to the endoscope tip lens such that its z-axis is normal to the lens. For simplicity of presentation, we assume that there are no motion constraints on the MBCR (e.g. induced by the external sheath). Such constraints may be dealt with as in [141].

The problem we wish to solve is to command the end-effector of the MBCR to track a desired twist $\dot{\boldsymbol{\xi}}$ while using redundancy to minimize visual occlusion. We assume that occlusion can be minimized by applying a proper force on the MBCR so that its resultant equilibrium configuration causes minimal occlusion. This static equilibrium is sought according to the virtual work principle by minimizing the potential energy of the system (The mechanical energy of the MBCR including elastic potential and an artificial potential due

to visual occlusion) subject to the kinematics of MBCR. Though a task priority redundancy resolution approach as presented in [210] is possible, we pursue a redundancy resolution using gradient projection for the simplicity:

$$\begin{aligned} &\text{Minimize} \quad \Pi \\ &\text{subject to} \quad \mathbf{J}_{x\tilde{\psi}}\dot{\tilde{\boldsymbol{\psi}}} = \boldsymbol{\xi} \end{aligned} \tag{7.1}$$

7.3 Solution Method

In motion planning by artificial potentials, the potential function U_r refers to an artificial *repulsive* potential that prevents *psp*'s (point subject to potential) to collide with the obstacles in the environment. This repulsive potential is added to *attractive* potential U_a so the robot can reach the goal by attraction toward it while avoiding the obstacles [211, 212]. The repulsive potential is chosen such that the rendered force on the robot vanishes after a certain *distance of influence* and approaches infinity as the psp approaches the obstacle. If psp's are selected appropriately, this ensures the robot never collides with the obstacles while satisfying the main task of tracking[1]. In this study, a similar approach is adopted in that a potential function is minimized locally, however there are key differences that are outlined here.

The first difference is in the choice of the potential function. In our study, this function has contributions from an artificial repulsive field as well as the gradient of the strain energy of the continuum robot. This potential function denoted hereafter Π stems from the application of principle of virtual work as will be shown. Also, the repulsive field generates a force that is designed to push the psp's outside the FOV. These forces do not grow infinite as the psp's collide with the FOV cone as that is a requisite to achieve the main task, rather they grow larger at an adjustable rate as the psp's move toward the inside of FOV and they

[1]The problem of reaching local minima may happen that causes the motion planning to stop prematurely. Supplementing the potential method with well-tuned randomized best-first algorithms to escape local minima can solve this problem [213].

diminish as the psp's move outside the FOV and the distance of influence.

A second difference is that no attractive potential is used to fulfil the main task. Instead, we use pseudo-inverse with gradient projection to resolve the redundancy at velocity level for the purpose of the real-time control while minimizing the occlusion.

7.3.1 Potential Function

The principle of virtual work states that the mechanical energy Π is stationary at an equilibrium point (i.e. $\delta\Pi \triangleq \delta(E - W) = 0$ where E and W represent the potential (elastic) energy and work of external force respectively. In our problem, the elastic energy E includes the bending strain energy of all the backbones. The gravitational and the axial strain energy of the backbones can be neglected for robots of small size as ours [214]. Therefore, the elastic energy is expressed as in [182]:

$$E = \sum_{i=1}^{3} (\pi/2 - \theta_{iL})^2 \left(\frac{E_p I_p}{2l_i} + \sum_{j=1}^{3} \frac{E_s I_{s,j}}{2l_{i,j}} \right) \tag{7.2}$$

where $E_p I_p$ and $E_s I_{s,j}$ is the flexural rigidity of the primary and the j^{th} secondary backbone, respectively. The infinitesimal work done by the repulsive force field is contributed by the work of the respective forces $\mathbf{f}_i$ on the i^{th} psp:

$$\delta W = \sum_i \mathbf{f}_i^{\mathrm{T}} \delta \mathbf{p}_i = \sum_i \mathbf{f}_i^{\mathrm{T}} \mathbf{J}_{v\tilde{\psi}}^{(i)} \delta\tilde{\boldsymbol{\psi}} \tag{7.3}$$

where $\mathbf{J}_{v\tilde{\psi}}^{(i)} \triangleq \frac{d\mathbf{p}_i}{d\tilde{\boldsymbol{\psi}}}$ is the translational Jacobian of the i^{th} psp. Considering $\delta\Pi = \frac{\partial\Pi}{\partial\tilde{\boldsymbol{\psi}}}\delta\tilde{\boldsymbol{\psi}}$, $\delta U = \frac{dE}{d\tilde{\boldsymbol{\psi}}}\delta\tilde{\boldsymbol{\psi}}$ and Eq (7.3),

$$\nabla_{\tilde{\psi}}\Pi = \nabla_{\tilde{\psi}} E - \sum_i \mathbf{J}_{v\tilde{\psi}}^{(i)^{\mathrm{T}}} \mathbf{f}_i \tag{7.4}$$

Thus,

$$\Pi = E - \int \sum_i \mathbf{f}_i^{\mathrm{T}} \mathbf{J}_{v\tilde{\psi}}^{(i)} d\tilde{\boldsymbol{\psi}} \tag{7.5}$$

The derivation of $\mathbf{J}^{(i)}_{v\tilde{\psi}}$ is straightforward given the Jacobian of each MBCR segment (see [215] for details).

7.3.2 Repulsive Force Field

A repulsive force field that can minimize image occlusion is characterized such that

- For a psp inside the cone, it increases at a rapid rate as the psp's distance to the cone face increases.
- For a psp outside the cone, it decreases as the psp's distance to the cone face increases.
- After a certain distance (distance of influence d_0), outside the cone, it vanishes.
- The closer the psp is to the vertex of the cone, the more the endoscopic occlusion, hence the greater the force.

To formulate a force field with the above characteristics, we first define distance variables with respect to the FOV cone.

7.3.2.1 Conical Distance Parameters

Fig. 7.2-a shows an arbitrary point ($\mathbf{psp}_i$) and the cone of FOV in its local frame ($\{lens\}$). We define *canonical distance* d and *canonical slant height* r as shown in Fig. 7.2-a. Canonical distance d is measured from the surface of the FOV cone to the psp. The slant height r is measured from the origin of the FOV cone to a point on the cone surface that is closest to the psp. The distance d is defined as:

$$d = \begin{cases} > 0 \text{ if point is outside the cone} \\ < 0 \text{ if point is inside the cone} \\ = 0 \text{ if point is on the cone} \end{cases} \tag{7.6}$$

To determine (d, r) given $\mathbf{psp}(x, y, z)$ and β, first, the position of $\mathbf{psp}$ in $(\{lens\})$ is calculated using a homogeneous transformation

$$ {}^{lens}\mathbf{psp} \triangleq \begin{bmatrix} x_l \\ y_l \\ z_l \end{bmatrix} = {}^{lens}\mathbf{R}_w \mathbf{psp} + {}^{lens}\mathbf{p}_{org,w} \tag{7.7} $$

where ${}^{lens}\mathbf{R}_w = e^{\alpha \hat{\mathbf{e}}_2{}^\wedge} e^{-\gamma \hat{\mathbf{e}}_3{}^\wedge}$ is the rotation transformation from $\{w\}$ to $\{lens\}$ and ${}^{lens}\mathbf{p}_{org,w} = [0, -d_o, 0]^{\mathrm{T}}$ is the position of the origin of $\{w\}$ described in $\{lens\}$ and d_o is the center-to-center distance of robot and endoscope channels (Fig. (7.1)-a). γ and α is the angle of rotation of endoscope and lens inclination angle respectively.

It is straightforward to show by geometry that the canonical distance of $\mathbf{psp}$ is:

$$ d = \cos(\beta)\sqrt{(x_l^2 + y_l^2)} - \sin(\beta) z_l \tag{7.8} $$

where β is the half of the vertex angle of the cone (Fig. (7.2)-(a)) and the canonical slant height is:

$$ r = \sin(\beta)\sqrt{(x_l^2 + y_l^2)} + \cos(\beta) z_l \tag{7.9} $$

7.3.2.2 Repulsive Force Field

Denoting f^* as the nominal force magnitude on the cone face at nominal slant height $r = r^*$, we define the repulsive force as:

$$ \mathbf{f}(d, r) = \begin{cases} \frac{f^*}{(r/r^*)^q} \left(\frac{d}{d_0} - 1 \right)^{2p} \hat{\mathbf{f}} & d/d_0 \leq 1, r \geq 0 \\ 0 & \text{otherwise} \end{cases} \tag{7.10} $$

r^* and f^* as well as power variables p and q in the above equation help determine the magnitude and the growth of the force field. $\hat{\mathbf{f}}$ is the unit direction vector of the force that

is $\hat{\mathbf{f}} = {}^{w}\mathbf{R}_{lens}\, {}^{lens}\hat{\mathbf{f}}$ where

$$ {}^{lens}\hat{\mathbf{f}} = \left[\frac{x_l \cos(\beta)}{\sqrt{(x_l^2 + y_l^2)}}, \frac{y_l \cos(\beta)}{\sqrt{(x_l^2 + y_l^2)}}, -\sin(\beta) \right]^{\mathrm{T}} \tag{7.11} $$

Fig. 7.2-b shows the plot of the force magnitude for $|d/d_0| \leq 1$, $p = 1, q = 2$ and multiple values of r/r^*.

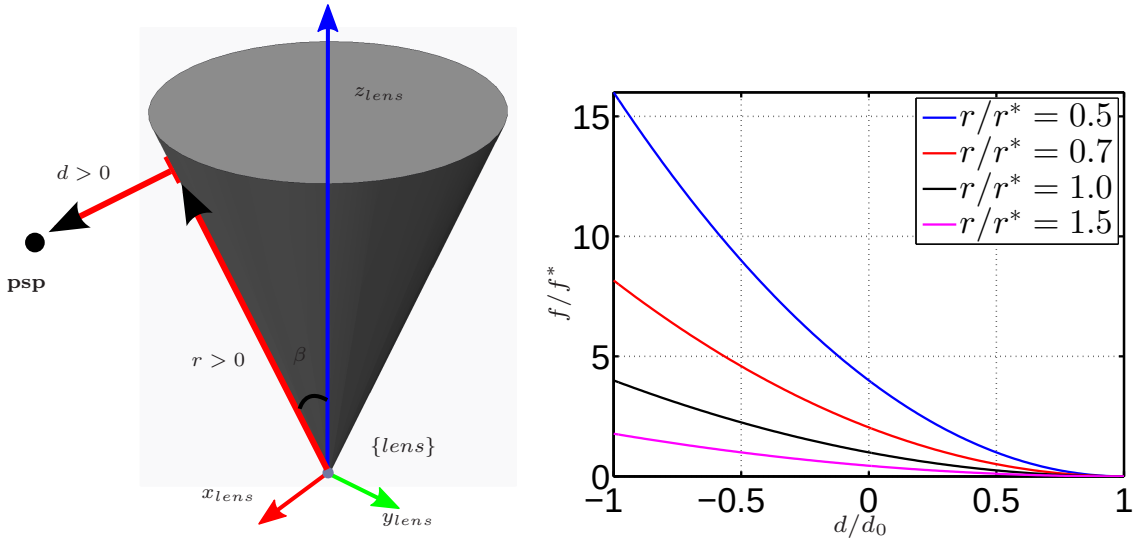

(a) (b)

Figure 7.2: (a) Conical distance parameters (r, d), (b) Force field magnitude as a function of canonical distance

7.3.3 Optimization Framework

The gradient descent method is adopted in order to minimize the potential function Π. This approach provides local minimization if certain conditions (convex function and Lipschitz gradient) are satisfied [216]. Therefore, the following $\dot{\tilde{\psi}}$ minimizes Π:

$$ \dot{\tilde{\psi}} = -\eta \nabla_{\tilde{\psi}} \Pi, \qquad \eta > 0 \tag{7.12} $$

The problem in Eq. (7.1) can be cast as a quadratic programming problem (QP) where the main task of tracking the command velocity is treated as a constraint.

$$\begin{aligned} \underset{\dot{\tilde{\boldsymbol{\psi}}}}{\text{Minimize}} \quad & \frac{1}{2}(\dot{\tilde{\boldsymbol{\psi}}} + \eta\nabla_{\tilde{\psi}}\Pi)^{\mathrm{T}}\mathbf{W}_1(\dot{\tilde{\boldsymbol{\psi}}} + \eta\nabla_{\tilde{\psi}}\Pi) \\ \text{subject to} \quad & \mathbf{J}_{x\tilde{\psi}}\dot{\tilde{\boldsymbol{\psi}}} = \boldsymbol{\xi} \end{aligned} \tag{7.13}$$

where $\mathbf{W}_1 \in \mathbb{R}^{7\times7}$ is a positive-definite weight matrix. The solution to this optimization problem that is also known as *Projected Gradient Method* ([212, 217]) is as follows

$$\dot{\tilde{\boldsymbol{\psi}}}^* = \mathbf{J}^{\dagger}_{x\tilde{\psi}}\boldsymbol{\xi} - \eta(\mathbf{I}_7 - \mathbf{J}^{\dagger}_{x\tilde{\psi}}\mathbf{J}_{x\tilde{\psi}})\nabla_{\tilde{\psi}}\Pi \tag{7.14}$$

where $\mathbf{I}_7 \in \mathbb{R}^{7\times7}$ is the identity matrix, $\nabla_{\tilde{\psi}}\Pi$ is substituted from Eq (7.4) and $(.)^{\dagger}$ represents the regularized weighted Moore-Penrose pseudo-inverse [149, 150]:

$$\mathbf{J}^{\dagger}_{x\tilde{\psi}} = \mathbf{W}_1^{-1}\mathbf{J}^{T}_{x\tilde{\psi}}(\mathbf{J}_{x\tilde{\psi}}\mathbf{W}_1^{-1}\mathbf{J}^{T}_{x\tilde{\psi}} + \epsilon\mathbf{I}_6)^{-1} \tag{7.15}$$

The regularizing term $\epsilon\mathbf{I}_6$ serves to redefine matrix inversion to avoid singularities. If ϵ is sufficiently small, this solution minimizes Π in the null-space of $\mathbf{J}_{x\tilde{\psi}}$ i.e. the null-space projector $\mathbf{I} - \mathbf{J}^{\dagger}_{x\tilde{\psi}}\mathbf{J}_{x\tilde{\psi}}$ projects the gradient vector $\nabla_{\tilde{\psi}}\Pi$ in the null-space of the Jacobian, therefore it does not violate the constraint given by the pseudo-inverse solution [212].

To use the endoscope rotation angle γ to minimize the end effector-FOV center-to-center distance d_c, we choose:

$$\dot{\gamma}^* = -\eta\frac{\partial d_c}{\partial\gamma}, \qquad \eta > 0 \tag{7.16}$$

d_c can be shown by geometry to be

$$d_c = \|^{lens}\mathbf{p}_{ee}\|\sin(\beta + \mu) \tag{7.17}$$

where ${}^{lens}\mathbf{p}_{ee}$ is the coordinates of the end effector frame origin in $\{lens\}$ and $\mu = \mathrm{Atan}(d_{ee}/r_{ee})$. r_{ee}, d_{ee} are the canonical distance parameters of the end effector frame origin.

7.3.4 Implementation

A resolved rate method is used to determine $\boldsymbol{\xi}$ in Eq (7.14) in order to track the desired end-effector pose. thus:

$$\begin{aligned} \boldsymbol{\xi} &= \begin{bmatrix} v_{des}\hat{\mathbf{e}}_p \\ \omega_{des}\hat{\mathbf{e}}_\zeta \end{bmatrix} \\ \hat{\mathbf{e}}_p &= \frac{\mathbf{p}_{ee,des} - \mathbf{p}_{ee}}{\|\mathbf{p}_{ee,des} - \mathbf{p}_{ee}\|}, \\ \hat{\mathbf{e}}_\zeta &= Axis(\mathbf{R}_{ee,des}\mathbf{R}_{ee}^{\mathrm{T}}) \end{aligned} \tag{7.18}$$

where v_{des} and ω_{des} are the desired end effector linear and rotational velocities, $\mathbf{p}_{ee,des}$, $\mathbf{R}_{ee,des}$, $\mathbf{p}_{ee}$ and $\mathbf{R}_{ee}$ are the desired and current end effector position and orientation respectively. $Axis(.)$ represents the axis of a rotation matrix in axis-angle orientation representation [212].

The Euler method is applied to solve Eq (7.14) and (7.16) to obtain $\tilde{\boldsymbol{\psi}}^*$ and γ^*. The steps to implement the algorithm are summarized in Algorithm (5).

Algorithm 5 Occlusion Minimization

Input: Δt,t_f,$\tilde{\boldsymbol{\psi}}_0$,$\gamma_0$
Output: $\tilde{\boldsymbol{\Psi}} = [\tilde{\boldsymbol{\psi}}_1, \tilde{\boldsymbol{\psi}}_2, ...]$,
$\boldsymbol{\gamma} = [\boldsymbol{\gamma}_1, \boldsymbol{\gamma}_2, ...]$ ▷ Solutions at each step
1: $\tilde{\boldsymbol{\psi}} = \tilde{\boldsymbol{\psi}}_0$, $\gamma = \gamma_0$, $\dot{\tilde{\boldsymbol{\psi}}} = 0$, $\dot{\gamma} = 0$, $k = 0$ ▷ Initialization
2: **while** $k\Delta t \leq t_f$ **do**
3: $k \leftarrow k + 1$
4: $\tilde{\boldsymbol{\psi}}_k = \tilde{\boldsymbol{\psi}}_{k-1} + \dot{\tilde{\boldsymbol{\psi}}}_{k-1}\Delta t$ ▷ Numerical integration
5: $\gamma_k = \gamma_{k-1} + \dot{\gamma}_{k-1}\Delta t$ ▷ Numerical integration
6: $\dot{\tilde{\boldsymbol{\psi}}}_{k-1} \leftarrow \mathbf{J}^{\dagger}_{x\tilde{\psi}}\boldsymbol{\xi} - \eta(\mathbf{I}_7 - \mathbf{J}^{\dagger}_{x\tilde{\psi}}\mathbf{J}_{x\tilde{\psi}})\nabla_{\tilde{\psi}}\Pi$ ▷ Eq (5.6), (7.4), (7.15) and (7.18)
7: $\dot{\gamma}_{k-1} \leftarrow -\eta\frac{\partial d_c}{\partial \gamma}$ ▷ Eq (7.16),(7.17)
8: **end while**

7.3.5 Visual Occlusion Index (VOI)

In order to compare the visual occlusion in different scenarios, a measure called *visual occlusion index* (VOI) is introduced. This measure is the ratio of the volume of the approximated occluded frustum to the volume of the cone of FOV whose base is at the end-effector tip. Figure (7.3a) illustrates a planar schematic of the approximate frustum of occlusion (hatched area) induced by an MBCR. ν is the maximum subtended angle of the MBCR structure from the point of entry into the cone. r_e and r_{max} is the canonical slant height of the entry point and the end effector respectively. As such, VOI can be shown to be

$$VOI = \frac{\left(1+\cot^2(\beta)\right)^2 \tan^2(\nu)}{4\left(\cot(\beta)+\tan(\nu)\right)^2}\left(1-\left(\frac{r_e}{r_{max}}\right)^3\right) \tag{7.19}$$

where ν is saturated at 2β, i.e. in situations where the MBCR passes across the cone, $\nu = 2\beta$.

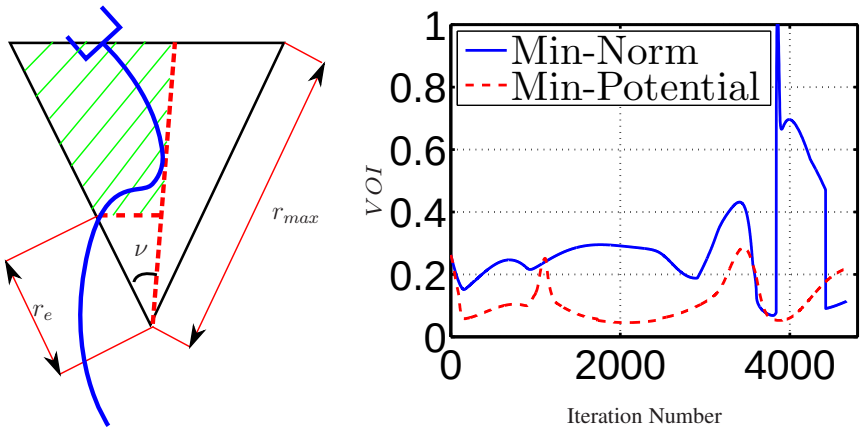

(a) (b)

Figure 7.3: (a) Illustration of occlusion frustum (hatched area), (b) Visual occlusion index in tracking a circle

7.4 Results & Discussions

To validate the proposed method, several simulations were performed in MATLAB® environment. Table 7.1 summarizes the parameters values used in the simulations.

psp's were situated as follows. $\frac{s_{1,L}}{l_1} = [0.5, 0.75, 1]$, $\frac{s_{2,L}}{l_2} = [0.25, 0.5, 0.75, 1]$ and $\frac{s_{3,L}}{l_3} = [0.25, 0.50, 0.75]$ where $s_{j,L}$ denotes the arc distances of psp's on the j^{th} segment. The locations were chosen by heuristics and also by inspection of simulation results.

Table 7.1: Simulation parameters

Param.	**Value**	**Param.**	**Value**	**Param.**	**Value**
Δt	1ms	η_1	30	η_2	30
ϵ	10^{-6}	d_o	4.47mm	α	30°
β	27.5°	d_0	5mm	r^*	60mm
f^*	5N	l_i	$\{26, 20, 19\}$mm	r_{disk}	2.5mm

The first task is to maintain the end effector pose with $\gamma = 0$ to examine the performance of the algorithm presented in algorithm (5). This simulation also helps select the locations and the number of psp's and to tune other parameters such as η_1 so as to elicit the desired behavior in converging to the equilibrium. Fig. (7.4) and the multimedia extension show the MBCR at the start and the end of simulation. The forces are shown by blue vectors and the base translation motion is represented by a magenta trail. The plots in Fig. (7.5a) and (7.5b) shows the potential energy and the VOI in the same simulation respectively.

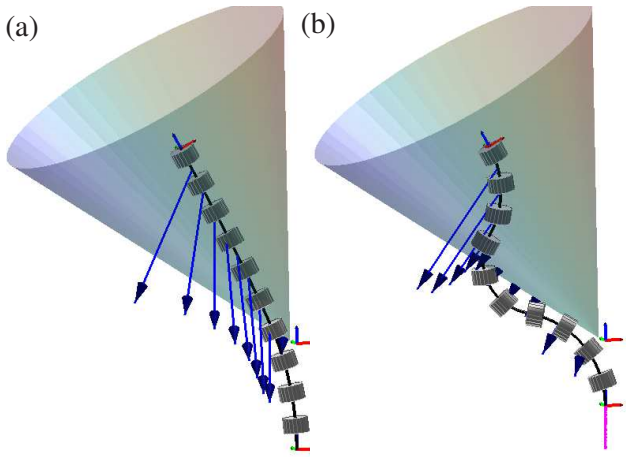

Figure 7.4: Maintaining end effector pose and converging to a minimal-occlusion posture (a) Initial posture, (b) Final Posture, Note there is no endoscope rotation.

At iteration $\approx 800(0.8secs)$, the MBCR is pushed outside the cone into the static equilibrium enforced by the imparting forces and the energy of the MBCR (Eq (7.2)) while the

tip remains stationary. The VOI converges to 0.16 from initial value of 0.25.

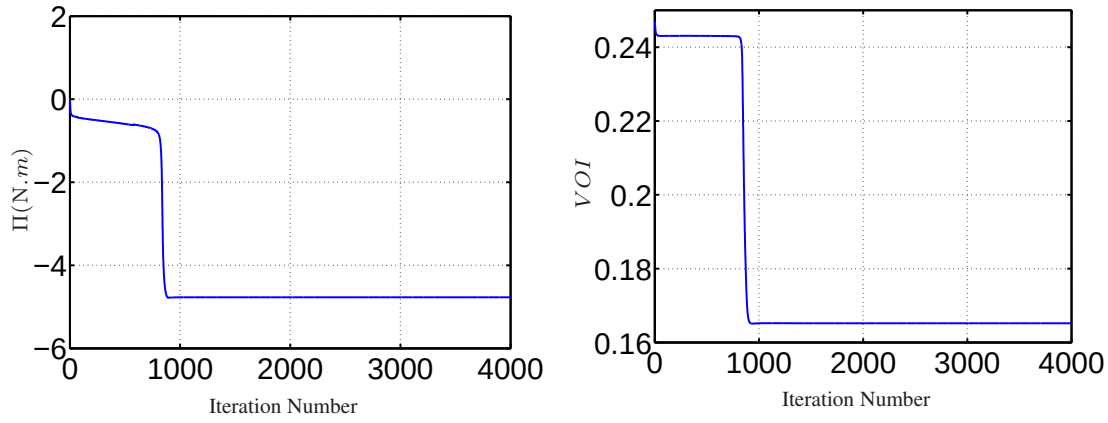

(a) (b)

Figure 7.5: Min-potential solution for the task of maintaining end effector pose: (a) Potential energy, (b) Visual occlusion index

A second task is to track a circle of radius $10mm$ while orienting the end effector central axis (blue axis at the tip) along the normal to the circle plane ($\hat{\mathbf{n}}$ in Fig. (7.6)). The center of the circle is fixed on the axis of the FOV cone at $t = 0$. To minimize d_c while the tip is tracking the circle, the endoscope rotates from $0°$ to $-23.7°$ and then goes to $25.1°$ and ends up close to $0°$ for a full circle tracking. The top snapshots in Fig. (7.6) demonstrate how the robot accomplished this task using a minimum-norm solution (pseudo-inverse). The bottom snapshots show the same task at the same instants accomplished by using minimum-potential solution in Eq (7.14). As it can be seen in the top pictures, most of the MBCR body is inside the FOV (or just outside of it). This is explained by the fact that a pseudo-inverse solution minimizes the configuration space change from the initial configuration (top left picture) to achieve the task. Examining the bottom pictures shows that the robot achieves the task of tracking by using the configurations that are generally leaning outside the FOV hence not obstructing the camera visual. Both these simulations are shown in the multimedia extension.

The plots of Fig. (7.3b) show the VOI for the two solutions. The average VOI for the minimum-potential and the minimum-norm solution are 0.11 and 0.29 respectively con-

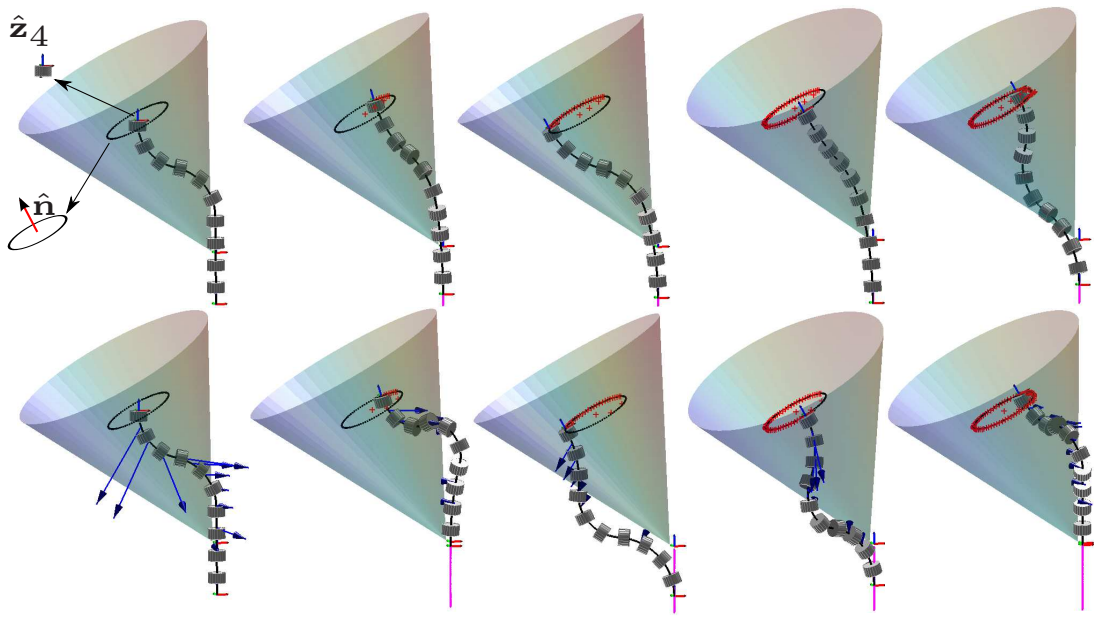

Figure 7.6: Application of Algorithm (5) for the main task of tracking a $\varnothing 20mm$ circle while keeping end effector's $\hat{\mathbf{z}}_4$ axis along the normal to the circle plane $\hat{\mathbf{n}}$. Top and bottom rows display min-norm and min-potential solutions respectively. Note endoscope rotation as observed by change in the orientation of the cone of field of view.

firming the efficacy of the minimum-potential solution. At iteration 3840, the VOI of the minimum-norm solution jumps from 0.08 to 1 and then starts falling back down at iteration 3864. During this period, the first segment enters the FOV and obstructs it very close to the cone vertex ($r = 2.3mm$ at iteration 3841) and then leaves it.

The choice of number and location of psp's affects the solution of the redundancy method and the computational cost. For instance, in our simulations, it was observed that using $\frac{s_{1,L}}{l_1} = [0.5 : 0.05 : 1]$, $\frac{s_{2,L}}{l_2} = [0.25 : 0.05 : 1]$ and $\frac{s_{3,L}}{l_3} = [0.25 : 0.05 : 0.75]$ caused the MBCR to be pushed further outward since more psp's increase the resultant forces. In our opinion, infinite number of points distributed evenly across the body of a planar MBCR (or a continuously distributed force) generates the globally minimal occlusion. However, apart from computational considerations, this may not be true for a general spatial continuum robot and requires more investigation. Although psp's selection was performed heuristically in our simulations, other approaches are worth investigating. For instance, it is possible to use *floating* psp's such that at each iteration of the algorithm, the closest point

to the cone per segment is assigned as a psp.

Note that it is also possible to affect the equilibrium configuration and the rate of convergence by adjusting the force magnitudes in Eq (7.10). Whether the same behavior can be achieved by changing the number of psp's remains to be investigated. Regardless, a caveat is that too many psp's or excessively large force magnitudes may cause excessive null-space motion that can intervene with the main task depending on the value of ϵ. Moreover, the time step Δt, η_1 and η_2 are important parameters too. Note that the gradient descent step size is ultimately determined by $\eta_1.\Delta t$ (or $\eta_2.\Delta t$).

The parameter ϵ in Eq (7.14) requires careful tuning. if it's too small (typically less than 10^{-6} in our simulations), the MBCR assumes extremely large configuration rates and loses tracking when it's close to singular configuration ($\theta_{iL} = \pi/2$). If it's too large (typically greater than 10^{-4} in our simulations), the main tracking task is jeopardized as the null-space solution loses its validity thus interfering with the tracking task.

7.5 Conclusions

In this chapter, a redundancy resolution method was developed to minimize the visual field occlusion caused by the presence of the robot in the field of view (FOV). The method is based on a modified artificial potential field that drives the robot outside the FOV in attempting to reach static equilibrium while achieving the main task of tracking. Simulations for the tasks of maintaining the end effector pose and tracking a circle confirmed the efficacy of the proposed method for a rotating camera. Although the proposed method was developed within the context of multi-backbone continuum robots, it can be generally applied to any redundant robot that requires to stay as clear of the visual field as possible, whether the redundancy is inherent to the robot (e.g. 7-DoF robot) or it is with respect to the task (e.g. Cartesian position tracking by a 6-DoF robot).

CHAPTER 8

ANALYSIS OF AN OPEN-ENDED WIRE-DRIVEN WRIST FOR ROBOTIC MIS

Most commercial surgical wrists use a pull/release *closed-loop* wire transmission where a single motor is used to drive a closed-loop wire in both directions as shown in Fig. (8.2)-a. In such designs, the number of actuators and the degrees of freedom are equal. The wire loop initially requires a pretensioning to ensure it does not slacken during operation. This actuation scheme is perhaps the most commonly known wire (or tendon) drive that is also used in a variety of industrial machinery. The da Vinci robot also uses this method of wire actuation. In an alternative wire transmission known as *open-ended* wire drive, one end of a wire is connected to the moving link while the other end is pulled by an actuator as illustrated in Fig. (8.2)-b. In this paradigm, the force transmission can only take place when wires are pulling since a wire cannot tolerate compression [218]. Morecki *et al.* showed that the minimum number of actuators required to fully control an n-DoF open-ended wire-driven mechanism is $n + 1$ [219].

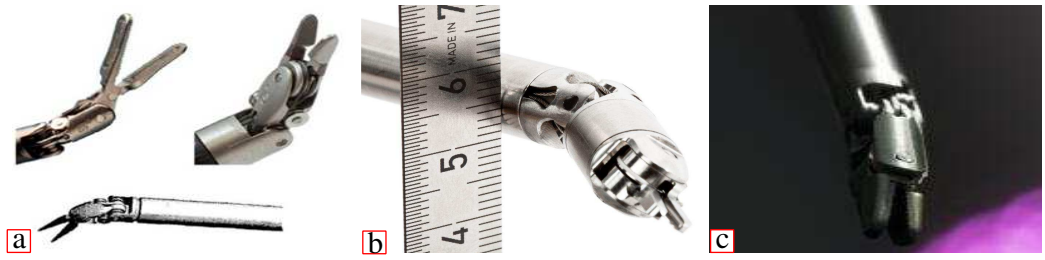

Figure 8.1: Commercial surgical wire-driven wrists, R,P,Y stand for roll, pitch and yaw respectively: (a) Intuitive Surgical's EndoWrist®(RPY), (b) MICA tool as a needle holder from DLR (German Aerospace Center) (PYY)[220], MICA was acquired by Medtronic, reproduced form https://www.dlr.de, (c) 5mm instrument from CMR Surgical (PYY), reproduced from https://cmrsurgical.com.

Even though open-ended wire drives require more actuators than the number of DoFs, they have an important advantage over closed-loop drives. In a closed-loop transmission, the required pretension is relatively high. This pretension can generate high friction and contribute to reduced fatigue life. Accurate compensation for this elastic deformation is not feasible as there is only one actuator for a single DoF. However, in an open-ended transmission, pretension of each wire is directly affected by its dedicated actuator which implies at some configurations, a wire may completely slacken if the wrist is not designed properly. However, as the number of actuators are more than the degrees of freedom, it is possible to have a more accurate compensation of motion losses due the wire elongation or creep effects. This allows a more accurate motion control and more robust design with increased life-span compared to the fixed-tension closed-loop design alternative. This is especially important when the actuators should be situated remotely e.g. in MRI-compatible robots. Such scenarios demand longer transmission lines that undergo larger elongation due to higher flexibility. Additionally, it is possible to design open-ended wrists without use of pulleys (such as [221]) hence eliminating an important factor in reduced fatigue life.

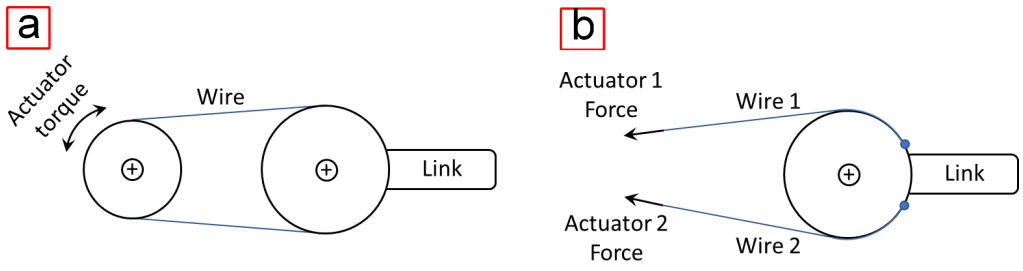

Figure 8.2: Wire transmission: (a) closed-loop, number of actuators and degrees of freedom is equal, (b) open-ended, number of actuators have to be at least one more than the number of degrees of freedom to fully control the mechanism.

In addition to more accurate motion control, such wrists can offer more accurate force sensing and control. This is due to two reasons: First, the wire forces can be directly measured with accurate load cells. Secondly, more measurements than the number of DoFs are taken into account. For example, for a single-DoF link with an open-ended actuation, two load cell measurements are required to determine an external force at the link. This 'redundancy' can provide more accurate force estimation and control. For the same reasons, stiffness modulation can be also pursued for this paradigm.

To be able to leverage the full advantages of an architecture with an open-ended wire transmission, it is important to consider the effect of wire forces in their design and analysis. The wire forces can decrease the physical workspace as it may not be feasible to counter an external force with a positive tension force at some configurations. Therefore, a *wrench-feasible workspace* should be defined where wires are guaranteed to remain in tension to balance pre-defined external loads. Furthermore, wires have a limited tensile strength. It is important to determine the maximum load bearing capabilities of these wrists under the assumption of limited wire strength. Moreover, the wire stiffness affects the positioning accuracy of these architectures. Thus, it is desired to know the *slop* of the wrist owing to the wire stiffness in the presence of external perturbations and also the propagation of wire motion errors to the positioning accuracy of the jaws.

In this chapter, a new avenue is explored that regards a thorough analysis of an open-ended wire-driven wrist for robotic MIS applications. The focus of this study is on the analysis of the architecture and the particular mechanical embodiment simply provides an example case study. Therefore, the developed tools and frameworks are general and can be applied to any open-ended wire-driven wrist.

The wrist mechanism concept was adapted and modified from [64] to design and fabricate a scaled-up wire-driven 3-DoF wrist as shown in Fig. (8.3)-a. The wrist has two parallelogram mechanisms for each of the jaws to ensure parallel grasping action incorporated with the design in [64]. This wrist has a pitch and dual-yaw (PYY) degree of

freedom and requires four linear actuation lines to drive the four wire cables. Referring to Fig. (8.3)-b, antagonistic actuation of τ_{l1},τ_{l2} and τ_{r1},τ_{r2} in pairs generates pitch motion while antagonistic actuation of τ_{l1} and τ_{l2} (τ_{r1} and τ_{r2}) yields left (right) yaw or grasping motion. Each actuator unit as shown in Fig. (8.3)-b is composed of a brushless DC motor (Maxon EC-max 22) with an encoder and a gearhead, a ball screw for linear motion generation, a load cell (Omega™, 200 N) to measure actuation force and a hook-up fixture to grip the cable wire.

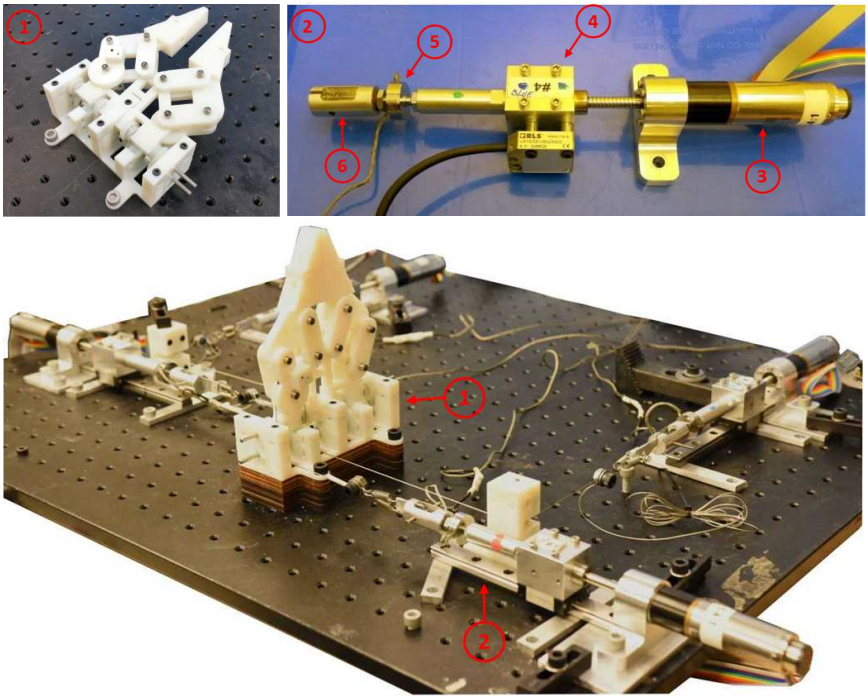

Figure 8.3: 3-DoF PYY (pitch,yaw,yaw) wrist: (1) wrist prototype. (2) Actuation module consisting of (3) brushless DC motor (Maxon EC-max 22) with an encoder and a gearhead, (4) ball-screw for linear motion generation, (5) load cell (Omega™, 200 N) to measure actuation force and (6) hook-up fixture with springs to grip the cable wire.

First, we present a review of the prior art. Then, we explain the modeling of the kinematics and the statics. We follow on analysis of positioning uncertainty due to actuator/wire errors/flexibility and homing error. A basic model is then presented for compensation of motion losses due to wires extension and backlash. We explore the workspace and characterize the wrist slop due to external perturbation. Before concluding this chapter, the maximum payload limited by wires strength is identified.

8.1 Background and Related Work

Surgery in confined spaces such as transoral, transanal and transurethral procedures requires more dexterous tools than is currently available. In multi-incision (laparoscopy) and single-incision or single-port access (SPA) surgery, the conventional instruments are no longer utilizable as the workspace is significantly smaller. Therefore, *distal dexterity* should be enhanced to assist the surgeons in accomplishing delicate tasks in confined spaces with narrow access. One way to achieve this is to use wrist mechanisms. For instance, one of the challenges encountered during the phantom studies was the difficulty in orienting the cautery loop at the tip of the MBCR. Adding a wrist with roll and pitch degrees of freedom at the end of the MBCR can remedy this issue by improving the distal dexterity of TURBot. Multi-DoF wrists are a critical component of most- if not all - of the present commercial surgical robots for MIS procedures (e.g. see Fig. (8.1)).

Developing small dexterous wrists for surgical applications has been an area of active research within the past three decades. A substantial number of the developed surgical wrists employ wire actuation or pulley-wire transmission. This paradigm offers numerous advantages that include improved miniaturization, simplified sterilization and low inertia due to remotization of actuation, backlash-free motion (if designed properly) and back-drivability. Such values have made wire actuation an integral part of the design of many surgical wrists. Liu *et al.* provided a classification of surgical wrists based on their DoFs and classified them based on roll (R), pitch (P) and yaw (Y) [222]. They also presented a partial review of the commercial and research surgical wrists up to 2016. Orekhov *et al.* conducted a thorough review of snake-like robots for MIS, SPA and intraluminal surgeries [223]. They differentiated snake-like robots against rigid robots or tools in surgery e.g. Intuitive Surgical's EndoWrist®. These robots can provide dexterous access and manipulation in confined spaces. Although they did not focus on the distal wrists, most of these snake-like robots utilize such wrists.

Open-ended wire-driven robots have been well studied in the past several decades. The different kinematic architectures of these robots can be loosely categorized as serial, parallel and hybrid. For the serial types with sufficient actuation (number of actuator is at least one more than the number of DoFs), Morecki at al discussed several issues in their bi-manual 15-DoF anthropomorphic manipulator [219]. The two most prominent robotic hands that use this architecture are Stanford/JPL hand [224,225] and Utah/MIT hand [226–228]. The first parallel wire-driven architecture was reported by Landsberger *et al.* where a 6-DoF manipulator with 6 parallel wires controlled the motion. A central 'spine' connecting the base to the moving platform provided rigidity [229]. Such architectures also knows as cable-driven parallel manipulators (CPM) have been explored comprehensively ever since. CPMs have the advantages of large workspace in contrast with classical parallel robots, high speeds and accelerations, lower inertias and relatively low costs.

In the area of open-ended wire-actuated robotic instruments in surgical applications, there are many devices and designs too numerous to mention. Le *et al.* reviewed some of the research and the commercial instruments that use this actuation scheme (and other schemes) [230]. Here, we review only a subset of the prior research which is more relevant. Wendlandt *et al.* presented a robotic platform for endoscopy applications as shown in Fig. (8.4)-a [231]. Their design was similar to a wire-driven version of a Stewart platform-Gough parallel robot. It had a spherical joint and three wires for actuation. Abdul Hamid *et al.* presented a PY universal-joint wire-driven wrist with a parallel architecture (Fig. (8.4)-b) [221]. They investigated the physical and the wrench-feasible workspace of the wrist. They also proposed and explored performance indices based on the singular values of the Jacobian. A safe wrench-closure workspace was also presented that accounted for wire extension. Liu at al performed a more detailed safe wrench-closure workspace analysis on the same wrist architecture and another one with a base roll [222]. Kilroy *et al.* presented a 3-DoF wrist shown in Fig. (8.4)-d [64]. The wrist had a pitch and dual-yaw (PYY) degrees of freedom and required four linear actuation wires. The example case in this chapter is

based on their design.

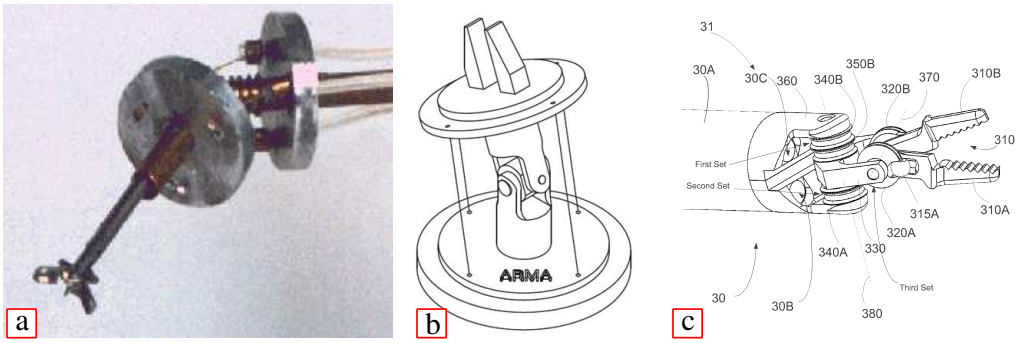

Figure 8.4: Open-ended wire-driven surgical wrists, R,P,Y stand for roll, pitch and yaw respectively: (a) Endo-platform, wire-actuated with three wires and a spherical joint [231], (b) PY wrist with a universal joint. It's possible to use 3 or more wires for actuation [221, 222], (c) PYY wrist with antagonistic actuation for pitch and pull/release pulley-wire transmission for independent yaws [64].

8.2 Kinematic Modeling

8.2.1 Direct Kinematics from Configuration Space to Task Space

Figure 8.5-a illustrates the wrist and its degrees of freedom. The wrist is a 3-DoF Pitch-Yaw-Yaw (PYY) mechanism. It is essentially composed of two PY serial kinematic chains that are coupled at the distal clevis (blue middle cross link in Fig. 8.5-a).

DH parameters are used to identify the kinematics. Accordingly, 7 frames are assigned and the pertaining DH parameters are identified as shown in Fig. 8.6 and table 8.1. Frame $\{0\}$ represents the world frame such that $\hat{\mathbf{z}}_0$ axis is aligned with the middle shaft centerline. Frame $\{1_l\}(\{1_r\})$ is attached to the distal clevis such that $\hat{\mathbf{z}}_{1l}(\hat{\mathbf{z}}_{1r})$ axis is aligned with the top left(right) pin hole centerline. It expresses the pitch of the wrist. Frame $\{2_l\}(\{2_r\}))$ is attached to the left(right) input link (grey component in Fig. 8.6) capturing the independent yaw motion generator. To move the jaws such that they always remain parallel, two parallelogram mechanisms are incorporated where the input links are actuated by two wires that are routed and terminated on the wire sheaves on the input links. These wires are shown as $\boldsymbol{\tau}_{l1}$,$\boldsymbol{\tau}_{l2}$ and $\boldsymbol{\tau}_{r1}$, $\boldsymbol{\tau}_{r2}$ for left and right input links respectively in fig. 8.5-b. The couplers of

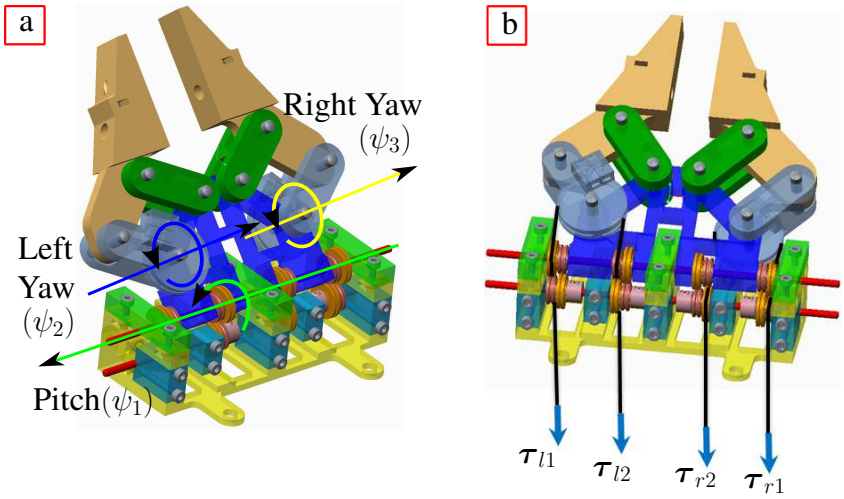

Figure 8.5: (a) Pitch and yaw definition for the wrist, (b) Wire routing: Antagonistic actuation of τ_{l1},τ_{l2} and τ_{r1},τ_{r2} in pairs generates pitch motion while antagonistic actuation of τ_{l1} and τ_{l2} (τ_{r1} and τ_{r2}) yields left (right) yaw or grasping motion.

the parallelograms constitute the wrist jaws. The motion of the jaws are captured by frames $\{g_l\}$ and $\{g_r\}$.

i	θ_i	d_i	α_i	a_i
1l	θ_1	$d_{1l} = 33.5mm$	$\frac{\pi}{2}$	$a_1 = 24\ mm$
1r	θ_1	$d_{1r} = -33.5mm$	$\frac{\pi}{2}$	$a_1 = 24\ mm$
2l	θ_{2l}	0	0	$a_2 = 28\ mm$
2r	θ_{2r}	0	0	$a_2 = 28\ mm$

Table 8.1: 3-DoF wrist frame assignments and DH parameters table

Kinematically, the wrist is composed of two serial chains, the one that ends in the left jaw and the one ending in the left jaw denoted by *lj* and *rj* respectively. These two open chains have the same kinematic model. Therefore, it suffices to derive the kinematics of the left jaw. Throughout the rest of this chapter, we will only consider *lj* chain unless otherwise mentioned. Therefore, the successive frame transformations are as follows: $\{0\} \rightarrow \{1l\} \rightarrow \{2_l\} \rightarrow \{g_l\}$. All the arguments hereafter can be equally applied to the right jaw due the geometric symmetry of the mechanism.

Based on the assigned frames, θ_1 is the rotation of $\hat{\mathbf{x}}_{1l}$ or $\hat{\mathbf{x}}_{1r}$ about $\hat{\mathbf{z}}_0$ measured from $\hat{\mathbf{x}}_0$. θ_{2r} is the rotation of $\hat{\mathbf{x}}_{2r}$ about $\hat{\mathbf{z}}_{1r}$ measured from $\hat{\mathbf{x}}_{1r}$. θ_{2l} is the rotation of $\hat{\mathbf{x}}_{2l}$ about

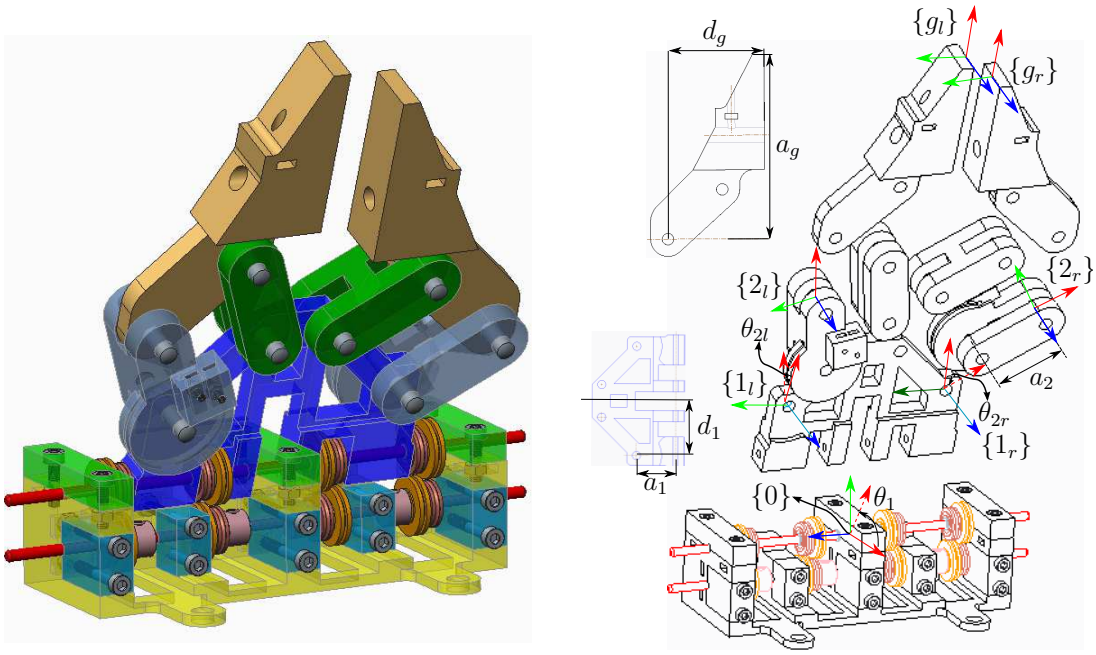

Figure 8.6: 3-DoF wrist frame assignments

$\hat{\mathbf{z}}_{1l}$ measured from $\hat{\mathbf{x}}_{1l}$. $d_{1l} = d_1 = 33.5mm$ ($d_{1r} = -d_1 = -33.5mm$) is the distance from $\hat{\mathbf{x}}_0$ to $\hat{\mathbf{x}}_{1l}$ (or $\hat{\mathbf{x}}_{1r}$) along $\hat{\mathbf{z}}_0$ direction. $d_g = 41.82mm$ and $a_g = 80mm$ are the dimensions of the jaws as shown in Fig. 8.6.

When the wrist is straight and upright (home configuration), $\boldsymbol{\theta} = [\pi/2, 0, 0]^{\mathrm{T}}$. Herein, we define *configuration vector* $\boldsymbol{\psi} \in \mathbb{R}^{3\times 1}$ such that:

$$\psi_1 \triangleq \theta_1 - \frac{\pi}{2}, \quad \psi_{2l} \triangleq \theta_{2l}, \quad \psi_{2r} \triangleq \theta_{2r} \tag{8.1}$$

Therefore, at home configuration, $\boldsymbol{\psi} = \mathbf{0}$. We will show that $\boldsymbol{\psi}$ has a linear relationship with wire displacements $\mathbf{s} \in \mathbb{R}^{4\times 1}$ in section 8.2.3.

Referring to the left jaw chain and applying successive homogeneous transformations denoted by ${}^{i-1}\mathbf{T}_i$ from the base frame to the last frame:

$${}^{0}\mathbf{T}_{g_l} = {}^{0}\mathbf{T}_{1l}\,{}^{1l}\mathbf{T}_{2l}\,{}^{2l}\mathbf{T}_{g_l} \tag{8.2}$$

where

$$ {}^{0}\mathbf{T}_{1l} = \begin{bmatrix} -s_1 & 0 & c_1 & -a_1 s_1 \\ c_1 & 0 & s_1 & a_1 c_1 \\ 0 & 1 & 0 & d_1 \\ 0 & 0 & 0 & 1 \end{bmatrix} \tag{8.3} $$

and

$$ {}^{1l}\mathbf{T}_{2l} = \begin{bmatrix} c_2 & -s_2 & 0 & a_2 c_2 \\ s_2 & c_2 & 0 & a_2 s_2 \\ 0 & 0 & 1 & 0 \\ 0 & 0 & 0 & 1 \end{bmatrix} \tag{8.4} $$

where $s_i = \sin(\psi_i)$ and $c_i = \cos(\psi_i)$. ${}^{2l}\mathbf{T}_{g_l}$ can be obtained by considering that $\{g_l\}$ always remains aligned to $\{1l\}$ due to the parallelogram mechanism. Thus:

$$ {}^{2l}\mathbf{T}_{g_l} = \begin{bmatrix} {}^{1l}\mathbf{R}_{2l}^{T} & {}^{1l}\mathbf{R}_{2l}^{T}\, {}^{g_l}\mathbf{p}_{2l,gl} \\ \mathbf{0}_{1\times 3} & 1 \end{bmatrix} \tag{8.5} $$

where ${}^{g_l}\mathbf{p}_{2l,gl} = [a_g, -d_g, 0]^{\mathrm{T}}$. After substitution:

$$ {}^{2l}\mathbf{T}_{g_l} = \begin{bmatrix} c_2 & s_2 & 0 & a_g c_2 - d_g s_2 \\ -s_2 & c_2 & 0 & -a_g s_2 - d_g c_2 \\ 0 & 0 & 1 & 0 \\ 0 & 0 & 0 & 1 \end{bmatrix} \tag{8.6} $$

This leads to the following transformation for the left jaw:

$$ {}^{0}\mathbf{T}_{2l} = \begin{bmatrix} -c_2 s_1 & s_1 s_2 & c_1 & -s_1(a_1 + a_2 c_2) \\ c_1 c_2 & -c_1 s_2 & s_1 & c_1(a_1 + a_2 c_2) \\ s_2 & c_2 & 0 & d_1 + a_2 s_2 \\ 0 & 0 & 0 & 1 \end{bmatrix} \tag{8.7} $$

and :

$$ {}^{0}\mathbf{T}_{g_l} = \begin{bmatrix} -s_1 & 0 & c_1 & -s_1(a_1 + a_g + a_2 c_2) \\ c_1 & 0 & s_1 & c_1(a_1 + a_g + a_2 c_2) \\ 0 & 1 & 0 & d_1 - d_g + a_2 s_2 \\ 0 & 0 & 0 & 1 \end{bmatrix} \tag{8.8} $$

The direct kinematics of the right jaw is presented in Appendix C.

8.2.2 Instantaneous Kinematics from Configuration Space to Task Space

In this section, we wish to determine the jaws twists given the configuration rates. To start, let us focus on the left jaw and define $\dot{\boldsymbol{\psi}}_l \triangleq [\dot{\boldsymbol{\psi}}_1, \dot{\boldsymbol{\psi}}_{2l}]^{\mathrm{T}} \in \mathbb{R}^{2\times 1}$ as the left jaw configuration vector rates and $\dot{\mathbf{x}}_{g_l} = [\mathbf{v}_{g_l}^{\mathrm{T}}, \boldsymbol{\omega}_{g_l}^{\mathrm{T}}]^{\mathrm{T}} \in \mathbb{R}^{6\times 1}$ as its associated twist. The problem is then to determine the mapping between these two vector spaces.

Using standard Jacobian derivation for a serial robot, the instantaneous kinematics of the left jaw serial chain from $\{0\}$ to $\{2_l\}$ is:

$$ \mathbf{J}_{x_{2l}\psi_l} \dot{\boldsymbol{\psi}}_l = \dot{\mathbf{x}}_{2l} \tag{8.9} $$

where $\dot{\mathbf{x}}_{2l} = [\mathbf{v}_{2_l}^{\mathrm{T}}, \boldsymbol{\omega}_{2_l}^{\mathrm{T}}]^{\mathrm{T}} \in \mathbb{R}^{6\times 1}$ is the associated twist of $\{2_l\}$. The Jacobian $\mathbf{J}_{x_{2l}\psi_l} \in \mathbb{R}^{6\times 2}$ is given by:

$$ \mathbf{J}_{x_{2l}\psi_l} = \begin{bmatrix} \mathbf{J}_{v_{2l}} \\ \mathbf{J}_{\omega_{2l}} \end{bmatrix} \tag{8.10} $$

where $\mathbf{J}_{v_{2l}}$ and $\mathbf{J}_{\omega_{2l}}$ are the translational and rotational Jacobians, respectively. These Jacobians are expressed as the following:

$$ \mathbf{J}_{v_{2l}} = \begin{bmatrix} -c_1(a_1 + a_2 c_2) & a_2 s_1 s_2 \\ -s_1(a_1 + a_2 c_2) & -a_2 c_1 s_2 \\ 0 & a_2 c_2 \end{bmatrix} \tag{8.11} $$

and,

$$\mathbf{J}_{\omega_{2l}} = \begin{bmatrix} 0 & c_1 \\ 0 & s_1 \\ 1 & 0 \end{bmatrix} \tag{8.12}$$

Next step is to determine the left jaw twist given $\dot{\mathbf{x}}_{2l}$ and $\dot{\boldsymbol{\psi}}_l$. The linear velocity is as follows:

$$\mathbf{v}_{g_l} = \mathbf{v}_{2l} + \boldsymbol{\omega}_{g_l} \times \boldsymbol{\rho}_{2_l,g_l} \tag{8.13}$$

where $\boldsymbol{\rho}_{2_l,g_l} = {}^0\mathbf{R}_{g_l}\, {}^{g_l}\boldsymbol{\rho}_{2_l,g_l}$ such that ${}^{g_l}\boldsymbol{\rho}_{2_l,g_l} = [a_g, -d_g, 0]$ is the vector joining the origin of $\{2_l\}$ to the origin of $\{g_l\}$. Substituting from Eq. (8.9) for $\mathbf{v}_{2l}$ and collecting terms and abstracting in a matrix form results in:

$$\mathbf{J}_{v_{2l}}\dot{\boldsymbol{\psi}}_l = [\mathbf{I}_3, (\boldsymbol{\rho}_{2_l,g_l})^\wedge]\, \dot{\mathbf{x}}_{g_l} \tag{8.14}$$

where $\mathbf{x}^\wedge$ denotes the cross-product matrix of vector $\mathbf{x}$. The angular velocity of the left jaw is:

$$\boldsymbol{\omega}_{g_l} = \boldsymbol{\omega}_{g_l/2_l} + \boldsymbol{\omega}_{2l} \tag{8.15}$$

In the above equations, $\boldsymbol{\omega}_{g_l/2_l} = -\dot{\boldsymbol{\psi}}_{2l}{}^0\mathbf{R}_{2l}\hat{\mathbf{k}}$ and $\hat{\mathbf{k}} \triangleq [0,0,1]^{\mathrm{T}}$ from the relative angular motion of the left jaw with respect to $\{2_l\}$. Substituting from Eq. (8.9) for $\boldsymbol{\omega}_{2l}$ and abstracting in a matrix form results in:

$$(\mathbf{J}_{\omega_{2l}} - {}^0\mathbf{R}_{2l}\hat{\mathbf{k}}\mathbf{s})\dot{\boldsymbol{\psi}}_l = [\mathbf{0}_3, \mathbf{I}_3]\, \dot{\mathbf{x}}_{g_l} \tag{8.16}$$

where $\mathbf{s} = [0,1]$. Finally, putting Eq. (8.14) and (8.16) together results in the Jacobian

of the left jaw:

$$\begin{aligned}
&\mathbf{M}_l\dot{\boldsymbol{\psi}}_l = \mathbf{N}_l\dot{\mathbf{x}}_{g_l},\\
&\mathbf{M}_l = \begin{bmatrix} \mathbf{J}_{\mathbf{v}_{2l}} \\ \mathbf{J}_{\boldsymbol{\omega}_{2l}} - {}^0\mathbf{R}_{2l}\hat{\mathbf{k}}\mathbf{s} \end{bmatrix} \in \mathbb{R}^{6\times 2}, \mathbf{N}_l = \begin{bmatrix} \mathbf{I}_3 & (\boldsymbol{\rho}_{2_l,g_l})^\wedge \\ \mathbf{0}_3 & \mathbf{I}_3 \end{bmatrix} \in \mathbb{R}^{6\times 6}
\end{aligned} \tag{8.17}$$

The above equation can be simplified by left-multiplying the inverse of the upper block-diagonal matrix $\mathbf{N}_l$ into the following equation:

$$\begin{aligned}
&\mathbf{J}_l\dot{\boldsymbol{\psi}}_l = \dot{\mathbf{x}}_{g_l},\\
&\mathbf{J}_l = \begin{bmatrix} \mathbf{J}_{v,l} \\ \mathbf{J}_{\omega,l} \end{bmatrix} \in \mathbb{R}^{6\times 2},\\
&\mathbf{J}_{v,l} = \mathbf{J}_{\mathbf{v}_{2l}} - (\boldsymbol{\rho}_{2_l,g_l})^\wedge (\mathbf{J}_{\boldsymbol{\omega}_{2l}} - {}^0\mathbf{R}_{2l}\hat{\mathbf{k}}\mathbf{s}),\\
&\mathbf{J}_{\omega,l} = \mathbf{J}_{\boldsymbol{\omega}_{2l}} - {}^0\mathbf{R}_{2l}\hat{\mathbf{k}}\mathbf{s}
\end{aligned} \tag{8.18}$$

Direct substitution into Eq. (8.18) and algebraic simplifications leads to the following formulations for the Jacobians of the left jaw of the 3-DoF wrist:

$$\mathbf{J}_{v,l} = \begin{bmatrix} -c_1(a_1 + a_g + a_2c_2) & a_2s_1s_2 \\ -s_1(a_1 + a_g + a_2c_2) & -a_2c_1s_2 \\ 0 & a_2c_2 \end{bmatrix} \tag{8.19}$$

and,

$$\mathbf{J}_{\omega,l} = \begin{bmatrix} 0 & 0 \\ 0 & 0 \\ 1 & 0 \end{bmatrix} \tag{8.20}$$

The Jacobian of the right jaw serial chain is obtained by adopting the same approach. We will not repeat the formulation for brevity. The reader is referred to Appendix C for more details.

8.2.3 Kinematic Relationship Between Wire Displacement and Configuration Space

Up to this point, the derivations have related task space twist (jaw linear and angular velocities) with the rates of configuration variables describing the serially articulated structure of the wrist. For control of the wrist, the mapping between the configuration variables and the actuation wire lengths is needed. This section presents the derivation of this mapping. This mapping depends on the wire routing topology and pulley diameters. In the subsequent derivations, fleet angles are assumed zero at all configurations of the wrist.

8.2.3.1 Calculation of Wire Wrap Angles

In order to determine the wire wrap angle on a pulley, the tangency constraint of the wire and pulley is used. Fig. 8.7 illustrates two pulleys 1 and 2. We assume that pulley 1 represents the middle pulley and pulley 2 represents the proximal pulley[1]. We also define wire forces $\boldsymbol{\tau}_a$ (actuation force) and $\boldsymbol{\tau}_j$ (jaw force) and the geometric parameters shown in the figure.

Referring to Fig. 8.7, the wrap angles of pulleys 1 and 2 are:

$$\psi_{w,1} \triangleq \alpha_1 + \phi, \qquad \psi_{w,2} \triangleq \alpha_2 + \phi \tag{8.21}$$

where

$$\alpha_1 = \begin{cases} +\psi_1 & \text{for wires } l_1, l_2 \\ -\psi_1 & \text{for wires } r_1, r_2 \end{cases} \tag{8.22}$$

ϕ is determined using the similarity of the two triangles $o_1 \overset{\triangle}{t_{1a}} t_m$ and $o_2 \overset{\triangle}{t_{2b}} t_m$ in Fig. 8.7,

$$\phi = \arcsin\left(\frac{r_1 + r_2}{c}\right) \tag{8.23}$$

[1]The term proximal refers to proximity to the actuation unit and distal refers to proximity to the jaw tip

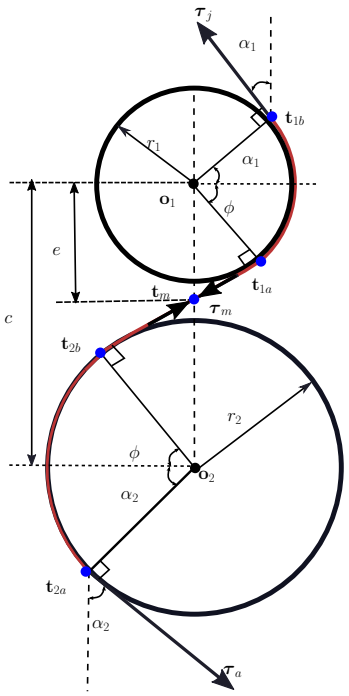

Figure 8.7: Geometry of pulley-wire system. Two arbitrary pulleys 1 and 2 are shown.

where $c = \overline{\mathbf{o}_1\mathbf{o}_2}$ is the center-to-center distance of the two pulleys.

8.2.3.2 Kinematics of Wire Displacement

Figure 8.8-a and b show the wrist wire and pulley numbers assignment. The wires are numbered as l_1, l_2, r_1 and r_2 where l and r denotes left and right jaw respectively. Let us consider a general wire routing. The underlying assumption is that the wire stiffness is infinitely large, hence its length remains constant. The fleet angle is assumed negligible.

Figure 8.9-a and b illustrate a schematic diagram of the wire l_2 at home configuration and at an arbitrary configuration respectively. The wire is shown by the red color. The dashed red lines mean that the wire is at the back of the pulley. The wire length at home configuration is

$$l^* = r_{d,l2}\frac{\pi}{2} + c_1 + r_1\psi^*_{w,m_{l2}} + (r_{m,l2} + r_{p,l2})\cot(\phi) + r_{p,l2}\psi^*_{w,p_{l2}} + l_{extra} \tag{8.24}$$

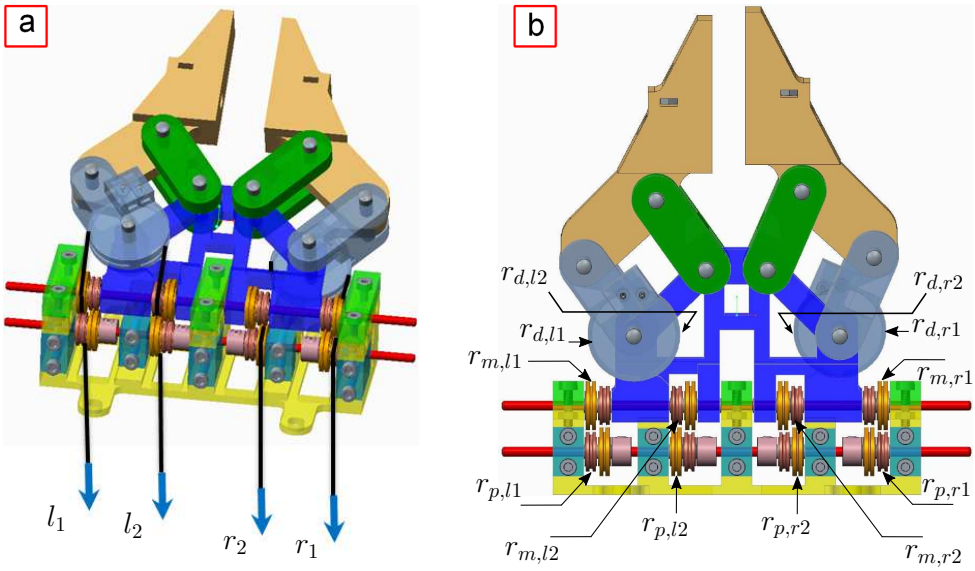

Figure 8.8: Number assignments for: (a) wire routes (l and r denotes left and right jaw respectively), (b) pulleys, (d, m and p denotes distal, middle and proximal respectively)

$\psi^*_{w,m_{l2}} = \psi^*_{w,p_{l2}} = \phi$ and ϕ is brought in Eq. (8.23). l_{extra} is the length from pulley p_{l2} tangent point to the end of the wire at the actuation capstan. Based on Fig. 8.9-b, the length of the wire at an arbitrary configuration is

$$l = r_{d,l2}(\frac{\pi}{2} + \psi_{2l}) + c_1 + r_{m,l2}\psi_{w,m_{l2}} + (r_{m,l2} + r_{p,l2})\cot(\phi) + r_2\psi^*_{w,p_{l2}} + l_{extra} + s_{l2} \quad (8.25)$$

But, based on Fig. 8.9-b,

$$\psi_{w,m_{l2}} = \psi^*_{w,m_{l2}} + \psi_1 \quad (8.26)$$

Substituting (8.26) in (8.25) and assuming that the wire extension remains constant (i.e. no significant change in external load) then the wire length remains constant i.e. $l = l^*$, thus the corresponding amount of joint travel[2] is given by:

$$s_{l2} = -r_{m,l2}\psi_1 - r_{d,l2}\psi_{2l} \quad (8.27)$$

[2]We assume the actuation unit pulls on the wires and we disregard the particular embodiment of the actuation unit.

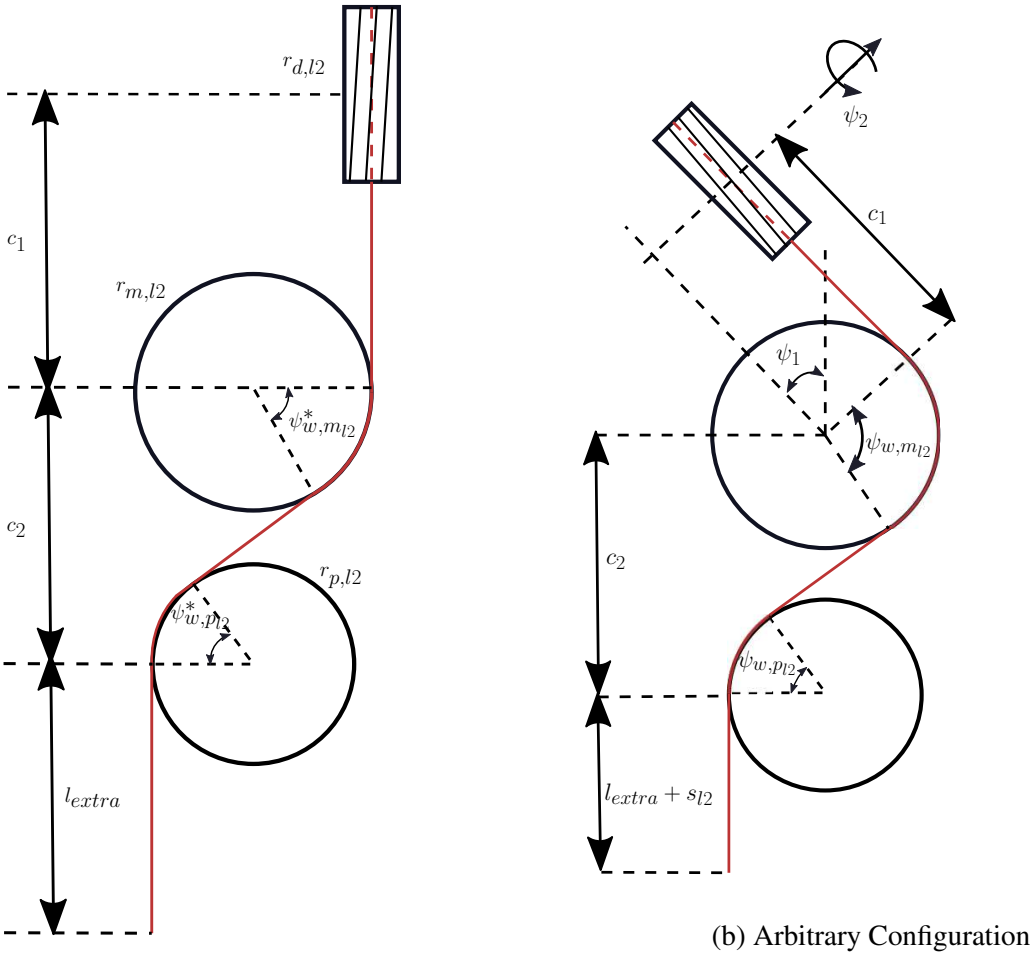

(a) Home Configuration

(b) Arbitrary Configuration

Figure 8.9: Displacement of a wire routing of the wrist

This procedure can be applied to the four transmission wires in Fig. (8.8-a). Therefore, the following four equations are ensued,

$$\begin{aligned} s_{l1} &= -r_{m,l1}\psi_1 + r_{d,l1}\psi_{2l}, \\ s_{l2} &= -r_{m,l2}\psi_1 - r_{d,l2}\psi_{2l}, \\ s_{r1} &= +r_{m,r1}\psi_1 - r_{d,r1}\psi_{2r}, \\ s_{r2} &= +r_{m,r2}\psi_1 + r_{d,r2}\psi_{2r} \end{aligned} \tag{8.28}$$

Equation (8.28) can be abstracted in the matrix format:

$$\mathbf{s} = \mathbf{A}\boldsymbol{\psi} \tag{8.29}$$

where $\mathbf{s} = [s_{l1}, s_{l2}, s_{r1}, s_{r2}]^{\mathrm{T}} \in \mathbb{R}^{4\times 1}$, $\boldsymbol{\psi} = [\psi_1, \psi_{2l}, \psi_{2r}]^{\mathrm{T}} \in \mathbb{R}^{3\times 1}$ and

$$\mathbf{A} = \begin{bmatrix} -r_{m,l1} & +r_{d,l1} & 0 \\ -r_{m,l2} & -r_{d,l2} & 0 \\ +r_{m,r1} & 0 & -r_{d,r1} \\ +r_{m,r2} & 0 & +r_{d,r2} \end{bmatrix} \tag{8.30}$$

Equation (8.29) is well-known in tendon-driven mechanisms literature (e.g. [218]) and the structural characteristics of the matrix $\mathbf{A}$ and methods to guarantee positive wire tensions have been well studied ([232–235]). This equation provides a linear mapping between configuration and joint speeds and is used for the wrist control.

8.3 Static Modeling

In this section, the static equation is derived in details for the 3-DoF wrist. Let us assume that the wrist resists the forces $f_{e,x_{gl}}, f_{e,y_{gl}}, f_{e,z_{gl}}$ and $f_{e,x_{gr}}, f_{e,y_{gr}}, f_{e,z_{gr}}$ on the left and the right jaws respectively as shown in Fig. (8.10). All the external forces on the wrist that are predominantly generated by actuating forces by the wires are included in the above mentioned forces. These forces include the grasping, the lateral and axial forces. All the external forces/moments are purely counteracted by constraint forces and hence are not considered. These generalized forces can be abstracted in a vector form as:

$$\mathbf{f}_{ee} \triangleq \left[f_{e,x_{gl}}, f_{e,y_{gl}}, f_{e,z_{gl}}, f_{e,x_{gr}}, f_{e,y_{gr}}, f_{e,z_{gr}}\right]^{\mathrm{T}} \tag{8.31}$$

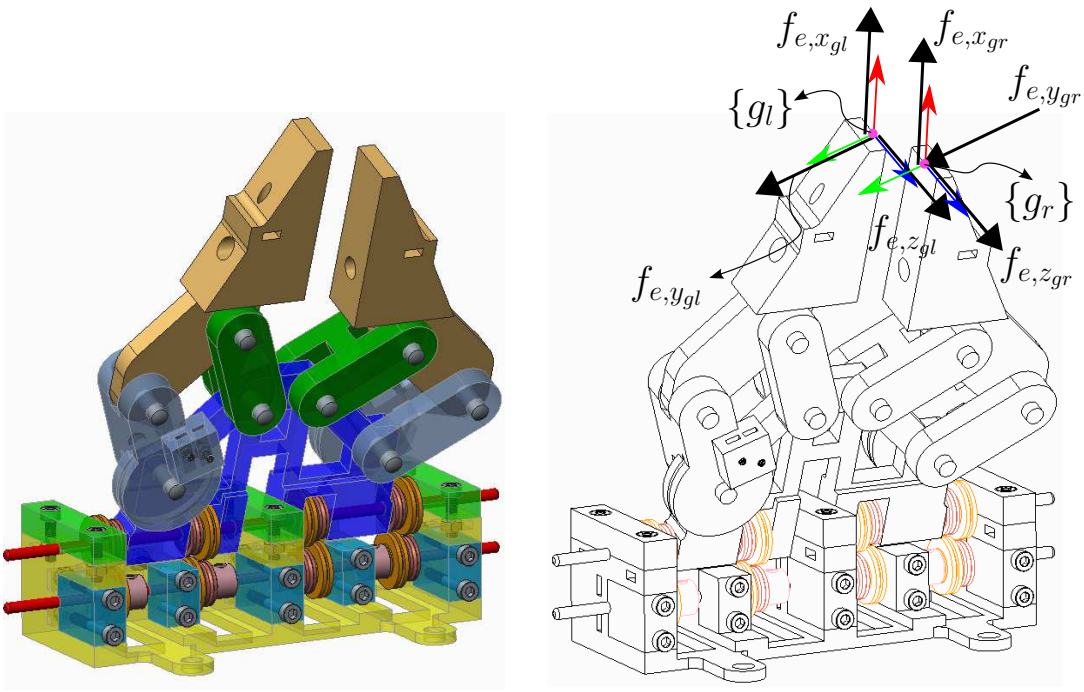

Figure 8.10: Forces at jaws tips. $\{f_{e,x_{gl}}, f_{e,x_{gr}}\}$,$\{f_{e,y_{gl}}, f_{e,y_{gr}}\}$ and $\{f_{e,z_{gl}}, f_{e,z_{gr}}\}$ are axial, grasping and lateral forces of left and right jaws respectively.

It is desired to obtain the Jacobian that maps actuation forces $\boldsymbol{\tau} = [\tau_{l1}, \tau_{l2}, \tau_{r1}, \tau_{r2}]^{\mathrm{T}} \in \mathbb{R}^{4\times 1}$ to the external wrench $\mathbf{f}_{ee}$. To find this Jacobian, the principle of virtual work is applied first:

$$\boldsymbol{\tau}^{\mathrm{T}}\mathbf{A}\delta\boldsymbol{\psi} + {}^{g_l}\mathbf{f}_{ee,l}^{\mathrm{T}}\,{}^{g_l}\delta\mathbf{p}_{g_l} + {}^{g_r}\mathbf{f}_{ee,r}^{\mathrm{T}}\,{}^{g_r}\delta\mathbf{p}_{g_r} = 0 \tag{8.32}$$

${}^{g_l}\mathbf{f}_{ee,l}$ and ${}^{g_r}\mathbf{f}_{ee,r}$ are the vector of forces applied on the right and left jaws described in their local frames $\{g_l\}$ and $\{g_r\}$ respectively. Thus:

$$\begin{aligned} {}^{g_l}\mathbf{f}_{ee,l} &= [f_{e,x_{gl}}, f_{e,y_{gl}}, f_{e,z_{gl}}]^{\mathrm{T}} \\ {}^{g_r}\mathbf{f}_{ee,r} &= [f_{e,x_{gr}}, f_{e,y_{gr}}, f_{e,z_{gr}}]^{\mathrm{T}} \end{aligned} \tag{8.33}$$

Therefore,

$$\begin{aligned} {}^{g_l}\mathbf{f}_{ee,l} &= \mathbf{S}_{1l}\mathbf{f}_{ee} \\ {}^{g_r}\mathbf{f}_{ee,r} &= \mathbf{S}_{1r}\mathbf{f}_{ee} \end{aligned} \tag{8.34}$$

where,

$$\mathbf{S}_{1l} = [\mathbf{I}_3, \mathbf{0}_3]\,,\ \mathbf{S}_{1r} = [\mathbf{0}_3, \mathbf{I}_3] \tag{8.35}$$

On the other hand,

$$\begin{aligned} {}^{0}\mathbf{R}_{g_l}^{\mathrm{T}}\,\mathbf{J}_{v,l}\delta\boldsymbol{\psi}_l &=^{g_l} \delta\mathbf{p}_{g_l} \\ {}^{0}\mathbf{R}_{g_r}^{\mathrm{T}}\,\mathbf{J}_{v,r}\delta\boldsymbol{\psi}_r &=^{g_r} \delta\mathbf{p}_{g_r} \end{aligned} \tag{8.36}$$

where $\mathbf{J}_{v,l} = [\mathbf{I}_3, \mathbf{0}_3]\,\mathbf{J}_l$ and $\mathbf{J}_{v,r} = [\mathbf{I}_3, \mathbf{0}_3]\,\mathbf{J}_r$ are the translational Jacobian components of $\mathbf{J}_l$ and $\mathbf{J}_r$ formulated in Eqs (8.18) and (C.4). $\delta\boldsymbol{\psi}_l$ and $\delta\boldsymbol{\psi}_r$ can be expressed as

$$\begin{aligned} \delta\boldsymbol{\psi}_l &= \mathbf{S}_l\delta\boldsymbol{\psi} \\ \delta\boldsymbol{\psi}_r &= \mathbf{S}_r\delta\boldsymbol{\psi} \end{aligned} \tag{8.37}$$

where,

$$\mathbf{S}_l = \begin{bmatrix} 1 & 0 & 0 \\ 0 & 1 & 0 \end{bmatrix}, \mathbf{S}_r = \begin{bmatrix} 1 & 0 & 0 \\ 0 & 0 & 1 \end{bmatrix} \tag{8.38}$$

Substitution of Eq. (8.37) in Eq. (8.36) and Eq (8.34) and (8.36) in virtual work Eq (8.32) and transposing gives:

$$\mathbf{A}^{\mathrm{T}}\boldsymbol{\tau} = -\mathbf{C}^{\mathrm{T}}\mathbf{f}_{ee} \tag{8.39}$$

where $\mathbf{C} \in \mathbb{R}^{6\times 3}$ is:

$$\mathbf{C} \triangleq \mathbf{S}_{1l}^{\mathrm{T}}\,{}^{0}\mathbf{R}_{g_l}^{\mathrm{T}}\mathbf{J}_{v,l}\mathbf{S}_l + \mathbf{S}_{1r}^{\mathrm{T}}\,{}^{0}\mathbf{R}_{g_r}^{\mathrm{T}}\mathbf{J}_{v,r}\mathbf{S}_r \tag{8.40}$$

Eq (8.39) can be also reformatted into the canonical form:

$$\mathbf{J}^{\mathrm{T}}\boldsymbol{\tau} = -\mathbf{f}_{ee} \tag{8.41}$$

where $\mathbf{J} \in \mathbb{R}^{4\times 6} \triangleq \mathbf{A}\mathbf{C}^{+}$.

8.4 Stiffness Modeling

Referring back to equation (8.39), the *configuration moment* denoted by $\mathbf{m}_\psi$ is as follows:

$$\mathbf{m}_\psi = \mathbf{A}^{\mathrm{T}}\boldsymbol{\tau} \tag{8.42}$$

we use the definition of the configuration space stiffness as:

$$\mathbf{K}_\psi \triangleq \frac{\partial \mathbf{m}_\psi}{\partial \boldsymbol{\psi}} \tag{8.43}$$

Using these definitions we obtain:

$$\mathbf{K}_\psi = \underbrace{\frac{\partial \mathbf{A}^{\mathrm{T}}}{\partial \boldsymbol{\psi}}\boldsymbol{\tau}}_{\text{active stiffness}} + \underbrace{\mathbf{A}^{\mathrm{T}}\frac{\partial \boldsymbol{\tau}}{\partial \boldsymbol{\psi}}}_{\text{passive stiffness}} \tag{8.44}$$

The active stiffness term is negligible and hence ignored. Using the wire stiffness matrix $\mathbf{K}_d = \mathit{diag}(k_{l1}, k_{l2}, k_{r1}, k_{r2})$ and considering $\frac{\partial \boldsymbol{\tau}}{\partial \boldsymbol{\psi}} = \mathbf{K}_d \frac{\partial \mathbf{s}}{\partial \boldsymbol{\psi}}$ and Eq. (8.29), we obtain:

$$\mathbf{K}_\psi = \mathbf{A}^{\mathrm{T}}\mathbf{K}_d\mathbf{A} \tag{8.45}$$

The passive stiffness is a characteristic of the wires and the wrist architecture. This formulation is used in section (8.8) to determine the slop of the wrist due to external perturbations.

8.5 Analysis of Positioning Uncertainty

In this section, we investigate the effect of two sources of error on the positioning accuracy of the wrist. The first source of error is on the wires displacements. The effect of this error is investigated through the attributed Jacobians that relate the infinitesimal motions in the joint space (space of wires displacements) to the infinitesimal motions in the

jaws position space. The second source of error originates from the error in homing. We show that this error is propagated throughout the configuration space of the wrist by the choice of the control algorithm (resolved rates) and a bias term due to the initial homing error. Note that only the left jaw of the the 3-DoF wrist is considered in the subsequent analyses. However, the same analyses can be applied for the right jaw.

8.5.1 Left Jaw Positioning Error Associated with Wire Displacement Uncertainty

It is desired to determine the error in the left jaw pose error due to the error at the actuation level i.e. wire displacement error. To achieve this, the Jacobian relationships between the configuration space and task space (Eq. (8.18)) and the joint space and configuration space (Eq. (8.29)) are used.

Orientation Error

Eq. (8.29) and (8.30) can be used to obtain the orientation error caused by wire displacement error:

$$\delta\boldsymbol{\psi} = \mathbf{A}^{+}\delta\mathbf{s} \tag{8.46}$$

where $\delta\mathbf{s} = [\delta s_{l1}, \delta s_{l2}, \delta s_{r1}, \delta s_{r2}]^{\mathrm{T}}$ is the joint-level error. Table (8.2) represents the pitch and the left/right jaw yaw errors due to several wire displacement error vectors. These values only serve as an estimates since $\delta\boldsymbol{\psi}$ from Eq. (8.46) is a least-norm solution.

Position Error

Referring to Eq. (8.29) and (8.30), and using the two left columns of $\mathbf{A}$ (since only the pitch and the left jaw yaw are considered), the following equation can be derived:

$$\delta\boldsymbol{\psi}_l = \mathbf{A}_l^{+}\delta\mathbf{s} \tag{8.47}$$

where $\mathbf{A}_l$ is the structure matrix associated with the left jaw and thus:

$$\mathbf{A}_l = \begin{bmatrix} -r_{m,l1} & +r_{d,l1} \\ -r_{m,l2} & -r_{d,l2} \\ +r_{m,r1} & 0 \\ +r_{m,r2} & 0 \end{bmatrix} \tag{8.48}$$

Then, using Eq. (8.47) in combination with Eq. (8.18), the following equation is obtained that is used to determine the sought error:

$$\delta \mathbf{p}_{g_l} = \mathbf{J}_{v_l,s} \delta \mathbf{s} \tag{8.49}$$

where $\delta \mathbf{p}_{g_l}$ is the position error of the left jaw tip and $\mathbf{J}_{v_l,s} \in \mathbb{R}^{3\times 4}$ is given by:

$$\mathbf{J}_{v_l,s} \triangleq \mathbf{J}_{v_l} \mathbf{A}_l^{+} \tag{8.50}$$

Table (8.2) represents the left jaw position error due to several wire displacement error vectors. Let us reiterate that these values only serve as an estimates since $\delta \boldsymbol{\psi}_l$ from Eq. (8.47) is a least-norm solution.

Table 8.2: Pose error due to wire displacements error

$\delta \mathbf{s}$ (mm)	**Pitch Error (degree)**	**Left Yaw Error(degree)**	**Right Yaw Error(degree)**	**Max Left Jaw Position Error(mm)**
$[0.5, 0.5, 0.3, 0.3]^{\mathrm{T}}$	0.8	0.4	0.4	1.8
$[0.3, 0.5, 0.3, 0.5]^{\mathrm{T}}$	0.0	0.4	0.4	0.2
$[1.0, 1.0, 0.5, 0.5]^{\mathrm{T}}$	2.0	0.1	0.1	4.6
$[0.5, 1.0, 0.5, 1.0]^{\mathrm{T}}$	0.0	1.0	1.0	0.5
$[0.8, 0.5, 1.0, 0.3]^{\mathrm{T}}$	0.0	0.6	1.3	0.5
$[0.4, 0.7, 1.0, 0.4]^{\mathrm{T}}$	0.6	0.5	1.1	1.7

8.5.2 Left Jaw Positioning Error Associated with Uncertainty in Home Configuration

In this section, the purpose is to draw an analytical derivation that offers a bound on the positioning accuracy of the left jaw assuming that the only source of uncertainty is in home

configuration.

Analysis

The analysis depends on the choice of the applied control method. A natural choice is the resolved rates method where an error feedback is used in the Jacobian equation to guarantee convergence of the positioning error. Briefly, $\dot{\boldsymbol{\psi}}_l$ is chosen as

$$\dot{\boldsymbol{\psi}}_l = \mathbf{J}_{v,l}^{+}(\mathbf{v}_{lg,des} + \mathbf{K}_p \mathbf{e}_{lg}) \tag{8.51}$$

$\mathbf{J}_{v,l}$ was brought in Eq. (8.18), $\mathbf{K}_p \in \mathbb{R}^{3\times 3} > 0$ and $\mathbf{e}_{lg} \triangleq \mathbf{p}_{lg,des} - \mathbf{p}_{lg}^{\#}$ is the positioning error of the left jaw where $.^{\#}$ designates perturbed home configuration $\boldsymbol{\psi}_l^*$ i.e. $\boldsymbol{\psi}_l^{\#} \triangleq \boldsymbol{\psi}_l^* + \delta\boldsymbol{\psi}_l^*$. Exponential convergence emerges by substituting the above equation in the instantaneous kinematic model $\mathbf{J}_{v,l}\dot{\boldsymbol{\psi}}_l = \mathbf{v}_{lg}$ from Eq. (8.18):

$$\dot{\mathbf{e}}_{lg} + \mathbf{K}_p \mathbf{e}_{lg} = 0 \tag{8.52}$$

Following this method, controlling the wrist (left jaw) starts by homing it first. Assume the desired position of the left jaw tip is $\mathbf{p}_{lg,des}$ and $\mathbf{v}_{lg,des} = 0$. Applying Eq (8.51) gives,

$$\mathbf{J}_{v,l}(\boldsymbol{\psi}_l^*)\dot{\boldsymbol{\psi}}_l = \mathbf{K}_p(\mathbf{p}_{lg,des} - \mathbf{p}_{lg}^*) \tag{8.53}$$

In the presence of homing configuration error denoted by $\delta\boldsymbol{\psi}_l^*$, the instantaneous kinematics is,

$$\mathbf{J}_{v,l}(\boldsymbol{\psi}_l^* + \delta\boldsymbol{\psi}_l^*)\dot{\boldsymbol{\psi}}_l = \mathbf{v}_{lg}^{\#} \tag{8.54}$$

From (8.53),(8.54) and application of first-order Taylor series expansion,

$$\mathbf{K}_p(\mathbf{p}_{lg,des} - \mathbf{p}_{lg}^*) - \mathbf{v}_{lg}^{\#} = -\frac{\partial \mathbf{J}_{v,l}}{\partial \boldsymbol{\psi}_l}(\boldsymbol{\psi}_l^*)\delta\boldsymbol{\psi}_l^* \mathbf{J}_{v,l}^{+}(\boldsymbol{\psi}_l^*)\mathbf{K}_p(\mathbf{p}_{lg,des} - \mathbf{p}_{lg}^*) \tag{8.55}$$

Let $\mathbf{p}_{lg}^{\#} \triangleq \mathbf{p}_{lg}(\boldsymbol{\psi}_l^* + \delta\boldsymbol{\psi}_l^*)$. Thus,

$$\dot{\mathbf{e}}_{lg} + \mathbf{K}_p\mathbf{e}_{lg} = -\mathbf{K}_p(\mathbf{p}_{lg}^{\#} - \mathbf{p}_{lg}^*) - \frac{\partial \mathbf{J}_{v,l}}{\partial \boldsymbol{\psi}_l}(\boldsymbol{\psi}_l^*)\delta\boldsymbol{\psi}_l^*\mathbf{J}_{v,l}^+(\boldsymbol{\psi}_l^*)\mathbf{K}_p(\mathbf{p}_{lg,des} - \mathbf{p}_{lg}^*) \tag{8.56}$$

$\mathbf{p}_{lg}^{\#}$ can be estimated by application of first-order Taylor series expansion,

$$\mathbf{p}_{lg}^{\#} = \mathbf{p}_{lg}^* + \mathbf{J}_{v,l}(\boldsymbol{\psi}_l^*)^{\mathrm{T}}\delta\boldsymbol{\psi}_l^* \tag{8.57}$$

Substituting (8.57) back into (8.56),

$$\dot{\mathbf{e}}_{lg} + \mathbf{K}_p\mathbf{e}_{lg} = -\mathbf{K}_p\mathbf{J}_{v,l}(\boldsymbol{\psi}_l^*)^{\mathrm{T}}\delta\boldsymbol{\psi}_l^* - \frac{\partial \mathbf{J}_{v,l}}{\partial \boldsymbol{\psi}_l}(\boldsymbol{\psi}_l^*)\delta\boldsymbol{\psi}_l^*\mathbf{J}_{v,l}^+(\boldsymbol{\psi}_l^*)\mathbf{K}_p(\mathbf{p}_{lg,des} - \mathbf{p}_{lg}^*) \tag{8.58}$$

The error in tip positioning due to the error in homing is the steady-state solution of the above equation as follows:

$$\mathbf{e}_{lg_{ss}} = -\mathbf{J}_{v,l}(\boldsymbol{\psi}_l^*)^{\mathrm{T}}\delta\boldsymbol{\psi}_l^* - \mathbf{K}_p^{-1}\frac{\partial \mathbf{J}_{v,l}}{\partial \boldsymbol{\psi}_l}(\boldsymbol{\psi}_l^*)\delta\boldsymbol{\psi}_l^*\mathbf{J}_{v,l}^+(\boldsymbol{\psi}_l^*)\mathbf{K}_p(\mathbf{p}_{lg,des} - \mathbf{p}_{lg}^*) \tag{8.59}$$

The first term in Eq (8.59) is a bias term because of initial configuration error $(\mathbf{p}_{lg}^{\#} - \mathbf{p}_{lg}^*)$ and the second term is the propagation of error due to the resolved rates algorithm. From Eq (8.59), an upper bound on the magnitude of position error can be determined.

$$\|\mathbf{e}_{lg_{ss}}\| \leq \left(\|\mathbf{J}_{v,l}(\boldsymbol{\psi}_l^*)\| + \|\frac{\partial \mathbf{J}_{v,l}}{\partial \boldsymbol{\psi}_l}(\boldsymbol{\psi}_l^*)\|_{\mathcal{F}}\|\mathbf{J}_{v,l}^+(\boldsymbol{\psi}_l^*)\|\|\mathbf{p}_{lg,des} - \mathbf{p}_{lg}^*\|\right)\|\delta\boldsymbol{\psi}_l^*\| \tag{8.60}$$

where $\|.\|$ is the Euclidean or associated induced norm and $\|.\|_{\mathcal{F}}$ is the Frobenius norm. However, this upper bound may be overconservative, therefore it is recommended to apply Eq (8.59) to find the position error as shown in the proceeding example.

An Example

Let us assume that there is 1 degree error in the pitch and the left yaw angle of the

3-DoF wrist due to homing. i.e.

$$\delta\boldsymbol{\psi}_l^* = (\pi/180)[1,1]^{\mathrm{T}} \tag{8.61}$$

This error may stem from limit switches or any other means of homing. Substitution of $\delta\boldsymbol{\psi}_l^*$ from above equation in Eq (8.59) yields $\mathbf{e}_{lg_{ss}}$ for a given $\mathbf{p}_{lg,des}$. The workspace of the left jaw ($|\psi_1|, |\psi_{2l}| \leq \pi/2$) was discretized and the forward kinematic model Eq. (8.8) was used to obtain $\mathbf{p}_{lg,des}$ in simulations. Figure (8.11a) shows the mesh plot of the magnitude of the error ($\|\mathbf{e}_{lg_{ss}}\|$) and Fig. (8.11b) is the associated contour plot. The maximum value of the error is $3.44mm$. Note that the homing bias magnitude ($\|\mathbf{J}_{v,l}(\boldsymbol{\psi}_l^*)^{\mathrm{T}}\delta\boldsymbol{\psi}_l^*\|$ is $2.35mm$ based on Eq (8.59)).

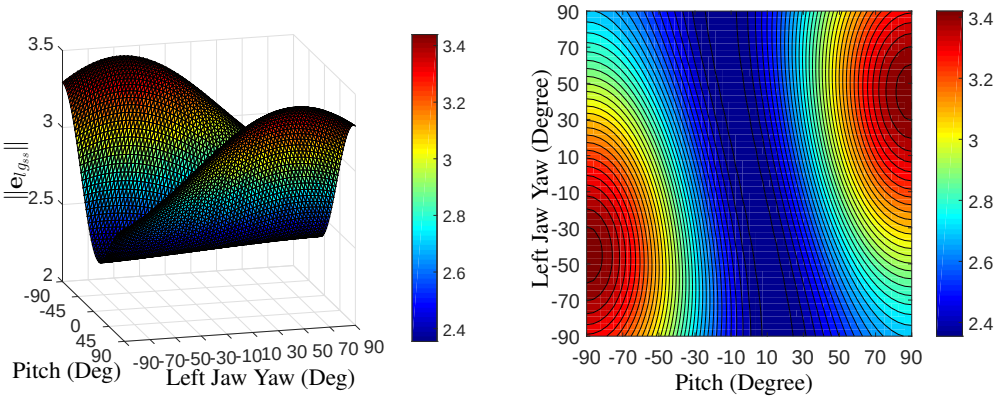

(a) Mesh plot of $\|\mathbf{e}_{lg_{ss}}\|$ (b) Contour plot of $\|\mathbf{e}_{lg_{ss}}\|$

Figure 8.11: Effect of homing error on the magnitude of the left jaw position error for $\delta\boldsymbol{\psi}_l^* = (\pi/180)[1,1]^{\mathrm{T}}$

The same simulation was repeated for several homing error values $\delta\boldsymbol{\psi}_l^*$. Table (8.3) summarizes the homing bias magnitude and the maximum errors throughout the workspace.

Table 8.3: Left jaw positioning error due to homing error for several values of $\delta\boldsymbol{\psi}_l^*$

$\delta\boldsymbol{\psi}_l^*$	**Homing Bias Error Mag.**(mm)	**Max Error**(mm)	$\delta\boldsymbol{\psi}_l^*$	**Homing Bias Error Mag.**(mm)	**Max Error**(mm)
$(\pi/180)[1,1]^{\mathrm{T}}$	2.35	3.44	$(\pi/180)[3,2]^{\mathrm{T}}$	6.98	10.03
$(\pi/180)[2,2]^{\mathrm{T}}$	4.71	6.88	$(\pi/180)[2,1]^{\mathrm{T}}$	4.63	6.62
$(\pi/180)[3,3]^{\mathrm{T}}$	7.06	10.32	$(\pi/180)[1,3]^{\mathrm{T}}$	2.73	4.33
$(\pi/180)[2,3]^{\mathrm{T}}$	4.83	7.24	$(\pi/180)[3,1]^{\mathrm{T}}$	6.93	9.84

8.6 Actuation Compensation

To control the pose of the jaws (e.g. left jaw), it is required to know the inverse kinematic from the task space (jaw pose) to the actuator space (wires displacements). To achieve this, a resolved rate scheme can be used to solve the inverse kinematics from the task space to the configuration space numerically. This gives the desired wrist configuration. Then, the inverse kinematic from the configuration space to the actuator space in Eq (8.29) is used to find the command joint-level motions. A PID control at the joint level eventually closes the motion control loop.

This model-based control scheme may not provide an accurate motion control since it relies on the accuracy of the kinematic model. In reality there are at least two unmodelled effects in the presented kinematic model: wires extension and backlash. Accounting for these effects, the command wire displacement is:

$$q_i = s_i + \epsilon_i \tag{8.62}$$

s_i was brought in Eq. (8.29), ϵ_i is the actuation compensation term for transmission wire i.

Several modeling and actuation compensation methods have been proposed to model and compensate for uncertainties or unmodelled effects. In the context of MBCR's, Xu and Simaan used recursive least-square estimation using joint position and configuration variables measurement to estimate backlash and compensation gains of elastic rod model [188]. Simaan *et al.* proposed an actuation compensation method that extended the model in [188] by the characterization of motion transmission losses and coupling using Fourier series approximation and applying the statics model of the MBCR [182]. Agrawal *et al.* proposed a tangent hyperbolic-based smooth backlash inverse and used it in a feedforward model preceding a PID controller to cancel the backlash [236]. Kesner *et al.* proposed actuation compensation of a robotic catheter for beating-heart surgery using a Coulomb friction model and a dead-zone function to characterize the backlash [22]. Bajo *et al.* proposed us-

ing both joint and configuration control feedback to enhance motion control accuracy of MBCRs [189]. Palli *et al.* presented modeling, identification and control of a wire-driven robotic hand. They modeled the friction between the wires and the pathways using LuGre friction model. They also employed viscoelastic models to identify the polymeric wire material [237]. Roy *et al.* developed the most comprehensive calibration model for actuation compensation of a multi-segment MBCR [187]. They modeled friction in the transmission lines, backbones extension, backlash and segments cross-coupling. Other methods to model backlash were presented in [238–240].

To determine the wires extension behavior, load-displacement curves should be obtained by measuring wire properties under various load conditions. To identify the backlash, data from the actual system is required. In the following, we outline a simple model for wires extension and backlash and then present a basic actuation compensation model.

8.6.1 Wire Extension

Elasticity in the wire ropes can be modeled by a unilateral spring-damper model. At low speeds, the damping can be neglected, hence a spring can model the wire rope elasticity. The spring stiffness comes from the axial stiffness of a beam of length l_i, elastic modulus E_i and circular section area of $A_i = \pi d_i^2/4$ where d_i is wire thickness. Hence, the stiffness of each wire in Fig. 8.5-b is:

$$k_i = E_i A_i / l_i \ , i = l1, l2, r1, r2, \tag{8.63}$$

8.6.2 Backlash Modeling

A backlash in the wire motions may stem from the friction between the pulleys and the wires or the lead screws that move the wires on the remote actuation unit. Let us assume that the backlash at transmission i eventually adds/subtracts a constant λ_i^+/λ_i^- to/from the

desired motion. One way to model this backlash is as follows:

$$\lambda_i = \begin{cases} \lambda_i^+ + \mathrm{e}^{-a_{i,1}(s_i - \breve{s}_i)} - (1+\lambda_i^+)\mathrm{e}^{-a_{i,2}(s_i-\breve{s}_i)} & \dot{s}_i \geq 0 \\ -\lambda_i^- - \mathrm{e}^{-a_{i,3}(s_i-\breve{s}_i)} + (1+\lambda_i^-)\mathrm{e}^{-a_{i,4}(s_i-\breve{s}_i)} & \dot{s}_i < 0 \end{cases} \tag{8.64}$$

The coefficients $a_{i,1}, a_{i,2}, a_{i,3}, a_{i,4}$ determine the transient behavior at switching and the rate of convergence to λ_i^+ and λ_i^-. $\breve{s}_i$ is the wire displacement absolute value at switching instant (when the direction of wire motion changes). Figure (8.12) shows the plots of backlash versus the wire displacement for several values of $a_{i,1}$ and $a_{i,2}$ assuming $\breve{s}_i = 0$, $\lambda_i^+ = 2mm$ and a positive $\dot{s}_i$. Note that $a_{i,1} = a_{i,2} = 300$ generates approximately a step (signum) behavior.

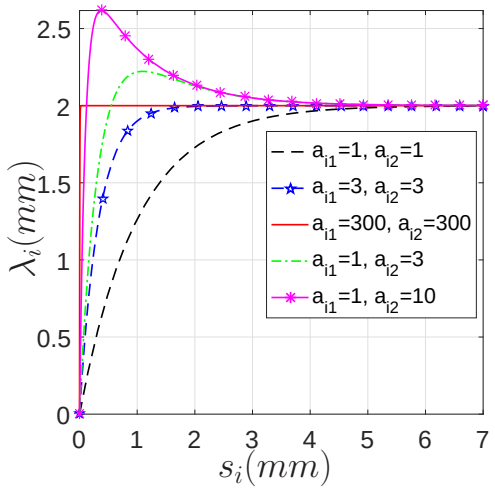

Figure 8.12: Backlash versus wire displacement for several values of $a_{i,1}$ and $a_{i,2}$ ($\breve{s}_i = 0$, $\lambda_i^+ = 2mm$, $\dot{s}_i \geq 0$)

To identify the parameters in Eq. (8.64), experiments should be performed to collect ground truth data. Then, a linear least square estimation can be applied to obtain the parameters. In the above equation, the exponential terms with tunable coefficients allow to conform to the physical backlash behavior.

8.6.3 Compensation Model

With the preceding extension and backlash models, the compensation term is formulated as:

$$\epsilon_i = \eta_i k_{w_i}^{-1} \tau_i + \lambda_i \tag{8.65}$$

The coefficient η_i allows adjustment of the extension model in Eq (8.63). For instance, the wire composition (e.g. twisted or laid, braided or plated) effect on stiffness can be lumped in η_i. k_{w_i} is the wire stiffness from Eq. (8.63). τ_i is measured from load cells.

8.7 Wrist Workspace

There are different workspaces for a wire-driven mechanism. The critical workspaces to be considered are *physical workspace* and *wrench-feasible workspace* [241]. The physical workspace of any mechanism – be it wire-actuated or not – is the actual workspace constrained only by the geometric/physical conditions of the mechanism. This workspace may have singularities within or on its boundaries that should be avoided for optimal performance. The wrench-feasible workspace (WFW) is only relevant for a wire-driven mechanism.

Abdul Hamid *et al.* presented the *safe wrench-closure workspace* of a parallel universal-joint wire-driven wrist [221]. By safety, it was implied that the limited wire stiffness was modeled and accounted in the analysis. They also presented preliminary design atlases for similar wrist architectures. Liu *et al.* studied the effect of wire stiffness on the reduction of wrench-feasible workspace in further details on a similar wrist architecture [222]. They also investigated the use of actuation redundancy for enlarging the workspace.

We explore the physical workspace and the WFW in the next subsections. We will discover that these subspaces are equivalent for the current wrist since the null-space vector of the transpose of structure matrix ($\mathbf{A}^{\mathrm{T}}$) is uni-sense.

8.7.1 Physical Workspace

8.7.1.1 Limitations on Attainable Pitch

The pitch angle of the wrist is limited by the tangency condition of the individual wires wrapped on the middle pulleys. Figure (8.7) illustrates pulleys 1 and 2 that are assumed to represent the wrist middle (m) and proximal (p) pulleys respectively. The arc $\mathbf{t}_{1a}\mathbf{t}_{1b}$ is where the wire wraps around the middle pulley and its subtended angle is the wrap angle of the middle pulley. This arc is required to be maintained at all wrist configurations. In order to guarantee this condition, the wrap angle of the middle pulley must always remain positive.

Recall from Eq (8.21) and Fig (8.7) that the wrap angle of the middle pulley associated with transmission wire i is a function of ϕ_i and α_2 where ϕ_i is a constant parameter determined from pulleys radii and the centerline distance and α_2 is $-\psi_1$ or $+\psi_1$ (See Eq.(8.22)). Therefore, in order for the wrap angles of all the wrist middle pulleys to remain positive, the pitch angle should never be higher than ϕ_i.

Figure (8.13) shows the plot of the maximum feasible pitch angle versus $\frac{r_{pi}+r_{mi}}{c}$ parameter. The diamond symbol ($\diamond$) represents the current wrist design. The maximum pitch angle is 72.2° that is the minimum of maximum pitch values that can be obtained from each wire route. This figure also shows a 90° pitch is feasible only when the pulleys pairs are tangent ($\frac{r_{pi}+r_{mi}}{c} = 1$).

8.7.1.2 Workspace Plot

The physical workspace of the 3-DoF wrist is constrained by the geometric limits on maximum pitch and yaw angles of the wrist. The pitch angle is also constrained by the maximum attainable pitch limitations explained in section (8.7.1.1). The yaw angles are bounded by interference with the side walls of the base of the wrist such that: $-17^\circ \leq \psi_{2l} \leq 63^\circ$ and $-63^\circ \leq \psi_{2r} \leq 17^\circ$. Furthermore, the yaws are bounded by

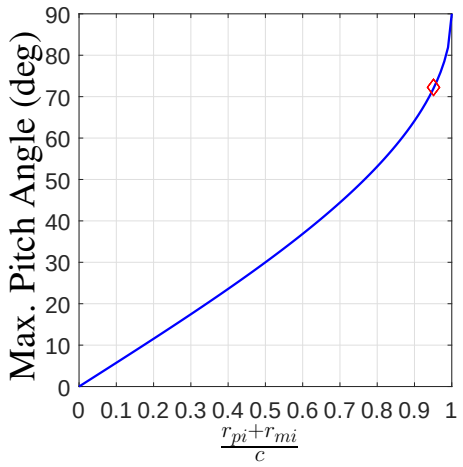

Figure 8.13: Maximum attainable pitch angle without the wire unwinding from pulley p. Red $\diamond$ represents current wrist prototype.

interference of the jaws with one another. Figure (8.14) shows the interference-free configurations of the jaws.

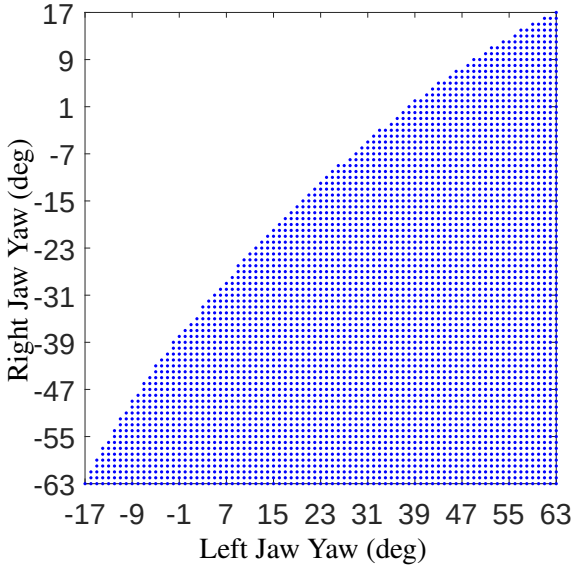

Figure 8.14: Physical workspace of 3-DoF wrist: plot of feasible yaws to avoid mechanical interference of jaws. Note maximum attainable pitch is $72.2°$.

After identification of the physical workspace, an important question to ask is whether there are any singularities within or on the boundaries of this workspace. Investigating the singular values of the Jacobian Eq. (8.18) showed that the 3-DoF wrist is singularity-free.

8.7.2 Wrench-Feasible Workspace

The wrench-feasible workspace (WFW) of the 3-DoF wrist is defined as the set of all poses within its physical workspace where three independent active forces (three out of the six components of $\mathbf{f}_{ee}$) can be generated by tension forces in the four wires (assuming wires never fail in tension). This is equivalent to the set of all poses where any arbitrary configuration moments $\mathbf{m}_\psi$ can be generated by tension wire forces and the matrix $\mathbf{C}$ that maps the configuration moments $\mathbf{m}_\psi$ to the external wrench $\mathbf{f}_{ee}$ (see Eq. (8.39)) is full-rank. Referring back to Eq (8.42), the wire forces are:

$$\boldsymbol{\tau} = -(\mathbf{A}^{\mathrm{T}})^{+}\mathbf{m}_\psi + \eta\mathbb{N}(\mathbf{A}^{\mathrm{T}}) \tag{8.66}$$

where $\mathbb{N}(\mathbf{A}^{\mathrm{T}})$ is the null-space vector of $\mathbf{A}^{\mathrm{T}}$ and η is an arbitrary scalar. Recall that $\eta\mathbb{N}(\mathbf{A}^{\mathrm{T}})$ constitutes the null-space solution of Eq (8.42). Based on Eq (8.66), the wire forces can be made positive for arbitrary values of $\mathbf{m}_\psi$ if the null-space vector $\mathbb{N}(\mathbf{A}^{\mathrm{T}})$ elements have the same sign (uni-sense) i.e. $\mathbb{N}(\mathbf{A}^{\mathrm{T}}) > 0$ or $\mathbb{N}(\mathbf{A}^{\mathrm{T}}) < 0$. Mathematically, this guarantees that regardless of the first term $-(\mathbf{A}^{\mathrm{T}})^{+}\mathbf{m}_\psi$, the contribution of the second term can be scaled up by increasing η such that all the elements of $\boldsymbol{\tau}$ are positive. The null-space of $\mathbf{A}^{\mathrm{T}}$ can be shown to be as follows:

$$\mathbb{N}(\mathbf{A}^{\mathrm{T}}) = [1, 1, 1, 1]^{\mathrm{T}} \tag{8.67}$$

Based on the above equation, all the elements of the null-space vector are positive. Therefore, regardless of the configuration, there can be found positive wire forces that generate the configuration moments. Furthermore, it can be shown that the matrix $\mathbf{C}$ is full-rank (rank 3). Hence, the wrench-feasible workspace of the 3-DoF wrist is the same as its physical workspace as discussed in section (8.7.1). Note that the flexibility of the wires does not affect WFW since $\mathbb{N}(\mathbf{A}^{\mathrm{T}})$ is uni-sense throughout the workspace.

The null-space formulation in Eq. (8.67) also determines a preliminary preloading strategy as well. Since all the elements of $\mathbb{N}(\mathbf{A}^{\mathrm{T}})$ are unit, wire preloads should be equal. In practice, modeling uncertainties varies this value. Nevertheless, it should serve as a proper starting point for preload adjustment.

8.8 Characterization of Slop/Compliance of the Wrist

A simple experiment on the wrist prototype verified that a lateral force on the wrist gripper causes it to open hence a loss of grasp. This spurious effect is a result of the particular wire coupling (manifested in structure matrix Eq. (8.30)) of the wrist. In this section, we will investigate this effect in a broader sense by drawing on the stiffness matrix of the mechanism and estimating the configuration change due to an external perturbation. The goal is to obtain an approximation for the wrist unwanted configuration change due to grasping and lateral forces.

Figure (8.15) shows the steps in finding the configuration change. An external force designated as $\mathbf{\Delta f}_{ee} = [\Delta f_{e,x_{gl}}, \Delta f_{e,y_{gl}}, \Delta f_{e,z_{gl}}, \Delta f_{e,x_{gr}}, \Delta f_{e,y_{gr}}, \Delta f_{e,z_{gr}}]^{\mathrm{T}}$ is assumed to apply on the jaws (see Fig. (8.10)). Next, the moments applied directly in the configuration space of the wrist are determined. These moments include the moment at the middle shaft (at the proximal side of the distal clevis in Fig. (8.10)) to generate pitch and the moments applied at the proximal ends of the left and right parallelogram input links to generate left and right yaws.

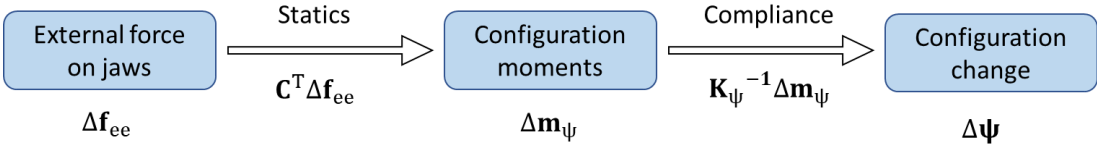

Figure 8.15: Finding configuration change due to external load on jaws

Recall that in Eq. (8.39), the left and right hand side determine the moment generated by the wire forces $\boldsymbol{\tau}$ and the external force $\mathbf{f}_{ee}$ in the configuration space respectively.

Therefore, the configuration moment caused by the external force is:

$$\boldsymbol{\Delta}\mathbf{m}_{\psi} = \mathbf{C}^{\mathrm{T}}\boldsymbol{\Delta}\mathbf{f}_{ee} \tag{8.68}$$

Next, we find how much the configuration moment $\boldsymbol{\Delta}\mathbf{m}_{\psi}$ can change the wrist configuration denoted by $\boldsymbol{\Delta\psi}$. This can be determined from the configuration space stiffness of the wrist $\mathbf{K}_{\boldsymbol{\psi}} \triangleq \frac{\partial \mathbf{m}_{\psi}}{\partial \boldsymbol{\psi}}$ that was discussed in section (8.4). The stiffness was shown to be $\mathbf{K}_{\boldsymbol{\psi}} = \mathbf{A}^{\mathrm{T}}\mathbf{K}_{w}\mathbf{A}$, where $\mathbf{K}_{w} \in \mathbb{R}^{4\times4}$ is the joint-space stiffness. Assuming infinitely rigid actuators, $\mathbf{K}_{w}$ reflects the wire stiffness (wire spring rate):

$$\mathbf{K}_{w} = diag([k_w, k_w, k_w, k_w]) \tag{8.69}$$

Having derived the stiffness matrix, the last step in finding the configuration change is to pre-multiply the inverse of the stiffness (compliance) by the configuration moment:

$$\boldsymbol{\Delta\psi} = \mathbf{K}_{\boldsymbol{\psi}}^{-1}\boldsymbol{\Delta}\mathbf{m}_{\psi} \tag{8.70}$$

8.8.1 Simulation Results

To obtain the wire stiffness, it was modeled as an Euler-Bernoulli beam under tension. The wire used in the wrist prototype is made of 18-8 stainless steel (Young Modulus $E_w = 200\,GPa$, Diameter $d_w = 0.024\,in$, length $l_w = 350\,mm$). Applying Hooke's law gives the stiffness as:

$$k_w = \frac{A_w E_w}{l_w} \approxeq 166.8[N/mm] \tag{8.71}$$

where A_w is the cross-section of the wire.

A Matlab code was written to plot the change in the pitch and the yaws of the wrist by application of a prescribed perturbation load on the jaws. The plots in Fig (8.16) show the results of the simulation for a perturbation of $\boldsymbol{\Delta}\mathbf{f}_{ee} = [0, 4, -2, 0, -4, 0]^{\mathrm{T}}\,kg$ i.e. a 4 kg

grasping force and 2 kg lateral force on the left jaw. The configuration change is only a function of the initial (unperturbed) jaw angles.

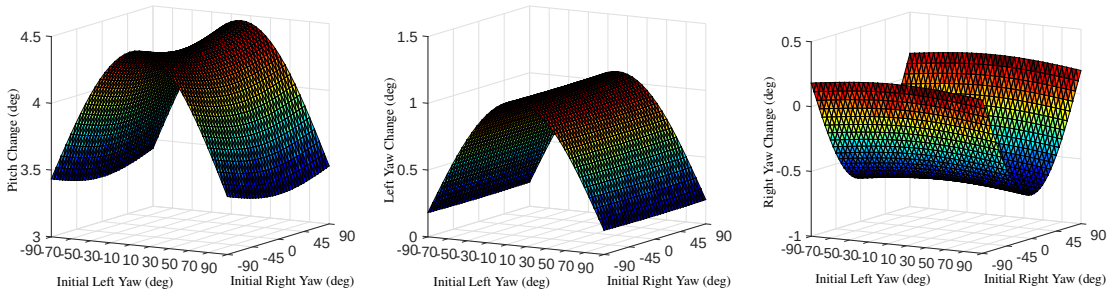

(a) (b) (c)

Figure 8.16: Change in 3-DoF wrist configuration in its workspace by application of a load perturbation of $\mathbf{\Delta f}_{ee} = [0, 4, -2, 0, -4, 0]^{\mathrm{T}}\, kg$ (4 kg grasping force, 2 kg lateral force on left jaw) : (a) change in pitch, (b) change in left yaw, (c) change in right yaw

Based on these plots, the external load can cause a minimum of $3.34°/0.18°/0°$ and a maximum of $4.46°/1.07°/0.66°$ change in the pitch/left yaw/right yaw angles. The minimum/maximum pitch change occurs at $|\psi_2| = 90°/0°, |\psi_3| = 0°/90°$. The minimum/maximum left yaw change occurs at $|\psi_2| = 90°/0°$ while the minimum/maximum right yaw change happens at $|\psi_2| = 90°/0°, |\psi_3| = 0°/90°$. Note the opposite signs of the left and the right yaws that verifies the grasp is released due to external load.

Several simulations were also conducted with other grasping and lateral forces. Table (8.4) shows the maximum angle change in these simulations and may serve as a quick reference to get an estimate of the configuration change.

Table 8.4: Approximate configuration change for several values of grasping and lateral forces on left jaw due to wires flexibility

Grasping Force (kg)	**Lateral Force (kg)**	**Max Change in pitch/l. yaw/r. yaw (deg)**	**Grasping Force (kg)**	**Lateral Force (kg)**	**Max Change in pitch/l. yaw/r. yaw (deg)**
0	2	4.36/0.23/0.23	2	0	0.05/0.42/0.42
0	4	8.72/0.46/0.46	4	0	0.10/0.84/0.84
2	4	8.77/0.88/0.46	4	2	4.46/1.07/0.66
4	4	8.81/1.30/0.48	2	2	4.41/0.65/0.24
6	2	4.51/1.50/1.08	6	4	8.86/1.73/0.90
8	2	4.55/1.92/1.51	8	4	8.91/2.15/1.32

8.9 Characterization of Maximum External Load (Payload)

In section 8.7.2, it was shown that there exist positive wire forces that balance any three external loads on the jaws of 3-DoF wrist regardless of the configuration. The reason was that since the null-space solution in eq. (8.66) is always positive, the wires preloads can be increased until all the wire forces are positive. However, the premise of this argument was that the wires can bear infinite loads. In this section, this assumption is relaxed and we assume that there is a permissible lower and upper bound on the wire tensions: $\tau_{min} \leq \tau_i \leq \tau_{max}$, $i = l1, l2, r1, r2$. The lower bound stems from the fact that a wire should have a minimum tension to remain sufficiently taut and the upper bound comes from the strength of the wire that is provided by manufacturers through experimental measurements.

In order to solve this problem at each configuration $\boldsymbol{\psi}$, we consider Eq (8.39) again. Using singular value decomposition and matrix algebraic manipulations, it can be proved that:

$$\|\mathbf{f}_{ee}\| \leq \frac{\|\mathbf{m}_{\psi}\|}{\underline{\sigma}(\mathbf{C})} \tag{8.72}$$

where $\|.\|$ and $\underline{\sigma}(.)$ represent Euclidean norm and minimum singular value respectively. An upper bound on $\|\mathbf{m}_{\psi}\|$ can be sought as follows. Referring to Eq (8.42):

$$\|\mathbf{m}_{\psi}\| \leq \overline{\sigma}(\mathbf{A})\|\boldsymbol{\tau}\| \tag{8.73}$$

where $\overline{\sigma}(.)$ represents the maximum singular value. Since the wire forces cannot exceed τ_{max}, the maximum value for $\|\boldsymbol{\tau}\|$ is $2\tau_{max}$. Therefore, the maximum value of $\|\mathbf{m}_{\psi}\|$ is:

$$\|\mathbf{m}_{\psi}\|_{max} = 2\overline{\sigma}(\mathbf{A})\tau_{max} \tag{8.74}$$

Substituting the above in Eq (8.72) gives the maximum external load:

$$\|\mathbf{f}_{ee}\|_{max} = \frac{2\tau_{max}\overline{\sigma}(\mathbf{A})}{\underline{\sigma}(\mathbf{C})} \tag{8.75}$$

In the above equation, the nominator is a constant for the current 3-DoF wrist, however, the denominator depends on the configuration.

8.9.1 Simulation Results

The singular values of matrix $\mathbf{C}$ can be shown to be:

$$\sigma_i(\mathbf{C}) = \begin{cases} a_2, & i = 1, 2 \\ \left[\left(a_1 + a_g + a_2\cos(\psi_2)\right)^2 + \left(a_1 - a_g + a_2\cos(\psi_3)\right)^2\right]^{1/2} & i = 3 \end{cases} \tag{8.76}$$

After substitution of the values of a_1, a_2, a_g of the current wrist prototype in the above equation, it turned out that $\underline{\sigma}(\mathbf{C}) = a_2$ regardless of the configuration. Thus, for the current wrist, the maximum safe load is a constant: $\|\mathbf{f}_{ee}\|_{max} = \frac{2\tau_{max}\overline{\sigma}(\mathbf{A})}{a_2}$. In most practical purposes, the axial forces on the wrist are negligible ($f_{e,x_{gl}} = f_{e,x_{gr}} \approxeq 0$ in Fig. (8.10)) and only grasping and lateral forces are present. Figure (8.17) shows the plots of the maximum safe grasping versus lateral forces for several values of wire strength τ_{max}.

8.10 Conclusion

This chapter presented a detailed analysis of an open-ended 3-DoF wire-driven wrist with potential applications in robot-assisted MIS. The unique feature of the wrist in contrast with most other existing counterparts (e.g. EndoWrist® from Intuitive Surgical) is that it has an open-ended wire routing. This can allow a accurate motion control, wire preload adjustment, stiffness modulation and interaction force measurement by sensing the wire forces due to actuation redundancy.

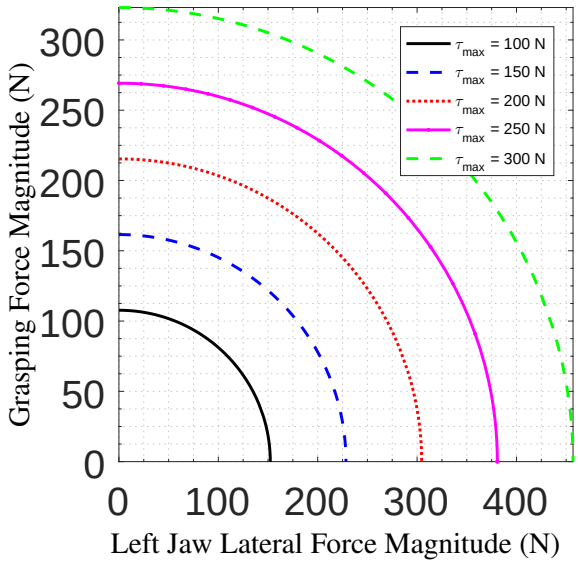

Figure 8.17: Maximum safe external load in workspace of 3-DoF wrist when no axial force exists and lateral force is applied on one of the jaws.

In section 8.2, the kinematics of the wrist was modeled by introducing task space (poses of the jaws), configuration space (pitch and yaws) and joint space (wire displacements) and finding the mathematical relationships relating these vector spaces. In section 8.2.2, the instantaneous kinematic model was developed between said spaces. In section 8.3, the statics of the wrist was thoroughly delineated. This was achieved by applying the principle of virtual work to obtain the relationship between the wire tensions and the external load on the wrist. A simple model for the wrist stiffness was presented in section 8.4.

In section 8.5.1, the Jacobian of the wrist from wire displacement space to the task space was used to establish a bound on the wrist positioning error as a function of the wire displacement error. In section 8.5.2, the effect of an error in homing on the positioning of the wrist was studied and simulated for several homing configuration errors. In section 8.6, a basic model was presented for compensation of motion losses due to wires extension and backlash.

The physical and the wrench-feasible workspace of the 3-DoF wrist was explored in section 8.7. It was shown that the physical workspace is constrained by the wire tangency

condition on the middle pulleys. As a result of this constraint the pitch of the current prototype was limited to $72.2°$. The wrench-feasible workspace was shown to be equivalent to the physical workspace due to the null-space of the transpose of the Jacobian having all its elements with the same sign. This means that one could always use preload to prevent wires from becoming slack. In practice, this is limited by wire strength and slop. The slop/compliance of the wrist due the wires flexibility was therefore characterized in section 8.8. Finally, in section 8.9, an equation was derived to compute the maximum external grasping and lateral forces that the 3-DoF wrist can withstand in its workspace before any of its wires fail.

CHAPTER 9

CONCLUSION

9.1 Summary of Findings

TURBT is a minimally-invasive surgical procedure used to diagnose bladder cancer and treat non-muscle invasive bladder cancer where a surgeon removes visible tumor with an electrosurgical loop that cuts the tumor out. Chapter 3 reported a first attempt at correlating theoretical measures for resection accuracy with experimental data. This chapter addressed the kinematic measures in TURBT procedure. After modeling the kinematics, several Jacobian-based measures were proposed including tangential kinematic conditioning index, tangential manipulability, tangential minimum singular value and normal singular value. Experimental trials simulating clinical TURBT was performed by three surgeons and the resection accuracy in tangential and normal (depth) directions were measured. It was verified that the surgeons generally under-resect. On further investigation, it was shown that the tangential accuracy correlated relatively strongly with normal singular value and moderately with tangential kinematic conditioning index and tangential minimum singular value. A weak linear correlation with tangential manipulability was substantiated hence disqualifying it as a measure. On the other hand, normal resection accuracy was demonstrated to be weakly correlated with any of the kinematic measures suggesting that other factors may influence this variable. It is believed by the author that visualization enhancement should considerably improve depth resection outcomes.

The certified measures were utilized to compare kinematic accuracy/dexterity locally in all bladder points based on the distance from the bladder neck and regionally in 16 bladder zones.

In chapter 4, prior art in tools and systems that aimed for increasing the performance of bladder surveillance and transurethral resection was reviewed. Then, a new telerobotic surgical platform called TURBot was presented for bladder cancer surveillance and resection. The design of TURBot was explained in details. Two of its primary constituents; namely the robotic slave and the robot-integrable resectoscope were explained in details. TURBot is the only system that offers precision and intra-vesicular dexterity while providing a platform for deploying new imaging techniques and supporting traditional wire loop cautery and/or laser tumor resection/ablation instruments.

Chapter 5 covered kinematic modeling, actuation compensation and calibration of TURBot system. The compensation of actuation included backlash compensation and calibrated gains in the joint-to-configuration direct kinematic model of the Multi-backbone Continuum Robot (MBCR). These gains were determined experimentally for discrete points in the workspace of MBCR and they were interpolated with cubic splines for all other points. The backlash originated from the application of flexible material in the motion transmission chain. The compensation of this backlash involved the measurement of this flexibility and adding to or subtracting from the command joint displacements at the instances of motion direction change.

Next, an eye-to-hand telemanipulation paradigm was discussed that provided a user that only had a 2D visual feedback of the workspace an intuitive telemanipulation framework. This image-based telemanipulation framework only required an extrinsic camera and robot pose information and did not need camera intrinsic parameters calibration.

Finally in the same chapter, a hierarchical resolved-rate algorithm was described for telemanipulation that accounted for the tubular constraint on the MBCR enforced by the resectoscope sheath. The algorithm utilized the insertion state to evaluate which segments

were constrained and assigned the task to the available free segments. This involved demoting a 5-DoF task of position-pitch-yaw tracking to a 3-DoF position tracking when there was only one free segment and promoting it back when at least two segments were available. It also ensured smooth switching between these different scenarios by re-initialization of command velocities and an appropriate modeling of instantaneous kinematic during switching instances.

Chapter 6 delineated two experimental studies. In the first part, a comparison of robot-assisted and manual TURBT performance on a bladder phantom was reported through an experimental user study. In the second part, the results of *in vivo* validation of TURBot in swine was explained.

The tangential error at resection of tumors in the bladder phantom lateral wall region was $1.18 \pm 0.38mm$ and $2.23 \pm 0.68mm$ for the manual and the robotic groups respectively. The resection duration at the same location was $50 \pm 21sec$ (manual) vs 139 ± 83. This demonstrated that the robotic performance was lower than manual. However, the robot was shown to be capable of resecting the neck region with retroflexing postures (average accuracy of $2.69 \pm 0.80mm$ and average duration of $202 \pm 112sec$) while this region was not accessible by the manual tool. The potential robot limitations hindering its performance were enumerated as flexible 3D-printed transmission components, joint limits at retroflexion, calibration, more user training requirement, lack of loop roll control and visual occlusion by robot body/loop.

The *in vivo* experiments demonstrated successful deployment of TURBot, complete bladder accessibility, successful tumor ablation, ability to retroflex within the bladder and ability to perform en-bloc resection using a combination of laser ablation and a grasper. The animal studies provided insights towards enabling robotic assistance for TURBT for clinical application.

In chapter 7, a redundancy resolution method was developed to minimize the visual field occlusion caused by the presence of the robot in the field of view (FOV). The method

was based on a modified artificial potential field that drove the robot outside the FOV in attempting to reach static equilibrium while achieving the main task of tracking. Simulations for the tasks of maintaining the end effector pose and tracking a circle confirmed the efficacy of the proposed method for a rotating camera. Although the proposed method was developed within the context of multi-backbone continuum robots, it can be generally applied to any redundant robot that requires to stay as clear of the visual field as possible.

In chapter 8, an analysis of a 3-DoF wire-driven wrist with potential applications in general robotic MIS was presented. The wrist had an open-ended wire routing allowing accurate motion control, wire preload adjustment, stiffness modulation and interaction force measurement by sensing the wire forces. The analysis of the wrist started with standard kinematic/static modeling. The derived equations were used in further analysis to determine positioning error due to actuator or homing error. The slop of the wrist due the wires flexibility caused by an external perturbation was identified. Finally, the load bearing capability of the wrist with limited wire strength was determined.

9.2 Future Research Directions

There are several directions to follow on in regards to robot-assisted transurethral resection or laser ablation. One key area of improvement is utilizing assistive features. *Virtual fixtures* that were introduced in 1993 by Rosenberg [242] are well-established algorithms that provide suitable constraints to improve safety or accuracy/speed of tasks. These virtual fixtures paradigms are sometimes called forbidden-region (FRVF) and guidance virtual fixtures (GVF) respectively [243]. The algorithms can be implemented on the master or on the slave robot. Development of a user-specified virtual fixture for TURBot is an interesting area to explore. One way to envision this is to add a teleoperation mode where the surgeon telemanipulates the MBCR around the perimeter of a region of interest. The robot controller would record this area and define a forbidden region wherein the MBCR tip is allowed to operate. A similar method can be applied to control the depth of resection

to guide safer robot-tissue interactions. For example, the surgeon can provide a desired maximum depth through a user interface. Then, the control algorithm filters all position commands that lead to over-penetration. A force-feedback cue can be applied through the master device on the surgeon's hand to warn him/her on approaching the maximum allowed depth.

Two hardware enhancements on TURBot should be pursued prior to the application of the virtual fixtures. To find the coordinates of the perimeter points, a triangulation mechanism such as a stereo vision module should be utilized. More importantly, the localization accuracy of the MBCR tip should be improved to ensure it stays within the prescribed region. Currently, the forward kinematic model is used to estimate the tip pose. The true pose deviates from this estimate due to unmodelled phenomena such as segments coupling and friction. In a telemanipulation scenario, these deviations are generally tolerated since the human operator closes the human-machine feedback loop and the MBCR repeatability is known to be high. However, with the introduction of the virtual fixture, the algorithm would require an accurate tip position information to ensure effective operation. Incorporation of an electromagnetic sensor at the tip is an option to provide this missing information. A more comprehensive calibration model for actuation compensation such as in [187] can also improve accuracy.

Another area to explore is incorporation of more recent imaging modalities reviewed in section 2.3 in TURBot control algorithm. This can provide a surgical suite that can potentially offer accurate staging and resection of bladder tumors simultaneously. It is the author's conjecture that a combination of NBI as an augmentative technology over the conventional white light cystoscopy and OCT or transurethral ultrasound for bladder wall penetration detection can yield promising results. Automated online segmentation of NBI (or PDD) images to demarcate the tumors merits attention. The tumor boundaries can be then fed into the user-specified virtual fixtures to assist the surgeon in resection/ablation. In addition, it is interesting to explore the capabilities of OCT as part of the robotic system for

in-situ biopsy of bladder tumors. The author envisions a robotic system where the surgeon utilizes augmented reality to see a 3D vision of the bladder. On the HUD display, s/he can see overlays from NBI/PDD/OCT/US feedback. This could be 2D cross-sectional pictures or post-processed 3D images with marked bladder layers and robot tip penetration depth. The robot can be also used in a surveillance mode where it automatically scans the entire inflated bladder surface and maps the tumors.

The visual occlusion minimization framework in chapter 7 should be validated on an experimental platform such as TURBot. The efficacy of the algorithm should be also verified in an actively controlled vision system that offers more degrees-of-freedom than a simple rotation.

In regards to the open-ended wrist architecture presented in chapter 8, a potential research problem is to introduce or use existing force sensing measures (such as [183]) and to evaluate that on the current and other similar wrist paradigms. It is also interesting to explore optimization of the wrist parameters based on such performance measures.

Another problem to consider is the modulation of the stiffness/compliance of the wrist. stiffness modulation may be desirable in NOTES applications where high structural flexibility may be required to deploy the tool in the body lumens while more rigidity is required during the operation of the robot for enhanced accuracy and high payload capability. Recall from Eqs (8.44) and (8.45) that the stiffness is a function of the wires and actuators stiffness ($\mathbf{K}_w$) and the derivative of the Jacobian from the actuator motion space to the configuration space and also the actuator forces/moments ($\frac{\partial \mathbf{A}^{\mathrm{T}}}{\partial \psi}\boldsymbol{\tau}$). In the current 3-DoF wrist, the latter term is not present as the Jacobian ($\mathbf{A}$) is constant. Yet, it is possible to change the stiffness by modification of the actuator stiffness. To achieve this, employment of a variable stiffness actuator (VSA) was suggested in the literature [244–246]. For a different cable-driven parallel wrist architecture such as [221], the Jacobian is a function of the configuration. This offers an opportunity to have yet another leverage to modulate the mechanism stiffness. It is of interest to explore different wrist mechanisms that offer such a feature.

APPENDIX A

INVERSE KINEMATIC SOLUTIONS OF 4-DOF RESECTOSCOPE

To solve the inverse kinematic problem for a point on the loop, given γ and ${}^0\mathbf{T}_5$, ${}^0\mathbf{T}_4$ is sought. Using successive transformations Eq. (3.1),

$$ {}^0\mathbf{T}_4 = {}^0\ \mathbf{T}_5\ {}^4\mathbf{T}_5^{-1} \tag{A.1} $$

where ${}^4\mathbf{T}_5$ is given by Eq. (3.3). Therefore,

$$ {}^4\mathbf{T}_5^{-1} = \begin{bmatrix} c_\gamma & s_\gamma & 0 & r_L \\ -s_\gamma & c_\gamma & 0 & 0 \\ 0 & 0 & 1 & 0 \\ 0 & 0 & 0 & 1 \end{bmatrix} \tag{A.2} $$

Now, algebraic method is utilized to determine solutions given ${}^0\mathbf{T}_4$

$$ {}^0\mathbf{T}_4 = \begin{bmatrix} r_{11} & r_{12} & r_{13} & p_x \\ r_{21} & r_{22} & r_{23} & p_y \\ r_{31} & r_{32} & r_{33} & p_z \\ 0 & 0 & 0 & 1 \end{bmatrix} \tag{A.3} $$

where all matrix elements are brought in Eq. (3.2). Since $r_{13} = c_1 c_2$ and $r_{23} = s_1 c_2$, therefore $c_1 = \frac{r_{13}}{\pm\sqrt{1-r_{33}^2}}$ and $s_1 = \frac{r_{23}}{\pm\sqrt{1-r_{33}^2}}$. This gives q_1

$$q_1 = atan2(\frac{r_{23}}{\pm\sqrt{1-r_{33}^2}}, \frac{r_{13}}{\pm\sqrt{1-r_{33}^2}}) \quad , if\ r_{33} \neq \pm 1 \tag{A.4}$$

from $r_{33} = s_2$,

$$q_2 = atan2(r_{33}, \pm\sqrt{1-r_{33}^2}) \tag{A.5}$$

Since $r_{32} = -c_2 s_3$ and $r_{31} = c_2 c_3$, therefore $s_3 = \frac{-r_{32}}{c_2} = \frac{-r_{32}}{\pm\sqrt{1-r_{33}^2}}$ and $c_3 = \frac{r_{31}}{c_2} = \frac{r_{31}}{\pm\sqrt{1-r_{33}^2}}$. This yields q_3

$$q_3 = atan2(\frac{-r_{32}}{\pm\sqrt{1-r_{33}^2}}, \frac{r_{31}}{\pm\sqrt{1-r_{33}^2}}) \quad , if\ r_{33} \neq \pm 1 \tag{A.6}$$

In case $r_{33} = \pm 1$, there are infinite solutions for q_1 and q_3. The solution are $q_1 + q_3 = atan2(r_{12}, -r_{22})$ or $q_1 - q_3 = atan2(r_{12}, -r_{22})$. As for q_4,

$$\begin{cases} q_4 = \frac{p_x - \nu r_{11}}{r_{13}} - \eta \quad , if\ r_{13} \neq 0 \\ q_4 = \frac{p_y - \nu r_{21}}{r_{23}} - \eta \quad , if\ r_{23} \neq 0 \\ q_4 = \frac{p_z - \nu r_{31}}{r_{33}} - \eta \quad , if\ r_{33} \neq 0 \end{cases} \tag{A.7}$$

APPENDIX B

COMPONENT SELECTION OF TURBOT ACTUATION UNIT

This components selection is delineated in [177]. It is also repeated here for convenience: Tables B.2 and B.1 summarize the specifications and expected performance of the gearmotors combined with lead screws for driving the backbones of each segment. To arrive at the choice of gear-motors and screws a Matlab code was written to parse the specifications of available lead screws and motors that fit the cylinders. To obtain a first order estimate of the power requirements of the actuators were calculated based on task specification assuming gearhead efficiency of 80% and lead screw efficiency of 70%. Once a list of motors that satisfies the power requirements was made, the Matlab code was used to cull the list down to motor and screw combinations that can satisfy force and speed requirements.

Table B.1: Motor combination design requirement

	Output gear torque		Power for maximal speed		Power for nominal speed		Max linear speed		Lead screw pitch
	Required	Provided	Required	Provided	Required	Provided	Required	Provided	
Maxon motor	36.206 Nmm	39.28 Nmm	2.205 W	3 W	2.115 W	2.37 W	4.7 mm/s	4.899 mm/s	0.60911 mm/turn
Micromo	9.320 Nmm	15.411 Nmm	2.711 W	3.11 W	0.688 W	1.003 W	9.4 mm/s	10.417 mm/s	0.60911 mm/turn

Table B.2: Motor Combinations

First Cylinder			
Motor Combination	Gearhead	Motor	Encoder
Maxon Motor 324553	GP13A 110314 (Series 17:1 3249/196 16.57653061:1 ratio)	Maxon Motor RE13 118638	MR 241062, 256 CPT
Second and Third Cylinder			
MICROMO 1331T006SRIE2-400+14/1 14:1+X0437	14/1 14:1 (Series 14/1 676/49 13.795918:1 ratio)	MICROMO 1331T006SRIE2	X0437 magnetic Encoder digital outputs, 2 channels, 400 lines per revolution

The required torque to raise/lower the piston against/along the direction of an external loaf F is calculated as:

$$\tau_{r,l} = \frac{Fdp}{2} \tan\left(\gamma \pm \lambda\right) + F\frac{dp_b}{2}\mu_{roll}\, b \tag{B.1}$$

where subscript r is for raising and l is for lowering a load. The first part accounts for friction between the screw and nut and the second part accounts for friction in the bearings supporting the lead screw. The lead screw friction angle γ is a function of screw geometry and friction coefficient between the screw and nut. The lead angle λ is a function of the screw pitch diameter d_p and lead L. Details of calculation of these angles can be found in [247].

APPENDIX C

KINEMATICS OF RIGHT JAW OF 3-DOF WRIST

By the same analogy as the left jaw of the 3-DoF wrist presented in section 8.2 (also shown here for convenience), the direct kinematic transformations for the right jaw is:

$$ {}^{0}\mathbf{T}_{2r} = \begin{bmatrix} -c_3 s_1 & s_1 s_3 & c_1 & -s_1(a_1 + a_2 c_3) \\ c_1 c_3 & -c_1 s_3 & s_1 & c_1(a_1 + a_2 c_3) \\ s_3 & c_3 & 0 & -d_1 + a_2 s_3 \\ 0 & 0 & 0 & 1 \end{bmatrix} \tag{C.1} $$

and :

$$ {}^{0}\mathbf{T}_{g_r} = \begin{bmatrix} -s_1 & 0 & c_1 & -s_1(a_1 + a_g + a_2 c_3) \\ c_1 & 0 & s_1 & c_1(a_1 + a_g + a_2 c_3) \\ 0 & 1 & 0 & -d_1 + d_g + a_2 s_3 \\ 0 & 0 & 0 & 1 \end{bmatrix} \tag{C.2} $$

The instantaneous kinematic relationship for the right jaw is as follows:

$$ \begin{aligned} &\mathbf{M}_r \dot{\boldsymbol{\psi}}_r = \mathbf{N}_r \dot{\mathbf{x}}_{g_r}, \\ &\mathbf{M}_r = \begin{bmatrix} \mathbf{J}_{\mathbf{v}_{2r}} \\ \mathbf{J}_{\boldsymbol{\omega}_{2r}} - {}^{0}\mathbf{R}_{2r}\hat{\mathbf{k}}\mathbf{s} \end{bmatrix} \in \mathbb{R}^{6\times 2}, \mathbf{N}_r = \begin{bmatrix} \mathbf{I}_3 & (\boldsymbol{\rho}_{2_r,g_r})^{\wedge} \\ \mathbf{0}_3 & \mathbf{I}_3 \end{bmatrix} \in \mathbb{R}^{6\times 6} \end{aligned} \tag{C.3} $$

where we define $\dot{\boldsymbol{\psi}}_r \triangleq [\dot{\psi}_1, \dot{\psi}_{2r}]^{\mathrm{T}} \in \mathbb{R}^{2\times 1}$ as the right jaw configuration rates vector and $\dot{\mathbf{x}}_{g_r} = [\mathbf{v}_{g_r}^{\mathrm{T}}, \boldsymbol{\omega}_{g_r}^{\mathrm{T}}]^{\mathrm{T}} \in \mathbb{R}^{6\times 1}$ as its associated twist. Referring to Fig. C.1, $\boldsymbol{\rho}_{2_r,g_r} =$

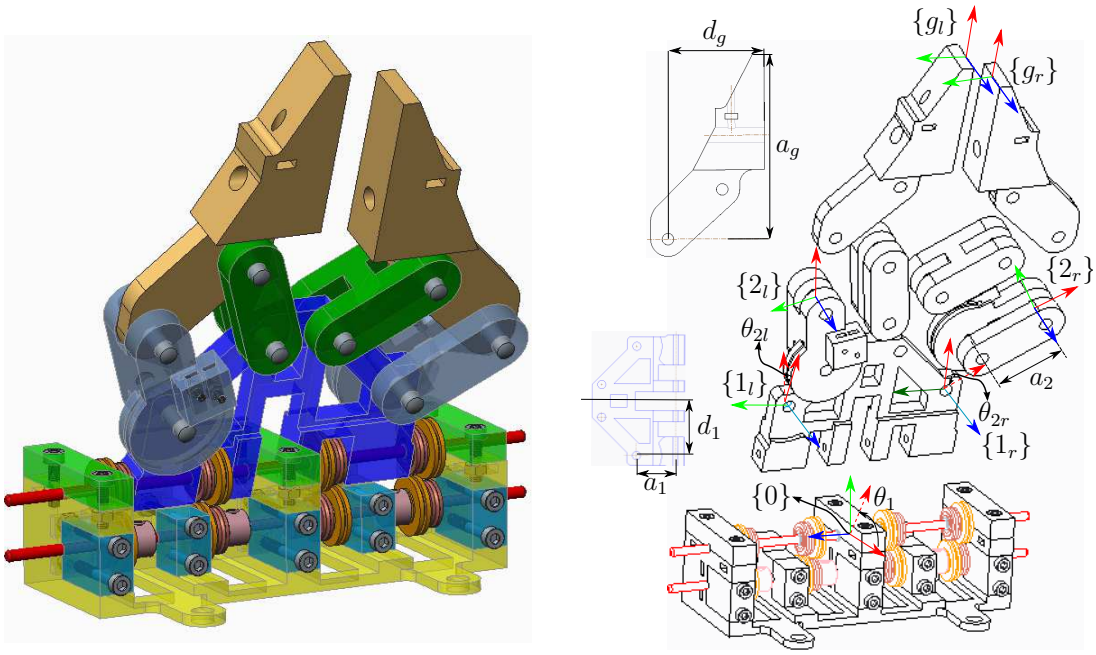

Figure C.1: 3-DoF wrist frame assignments

${}^0\mathbf{R}_{g_r}\,{}^{g_r}\boldsymbol{\rho}_{2_r,g_r}$ such that ${}^{g_r}\boldsymbol{\rho}_{2_r,g_r} = [a_g, d_g, 0]$ is the vector joining the origin of $\{2_r\}$ to the origin of $\{g_r\}$. Left-multiplying the inverse of the upper block-diagonal matrix $\mathbf{N}_r$ results in:

$$\begin{aligned} &\mathbf{J}_r\dot{\boldsymbol{\psi}}_r = \dot{\mathbf{x}}_{g_r}, \\ &\mathbf{J}_r = \begin{bmatrix} \mathbf{J}_{\mathbf{v}_{2r}} - (\boldsymbol{\rho}_{2_r,g_r})^{\wedge}\left(\mathbf{J}_{\boldsymbol{\omega}_{2r}} - {}^0\mathbf{R}_{2r}\hat{\mathbf{k}}\mathbf{s}\right) \\ \mathbf{J}_{\boldsymbol{\omega}_{2r}} - {}^0\mathbf{R}_{2r}\hat{\mathbf{k}}\mathbf{s} \end{bmatrix} \in \mathbb{R}^{6\times 2} \end{aligned} \tag{C.4}$$

Direct substitution into Eq. (C.4) and algebraic simplifications leads to the following formulations for the Jacobians of the right jaw of the 3-DoF wrist:

$$\mathbf{J}_{v,r} = \begin{bmatrix} -c_1(a_1 + a_g + a_2c_3) & a_2s_1s_3 \\ -s_1(a_1 + a_g + a_2c_3) & -a_2c_1s_3 \\ 0 & a_2c_3 \end{bmatrix} \tag{C.5}$$

and,

$$\mathbf{J}_{\omega,r} = \begin{bmatrix} 0 & 0 \\ 0 & 0 \\ 1 & 0 \end{bmatrix} \tag{C.6}$$

BIBLIOGRAPHY

[1] Yik San Kwoh, Joahin Hou, Edmond A Jonckheere, and Samad Hayati. A robot with improved absolute positioning accuracy for ct guided stereotactic brain surgery. *IEEE Transactions on Biomedical Engineering*, 35(2):153–160, 1988.

[2] András Hoznek. History of robotic surgery in urology. In *Robotic Urology*, pages 1–9. Springer, 2008.

[3] A Wolf, B Jaramaz, B Lisien, and AM DiGioia. Mbars: mini bone-attached robotic system for joint arthroplasty. *The International Journal of Medical Robotics and Computer Assisted Surgery*, 1(2):101–121, 2005.

[4] Russell H Taylor, Brent D Mittelstadt, Howard A Paul, William Hanson, Peter Kazanzides, Joel F Zuhars, Bill Williamson, Bela L Musits, Edward Glassman, and William L Bargar. An image-directed robotic system for precise orthopaedic surgery. *IEEE Transactions on Robotics and Automation*, 10(3):261–275, 1994.

[5] Francois Leitner, Frederic Picard, Richard Minfelde, H Schulz, Philippe Cinquin, and Dominique Saragaglia. Computer-assisted knee surgical total replacement. In *CVRMed-MRCAS'97*, pages 629–638. Springer, 1997.

[6] Jongwon Lee, Keehoon Kim, Wan Kyun Chung, Seungmoon Choi, and Young Soo Kim. Human-guided surgical robot system for spinal fusion surgery: Corass. In *Robotics and Automation, 2008. ICRA 2008. IEEE International Conference on*, pages 3881–3887. IEEE, 2008.

[7] T Cill Kienzle, S David Stulberg, Michael Peshkin, Arthur Quaid, Jon Lea, A Goswani, and Chi-haur Wu. Total knee replacement. *IEEE Engineering in Medicine and Biology Magazine*, 14(3):301–306, 1995.

[8] Peter Kazanzides, Brent D Mittelstadt, Bela L Musits, William L Bargar, Joel F Zuhars, Bill Williamson, Phillip W Cain, and Emily J Carbone. An integrated system for cementless hip replacement. *IEEE Engineering in Medicine and Biology Magazine*, 14(3):307–313, 1995.

[9] Marco Fadda, D Bertelli, Sandra Martelli, Maurilio Marcacci, Paolo Dario, Cristiano Paggetti, D Caramella, and D Trippi. Computer assisted planning for total knee arthroplasty. In *CVRMed-MRCAS'97*, pages 617–628. Springer, 1997.

[10] Sharon J Harris, WJ Lin, KL Fan, Roger D Hibberd, Justin Cobb, R Middleton, and Brian L Davies. Experiences with robotic systems for knee surgery. In *CVRMed-MRCAS'97*, pages 757–766. Springer, 1997.

[11] BL Davies, KL Fan, RD Hibberd, M Jakopec, and SJ Harris. Acrobot-using robots and surgeons synergistically in knee surgery. In *Advanced Robotics, 1997. ICAR'97. Proceedings., 8th International Conference on*, pages 173–178. IEEE, 1997.

[12] BL Davies, FM Rodriguez y Baena, ARW Barrett, MPSF Gomes, SJ Harris, M Jakopec, and JP Cobb. Robotic control in knee joint replacement surgery. *Proceedings of the Institution of Mechanical Engineers, Part H: Journal of Engineering in Medicine*, 221(1):71–80, 2007.

[13] SC Ho, RD Hibberd, and BL Davies. Robot assisted knee surgery. *IEEE Engineering in Medicine and Biology Magazine*, 14(3):292–300, 1995.

[14] R Nakamura, S Omori, Y Muragaki, K Miura, M Doi, I Sakuma, and H Iseki. A robotic neurosurgery system with autofocusing motion control for mid-infrared laser

ablation. In *MICCAI2006 Workshop Proceedings, MICCAI 2006 Medical Robotics Workshop, Copenhagen*, pages 108–115, 2006.

[15] Kazuhiro Hongo, Shigeaki Kobayashi, Yukinari Kakizawa, Jun-ichi Koyama, Tetsuya Goto, Hiroshi Okudera, Kazutoshi Kan, Masakatsu G Fujie, Hiroshi Iseki, and Kintomo Takakura. Neurobot: telecontrolled micromanipulator system for minimally invasive microneurosurgerypreliminary results. *Neurosurgery*, 51(4):985–988, 2002.

[16] Daisuke Asai, Surman Katopo, Jumpei Arata, Shinichi Warisawa, Mamoru Mitsuishi, Akio Morita, Shigeo Sora, Takaaki Kirino, and Ryo Mochizuki. Microneurosurgical system in the deep surgical field. *Medical Image Computing and Computer-Assisted Intervention–MICCAI 2004*, pages 33–40, 2004.

[17] M Cenk Çavuşoğlu, Winthrop Williams, Frank Tendick, and S Shankar Sastry. Robotics for telesurgery: Second generation berkeley/ucsf laparoscopic telesurgical workstation and looking towards the future applications. *Industrial Robot: An International Journal*, 30(1):22–29, 2003.

[18] Ana Luisa Trejos and Rajnikant V Patel. Port placement for endoscopic cardiac surgery based on robot dexterity optimization. In *Robotics and Automation, 2005. ICRA 2005. Proceedings of the 2005 IEEE International Conference on*, pages 912–917. IEEE, 2005.

[19] Olivier Schneider, Jocelyne Troccaz, Olivier Chavanon, and Dominique Blin. Padyc: a synergistic robot for cardiac puncturing. In *Robotics and Automation, 2000. Proceedings. ICRA'00. IEEE International Conference on*, volume 3, pages 2883–2888. IEEE, 2000.

[20] Nicholas Patronik, Marco Zenati, and Cameron Riviere. Crawling on the heart: a mobile robotic device for minimally invasive cardiac interventions. *Medical Image Computing and Computer-Assisted Intervention–MICCAI 2004*, pages 9–16, 2004.

[21] Takeyoshi Ota, Amir Degani, David Schwartzman, Brett Zubiate, Jeremy McGarvey, Howie Choset, and Marco A Zenati. A novel highly articulated robotic surgical system for epicardial ablation. In *Engineering in Medicine and Biology Society, 2008. EMBS 2008. 30th Annual International Conference of the IEEE*, pages 250–253. IEEE, 2008.

[22] Samuel B Kesner and Robert D Howe. Position control of motion compensation cardiac catheters. *IEEE Transactions on Robotics*, 27(6):1045–1055, 2011.

[23] Amir Degani, Howie Choset, Alon Wolf, and Marco A Zenati. Highly articulated robotic probe for minimally invasive surgery. In *Robotics and Automation, 2006. ICRA 2006. Proceedings 2006 IEEE International Conference on*, pages 4167–4172. IEEE, 2006.

[24] Jeremy W Cannon, Jeffrey A Stoll, Shaun D Selha, Pierre E Dupont, Robert D Howe, and David F Torchiana. Port placement planning in robot-assisted coronary artery bypass. *IEEE transactions on Robotics and Automation*, 19(5):912–917, 2003.

[25] Paurush Babbar, Ashok K Hemal, et al. Robot-assisted urologic surgery in 2010-advancements and future outlook. *Urology annals*, 3(1):1, 2011.

[26] Li-Ming Su, Balazs P Vagvolgyi, Rahul Agarwal, Carol E Reiley, Russell H Taylor, and Gregory D Hager. Augmented reality during robot-assisted laparoscopic partial nephrectomy: toward real-time 3d-ct to stereoscopic video registration. *Urology*, 73(4):896–900, 2009.

[27] Sanjeev Kaul, Rajesh Laungani, Richard Sarle, Hans Stricker, James Peabody, Ray Littleton, and Mani Menon. da vinci-assisted robotic partial nephrectomy: technique and results at a mean of 15 months of follow-up. *European urology*, 51(1):186–192, 2007.

[28] Evangelos Liatsikos, Panagiotis Kallidonis, Minh Do, Anja Dietel, Abdulrahman Al-Aown, Constantinos Constantinidis, and Jens-Uwe Stolzenburg. Laparoscopic radical and partial nephrectomy: technical issues and outcome. *World journal of urology*, 31(4):785–791, 2013.

[29] Craig Rogers, Shyam Sukumar, and Inderbir S Gill. Robotic partial nephrectomy: the real benefit. *Current opinion in urology*, 21(1):60–64, 2011.

[30] Michael W Phelan, Kent T Perry, John Gore, and Peter G Schulam. Laparoscopic partial nephrectomy and minimally invasive nephronsparing surgery. *Current urology reports*, 4(1):13–20, 2003.

[31] Georges-Pascal Haber, Michael A White, Riccardo Autorino, Pedro F Escobar, Matthew D Kroh, Sricharan Chalikonda, Rakesh Khanna, Sylvain Forest, Bo Yang, Fatih Altunrende, et al. Novel robotic da vinci instruments for laparoendoscopic single-site surgery. *Urology*, 76(6):1279–1282, 2010.

[32] Yu Gong, Chuanjun Du, David Y Josephson, Timothy G Wilson, and Rebecca Nelson. Four-arm robotic partial nephrectomy for complex renal cell carcinoma. *World journal of urology*, 28(1):111–115, 2010.

[33] Tom Deklaj, David A Lifshitz, Sergey A Shikanov, Mark H Katz, Kevin C Zorn, and Arieh L Shalhav. Laparoscopic radical versus laparoscopic partial nephrectomy for clinical t1bn0m0 renal tumors: comparison of perioperative, pathological, and functional outcomes. *Journal of endourology*, 24(10):1603–1607, 2010.

[34] P Chatzilias, Z Kamarianakis, S Golemati, and M Christodoulou. Robotic control in hand-assisted laparoscopic nephrectomy in humans-a pilot study. In *Engineering in Medicine and Biology Society, 2004. IEMBS'04. 26th Annual International Conference of the IEEE*, volume 1, pages 2742–2745. IEEE, 2004.

[35] Geoffrey N Box, Hak J Lee, Ricardo JS Santos, Jose Benito A Abraham, Michael K Louie, Aldrin Joseph R Gamboa, Reza Alipanah, Leslie A Deane, Elspeth M McDougall, and Ralph V Clayman. Rapid communication: robot-assisted notes nephrectomy: initial report. *Journal of Endourology*, 22(3):503–506, 2008.

[36] B L Davies, R D Hibberd, W S Ng, A G Timoney, and J E A Wickham. The development of a surgeon robot for prostatectomies. *Proceedings of the Institution of Mechanical Engineers, Part H: Journal of Engineering in Medicine*, 205(35):35–38, 1991.

[37] Carter Q Le, Khai-Linh V Ho, and Matthew T Gettman. Davinci-assisted laparoscopic radical prostatectomy: the learning curve. In *Biomedical Optics (BiOS) 2007*, pages 642412–642412. International Society for Optics and Photonics, 2007.

[38] WS Ng, BL Davies, AG Timoney, and RD Hibberd. The use of ultrasound in automated prostatectomy. *Medical and Biological Engineering and Computing*, 31(4):349–354, 1993.

[39] Samuel P Sterrett, Timo Laurila, Gaurav Bandi, and David F Jarrard. Identification and preservation of accessory pudendal vessels during robot-assisted laparoscopic radical retropubic prostatectomy. *Journal of Robotic Surgery*, 2(1):31–34, 2008.

[40] SP DiMaio, GS Fischer, SJ Haker, N Hata, I Iordachita, CM Tempany, R Kikinis, and G Fichtinger. A system for MRI-guided prostate interventions. In *Biomedical Robotics and Biomechatronics, 2006. BioRob 2006. The First IEEE/RAS-EMBS International Conference on*, pages 68–73. IEEE, 2006.

[41] Tarun K Podder, Ivan Buzurovic, and Yan Yu. Multichannel robot for image-guided brachytherapy. In *BioInformatics and BioEngineering (BIBE), 2010 IEEE International Conference on*, pages 209–213. IEEE, 2010.

[42] Gabor Fichtinger, Jonathan P Fiene, Christopher W Kennedy, Gernot Kronreif, Iulian Iordachita, Danny Y Song, Everette C Burdette, and Peter Kazanzides. Robotic assistance for ultrasound-guided prostate brachytherapy. *Medical image analysis*, 12(5):535–545, 2008.

[43] John W Hill, Philip S Green, Joel F Jensen, Yonael Gorfu, and Ajit S Shah. Telepresence surgery demonstration system. In *Robotics and Automation, 1994. Proceedings., 1994 IEEE International Conference on*, pages 2302–2307. IEEE, 1994.

[44] Paul S Schenker, HO Das, and R Timothy. Development of a new high-dexterity manipulator for robot-assisted microsurgery. In *Proceedings of SPIE-The International Society for Optical Engineering: Telemanipulator and Telepresence Technologies*, volume 2351, pages 191–198, 1995.

[45] Russell H Taylor, Janez Funda, Ben Eldridge, Steve Gomory, Kreg Gruben, David LaRose, Mark Talamini, Louis Kavoussi, and James Anderson. A telerobotic assistant for laparoscopic surgery. *IEEE Engineering in Medicine and Biology Magazine*, 14(3):279–288, 1995.

[46] SW Unger, HM Unger, and RT Bass. Aesop robotic arm. *Surgical endoscopy*, 8(9):1131–1131, 1994.

[47] Jonathan M Sackier and Yulun Wang. Robotically assisted laparoscopic surgery. *Surgical endoscopy*, 8(1):63–66, 1994.

[48] A Imme, P Caglia, L Gandolfo, G Cavallaro, M Donati, and C Amodeo. Robotic techniques in laparoscopic surgery. *Chirurgia italiana*, 54(1):111–113, 2002.

[49] Garth H Ballantyne. Robotic surgery, telerobotic surgery, telepresence, and telementoring. *Surgical endoscopy*, 16(10):1389–1402, 2002.

[50] The kindness of strangers. https://www.economist.com/blogs/babbage/2012/01/surgical-robots, January 2012. Accessed: 2017-06-30.

[51] Intuitive Surgical® FAQs page. https://www.intuitivesurgical.com/company/faqs.html#5. Accessed: 2017-06-30.

[52] KK Badani, S Kaul, M Menon, and David I Lee. Evolution of robotic radical prostatectomy: assessment after 2766 procedures. *Journal of Endourology*, 22(2):241–242, 2008.

[53] Jacques Ferlay, Isabelle Soerjomataram, Rajesh Dikshit, Sultan Eser, Colin Mathers, Marise Rebelo, Donald Maxwell Parkin, David Forman, and Freddie Bray. Cancer incidence and mortality worldwide: sources, methods and major patterns in globocan 2012. *International journal of cancer*, 136(5), 2015.

[54] *Cancer Facts & Figures 2016*. Atlanta, Ga: American Cancer, 2016.

[55] Marko Babjuk, Andreas Böhle, Maximilian Burger, Otakar Capoun, Daniel Cohen, Eva M Compérat, Virginia Hernández, Eero Kaasinen, Joan Palou, Morgan Rouprêt, et al. Eau guidelines on non–muscle-invasive urothelial carcinoma of the bladder: update 2016. *European urology*, 71(3):447–461, 2017.

[56] David Pan and Mark S Soloway. The importance of transurethral resection in managing patients with urothelial cancer in the bladder: proposal for a transurethral resection of bladder tumor checklist. *European urology*, 61(6):1199–203, June 2012.

[57] Kishore T Adiyat, Devendar Katkoori, Cynthia T Soloway, Rosely De los Santos, Murugesan Manoharan, and Mark S Soloway. ”Complete transurethral resection of

bladder tumor": are the guidelines being followed? *Urology*, 75(2):365–7, February 2010.

[58] Maurizio Brausi, Laurence Collette, Karlheinz Kurth, Adrian P. Van Der Meijden, Wim Oosterlinck, J. A. Witjes, Donald Newling, Christian Bouffioux, and Richard J. Sylvester. Variability in the recurrence rate at first follow-up cystoscopy after TUR in stage Ta T1 transitional cell carcinoma of the bladder: A combined analysis of seven EORTC studies. *European Urology*, 41:523–531, 2002.

[59] Marc F Botteman, Chris L Pashos, Alberto Redaelli, Benjamin Laskin, and Robert Hauser. The health economics of bladder cancer: a comprehensive review of the published literature. *PharmacoEconomics*, 21:1315–1330, 2003.

[60] K. D. Sievert, B. Amend, U. Nagele, D. Schilling, J. Bedke, M. Horstmann, J. Hennenlotter, S. Kruck, and A. Stenzl. Economic aspects of bladder cancer: What are the benefits and costs? *World Journal of Urology*, 27:295–300, 2009.

[61] Kyle A Richards, Norm D Smith, and Gary D Steinberg. The Importance of Transurethral Resection of Bladder Tumor in the Management of Nonmuscle Invasive Bladder Cancer: A Systematic Review of Novel Technologies. *The Journal of urology*, 191(6):1655–1664, February 2014.

[62] R. Goldman, A. Bajo, L. MacLachlan, R. Pickens, S. Herrell, and N. Simaan. Design and Performance Evaluation of a Minimally Invasive Telerobotic Platform for Transurethral Surveillance and Intervention. *IEEE Transactions on Biomedical Engineering*, pages 1–1, 2013.

[63] Ryan B. Pickens, Andrea Bajo, Nabil Simaan, and Duke Herrell. A Pilot Ex Vivo Evaluation of a Telerobotic System for Transurethral Intervention and Surveillance. *Journal of Endourology*, 29:231–234, 2015.

[64] Pablo Eduardo Garcia Kilroy, Kenneth C Miller, Thomas D Egan, Thomas P Low, Arthur Maxwell Crittenden, and Karen Shakespear Koenig. Compact robotic wrist, March 13 2014. US Patent App. 14/388,208.

[65] BL Davies, RD Hibberd, MJ Coptcoat, and JEA Wickham. A surgeon robot prostatectomya laboratory evaluation. *Journal of medical engineering & technology*, 13(6):273–277, 1989.

[66] SJ Harris, F Arambula-Cosio, Q Mei, RD Hibberd, BL Davies, JEA Wickham, MS Nathan, and B Kundu. The probotan active robot for prostate resection. *Proceedings of the Institution of Mechanical Engineers, Part H: Journal of Engineering in Medicine*, 211(4):317–325, 1997.

[67] Kevin Cleary and Charles Nguyen. State of the art in surgical robotics: clinical applications and technology challenges. *Computer Aided Surgery*, 6(6):312–328, 2001.

[68] Janez Funda, Russell H Taylor, Ben Eldridge, Stephen Gomory, and Kreg G Gruben. Constrained cartesian motion control for teleoperated surgical robots. *IEEE Transactions on Robotics and Automation*, 12(3):453–465, 1996.

[69] Vipul R Patel. *Robotic urologic surgery*. Springer, 2012.

[70] Jacques Marescaux, Joel Leroy, Michel Gagner, Francesco Rubino, Didier Mutter, Michel Vix, Steven E Butner, and Michelle K Smith. Transatlantic robot-assisted telesurgery. *Nature*, 413(6854):379, 2001.

[71] Monish Aron, Georges-Pascal Haber, Mihir M Desai, and Inderbir S Gill. Flexible robotics: a new paradigm. *Current Opinion in Urology*, 17(3):151–155, 2007.

[72] Mihir M Desai, Monish Aron, Inderbir S Gill, Georges Pascal-Haber, Osamu Ukimura, Jihad H Kaouk, Gregory Stahler, Federico Barbagli, Christopher Carl-

son, and Fredric Moll. Flexible robotic retrograde renoscopy: description of novel robotic device and preliminary laboratory experience. *Urology*, 72(1):42–46, 2008.

[73] Mihir M Desai, Rishi Grover, Monish Aron, Georges-Pascal Haber, Arvind Ganpule, Jihad H Kaouk, Mahesh Desai, and Inderbir S Gill. Remote robotic ureteroscopic laser lithotripsy for renal calculi: initial clinical experience with a novel flexible robotic system. *The Journal of Urology*, 179(4):435, 2008.

[74] *Publications section of TransEnterix portal®*, accessed August 8 2017.

[75] Salvatore Gueli Alletti, C Rossitto, S Cianci, E Perrone, S Pizzacalla, G Monterossi, G Vizzielli, S Gidaro, and G Scambia. The senhance surgical robotic system (senhance) for total hysterectomy in obese patients: a pilot study. *Journal of Robotic Surgery*, pages 1–6, 2017.

[76] Kai Xu, Roger E Goldman, Jienan Ding, Peter K Allen, Dennis L Fowler, and Nabil Simaan. System design of an insertable robotic effector platform for single port access (spa) surgery. In *Intelligent Robots and Systems, 2009. IROS 2009. IEEE/RSJ International Conference on*, pages 5546–5552. IEEE, 2009.

[77] Jens J Rassweiler, Riccardo Autorino, Jan Klein, Alex Mottrie, Ali Serdar Goezen, Jens-Uwe Stolzenburg, Koon H Rha, Marc Schurr, Jihad Kaouk, Vipul Patel, et al. Future of robotic surgery in urology. *BJU international*, 2017.

[78] Jacques Ferlay, Isabelle Soerjomataram, Rajesh Dikshit, Sultan Eser, Colin Mathers, Marise Rebelo, Donald Maxwell Parkin, David Forman, and Freddie Bray. Cancer incidence and mortality worldwide: sources, methods and major patterns in globocan 2012. *International journal of cancer*, 136(5):E359–E386, 2015.

[79] *Cancer Facts & Figures 2017*. Atlanta, Ga: American Cancer, 2017.

[80] Evelyne CC Cauberg, Daniël M de Bruin, Dirk J Faber, Ton G van Leeuwen, Jean JMCH de la Rosette, and Theo M de Reijke. A new generation of optical diagnostics for bladder cancer: technology, diagnostic accuracy, and future applications. *European urology*, 56(2):287–297, 2009.

[81] Liang Cheng, Rodolfo Montironi, Darrell D Davidson, and Antonio Lopez-Beltran. Staging and reporting of urothelial carcinoma of the urinary bladder. *Modern Pathology*, 22:S70–S95, 2009.

[82] Harry W Herr and S Machele Donat. Quality control in transurethral resection of bladder tumours. *BJU international*, 102(9 Pt B):1242–6, November 2008.

[83] Misop Han and Mark P Schoenberg. The use of molecular diagnostics in bladder cancer. In *Urologic Oncology: Seminars and Original Investigations*, volume 5, pages 87–92. Elsevier, 2000.

[84] Karl D Sievert, B Amend, U Nagele, D Schilling, J Bedke, M Horstmann, J Hennenlotter, S Kruck, and A Stenzl. Economic aspects of bladder cancer: what are the benefits and costs? *World journal of urology*, 27(3):295–300, 2009.

[85] Maurizio Brausi, Laurence Collette, Karlheinz Kurth, Adrian P van der Meijden, Wim Oosterlinck, JA Witjes, Donald Newling, Christian Bouffioux, Richard J Sylvester, EORTC Genito-Urinary Tract Cancer Collaborative Group, et al. Variability in the recurrence rate at first follow-up cystoscopy after tur in stage ta t1 transitional cell carcinoma of the bladder: a combined analysis of seven eortc studies. *European urology*, 41(5):523–531, 2002.

[86] Harry W Herr and S Machele Donat. Quality control in transurethral resection of bladder tumours. *BJU international*, 102(9b):1242–1246, 2008.

[87] MA Zurkirchen, T Sulser, A Gaspert, and D Hauri. Second transurethral resection of superficial transitional cell carcinoma of the bladder: a must even for experienced urologists. *Urologia internationalis*, 72(2):99–102, 2004.

[88] Rauf Taner Divrik, Ümit Yildirim, Ferruh Zorlu, and Haluk Özen. The effect of repeat transurethral resection on recurrence and progression rates in patients with t1 tumors of the bladder who received intravesical mitomycin: a prospective, randomized clinical trial. *The Journal of urology*, 175(5):1641–1644, 2006.

[89] Wansuk Kim, Cheryn Song, Sejun Park, Jongwon Kim, Jinsung Park, Seong Cheol Kim, Yong Mee Cho, Bumsik Hong, and Hanjong Ahn. Value of immediate second resection of the tumor bed to improve the effectiveness of transurethral resection of bladder tumor. *Journal of endourology*, 26(8):1059–1064, 2012.

[90] Marc F Botteman, Chris L Pashos, Alberto Redaelli, Benjamin Laskin, and Robert Hauser. The health economics of bladder cancer. *Pharmacoeconomics*, 21(18):1315–1330, 2003.

[91] Eleanor R Ray and Tim S OBrien. Should urologists be spending more time on the golf course? *BJU international*, 100(4):728–729, 2007.

[92] Rinzo Ukai, Eiso Kawashita, and Hiroshi Ikeda. A new technique for transurethral resection of superficial bladder tumor in 1 piece. *The Journal of urology*, 163(3):878–879, 2000.

[93] Toshio Kawada, Kazunori Ebihara, Takanori Suzuki, Kyoichi Imai, and Hidetoshi Yamanaka. A new technique for transurethral resection of bladder tumors: rotational tumor resection using a new arched electrode. *The Journal of urology*, 157(6):2225–2226, 1997.

[94] Michele Lodde, Lukas Lusuardi, Salvatore Palermo, Diego Signorello, Klaus Maier, Rudolf Hohenfellner, and Armin Pycha. En bloc transurethral resection of bladder tumors: use and limits. *Urology*, 62(6):1089–1091, 2003.

[95] Evelyne CC Cauberg, Jean JMCH de la Rosette, and Theo M de Reijke. How to improve the effectiveness of transurethral resection in nonmuscle invasive bladder cancer? *Current opinion in urology*, 19(5):504–510, 2009.

[96] Nicholas A Maruniak, Kimiko Takezawa, and William M Murphy. Accurate pathological staging of urothelial neoplasms requires better cystoscopic sampling. *The Journal of urology*, 167(6):2404–2407, 2002.

[97] Ronald OP Draga, Matthijs CM Grimbergen, Esther T Kok, Trudy N Jonges, Christiaan FP van Swol, and Ruud JLH Bosch. The quality of 5-aminolevulinic acid-induced photodynamic diagnosis and transurethral resection of bladder tumors: does the urologist play a role? *Urologia internationalis*, 89(3):326–331, 2012.

[98] Harry W Herr. The value of a second transurethral resection in evaluating patients with bladder tumors. *The Journal of urology*, 162(1):74–76, 1999.

[99] Rauf Taner Divrik, Umit Yildirim, Ferruh Zorlu, and Haluk Ozen. The effect of repeat transurethral resection on recurrence and progression rates in patients with t1 tumors of the bladder who received intravesical mitomycin: a prospective, randomized clinical trial. *The Journal of urology*, 175(5):1641–1644, 2006.

[100] Ralph Madeb, Dragan Golijanin, Katia Noyes, Susan Fisher, Judith J Stephenson, Stacey R Long, Joy Knopf, Gary H Lyman, and Edward M Messing. Treatment of nonmuscle invading bladder cancer: do physicians in the united states practice evidence based medicine? *Cancer*, 115(12):2660–2670, 2009.

[101] Pravin K Rao and J Stephen Jones. Routine perioperative chemotherapy instillation with initial bladder tumor resection. *Cancer*, 115(5):997–1004, 2009.

[102] Olivier Traxer, Federico Pasqui, Bernard Gattegno, and Margaret S Pearle. Technique and complications of transurethral surgery for bladder tumours. *BJU international*, 94(4):492–496, 2004.

[103] R. Ukai, E. Kawashita, and H. Ikeda. A new technique for transurethral resection of superficial bladder tumor in 1 piece. *The Journal of urology*, 163(3):878–9, March 2000.

[104] Daniel Wilby, Kay Thomas, Eleanor Ray, Barnaby Chappell, and Timothy OBrien. Bladder cancer: new tur techniques. *World journal of urology*, 27(3):309, 2009.

[105] T Kawada, K Ebihara, T Suzuki, K Imai, and H Yamanaka. A new technique for transurethral resection of bladder tumors: rotational tumor resection using a new arched electrode., 1997.

[106] Angelo Naselli, Carlo Introini, Francesco Germinale, Bruno Spina, and Paolo Puppo. En bloc transurethral resection of bladder lesions: a trick to retrieve specimens up to 4.5 cm. *BJU international*, 109(6):960–963, 2012.

[107] Daniel A Barocas, Denise R Globe, Danielle C Colayco, Ahunna Onyenwenyi, Amanda S Bruno, Thomas J Bramley, and Rachel J Spear. Surveillance and treatment of non-muscle-invasive bladder cancer in the usa. *Advances in urology*, 2012, 2012.

[108] W. J. Yoon, S. Park, P. G. Reinhall, and E. J. Seibel. Development of an Automated Steering Mechanism for Bladder Urothelium Surveillance. *J Med Device*, 3(1):11004, Mar 2009.

[109] A Saad, DC Hanbury, TA McNicholas, GB Boustead, S Morgan, and AC Woodman. A study comparing various noninvasive methods of detecting bladder cancer in urine. *BJU international*, 89(4):369–373, 2002.

[110] Patrice Jichlinski. New diagnostic strategies in the detection and staging of bladder cancer. *Current opinion in urology*, 13(5):351–355, 2003.

[111] Thomas Filbeck, Uwe Pichlmeier, Ruth Knuechel, Wolf F Wieland, and Wolfgang Roessler. Clinically relevant improvement of recurrence-free survival with 5-aminolevulinic acid induced fluorescence diagnosis in patients with superficial bladder tumors. *The Journal of urology*, 168(1):67–71, 2002.

[112] Marko Babjuk, Viktor Soukup, Radko Petrik, Milan Jirsa, and Jan Dvoracek. 5-aminolaevulinic acid-induced fluorescence cystoscopy during transurethral resection reduces the risk of recurrence in stage ta/t1 bladder cancer. *BJU international*, 96(6):798–802, 2005.

[113] Angelo Naselli, Carlo Introini, Franco Bertolotto, Bruno Spina, and Paolo Puppo. Feasibility of transurethral resection of bladder lesion performed entirely by means of narrow-band imaging. *Journal of Endourology*, 24(7):1131–1134, 2010.

[114] Jen-Jane Liu, Michael J Droller, and Joseph C Liao. New optical imaging technologies for bladder cancer: considerations and perspectives. *The Journal of urology*, 188(2):361–368, 2012.

[115] Harry W Herr and S Machele Donat. A comparison of white-light cystoscopy and narrow-band imaging cystoscopy to detect bladder tumour recurrences. *BJU international*, 102(9):1111–1114, 2008.

[116] Evelyne CC Cauberg, Sarah Kloen, Mike Visser, Jean JMCH de la Rosette, Marko Babjuk, Viktor Soukup, Michael Pesl, Jaroslava Duskova, and Theo M de Reijke. Narrow band imaging cystoscopy improves the detection of non–muscle-invasive bladder cancer. *Urology*, 76(3):658–663, 2010.

[117] Katsunori Tatsugami, Kentaro Kuroiwa, Toshiyuki Kamoto, Hiroyuki Nishiyama, Jun Watanabe, Satoru Ishikawa, Nobuo Shinohara, Ataru Sazawa, Shoji Fukushima,

and Seiji Naito. Evaluation of narrow-band imaging as a complementary method for the detection of bladder cancer. *Journal of endourology*, 24(11):1807–1811, 2010.

[118] Harry W Herr and Sherri M Donat. Reduced bladder tumour recurrence rate associated with narrow-band imaging surveillance cystoscopy. *BJU international*, 107(3):396–398, 2011.

[119] Michael J Manyak, Natalia D Gladkova, John H Makari, Arnold M Schwartz, Elena V Zagaynova, Ladan Zolfaghari, Jason M Zara, Rashid Iksanov, and Felix I Feldchtein. Evaluation of superficial bladder transitional-cell carcinoma by optical coherence tomography. *Journal of endourology*, 19(5):570–574, 2005.

[120] Seth P Lerner, Alvin C Goh, Nancy J Tresser, and Steven S Shen. Optical coherence tomography as an adjunct to white light cystoscopy for intravesical real-time imaging and staging of bladder cancer. *Urology*, 72(1):133–137, 2008.

[121] A Karl, H Stepp, E Willmann, A Buchner, Y Hocaoglu, C Stief, and S Tritschler. Optical coherence tomography for bladder cancer-ready as a surrogate for optical biopsy?-results of a prospective mono-centre study. *European journal of medical research*, 15(3):131, 2010.

[122] Jens Gammelgaard and Hans Henrik Holm. Transurethral and transrectal ultrasonic scanning in urology. *The Journal of urology*, 124(6):863–868, 1980.

[123] BB Goldberg and JB Liu. Endoluminal urologic ultrasound. *Scandinavian journal of urology and nephrology. Supplementum*, 137:147–154, 1991.

[124] Mamdouh Koraitim, Baher Kamal, Nabila Metwalli, and Yehia Zaky. Transurethral ultrasonographic assessment of bladder carcinoma: its value and limitation. *The Journal of urology*, 154(2):375–378, 1995.

[125] Kazutaka Horiuchi, Narumi Tsuboi, Hiroyuki Shimizu, Ichiro Matsuzawa, Go Kimura, Kazuhiro Yoshida, and Masao Akimoto. High-frequency endoluminal ultrasonography for staging transitional cell carcinoma of the bladder. *Urology*, 56(3):404–407, 2000.

[126] W. Sakamoto, S. Nishio, and M. Maekawa. Diagnosis of bladder cancer by transurethral ultrasonic scanning. *Hinyokika Kiyo.*, 29(9):1015–1018, 1983.

[127] Giuseppe Caruso, Giuseppe Salvaggio, Antonella Campisi, Darwin Melloni, Massimo Midiri, Michele Bertolotto, and Roberto Lagalla. Bladder tumor staging: comparison of contrast-enhanced and gray-scale ultrasound. *American Journal of Roentgenology*, 194(1):151–156, 2010.

[128] C Nicolau, L Bunesch, L Peri, R Salvador, JM Corral, C Mallofre, and C Sebastia. Accuracy of contrast-enhanced ultrasound in the detection of bladder cancer. *The British journal of radiology*, 84(1008):1091–1099, 2011.

[129] Qiu-yang Li, Jie Tang, En-hui He, Yan-mi Li, Yun Zhou, Xu Zhang, and Guangfu Chen. Clinical utility of three-dimensional contrast-enhanced ultrasound in the differentiation between noninvasive and invasive neoplasms of urinary bladder. *European journal of radiology*, 81(11):2936–2942, 2012.

[130] *Cancer Facts & Figures 2015*. Atlanta, Ga: American Cancer, 2015.

[131] Friedrich-Carl von Rundstedt. New imaging techniques for nonmuscle invasive bladder cancer. *Current opinion in urology*, 24:532–539, 2014.

[132] A Dick, R Barnes, H Hadley, RT Bergman, and CA Ninan. Complications of transurethral resection of bladder tumors: prevention, recognition and treatment. *The Journal of urology*, 124(6):810811, December 1980.

[133] Jan Ekengren, Peter Conner, Marianne Lindholm, and Robert G. Hahn. Fluid absorption during transurethral bladder surgery. *Scandinavian Journal of Urology and Nephrology*, 29(4):519–520, 1995.

[134] S. Z. Freed. Vesicoureteral reflux following transurethral resection of bladder tumors. *Jornal of Urology*, 116(2):184–187, Aug 1976.

[135] Maurizio Brausi, J. Alfred Witjes, Donald Lamm, Raj Persad, Joan Palou, Marc Colombel, Roger Buckley, Mark Soloway, Hideyuki Akaza, and Andreas Bhle. A review of current guidelines and best practice recommendations for the management of nonmuscle invasive bladder cancer by the international bladder cancer group. *The Journal of Urology*, 186(6):2158 – 2167, 2011.

[136] Peter Black. Bladder Tumor Resection: Doing it Right. *The Journal of urology*, pages 1646–7, March 2014.

[137] Sang Eun Lee, In Gab Jeong, Ja Hyeon Ku, Cheol Kwak, Eunsik Lee, and Jin Soo Jeong. Impact of transurethral resection of bladder tumor: analysis of cystectomy specimens to evaluate for residual tumor. *Urology*, 63(5):873–7; discussion 877, May 2004.

[138] Daniel Wilby, Thomas Kay, Eleanor Ray, Barnaby Chappell, and Timothy OBrien. Bladder cancer: new tur techniques. *World Journal of Urology*, 27:309–312, 2009.

[139] E. Sanchez de Badajoz, A. Jimenez Garrido, F. Garcia Vacas, V. F. Munoz Martinez, J. Gomez de Gabriel, J. Fernandez Lozano, and A. Garcia Cerezo. New master arm for transurethral resection with a robot. *Arch. Esp. Urol.*, 55(10):1247–1250, Dec 2002.

[140] R. Hashimoto, Daeyoung Kim, N. Hata, and T. Dohi. A tubular organ resection manipulator for transurethral resection of the prostate. In *Intelligent Robots and*

Systems, 2004. (IROS 2004). Proceedings. 2004 IEEE/RSJ International Conference on, volume 4, pages 3954–3959, Sept 2004.

[141] Andrea Bajo, Latif M. Dharamsi, James L. Netterville, Catlyn. G. Garret, and N. Simaan. Robotic-Assisted Micro-Surgery of the Throat: the Trans-Nasal Approach. In *Proc. IEEE Int. Conf. on Robotics and Automation*, pages pp. 232–238, Karlsruhe, Germany, 2013.

[142] Marko Babjuk. Transurethral resection of nonmuscle-invasive bladder cancer. *European Urology Supplements*, 8(7):542–548, sep 2009.

[143] N. Sarli, T. Marien, S.D. Herrell, and N. Simaan. Characterization of resection dexterity in transurethral resection of bladder tumor: A kinematic study. In *IEEE International Conference on Robotics and Automation (ICRA)*, pages 5324–5329, May 2015.

[144] John W. Hole. *Human Anatomy and Physiology*. Dubuque, 2nd edition, 1981.

[145] Tsuneo Yoshikawa. Manipulability of robotic mechanisms. *The international journal of Robotics Research*, 4(2):3–9, 1985.

[146] Tsuneo Yoshikawa. *Foundations of robotics: analysis and control*. Mit Press, 1990.

[147] Jorge Angeles. *Fundamentals of Robotic Mechanical Systems*. Springer-Verlag, 2nd edition, 2003.

[148] Charles A. Klein and Bruce E. Blaho. Dexterity measures for the design and control of kinematically redundant manipulators. *Int. J. Rob. Res.*, 6(2):72–83, 1987.

[149] Eliakim Hastings Moore. On the reciprocal of general algebraic matrix. *Bulletin of the American Mathematical Society*, 26(9):394–395, 1920.

[150] Peter Lancaster and Miron Tismenetsky. *The Theroy of Mastrices with Applications*. Academic Press, 2 edition, 1985.

[151] Richard J Hendrick, S D Herrell, and Robert J Webster III. A Multi-Arm Hand-Held Robotic System for Transurethral Laser Prostate Surgery. In *IEEE International Conference on Robotics and Automation*, pages 2850–2855, 2014.

[152] John J. Craig. *Introduction to Robotics: Mechanics and Control*. Addison-Wesley Longman Publishing Co., Inc., 2nd edition, jan 1989.

[153] J. Carpenter and J. Bithell. Bootstrap confidence intervals: when, which, what? A practical guide for medical statisticians. *Stat Med*, 19(9):1141–1164, May 2000.

[154] Allan J Pantuck, Jack Baniel, Ziya Kirkali, Tobias Klatte, Nazy Zomorodian, Ofer Yossepowitch, and Arie S Belldegrun. A novel resectoscope for transurethral resection of bladder tumors and the prostate. *The Journal of urology*, 178(6):2331–2336, 2007.

[155] U Nagele, M Kugler, A Nicklas, AS Merseburger, U Walcher, G Mikuz, and TR Herrmann. Waterjet hydrodissection: first experiences and short-term outcomes of a novel approach to bladder tumor resection. *World journal of urology*, 29(4):423–427, 2011.

[156] Hans-Martin Fritsche, Wolfgang Otto, Fabian Eder, Ferdinand Hofstädter, Stefan Denzinger, Christian G Chaussy, Christian Stief, Wolf F Wieland, and Maximilian Burger. Water-jet–aided transurethral dissection of urothelial carcinoma: A prospective clinical study. *Journal of endourology*, 25(10):1599–1603, 2011.

[157] Andrew A Goldenberg, John Trachtenberg, Walter Kucharczyk, Yang Yi, Masoom Haider, Leo Ma, Robert Weersink, and Cyrus Raoufi. Robotic system for closed-bore mri-guided prostatic interventions. *IEEE/ASME Transactions On Mechatronics*, 13(3):374–379, 2008.

[158] Junichi Tokuda, Gregory S Fischer, Simon P DiMaio, David G Gobbi, Csaba Csoma, Philip W Mewes, Gabor Fichtinger, Clare M Tempany, and Nobuhiko Hata. Inte-

grated navigation and control software system for mri-guided robotic prostate interventions. *Computerized Medical Imaging and Graphics*, 34(1):3–8, 2010.

[159] Pierre C Mozer, Alan W Partin, and Dan Stoianovici. Robotic image-guided needle interventions of the prostate. *Rev. Urol*, 11(1):7–15, 2009.

[160] Peter Gilling, Rana Reuther, Arman Kahokehr, and Mark Fraundorfer. Aquablation–image-guided robot-assisted waterjet ablation of the prostate: initial clinical experience. *BJU international*, 117(6):923–929, 2016.

[161] E Sánchez de Badajoz, A Jimenez Garrido, VF Muñoz Martínez, JM GOMEZ DE-GABRIEL, and A García Cerezo. Reseccion transuretral mediante control remoto. *Archivos españoles de urología*, 51(5):445–449, 1998.

[162] de Badajoz E Sánchez, Garrido A Jiménez, Vacas F García, Martínez VF Muñoz, de Gabriel J Gómez, Lozano J Fernández, and Cerezo A García. New master arm for transurethral resection with a robot. *Archivos espanoles de urologia*, 55(10):1247–1250, 2002.

[163] Ryuji Hashimoto, Daeyoung Kim, Nobuhiko Hata, and Takeyoshi Dohi. A tubular organ resection manipulator for transurethral resection of the prostate. In *Intelligent Robots and Systems, 2004.(IROS 2004). Proceedings. 2004 IEEE/RSJ International Conference on*, volume 4, pages 3954–3959. IEEE, 2004.

[164] Rajiv Chopra, Alexandra Colquhoun, Mathieu Burtnyk, William A Ndjin, Ilya Kobelevskiy, Aaron Boyes, Kashif Siddiqui, Harry Foster, Linda Sugar, Masoom A Haider, et al. Mr imaging–controlled transurethral ultrasound therapy for conformal treatment of prostate tissue: Initial feasibility in humans. *Radiology*, 265(1):303–313, 2012.

[165] Sascha A Ahyai, Karin Lehrich, and Rainer M Kuntz. Holmium laser enucleation versus transurethral resection of the prostate: 3-year follow-up results of a randomized clinical trial. *European urology*, 52(5):1456–1464, 2007.

[166] Gideon Ho, Wan Sing Ng, Ming Yeong Teo, Chee-Keong Kwoh, and Wai SC Cheng. Computer-assisted transurethral laser resection of the prostate (calrp): theoretical and experimental motion plan. *IEEE transactions on biomedical engineering*, 48(10):1125–1133, 2001.

[167] Sheila Russo, Paolo Dario, and Arianna Menciassi. A novel robotic platform for laser-assisted transurethral surgery of the prostate. *IEEE Transactions on Biomedical Engineering*, 62(2):489–500, 2015.

[168] Richard J Hendrick, Christopher R Mitchell, S Duke Herrell, and Robert J Webster III. Hand-held transendoscopic robotic manipulators: A transurethral laser prostate surgery case study. *The International journal of robotics research*, 34(13):1559–1572, 2015.

[169] Eric J Seibel, Richard S Johnston, and C David Melville. A full-color scanning fiber endoscope. In *Proc. SPIE*, volume 6083, page 608303, 2006.

[170] Timothy D Soper, Michael P Porter, and Eric J Seibel. Surface mosaics of the bladder reconstructed from endoscopic video for automated surveillance. *IEEE Transactions on Biomedical Engineering*, 59(6):1670–1680, 2012.

[171] Matthew R Burkhardt, Timothy D Soper, Woon Jong Yoon, and Eric J Seibel. Controlling the trajectory of a flexible ultrathin endoscope for fully automated bladder surveillance. *IEEE/ASME Transactions on Mechatronics*, 19(1):366–373, 2014.

[172] Xianming Ye, Yuanzheng Gong, and W Jong Yoon. Development of multisegment steering mechanism and 3-d panorama for automated bladder surveillance system. *IEEE/ASME Transactions on Mechatronics*, 21(2):993–1003, 2016.

[173] S. Coemert, M. Kollmer, M. Olmeda, Y. S. Krieger, S. V. Brecht, and T. C. Lueth. Development of a double arm endoscopic mini-manipulator system for transurethral resection of bladder tumors (TURBT). In *2017 IEEE/RSJ International Conference on Intelligent Robots and Systems (IROS)*, pages 1670–1676, Sept 2017.

[174] Kai Xu, Bo Liang, Zhengchen Dai, Jiangran Zhao, Bin Zhao, Huan Liu, Liang Xiao, and Yinghao Sun. Preliminary development of a continuum dual-arm surgical robotic system for transurethral procedures. In *International Conference on Intelligent Robotics and Applications*, pages 311–322. Springer, 2017.

[175] Oliver W Hakenberg, Clemens Linne, Andreas Manseck, and Manfred P Wirth. Bladder wall thickness in normal adults and men with mild lower urinary tract symptoms and benign prostatic enlargement. *Neurourology and urodynamics*, 19(5):585–593, 2000.

[176] Xi Zhang, Yang Liu, Baojuan Li, Guopeng Zhang, Zhengrong Liang, and Hongbing Lu. A pilot study on bladder wall thickness at different filling stages. In *SPIE Medical Imaging*, pages 94143O–94143O. International Society for Optics and Photonics, 2015.

[177] Giuseppe Del Giudice, Nima Sarli, Stanley D Herrell, and Nabil Simaan. Design considerations for continuum robot actuation units enabling dexterous transurethral bladder cancer resection. In *ASME 2016 International Design Engineering Technical Conferences and Computers and Information in Engineering Conference*, pages V05AT07A030–V05AT07A030. American Society of Mechanical Engineers, 2016.

[178] Nabil Simaan. Snake-Like Units Using Flexible Backbones and Actuation Redundancy for Enhanced Miniaturization. In *Proceedings of the 2005 IEEE International Conference on Robotics and Automation*, pages 3012–3017, Barcelona, Spain, 2005. IEEE.

[179] Nabil Simaan, Russell Taylor, and Paul Flint. High Dexterity Snake-like Robotic Slaves for Minimally Invasive Telesurgery of the Upper Airway. In C Barillot, D R Haynor, and P Hillier, editors, *International Conference on Medical Image Computing and Computer-Assisted Intervention (MICCAI '04) , LNCS 3217*, volume LNCS 3217, pages 17–24, 2004.

[180] Bryan A. Jones and Ian D. Walker. Practical kinematics for real-time implementation of continuum robots. *IEEE Trans. Robot. IEEE Transactions on Robotics*, 22(6):10871099, 2006.

[181] I.A. Gravagne and I.D. Walker. Kinematic transformations for remotely-actuated planar continuum robots. In *Proceedings 2000 ICRA. Millennium Conference. IEEE International Conference on Robotics and Automation. Symposia Proceedings (Cat. No.00CH37065)*, volume 1, pages 19–26. IEEE.

[182] N. Simaan, K. Xu, A. Kapoor, W. Wei, P. Kazanzides, P. Flint, and R. Taylor. Design and Integration of a Telerobotic System for Minimally Invasive Surgery of the Throat. *Int J Rob Res*, 28(9):1134–1153, Sep 2009.

[183] Kai Xu and Nabil Simaan. Intrinsic wrench estimation and its performance index for multisegment continuum robots. *Robotics, IEEE Transactions on*, 26(3):555–561, June 2010.

[184] Nabil Simaan, Russell H. Taylor, and Paul Flint. A Dexterous System for Laryngeal Surgery. In *2004 IEEE International Conference on Robotics and Automation*, pages 351–357, New Orleans, LA, 2004. IEEE.

[185] Roger E. Goldman, Andrea Bajo, and Nabil Simaan. Compliant motion control for multisegment continuum robots with actuation force sensing. *IEEE Transactions on Robotics*, 30(4):890–902, 2014.

[186] Nabil Simaan, Kai Xu, Wei Wei, Ankur Kapoor, Peter Kazanzides, Russell Taylor, and Paul Flint. Design and integration of a telerobotic system for minimally invasive surgery of the throat. *The International Journal of Robotics Research*, 28(9):1134–1153, 2009.

[187] R. Roy, L. Wang, and N. Simaan. Modeling and estimation of friction, extension, and coupling effects in multisegment continuum robots. 22(2):909–920, April 2017.

[188] Kai Xu and Nabil Simaan. Actuation Compensation for Flexible Surgical Snake-like Robots with Redundant Remote Actuation. In *2006 IEEE International Conference on Robotics and Automation*, number May, pages 4148–4154, Orlando, FL, USA, 2006.

[189] A. Bajo, R. E. Goldman, and N. Simaan. Configuration and joint feedback for enhanced performance of multi-segment continuum robots. In *2011 IEEE International Conference on Robotics and Automation*, pages 2905–2912, May 2011.

[190] J. Ding, K. Xu, R. Goldman, P. Allen, D. Fowler, and N. Simaan. Design, simulation and evaluation of kinematic alternatives for insertable robotic effectors platforms in single port access surgery. In *2010 IEEE International Conference on Robotics and Automation*, pages 1053–1058, May 2010.

[191] Yoshihiko Nakamura, Hideo Hanafusa, and Tsuneo Yoshikawa. Task-priority based redundancy control of robot manipulators. *The International Journal of Robotics Research*, 6(2):3–15, 1987.

[192] Andrea Bajo, Ryan B. Pickens, S. Duke Herrell, and Nabil Simaan. Constrained motion control of multisegment continuum robots for transurethral bladder resection and surveillance. In *Proceedings - IEEE International Conference on Robotics and Automation*, pages 5837–5842, 2013.

[193] Tan Fung Chan and Rajiv V Dubey. A weighted least-norm solution based scheme for avoiding joint limits for redundant joint manipulators. 11(2):286–292, 1995.

[194] Fan-Tien Cheng, Tzung-Liang Hour, York-Yin Sun, and Tsing-Hua Chen. Study and resolution of singularities for a 6-dof puma manipulator. 27(2):332–343, 1997.

[195] Intuitive Surgical® press release. http://investor.intuitivesurgical.com/phoenix.zhtml?c=122359&p=irol-newsArticle&ID=1920546&highlight=. Accessed: 2017-06-30.

[196] A. Bajo, R. E. Goldman, L. Wang, D. Fowler, and N. Simaan. Integration and preliminary evaluation of an insertable robotic effectors platform for single port access surgery. In *2012 IEEE International Conference on Robotics and Automation*, pages 3381–3387, May 2012.

[197] Nima Sarli, Giuseppe Del Giudice, Duke S Herrell, and Nabil Simaan. A resectoscope for robot-assisted transurethral surgery. *J Med Device*, 10(2):020911, 2016.

[198] Alexander T Hillel, Ankur Kapoor, Nabil Simaan, Russell H Taylor, and Paul Flint. Applications of robotics for laryngeal surgery. *Otolaryngologic Clinics of North America*, 41(4):781–791, 2008.

[199] J. Li and J. Xiao. Task-constrained continuum manipulation in cluttered space. In *2014 IEEE International Conference on Robotics and Automation (ICRA)*, pages 2183–2188, May 2014.

[200] Austin Reiter and Peter K Allen. An online learning approach to in-vivo tracking using synergistic features. In *Intelligent Robots and Systems (IROS), 2010 IEEE/RSJ International Conference on*, pages 3441–3446. IEEE, 2010.

[201] Lydia E. Kavraki, Petr Svestka, Jean Claude Latombe, and Mark H. Overmars. Probabilistic roadmaps for path planning in high-dimensional configuration spaces. *IEEE Transactions on Robotics and Automation*, 12(4):566–580, 1996.

[202] Matthew A. Baumann, Donna C. Dupuis, Simon Leonard, Elizabeth A. Croft, and James J. Little. Occlusion-free path planning with a probabilistic roadmap. *2008 IEEE/RSJ International Conference on Intelligent Robots and Systems, IROS*, pages 2151–2156, 2008.

[203] Matthew Baumann, Simon Leoonard, Elizabeth A. Croft, and James J. Little. Path planning for improved visibility using a probabilistic road map. *IEEE Transactions on Robotics*, 26(1):195–200, 2010.

[204] Simon Leonard, Elizabeth A. Croft, and James J. Little. Planning collision-free and occlusion-free paths for industrial manipulators with eye-to-hand configuration. *2009 IEEE/RSJ International Conference on Intelligent Robots and Systems, IROS 2009*, pages 5083–5088, 2009.

[205] Guillaume Morel, Thomas Liebezeit, Jérôome Szewczyk, Sylvie Boudet, and Jacques Pot. Explicit incorporation of 2D constraints in vision based control of robot manipulators. In *Experimental Robotics VI*, pages 99–108. Springer London, London, 2000.

[206] P.I. Corke and S.A. Hutchinson. A new partitioned approach to image-based visual servo control. *IEEE Transactions on Robotics and Automation*, 17(4):507–515, 2001.

[207] Youcef Mezouar and François Chaumette. Avoiding self-occlusions and preserving visibility by path planning in the image. *Robotics and Autonomous Systems*, 41(2):77–87, 2002.

[208] Noah Cowan. Binocular visual servoing with a limited field of view. In *In Mathematical Theory of Networks and Systems, Notre*, 2002.

[209] V. Lippiello, B. Siciliano, and L. Villani. An Occlusion Prediction Algorithm for Visual Servoing Tasks in a Multi-Arm Robotic Cell. In *2005 International Symposium on Computational Intelligence in Robotics and Automation*, pages 733–738. IEEE, 2005.

[210] Anthony A Maciejewski and Charles A Klein. Obstacle avoidance for kinematically redundant manipulators in dynamically varying environments. *The international journal of robotics research*, 4(3):109–117, 1985.

[211] Oussama Khatib. Real-Time Obstacle Avoidance for Manipulators and Mobile Robots. *The International Journal of Robotics Research*, 5(1):90–98, 1986.

[212] Bruno Siciliano, Lorenzo Sciavicco, Luigi Villani, and Giuseppe Oriolo. *Robotics: Modelling, Planning and Control*. Springer Publishing Company, Incorporated, 1st edition, 2008.

[213] Jean-Claude. Latombe. *Robot motion planning*. Kluwer Academic Publishers, 1991.

[214] Kai Xu and Nabil Simaan. An investigation of the intrinsic force sensing capabilities of continuum robots. *IEEE Transactions on Robotics*, 24(3):576–587, 2008.

[215] A. Bajo and N. Simaan. Kinematics-based detection and localization of contacts along multisegment continuum robots. *IEEE Transactions on Robotics*, 28(2):291–302, April 2012.

[216] Stephen Boyd and Lieven Vandenberghe. *Convex Optimization*. Cambridge University Press, New York, NY, USA, 2004.

[217] Alain Liegeois. Automatic Supervisory Control of the Configuration and Behavior of Multibody Mechanisms. *IEEE Transactions on Systems, Man, and Cybernetics*, 7(12):868–871, 1977.

[218] Lung-Wen Tsai. *Robot Analysis and Design: The Mechanics of Serial and Parallel Manipulators*. John Wiley & Sons, Inc., New York, NY, USA, 1st edition, 1999.

[219] A Morecki. Synthesis and control of the anthropomorphic two-handed manipulator. In *Proc. 10th Int. Symposium on Industrial Robots*, volume 461, 1980.

[220] Sophie Thielmann, Ulrich Seibold, Robert Haslinger, Georg Passig, Thomas Bahls, Stefan Jörg, Mathias Nickl, Alexander Nothhelfer, Ulrich Hagn, and Gerd Hirzinger. Mica-a new generation of versatile instruments in robotic surgery. In *Intelligent Robots and Systems (IROS), 2010 IEEE/RSJ International Conference on*, pages 871–878. IEEE, 2010.

[221] Saleem Abdul Hamid and Nabil Simaan. Design and synthesis of wire-actuated universal-joint wrists for surgical applications. In *Robotics and Automation, 2009. ICRA'09. IEEE International Conference on*, pages 1807–1813. IEEE, 2009.

[222] Zhangshi Liu. *Analysis and Modeling of Wire-actuated Wrist with a Universal Joint*. Master's thesis, Vanderbilt University, 2016.

[223] Andrew Orekhov, Colette Abah, and Nabil Simaan. Snake-like robots for minimally invasive, single port, and intraluminal surgeries. In *The Encyclopedia of Medical Robotics*, volume 1, chapter 8. World Scientific, 2018.

[224] J Kenneth Salisbury and B Roth. Kinematic and force analysis of articulated mechanical hands. *Journal of Mechanisms, Transmissions, and Automation in Design*, 105(1):35–41, 1983.

[225] Carl F Ruoff and J Kenneth Salisbury Jr. Multi-fingered robotic hand, May 1 1990. US Patent 4,921,293.

[226] Steve C Jacobsen, John E Wood, DF Knutti, and Klaus B Biggers. The utah/mit dextrous hand: Work in progress. *The International Journal of Robotics Research*, 3(4):21–50, 1984.

[227] Steve Jacobsen, Edwin Iversen, D Knutti, R Johnson, and K Biggers. Design of the utah/mit dextrous hand. In *Robotics and Automation. Proceedings. 1986 IEEE International Conference on*, volume 3, pages 1520–1532. IEEE, 1986.

[228] Stephen C Jacobsen, Hiekeun Ko, Edwin K Iversen, and Clark C Davis. Antagonistic control of a tendon driven manipulator. In *1989 IEEE International Conference on Robotics and Automation*, pages 1334–1339. IEEE, 1989.

[229] Samuel Ernest Landsberger. A new design for parallel link manipulators. In *Proc. of the IEEE International Conference on Systems*, pages 812–814, 1985.

[230] Huu Minh Le, Thanh Nho Do, and Soo Jay Phee. A survey on actuators-driven surgical robots. *Sensors and Actuators A: Physical*, 247:323–354, 2016.

[231] Jeff M Wendlandt and S Shankar Sastry. Design and control of a simplified stewart platform for endoscopy. In *Decision and Control, 1994., Proceedings of the 33rd IEEE Conference on*, volume 1, pages 357–362. IEEE, 1994.

[232] A Morecki, Z Busko, H Gasztold, and K Jaworek. Synthesis and control of the anthropomorphic two-handed manipulator. In *Proceedings of the 10th international symposium on industrial robots*, pages 461–474, 1980.

[233] Lung-Wen Tsai and Jyh-Jone Lee. Kinematic analysis of tendon-driven robotic mechanisms using graph theory. *Journal of mechanisms, transmissions, and automation in design*, 111(1):59–65, 1989.

[234] Jyh-Jone Lee and Lung-Wen Tsai. The structural synthesis of tendon-driven manipulators having a pseudotriangular structure matrix. *The International Journal of Robotics Research*, 10(3):255–262, 1991.

[235] Hiroaki Kobayashi, Kazuhito Hyodo, and Daisuke Ogane. On tendon-driven robotic mechanisms with redundant tendons. *The International Journal of Robotics Research*, 17(5):561–571, 1998.

[236] V. Agrawal, W. J. Peine, B. Yao, and S. Choi. Control of cable actuated devices using smooth backlash inverse. In *2010 IEEE International Conference on Robotics and Automation*, pages 1074–1079, May 2010.

[237] Gianluca Palli, Gianni Borghesan, and Claudio Melchiorri. Modeling, identification, and control of tendon-based actuation systems. *IEEE Transactions on Robotics*, 28(2):277–290, 2012.

[238] L. Chen, X. Wang, and W. L. Xu. Inverse transmission model and compensation control of a single-tendon-sheath actuator. *IEEE Transactions on Industrial Electronics*, 61(3):1424–1433, March 2014.

[239] T.N. Do, T. Tjahjowidodo, M.W.S. Lau, T. Yamamoto, and S.J. Phee. Hysteresis modeling and position control of tendon-sheath mechanism in flexible endoscopic systems. *Mechatronics*, 24(1):12 – 22, February 2014.

[240] Z. Sun, Z. Wang, and S. J. Phee. Elongation modeling and compensation for the flexible tendon–sheath system. *IEEE/ASME Transactions on Mechatronics*, 19(4):1243–1250, Aug 2014.

[241] Marc Gouttefarde, Jean-Pierre Merlet, and David Daney. Wrench-feasible workspace of parallel cable-driven mechanisms. In *Robotics and Automation, 2007 IEEE International Conference on*, pages 1492–1497. IEEE, 2007.

[242] Louis B Rosenberg. Virtual fixtures as tools to enhance operator performance in telepresence environments. In *Telemanipulator technology and space telerobotics*, volume 2057, pages 10–22. International Society for Optics and Photonics, 1993.

[243] Gabor Fichtinger, Peter Kazanzides, Allison M Okamura, Gregory D Hager, Louis L Whitcomb, and Russell H Taylor. Surgical and interventional robotics: Part ii. *IEEE Robotics & Automation Magazine*, 15(3), 2008.

[244] SH Yeo, G Yang, and WB Lim. Design and analysis of cable-driven manipulators with variable stiffness. *Mechanism and Machine Theory*, 69:230–244, 2013.

[245] Bram Vanderborght, Alin Albu-Schäffer, Antonio Bicchi, Etienne Burdet, Darwin G Caldwell, Raffaella Carloni, MG Catalano, Oliver Eiberger, Werner Friedl, Ganesh Ganesh, et al. Variable impedance actuators: A review. *Robotics and autonomous systems*, 61(12):1601–1614, 2013.

[246] Jinoh Lee, Arash Ajoudani, Enrico Mingo Hoffman, Alessio Rocchi, Alessandro Settimi, Mirko Ferrati, Antonio Bicchi, Nikolaos G Tsagarakis, and Darwin G Caldwell. Upper-body impedance control with variable stiffness for a door opening task. In *Humanoid Robots (Humanoids), 2014 14th IEEE-RAS International Conference on*, pages 713–719. IEEE, 2014.

[247] Joseph Edward. Shigley and Charles R. Mischke. *Mechanical engineering design*. McGraw-Hill, 1989.